Non-linear, Non-spherical Bubble Dynamics Near a Two Fluid Interface

by

Geoffrey Aylwyn Curtiss

A thesis submitted to
The University of Birmingham
for the degree of
Doctor of Philosophy

School of Mathematics
The University of Birmingham
June 2009

Abstract

The interactions of bubbles with rigid and free boundaries have been well documented. Toroidal bubble formation has been observed, with jetting directed toward and away from the two types of interface respectively. This work generalises these interactions by studying the effect of a two fluid interface supporting a density discontinuity. Such interactions may provide significant new insight into the mechanisms present in bubble assisted mixing processes, and in biomedical procedures including laser ablation and sonoporation.

A numerical investigation has been conducted to examine the essentially incompressible fluid dynamics of the exterior liquid layers, based on a boundary integral implementation coupled with the vortex ring toroidal bubble model [53].

The transition through the null impulse state has been investigated, demonstrating excellent agreement with the water/white spirit experiments of Chahine and Bovis [23]. Close standoff distance simulations have illustrated the retardation of surface spiking with increasing density ratios, and have shown how the toroidal phase can be beneficial to mixing processes. Multi-bubble simulations have demonstrated that the deformation to the interface is greatly affected by the configuration of the bubble column. The acoustic driving of ultrasound contrast agents near tissue layers has also been investigated, demonstrating a new mechanism for tissue damage due to the toroidal re-expansion, the membrane peeling phenomenon.

Acknowledgements

I would like to express my sincere gratitude to Professor John Blake, and Doctors David Leppinen, Quan Xi Wang and Michael Calvisi, my supervisors and the bubble dynamics group at the University of Birmingham. They have provided me with a great deal of valuable insight, motivation and advice in tackling the problems I have investigated, and for that I remain eternally indebted.

I would also like to thank all those at NAG and the Smith Institute for the opportunity to partake in an excellent internship. As I write this I look forward to many more years with NAG, something that would not have happened if it were not for this experience.

I am also very grateful to the EPSRC for funding me throughout my PhD.

Less formally, I would like to thank those who have assisted my study of bubbly flows through the mediums of fermented beverages and cake. In particular, I would like to explicitly thank those in office 312 for their encyclopedic knowledge of flash games, Star Wars, the military history of the British Empire, Aberystwyth, silent film, distance running and cricket. All of these were invaluable in the formation of this thesis.

Thanks must also go to my family. Their support has been crucial in the completion of this thesis, and indeed throughout everything that has been before and everything that is going to come.

Et Marianne, merci pour tout.

Contents

1 Introduction **1**
- 1.1 Motivation for the study of cavitation . . . 1
- 1.2 Aim: Understanding cavitation collapse near complex interfaces . . . 16
- 1.3 Thesis Overview . . . 16

2 Spherical Bubble Dynamics and the Kelvin Impulse **21**
- 2.1 The Rayleigh-Plesset equation . . . 21
- 2.2 Behaviour in the absence of acoustic forcing . . . 25
- 2.3 Behaviour in the presence of acoustic forcing . . . 28
- 2.4 Viscous effects and shell encapsulation . . . 30
- 2.5 Spherical approximation to the two fluid problem . . . 35
- 2.6 Approximating the Kelvin impulse . . . 41
- 2.7 Chapter summary . . . 43

3 The Boundary Integral Method for Cavitation Bubbles Collapsing Near a Fluid-Fluid Interface **45**
- 3.1 Boundary value problem . . . 48
  - 3.1.1 Surface interpolation using splines . . . 48
  - 3.1.2 Calculation of the surface curvature . . . 58
  - 3.1.3 Kinematic and dynamic boundary conditions . . . 59
  - 3.1.4 Green's Integral Formula . . . 64
  - 3.1.5 Discretisation and function interpolation . . . 68
  - 3.1.6 The integral formula in the context of the two fluid interface . . . 72
  - 3.1.7 Initial conditions . . . 76
  - 3.1.8 Time-stepping . . . 76
  - 3.1.9 The calculation of the time interval dt . . . 79
  - 3.1.10 The evaluation of surface integrals with singular integrands . . . 80
  - 3.1.11 Far field approximations . . . 83
  - 3.1.12 Nodal re-gridding and surface smoothing . . . 88
  - 3.1.13 Field solutions and the calculation of physical quantities . . . 90
- 3.2 Chapter summary . . . 95

4 Toroidal bubble model **96**
4.1 Vortex ring bubbles . . . 96
4.1.1 Numerical toroidalisation procedure . . . 98
4.1.2 Decomposed surface boundary conditions . . . 103
4.1.3 Coupled boundary integral equations . . . 104
4.2 Chapter summary . . . 106

5 Boundary integral method verification and comparison with experiments **107**
5.1 Spline verification . . . 108
5.1.1 Curvature calculations . . . 113
5.2 Comparison with analytic solutions . . . 115
5.2.1 Incompressible spherical droplet . . . 115
5.2.2 Comparison with Rayleigh-Plesset equations . . . 121
5.2.3 Infinite surface verification . . . 130
5.3 Pressure field comparisons . . . 132
5.4 Failure due to surface intersection . . . 134
5.4.1 Existing methods for increasing stability . . . 136
5.5 Comparison with experimental solutions . . . 138
5.5.1 Free surface comparison . . . 138
5.5.2 Rigid boundary comparison . . . 139
5.5.3 Comparisons with existing research involving fluid-fluid interfaces and the null impulse state . . . 141
5.6 Chapter summary . . . 149

6 Single bubble interactions with the two fluid interface **152**
6.1 Standoff distance effects on bubble behaviour . . . 153
6.2 Interfacial spiking at low density ratios . . . 160
6.3 Interfacial indentation . . . 166
6.4 Behaviour as the density ratio approaches unity . . . 169
6.5 Bubble attraction and toroidal jetting for $\rho > 1$ . . . 171
6.6 Summary . . . 180

7 Multi-bubble behaviour near a density jump **185**
7.1 Two bubbles in a homogeneous configuration . . . 186
7.2 Two bubbles in a heterogeneous configuration . . . 190
7.3 Three bubble heterogeneous configurations . . . 200
7.4 Chapter Summary . . . 208

8 Ultrasound activated cavities and their interaction with a tissue layer **210**
8.1 Initial conditions . . . 210
8.2 Membrane effects . . . 212
8.3 The influence of rigid backing . . . 216
8.3.1 Membrane peeling at sub-MHz frequencies . . . 218

8.3.2 Backed behaviour at 1 MHz 224
8.3.3 New experimental evidence of peeling 237
8.4 Chapter summary 237

9 Conclusions and avenues for future research **240**
9.1 Conclusions 241
9.2 Avenues for future research 247

List of References **249**

Chapter 1

Introduction

1.1 Motivation for the study of cavitation

The simplest form of a bubble is a volume of gas surrounded by a liquid. Many natural mechanisms exist for their creation, including the expulsion of air from marine mammals, and the trapping of air by overturning waves. Such bubbles behave in a relatively stable manner, rising due to their buoyancy until they reach the surface of the liquid. They are also generated through many biological and chemical processes, such as fermentation and the reaction of sodium in water. The research presented in this thesis however, is concerned with the rapid and violent behaviour symptomatic of cavitation and explosion bubbles.

Cavitation bubbles occur when the pressure in a volume of liquid drops below the corresponding vapour pressure, causing a rapid phase transition that literally tears the liquid apart. Their subsequent motions can cause severe degradation to surrounding structures, such as dam spill ways and reactor coolant piping. The mechanisms for damage are however beneficial in many biomedical and industrial processes, and hence their understanding is of great importance. Similarly, very high pressure bubbles, such as those generated by a torpedo or underwater mine, are highly destructive. Indeed the fluid

dynamics following their creation will often cause more damage than the shock from the explosion itself. As with the cavitation bubbles, effective manipulation of the fluid motion can be greatly beneficial when employed in laser based surgical techniques, where high pressure micro-bubbles are formed through laser vapourisation of the liquid.

The original interest in cavitation was as an explanation for marine corrosion. In some famous historical examples, such as the case of RMS Lusitania, ship propellers were found to disintegrate rapidly once in use, with turbulent cavitated flows observed in their vicinity. It was postulated that this damage resulted from collapsing cavitation bubbles on or near the surface of the propellers. This motivated the work of Lord Rayleigh [73] amongst others, who investigated the growth and collapse of an oscillating spherical cavity due to a constant external pressure. In this inertially driven flow, extremely high pressures were shown to be obtained close to the bubble surface and resultantly the link between cavitation bubbles and the observed corrosion was verified. This pioneering foray laid the foundation for the following century of both theoretical and experimental research into cavitation. The spherical model has since been further developed by many authors, with the notable contribution by Plesset of the incorporation of surface tension and viscous effects, creating what is now known as the Rayleigh-Plesset equation [67]. Dimensional analysis of this equation illustrates that for bubbles of radii $\sim o(1mm)$, buoyancy effects are negligible whereas surface tension should be included. In large bubbles, with radii $\sim O(cm)$ and greater, buoyancy will dominate surface tension and viscosity. Further spherical bubble analysis and relevant adaptations are given in Chapter 2.

Naval warfare, particularly during the Second World War, generated substantial interest as the effect of underwater explosions provided excellent examples of inertially dominant bubbles. A famous example of the effect of detonating an explosive underwater, as opposed to on land or in air, is the attacks on the Eder and Möhne dams. Due to the influence of the water, much smaller explosives were required to breach the dams

than would have been the case for a direct overhead hit. Much of the research during this period concerned spherical bubbles, as this is the behaviour experimentally observed during the bulk of the lifetime of an underwater explosion. A review of this period of research is provided by Cole [28].

A major feature of cavitation, and of key importance in cavitation erosion, remained unproven until the work of Benjamin and Ellis [4]. The experiments they conducted showed that the presence of a flat solid boundary caused the formation of a liquid jet through the axis of a bubble in the direction of the rigid boundary. This would impact the opposing bubble pole to form a toroid. Such behaviour has been observed in many other experiments since, when using both high pressure and acoustically driven bubbles [7-12]. The speed of this jet in the absence of buoyancy is observed to strongly depend on the standoff distance. This is the distance between the bubble centroid at inception and the boundary, normalised by the maximum radius the bubble would reach in an infinite fluid[1], either determined experimentally or derived in some way from the Rayleigh-Plesset equation (see Chapter 2). Jet speeds have been shown to be greatest in laser generated bubbles for standoff distances of about three maximum bubble radii [17].

Aside from the behaviour near solid interfaces, toroidal features are also observed when a bubble collapses near a free surface. In such conditions bubble jetting may be directed away from the surface, and may be accompanied by the formation of a counter jet causing the surface to spike. Experiments by Gibson and Blake [36] using spark generated bubbles under free fall conditions, and Chahine and Bovis [23] in normal gravity, showed this counter jet to be greatly influenced by the standoff distance. Bubbles formed very close to the surface result in very pronounced vertical jets as shown in figure 5.21, whilst those at greater distances cause much smaller deformations. Beyond a critical standoff distance no surface spike will form and the only deformation to the interface will be from

[1]The equilibrium radius is used in some instances, particularly for bubbles subjected to strong acoustic fields [21].

the volume of the bubble.

Experiments have also demonstrated that gravity can effect bubble migration and the direction of the high speed threading jets, most predominantly in bubbles with radii greater than 1 cm. If buoyancy is large enough, the repulsive effect of a free surface and the attractive nature of a rigid boundary can in fact be overcome. This interaction with gravity has been studied analytically by using the Kelvin impulse as a measure of the fluid inertia [8]. First named by Benjamin and Ellis [4], this approach describes the effect of applying 'an impulsive wrench' to the fluid. Point source approximations for this have shown excellent agreement with experiments, both with rigid boundaries and free surfaces for standoff distances greater than one maximum bubble radii [8]. As will be shown in the simulations and experiments illustrated in Chapter 5, these are also valid for a fluid-fluid interface supporting a density discontinuity.

Perturbation methods have been applied to the spherical model to investigate deformations to bubble shapes, and have also been used for the inclusion of viscous and thermal effects across the surface of a cavity (see for example [71, 39, 16]). Yet by the nature of these approximations, they cannot account for large deformations crossing the bubble centroid, deformations that certainly occur during bubble jetting. Therefore, in order to accurately model the bubble behaviour near boundaries numerical models must be employed. Various field based approaches have been used for this endeavour. These have included using volume of fluid methods [68], finite element methods coupled with level set boundary tracking [80, 61] and recently Lattice Boltzmann methods [82]. Due to the rapidly evolving flow fields however, these require high resolution meshes to remain stable and to capture the liquid/gas interface at the bubble surface. Resultantly these can be computationally expensive, particularly when allowing for liquid compressibility.

Other approaches have been constructed using boundary integral methods, BIM, under the assumption that the surrounding fluid is essentially incompressible, at least in

comparison to the gas contents of the bubbles. This simplification however, provides only a leading order approximation in terms of the reciprocal of the speed of sound in the liquid [41]. Indeed the effects of liquid compressibility have been seen experimentally near minimum bubble volumes, as evidenced by the presence of shock waves emanating from the cavities [66, 18]. However, the results gained using BIM techniques have shown excellent agreement with experimental bubble shapes and oscillation times when jetting is at sub-sonic velocities. This is typical for shallow to intermediate standoff distances [64], yet may no longer be appropriate in some acoustically driven instances [21]. Whilst the field based approaches mentioned can be used to include viscosity, compressibility and rotation into the fluid domain, the effect these may have on the predominantly inertial characteristics investigated herein is not thought to outweigh their substantial increase in computational cost over the boundary integral method. These effects are presumed to be minimal in all but the most violent bubble motion, and so this work will employ a realisation of the boundary integral method.

Boundary integral simulations of both the expansion and collapse of a simply connected bubble in the vicinity of both a rigid wall and a free surface were achieved by Taib for moderate standoff distances [81, 10, 11]. The use of the this method, coupled with an axisymmetric model for the flow field, allowed the three dimensional problem to be effectively reduced to one dimension. Previous investigations using this method were initiated from a spherical cavity of maximum radius, and gave no account for small non-spherical effects in the expansion phase [50]. The numerical results gained by including the expansion phase were in excellent agreement with experimental collapses near rigid boundaries [81, 10]. These results illustrated that high pressures are concentrated on the bubble axis, on the opposing side to the solid wall. Slower, broader jets were observed for shallower standoff distances than for larger standoff distances, and simulations also demonstrated the transition between the domination of the Bjerknes forces associated

with the boundary and gravity. However, due in part to the lack of computational power at the time, these simulations could not accurately capture the motion of the slender threading jets associated with free surface collapses at small standoff distances up to the point of jet impact. Subsequent improvements to this model are now capable of simulating this to a high degree of accuracy [25, 30-33]. It has also been used to model the bursting of entrained bubbles at a free surface, demonstrating how a surface spike can be generated from the base of the bubble pit as the burst edge recedes [15, 14, 35]. This is in fact the mechanism for the formation of liquid jets and droplets in champagne and at ocean surfaces, and leads to much higher heat transfer rates than that associated with an unperturbed surface alone.

Proceeding through the transition from a simply connected bubble to a toroidal bubble, and modelling the subsequent fluid motion, provides a difficulty for the boundary integral approach. The domain becomes doubly connected negating the uniqueness of the solution to Laplace's equation upon which the method is based. The Kelvin impulse must also be conserved, resulting in a circulation about the toroid which is not present if one simply equates the potential at the site of jet impact [8].

An effective method developed by Best [5] involves maintaining a singly connected domain by the introduction of a contour across the potential discontinuity at the time when the bubble becomes toroidal. The solution to the system is modified by maintaining a jump in potential across the contour, and including the associated surface integrals into the numerical scheme. Initial work with this method tracked the circulation of the contour about the bubble, and hence became computationally inhibitive as the contour became more convoluted. This was enhanced by allowing the contour to be arbitrarilly mapped to a simple disk, as the fluid velocity is only dependent on the gradient of the potential [7]. Results gained using this approach agree strongly with experimental observations in the vicinity of both rigid boundaries [6, 17], and free surfaces [64, 74]. However the Best

contour, or domain cut, technique is restricted to axisymmetric cases and presumes the influence of the vortex sheet surrounding the jet after impact to be negligible.

Maintaining the vortex sheet formed by the impacting jet has been attempted by Zhang *et al* [91]. In this technique the bubble is attached to the advancing vortex sheet at a geometric triple point, with the surface and potential interpolated across both the bubble and each side of the sheet. The bubble interior at the triple point takes the form of a cusp. Results gained from this time intensive approach differ from those obtained using the technique of Best, showing far less rotation about the bubble toroid [90]. Additionally, whereas the previous method shows a single high pressure region at the impact site, the results of this method show the formation of a high pressure ring about the penetrating jet.

An alternative approach, initially proposed by Lundgren and Mansour [53] and improved by Wang *et al* [89], is to thread the bubble with a vortex ring. This accounts for the circulation in the fluid caused by the bubble threading and renders the remaining potential unique [89]. As with the method of Best [5], this has been employed for axisymmetric bubbles in the vicinity of both rigid boundaries and free surfaces, showing excellent agreement both with experiments and the aforementioned simulations. It also has the advantage of being readily implemented in three dimensional simulations without axial symmetry, essential for the accurate modelling of bubble motion in complicated geometries [87, 88, 92]. This does however currently require the manual reconnection of the bubble jet tip and the impact site due to the complexities of fully three dimensional surface discretisation. These simulations have shown free surface spiking to be lessened by the presence of multiple bubbles, and have shown the influence on bubble jetting of buoyancy in the case of a bubble near an inclined wall [87]. Like the domain cut technique, this method also ignores the effect of the vortex sheet formed about the liquid jet after it impacts on the far side of bubble. This approach is employed herein and details

of its implementation may be found in Chapter 4.

The simulation of two incompressible and inviscid liquid flows has also been extensively investigated in many different contexts. These range from the development of interfacial waves between fresh and salt water, to the capillary pinch-off of droplets surrounded by fluid. Many numerical methods have been used depending on the context and severity of the interfacial disturbances. In capillary pinch off for example, source distribution methods are viable. The full boundary integral formulation has been used in each fluid region [42, 31], although it is often more efficient computationally to use dipole distributions to eliminate the normal velocity balance from the inversion step [51, 53]. More computationally intensive vortex sheet methods have also been used to calculate the dynamics based on vorticity contained within the fluid surfaces themselves. These involve the evaluation of the principal value of the Biot-Savart integral along the two fluid interfaces, and require continuous surface curvatures everywhere [62, 69, 63].

In larger scale applications, such as the modelling of internal waves between stratified layers in coastal oceans, large interfacial waves can develop. These can exhibit strongly non-linear behaviour, with significantly broad wave peaks. Further these waves may overturn in some circumstances [40, 34]. This renders weakly non-linear approximations, including the Körteweg de Vries and intermediate long wave models, at best qualitative in their solution [40, 38, 25]. Furthermore, in such cases the above source distribution methods can become unstable. Alternative methods have been developed, such as the use of Cauchy's equation by Grue *et al* [38] in the simulation of two dimensional interfacial waves. Other approaches have used field solutions, such as that employed by Shin [76] using a level set tracked interface in collaboration with an unstructured ghost fluid method.

The dipole and vortex sheet methods both require knowledge of the tangential and normal fluid velocities on either side of all the interfaces. This information is not however

known for the interior of the bubbles investigated here, as this would require the solution of the fully compressible Euler equations throughout the entire simulation in every bubble volume. This would be extremely computationally expensive, whilst most likely not significantly affecting the inertially dominated dynamics of the surrounding liquid layers. As a result the incorporation of these methods is not performed in this work. Further, the bubble lifetime in the cases investigated herein is of a much shorter time scale than that required for significant wave effects to propagate along the two fluid interface. It is assumed that the governing dynamics are essentially axisymmetric and that resultantly a fully three dimensional approach is not required. Nevertheless, an axisymmetric model is still three dimensional, and therefore the use of complex integral techniques is not valid. Hence in this work, the interfacial motion is tracked through the solution of the full boundary integral equations in each exterior fluid, as is expressed in equation (3.26) in Chapter 3, coupled through the normal stress balance and continuity of normal velocity at the two fluid interface.

Whilst industrial and military uses for cavitation have now long been established, recent advances in medicine have also created new avenues for cavitation, thus motivating the current research. The phenomena, whilst originally occurring as an unwanted side effect, is now being developed as an effective, targetable mechanism for damaging organic structures. It may be particularly prevalent in various types of laser surgery. These include techniques such as laser angioplasty, myocardial laser revascularisation, laser thrombolysis and intraocular photodisruption [18]. Figure 1.1 shows an experimental example of the type of damage which may be inflicted upon a cornea during intraocular photodisruption. Here a bubble has been created using a focused laser beam parallel to a cornea specimen at a standoff distance of 0.45. The result of the subsequent collapse of this cavity is very apparent, with a puncture clearly visible in the centre of the affected region almost certainly created by the high speed jet that would have thread the bubble. A large region

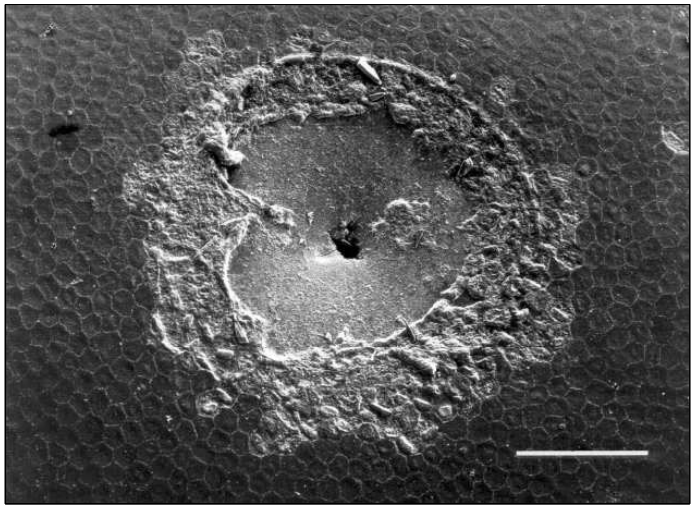

Figure 1.1: Cavitation damage to a cornea specimen. The white bar represents a distance of $100\mu m$, whilst the laser generated bubble was formed at a standoff distance of 0.45 maximum bubble radii [86].

of surface tissue has also been scrapped away during the bubble motions. The mechanisms for this are as yet unknown, with the high shear stresses caused by the high speed flow between the bubble and substrate thought to be a contributing factor [86, 18]. Results gained through this research however, and presented in Chapter 8, demonstrate that the re-expansion of the bubble toroid may also play a significant role, and may even be the primary mechanism for such surface scouring.

Aside from laser generated high pressure bubbles, sonically driven cavitation is also prevalent in modern medical procedures. One such procedure is shockwave lithotripsy. In this a semi-ellipsoidal structure is placed adjacent to a patient, focusing shockwaves generated at the external focus to the focus located inside the body. Removal of kidney and bladder stones via this procedure benefits from the collapse phenomena, with the focusing of the shockwave creating tiny cavities close to the surface of the target object [77]. The side effects of this technique, potentially magnified by unwanted cavitation, can

be problematic and can include major vain thrombosis and gastro-intestinal injuries such as colon perforation [77].

Other medical techniques have been developed using both low and high frequency ultrasound to acoustically activate cavitation during diagnostic procedures. The use of ultrasound contrast agents (UCA) to improve the echogenicity of biological fluids is one such technique. These are encapsulated micron scale gas bubbles with thin shells, which can be easily administered to a patient through injection or ingestion. Examples of such products include protein shelled encapsulated air UCA's such as Albunex, and modern soft lipid shelled perflurocarbon encapsulated UCA's such as SonoVue [29, 54]. The acoustic signature produced by the compressible UCA's is significantly higher than that of the near incompressible tissues, and provides great improvement in visualisation, particularly in detecting focal liver lesions [26, 13, 29].

At higher ultrasound amplitudes, UCA's will break down in the acoustic field. This structural failure allows for their potential use as locally targetable drug delivery vesicles [29, 72, 75]. Of particular note is the manner in which breakdown occurs, and the damage it can cause to surrounding tissue. An example of the damaging effect caused by such operations can be seen in figure 1.2, showing samples of mouse abdominal muscle after ultrasound exposure, using a $2.5MHz$ transducer at an amplitude of $2.6MPa$ with and without the contrast agent Optison. Peterial haemorrhages are visible in abundance as red dots and streaks in the agent treated sample, yet there are few, if any, in the untreated case [57].

This seemingly unwanted side affect has recently been pioneered as a local delivery method for large molecules. In particular it can be used to deliver DNA, and hence is being actively researched as a non-viral method for gene transfection [59, 58, 13]. This process, termed sonoporation, involves the local induction of cavitation dynamics using ultrasound to permeate cell membranes, thereby allowing DNA introduced into the extracellular envi-

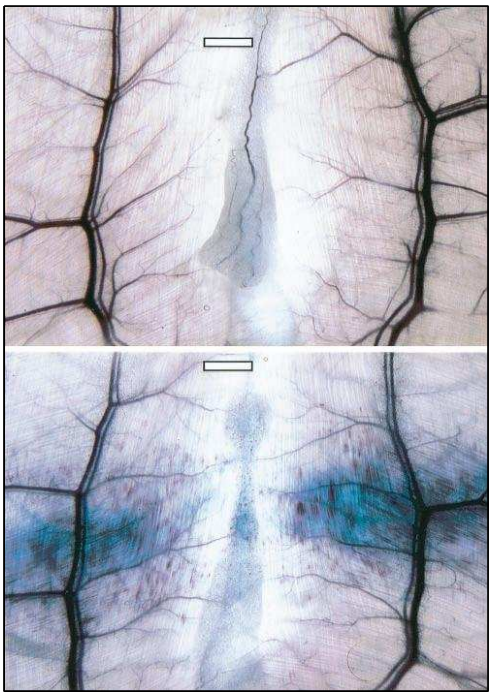

Figure 1.2: Abdominal mouse muscle and fat after ultrasound exposure using a $2.5MHz$ transducer at an amplitude of $2.6MPa$. The contrast agent Optison was used in the specimen displayed in the lower image. Abundant peterial haemorrhages are visible in the lower sample as red dots and streaks. The white bar represents 1mm [57].

ronment to enter the target cells [58]. The potential benefits of sonoporation over existing transfection techniques are considerable. Viral encapsulation delivery systems suffer from possible toxicological and mutagenic side effects, whilst other encapsulation techniques such as lipid coating, are not locally focusable [59]. Locally targeted non-encapsulation methods also exist, although these have difficulties with implementation. Electroporation for example requires electrodes to be inserted into the target area to induce cell membrane separation, and the direct injection of DNA into cells is naturally restricted to external applications. Transfection through sonoporation in contrast is easily administered externally, and is readily locally focused. Excessive cavitation caused during the application can however cause significant damage and cell death [47], with the generation of sonopores on the size order of magnitude of a cell [70]. To minimise the amount of cell death, and to determine the mechanisms from which it arises, the fluid dynamics of both the intra and extracellular environments need to be examined. Similarly to help maximise the viable poration of cell membranes, the dynamics associated with the collapse of the UCA's is of critical importance.

The organic environments with which these cavities interact can not in general be viewed simply as rigid boundaries. Aside from the complex topology of the surroundings, the elasticity of the cell membranes and the fluid which they enclose must be taken into consideration. This is evident from recent experiments with initially flat elastic surfaces. These have shown that the elastic modulus of the substrate and the standoff distance of the interacting bubble have drastic effects on the bubble dynamics, both with regards to the translation of the bubble and the jet direction [18, 19]. Indeed in some cases horizontal bubble splitting is observed, resulting in very slender high speed jets forming in opposing directions. This potentially has a significant impact on membrane permeation, and explains the significant maximum bubble radius to jet width ratio of 60:1 observed in the experiment shown in figure 1.1 [18, 86].

Recent numerical investigations using BIM techniques by Klaseboer and Khoo [45, 46] accounting for these interfacial properties have shown qualitative agreement with such experiments. In their simulations, it was assumed that the jump in tangential velocities across the fluid-fluid interface was sufficiently small to be neglected from the dynamic boundary conditions, with marginal discrepancies observed in their test cases. The procedure employed depended upon a geometrical argument valid for a single bubble in an infinite fluid, utilising the trivial density ratio of 1. This allowed for the interfacial potential in the cavitated fluid to be found independently of the normal velocity of the two fluid interface, by equating various aspects of the coefficient matrices. Elastic effects were also investigated by means of a modification to the pressure in the fluid not containing the cavitation, and hence a modification to the dynamic condition on the liquid-liquid boundary [46]. This showed marked differences to the case where no elasticity is present, allowing for the aforementioned bubble splitting to be observed. Further investigations using this implementation have researched acoustically driven bubble behaviour at sub-atmospheric pressure amplitudes near an interface given realistic biological parameters, demonstrating some of the shapes the bubbles may attain during pre-toroidal motions [33]. As in the experiments near elastic interfaces, these simulations have shown bubble motion and jet direction to both be affected by the properties of the material. Prior to the research contained herein however, toroidal effects have not been investigated in this context.

Coupled BIM-FEM systems have recently been developed to account for elastic boundaries near bubbles. Maio and Graciewski [56] used this to simulate linearly elastic axisymmetric interactions, both of a bubble near an infinite elastic surface and a bubble confined in an elastic tube. The results for the infinite plate were in agreement with the experiments of Brujan [18], and the tube encapsulated simulations have shown the generation of ellipsoidal bubbles and consequent perpendicular pinching behaviour. The limitation of

the axisymmetric geometry however did not permit off centre interactions, as the development of jets towards the tube walls was impossible. Three dimensional interactions with a toroidal bubble and an elastic plate have been also simulated by Klaseboer *et al* [44] in the context of an underwater explosion, using a BIM/vortex ring method for the fluid dynamics coupled with an FEM model for the plate. This was successful in capturing the plastic deformations to a steel plate caused by the dynamics associated with a collapsing explosion bubble.

Acoustic cavitation also provides opportunities for industrial applications. It has been shown experimentally that upon the collapse of a spherical cavity, the encapsulated gas reaches a high enough temperature to emit light. This phenomenon is known as sonoluminescence [2]. Recent experiments have shown these high temperatures to reach upwards of 15000K, leading to speculation that temperatures could reach the level required for nuclear fusion [32]. Regardless of this, free radicals are produced during the high temperature period, which are subsequently re-absorbed into the surrounding fluid. Such reagents may greatly affect ongoing chemical processes in the vicinity of the bubble, and may in fact initiate the creation of other chemical species. The applications for this in sonochemistry, where many micro bubbles are acoustically driven in a reactant tank, are substantial and present new avenues for the cost effective production of chemicals on industrial scales [79, 78, 30]. However the presence of multiple bubbles will cause non-spherical behaviour to become prevalent. This results in temperatures which are generally lower, as well as a difference in the quantity and species of the free radicals produced [55]. Hence if one wishes to use sonochemistry to react chemicals of different densities, the non-spherical effects of the density jump must be understood in order to maximise catalytic rates. Aside from the negative effect on bubble temperatures however, these non-spherical effects could be used to promote mixing as liquid is propelled through the high speed threading jets.

1.2 Aim: Understanding cavitation collapse near complex interfaces

This research is undertaken to generate a greater understanding of the various phenomena associated with cavitation collapse near complex interfaces. It focuses on the interactions associated with bubbles generated in the vicinity of a fluid-fluid interface supporting a discontinuity in density, with relevance to many industrial and biomedical applications. It has led to the development of a robust numerical procedure capable of simulating multiple toroidal bubbles in various axisymmetric configurations. Through the implementation of this many previously unseen features have been shown to occur, which benefit the associated applications.

1.3 Thesis Overview

This first chapter has introduced the phenomenon of cavitation, with reference to the historical development of the field. The evolution of the boundary integral approach adapted for the computations in this thesis, and the various mechanisms to continue simulations beyond the impact of an axial threading jet have been identified. Motivation has been presented for the investigation of the effect of a density jump between fluid layers, with reference to sonochemical industrial processes, as well as recent biomedical advances such as the laser ablation of tissues and gene transfection via sonoporation.

Chapter 2 illustrates the motion of a spherical bubble in an infinite fluid by means of the Rayleigh-Plesset equation. The solutions of this ordinary differential equation (ODE) associated with high pressure instantaneously generated bubbles, such as those generated by laser heating, and ultrasound activated cavities are shown. Advancements to the equation to account for fluid viscosity and thin shell effects are also included. This spherical model is used to construct a low order solution for the two-fluid case, by means

of a point source approximation valid for bubbles at large standoff distances. The Kelvin impulse is introduced briefly, and information gained from its evaluation using the point source approximation is used to predict the movement of a bubbles centroid under the action of gravity and the Bjerknes interaction with the interface.

Following the spherical bubble introduction of Chapter 2, Chapter 3 presents a detailed account of the numerical procedures utilised to simulate the severe non-spherical deformations associated with the fluid dynamics. The derivation of the surface spline approximations is included for both cubic and quintic arc length based variants, with a description of the knot conditions associated with axial symmetry and toroidal interpolation. The dynamic and kinematic conditions on all surfaces are derived incorporating inertial, gravitational and surface curvature factors. Surface integrals of free space Green's functions are then developed for axisymmetric geometries, incorporating the relevant modifications to account for the differing end node conditions. These are deployed in order to solve for the unknown potentials and normal velocities as solutions to Laplace's equation in both exterior fluids. Extensions to these are derived to account for the singularities present at source points, and their accurate evaluation over the infinite portion of the two fluid interface. The method developed allows for an unlimited number of vertically stacked bubbles in either fluid layer. Several time stepping routines are described for the explicit advancement of the known surface quantities. The evaluation of field quantities using finite differences is shown, with time derivatives calculated numerically using Eulerian and Lagrangian co-ordinates, and analytically through direct differentiation of the boundary integral equations. The advantages and disadvantages of the three methods are outlined.

The advancement to toroidal geometry is demonstrated in Chapter 4 using the vortex ring method of Lundgren and Mansour [53]. The relevant equations for the evaluation of both the vortex ring potential and velocity are derived for the axisymmetric geometry

using elliptic integrals of the first and second kind. The accurate incorporation of the vortex ring into the numerical scheme is described, including the explicit dependence on the vortex ring velocities in the Laplace solver, as well as in the kinematic and dynamic conditions.

The numerical treatment is verified in Chapter 5. The splines and their derivatives are compared to known analytic solutions with varying nodal densities and placements. This showed the quintic splines to be a significant improvement over the cubic variant, albeit with some loss of accuracy as numerical precision is approached. The advantages of using least-squares fitted polynomials to calculate the surface curvature is also shown. The boundary integral method is then verified. Excellent agreement is found in the evolution of incompressible spherical droplets perturbed with spherical harmonics and acting only under surface tension. Near perfect agreement is then found between the ODE solution of the Rayleigh-Plesset equation, and the BIM simulation of the same problem. This agreement is further ratified when the fluid-fluid interface is introduced with the special case of $\rho = 1$, where the non-dimensional ratio $\rho = \frac{\rho_2}{\rho_1}$. Truncation of the interface is investigated, showing non-sphericity becoming problematic when no far-field evaluation is undertaken and numerical infinity is insufficiently large. This is overcome with the computationally efficient far field approximation described in Chapter 3. The code is verified against free surface and rigid boundary experiments in both the pre and post jet impact phases, corresponding to the behaviour of the two fluid problem as $\rho \to 0$ and $\rho \to \infty$ respectively. Further the influence of buoyancy on the system is verified against experiments near a water/white spirit interface as performed by Chahine and Bovis [23], and to the numerical simulations of Klaseboer and Khoo [45]. These are shown to be in agreement with the Kelvin impulse theory derived in Chapter 2. The null impulse states are also examined, demonstrating the transition from buoyancy domination to interfacial attraction and repulsion.

A greater range of non-trivial density ratios are then investigated under inertial action in Chapter 6. Simulations are conducted over multiple density ratios and standoff distances to observe the general bubble migration and interfacial deformation for bubbles small enough to neglect the influence of gravity. Bubble jetting is always seen to be in the direction of the denser fluid, with the bubble being entrained into the two fluid interface at close standoff distances for $\rho > 1$, and repulsed for $\rho < 1$. Surface spiking at very close standoff distances is seen to quickly diminish as ρ increase towards 1, being negligible when $\rho > 0.4$ even at small standoff distances of $h = 0.5$. Where appropriate, the toroidal evolution is investigated, illustrating as yet unseen fluid motions directly relevant to industrial mixing problems. It is shown that the deformation to the interface can be significantly increased by the bubble jet, even when the bubble volume is low.

The influence of additional bubbles is investigated in Chapter 7. This has shown that a second bubble in a homogeneous configuration will likely inhibit any bubble jet interaction with the fluid-fluid interface during the first oscillation unless the separation distance of the two bubbles is significantly greater than the standoff distance of the closest bubble. In a heterogeneous configuration, the slower behaviour of the bubble in the denser layer allows the opposing bubble jet to significantly disturb the interface, and potentially prevent the slower bubble from forming a jet through bubble-bubble attraction. The addition of a third bubble is seen to further perturb the infinite fluid behaviour, causing the central bubble to jet at a much earlier time.

The penultimate chapter, Chapter 8, investigates the non-spherical behaviour of ultrasound activated micro bubbles, directly relevant to the new biomedical procedure sonoporation. The influence of a tension laden membrane boundary is investigated using practical density ratios, showing significant deviations in bubble shape from the spherical mode. Moreover the influence of a solid backing to a cell layer is investigated, and has demonstrated new phenomena. These include the peeling of the cell layer by the

re-expanding toroidal bubble when the cell layer depth is sufficiently less than the maximum bubble radius, as well as the injection behaviour generated by smaller bubbles under high driving frequencies near thicker layers. It is clearly demonstrated that the jet may cause significant damage to the cell layer, implying that the targeting of cells for transfection using ultrasound activated contrast agents should include the expected non-spherical behaviour after jet impact has occurred.

Finally the conclusions gained in the numerical investigation are summarised in Chapter 9. Areas for future research are introduced, including the incorporation of elastic effects into the fluid-fluid boundary to more accurately model biological applications, and the required extension to fully 3D systems to investigate the complicated geometrical influences present in vivo.

Chapter 2

Spherical Bubble Dynamics and the Kelvin Impulse

Although a gas pocket in the absence of gravity will eventually form a sphere due to surface tension effects, bubble motion is not in general spherical. High speed jets are known to thread collapsing bubbles, caused by many factors including the action of boundaries to the fluid and gravity. Nevertheless, for a spherically created bubble it has been shown that for much of the bubble lifetime, the bubble does remain roughly spherical [81, 5], and in certain situations maintains sphericity through several oscillations. Much information has been gained using the spherical model, including approximations to the Kelvin impulse providing information on the direction of the threading jets and the motion of the bubble centroid [8]. As such it is prudent to provide a brief overview of spherical bubble dynamics and how this can be applied to the problem under investigation.

2.1 The Rayleigh-Plesset equation

The Rayleigh-Plesset equation is a second order ordinary differential equation providing the time dependent radius of a spherically symmetric oscillating bubble under the constraints of the Navier-Stokes equations in an infinite, incompressible fluid [73]. Its uses

in the context of the non-spherical dynamics investigated herein include the calculation of the initial conditions for the latter numerical simulations when appropriate, and as an analytical test case for the influence of a zero density jump between fluid layers.

As the bubble behaves spherically, only radial motion is considered and hence the velocity of the fluid is $\mathbf{u} = u\mathbf{e}_r$. The continuity and spherically symmetric Navier-Stokes equations are therefore,

$$\begin{aligned} \frac{\partial u}{\partial r} + \frac{2u}{r} &= 0, \\ \rho_1 \left(\frac{\partial u}{\partial t} + u\frac{\partial u}{\partial r} \right) &= -\frac{\partial p}{\partial r} + \mu_l \left(\frac{\partial^2 u}{\partial r^2} + \frac{2}{r}\frac{\partial u}{\partial r} - \frac{2u}{r^2} \right), \end{aligned} \tag{2.1}$$

where ρ_1 and μ_l are the density and viscosity of the exterior liquid.

The continuity equation may be integrated immediately to give $r^2 u = \chi(t)$, where $\chi(t)$ is an as yet unknown temporal function of integration. If the radius of the bubble is given by $r = R(t)$, then the velocity at the bubble surface is given as $u|_{r=R(t)} = \dot{R}(t)$, where a dot denotes differentiation with respect to time. The temporal function of integration is therefore $\chi(t) = R^2\dot{R}$. Resultantly the external liquid velocity is given by,

$$u = \frac{R^2\dot{R}}{r^2}. \tag{2.2}$$

Evaluating the vector Laplacian with this velocity immediately yields $\nabla^2\mathbf{u} = 0$, and therefore viscosity can only enter through the boundary conditions placed on the bubble. As a corollary to this, the solutions to the Navier-Stokes and Euler equations are identical in this case.

As the fluid is irrotational and incompressible a velocity potential ϕ, satisfying $\mathbf{u} = \nabla\phi$, may also be found as,

$$\phi = -\frac{R^2\dot{R}}{r}. \tag{2.3}$$

Upon substituting the velocity (2.2) into the governing equations (2.1) and integrating spatially, the Euler equations may be expressed in terms of the bubble radius and an unknown function $\chi(t)$ as,

$$\rho_1 \left(-\frac{2R\dot{R}^2 + \ddot{R}R^2}{r} + \frac{R^4\dot{R}^2}{2r^4} \right) = -p + \chi(t).$$

The flow velocity approaches zero as $r \to \infty$, and so the pressure at infinity must be given as a function of time only, $p = p_\infty(t)$. The function of integration χ must therefore satisfy $\chi(t) = p_\infty(t)$, yielding,

$$-\frac{2R\dot{R}^2 + \ddot{R}R^2}{r} + \frac{R^4\dot{R}^2}{2r^4} = \frac{p_\infty(t) - p}{\rho_1}.$$

Neglecting viscosity in the normal stress balance at the interface, the pressure at the liquid side of the bubble surface, $r = R(t)$, can be given via the Young-Laplace equation as $p = p_b - \sigma\nabla \cdot \mathbf{e}_r$, where p_b is the pressure exerted by the gas inside the bubble, σ is the surface tension and $\mathbf{e}_r$ is the normal vector to the surface. The elimination of the spatial dependence r in this way now yields an ODE for the bubble radius $R(t)$ as a function of time only,

$$\rho_1 \left(\ddot{R}R + \frac{3\dot{R}^2}{2} \right) = -p_\infty(t) + p_b - \sigma\nabla \cdot \mathbf{e}_r. \tag{2.4}$$

Acoustic driving may be incorporated by setting $p_\infty(t) = p_\infty + p_{a\infty}\sin(-\omega t)$, the effects of which are detailed later in this chapter. The negative sign is taken to imply an initially negative pressure wave.

For the majority of the lifetime of the bubble, it is reasonable to assume that thermal effects and mass diffusion across the bubble wall may be neglected. In some situations, such as bubble-shockwave interactions, this is no longer true [21, 71, 20]. This work will

not however investigate such extreme phenomena.

Under such assumptions, the gas inside the bubble will behave in an adiabatic manner, and therefore one may relate the internal gas pressure to the bubble volume. This results in a relation of the type $p_b = p_v + p_0 \left(\frac{V_0 - b}{V - b}\right)^\gamma$, where $V_0 = \frac{4}{3}\pi R_0^3$ is some reference volume with radius R_0, taken as the minimum bubble radius where appropriate [5, 21]. Here p_v is the pressure exerted by the condensible vapour of the surrounding liquid, whilst p_0 is some reference pressure to that exerted by non-condensible contaminate gas. Typically this contaminate gas is present in cavitation and explosion bubbles, as opposed to pure vapour bubbles. It may be present by directly seeding the liquid with a Noble gas such as Argon in sonoluminescence [32], or through the violent initiation of the bubble using spark discharge, laser heating or explosives. The variable b may be included as a representation of the physical molecular volume of the bubble contents. For an ideal gas $b = 0$, whereas for a Van der Waals type gas, ignoring molecular attraction, b is the total volume of gas molecules assuming each molecule is a rigid sphere [21, 2, 20]. A further use is to incorporate the volume of the shell of an ultrasound contrast agent, preventing the bubble volume from reaching an infeasible minimum.

With these pressures incorporated, and assuming the gas to be ideal for simplicity, one obtains a non-linear equation for the radius of a spherical bubble in an infinite fluid in the absence of gravity.

$$\ddot{R}R + \frac{3}{2}\dot{R}^2 = -\frac{p_\infty + p_{a\infty}\sin(-\omega t) - \left(p_v + p_0\left(\frac{R_0}{R}\right)^{3\gamma}\right) + \sigma\nabla\cdot\mathbf{e}_r}{\rho_1}. \tag{2.5}$$

The system is now non-dimensionalised with respect to the maximum bubble radius, R_{max}, and the difference between the pressure at infinity and the vapour pressure of the bubble, $\Delta_p = p_\infty - p_v$. This gives the non-dimensional variables, identified by an over bar, as $\bar{R} = RR_{max}^{-1}$ and $\bar{t} = tR_{max}^{-1}\sqrt{\rho_1^{-1}\Delta_p}$. Consequently, the non-dimensional potential

is given by $\bar{\phi} = \phi R_{max}^{-1}\sqrt{\rho_1 \Delta_p^{-1}}$, with pressure scaling as $p = \Delta_p \bar{p} + p_v$. The coefficient of surface tension becomes $\bar{\sigma} = \frac{\sigma}{\Delta_p R_{max}}$ and the curvature is immediately evaluated as $\nabla \cdot \mathbf{e}_r = \frac{2}{R}$. Substituting these back into (2.5) gives the second order ODE,

$$\ddot{\bar{R}}\bar{R} + \frac{3}{2}\dot{\bar{R}}^2 = \epsilon \left(\frac{\bar{R}_0}{\bar{R}}\right)^{3\gamma} - 1 - p_a \sin(-\bar{\omega}t) - \frac{2\bar{\sigma}}{\bar{R}}. \tag{2.6}$$

The parameters in (2.6) are given as,

$$\epsilon = \frac{p_0}{\Delta_p},\ p_a = \frac{p_{a\infty}}{\Delta_p},\ \bar{\omega} = \frac{\omega}{R_{max}}\sqrt{\frac{\rho_1}{\Delta_p}},\ \bar{\sigma} = \frac{\sigma}{\Delta_p R_{max}}. \tag{2.7}$$

From here onwards, the over bars will be dropped for brevity. Unless otherwise stated the variables used will be dimensionless.

The ratio of specific heats of the incondensable interior gases are given by γ. For air, $\gamma = 1.4$, for TNT $\gamma = 1.25$ [28], for Argon, relevant to sonoluminescence, $\gamma = 1.66$ and for tetraflurocarbon used in some UCA's, $\gamma = 1.08$.

The parameter ϵ is known as the strength parameter, and is the ratio of the contaminate gas pressure inside the bubble to the pressure scale Δ_p. The magnitude of this parameter can drastically alter the behaviour of a collapsing bubble, particularly with regards to any jetting behaviour.

Equation (2.6) is readily solved numerically. However further information may be found analytically under certain conditions.

2.2 Behaviour in the absence of acoustic forcing

In the absence of acoustic forcing, $p_{a\infty} = 0$, multiplying (2.6) by $2R^2\dot{R}$ allows the equation to be integrated once analytically yielding,

$$R^3\dot{R}^2 = \frac{2}{3}\left(\frac{\epsilon}{1-\gamma}\left(\frac{R_0}{R}\right)^{3\gamma} R^3 - R^3\right) - 2\sigma R^2 + C. \tag{2.8}$$

ϵ	50	100	500	1000	10000	100000
R_{min}	0.210	0.165	0.095	0.075	0.034	0.016

Table 2.1: Some initial radii given high values of ϵ, with $\sigma = 0$

The velocity at the non-dimensional maximum bubble radius satisfies $\dot{R}|_{R=1} = 0$. This yields the constant of integration C as,

$$C = \frac{2}{3}\left(3\sigma + 1 - \frac{\epsilon}{1-\gamma}\left(R_0\right)^{3\gamma}\right). \tag{2.9}$$

Substituting C back into equation (2.8) now gives a non-linear expression for the bubble wall velocity,

$$\dot{R}^2 = \frac{2}{3}\frac{\epsilon R_0^{3\gamma}}{(1-\gamma)}\left(\frac{1}{R^{3\gamma}} - \frac{1}{R^3}\right) + \frac{2}{3}\left(\frac{1}{R^3} - 1\right) + 2\sigma\left(\frac{1}{R^3} - \frac{1}{R}\right). \tag{2.10}$$

For fixed values of γ, ϵ and σ, this equation does not produce real valued solutions for all radii $R \in (0, 1)$. Indeed the minimum radius bubble satisfying the adiabatic criterion may be found using $\dot{R} = 0$ at $R = R_{min}$. Applying this now yields an equation for R_{min} which may be found iteratively, and in this work is found using a Newton-Raphson scheme. Higher values of ϵ lead to smaller initial radii under the constraint that the maximum radius is 1. This corresponds dimensionally to a greater initial pressure resulting in a greater bubble radius. Some examples are given in table 2.1. One notes that for $\epsilon = 1$ and $\sigma = 0$, the minimum and maximum radii are the same, as the gas pressure exactly matches the far field pressure at minimum volume. Therefore, without external forcing such a bubble will retain a constant volume with zero surface velocity.

Given this information, it is possible to find the period of time, t_a, the bubble will take to reach a specific radius R_a. In particular the time taken to reach the maximum radius of the bubble from initiation, the bubble half life, may be found and by extension,

the total oscillation time of the bubble. After some manipulation t_a is found as,

$$t_a = \frac{1}{\sqrt{6}} \int_{R_0^{\frac{1}{3}}}^{R_a^{\frac{1}{3}}} \frac{y^{\frac{5}{6}}(1-y)^{\frac{-1}{2}}}{\sqrt{1+\frac{\epsilon R_0^{3\gamma}}{(1-\gamma)y^\gamma}\left[1-\frac{y^\gamma-1}{y-1}\right]+3\sigma\left[\frac{y-1}{y-y^{\frac{1}{3}}}\right]}} dy. \tag{2.11}$$

In the absence of adiabatic effects ($\epsilon = 0,\ R_0 = 0$) and surface tension ($\sigma = 0$), this is the incomplete beta function, $\beta_{R_a^{\frac{1}{3}}}(5/6, 1/2)$ [1]. The bubble half life, t_h, can hence be calculated using $R_a = 1$, and is therefore the complete beta function. The period of one complete oscillation is therefore $t_c = 2t_h$.

Importantly this allows for initial data for the potential at the bubble surface to be found if the enclosed gas is assumed to exert a constant pressure on the cavity wall. This potential is given as $\phi_{init} = -R_{init}\dot{R}_{init}$ at the time at which this radius is achieved [5].

Information about the pressure in the exterior fluid may also be extrapolated. Non-dimensionalising the Bernoulli equation with the above scalings yields the field pressure as,

$$\frac{\partial \phi}{\partial t} + \frac{|\nabla \phi|^2}{2} = 1 - p. \tag{2.12}$$

Substituting ϕ from (2.3) into equation (2.12) gives the pressure in the field exterior as,

$$p = 1 - \left(-\frac{R\left(\frac{\dot{R}^2}{2} + \epsilon\left(\frac{R_0}{R}\right)^{3\gamma} - 1\right)}{r} + \frac{R^4\dot{R}^2}{2r^4} \right). \tag{2.13}$$

Differentiating (2.13) with respect to r and equating the pressure derivative to zero provides the distance from the bubble surface of the maximum absolute pressure at any

[1] $\beta_a(c,d) = \int_0^a x^{c-1}(1-x)^{d-1}dx$ [1]

given time,

$$\begin{aligned} 0 &= \frac{R\left(\frac{\dot{R}^2}{2}+\epsilon\left(\frac{R_0}{R}\right)^{3\gamma}-1\right)}{r^2}-\frac{2R^4\dot{R}^2}{r^5} \\ \Rightarrow r &= \sqrt[3]{\frac{2R^3\dot{R}^2}{\frac{\dot{R}^2}{2}+\epsilon\left(\frac{R_0}{R}\right)^{3\gamma}-1}}. \end{aligned} \tag{2.14}$$

One may then substitute $\dot{R}^2$ from equation (2.10) to render the equation (2.14) in terms of R only. This expression is however only valid when the absolute pressure maximum exceeds the pressure at infinity, as at all other times the pressure maximum will naturally be located at $r = \infty$. Similarly, it is only valid for $r > R_0$ when $\epsilon > 0$, as the equation for pressure is only valid in the exterior liquid domain. When $R = R_0$, the maximum pressure will be located at $r = R_0$ provided $\epsilon > 1$.

As an example, consider the constant volume vapour bubble, with $R = 0.1$, $\dot{R} = 25.806976$, $\epsilon = 0, t = 0.0015527$ [5]. The maximum pressure occurs at a distance $r \approx 0.1261$ with magnitude $p \approx 132$.

2.3 Behaviour in the presence of acoustic forcing

Whereas the initial motions of a high pressure bubble are governed by the internal gas dynamics, the initial behaviour of an acoustically forced cavity is naturally dependent on the exterior pressure field. In the absence of any external forcing, these bubbles are presumed to be stable in time and space. The interior pressure exerted at the bubble wall must be in equilibrium with the exterior pressure of the surrounding fluid. At reference volume, a sphere with radius R_{ref}, this results in the internal gas pressure satisfying,

$$p_b = \epsilon = 1 + \frac{2\sigma}{R_{ref}}. \tag{2.15}$$

Any deviation from this state requires the application of an external force, which in

this work is exclusively given by the sinusoidal pressure term $p_{a\infty}\sin(-\omega t)$. In all simulations this will initially apply a negative pressure, causing the bubble to initially expand ($\omega > 0$). The opposite may of course be used if desired, resulting in the initial compression of the bubble volume. As the acoustic terms prevent a similar integration to that used in the previous section, neither the minimum nor maximum radius of the bubble can be determined analytically, nor indeed will these be necessarily unique throughout the bubble lifetime. Instead the maximum radius used for non-dimensionalisation is determined through the numerical solution of equation (2.7) given the initial conditions $R = R_{ref},\ \dot{R} = 0$. One typically here uses a dimensional initial radius of $2.5\mu m$ and pressure amplitudes $p_{a\infty} \sim O(MPa)$, as have been employed in some sonoporation experiments [70]. Figure 2.1 illustrates some examples with various frequencies and amplitudes. In the lower pressure cases, the bubble is able to rebound easily, resulting in the ringing behaviour for several oscillations. One notes how the behaviour at higher amplitudes may include incomplete oscillations above reference volume, which subsequently result in a sudden violent collapse. This may be beneficial in biomedical applications, as the onset of aspherical effects may thereby be accompanied by bubble expansion, allowing for a prolonged jet lifetime.

The length scale for the results in Chapter 8 is chosen as the largest radius achieved during two periods of the acoustic forcing, or until the dimensional bubble radius has dipped below $0.25\mu m$. In these non-spherical simulations, jetting will often occur during the collapse from this volume, as the inertia of the surrounding fluid will have the greatest effect. This choice is also more appropriate when comparing the solutions to those of the high pressure bubbles, as their maximum volume does not increase after the first oscillation.

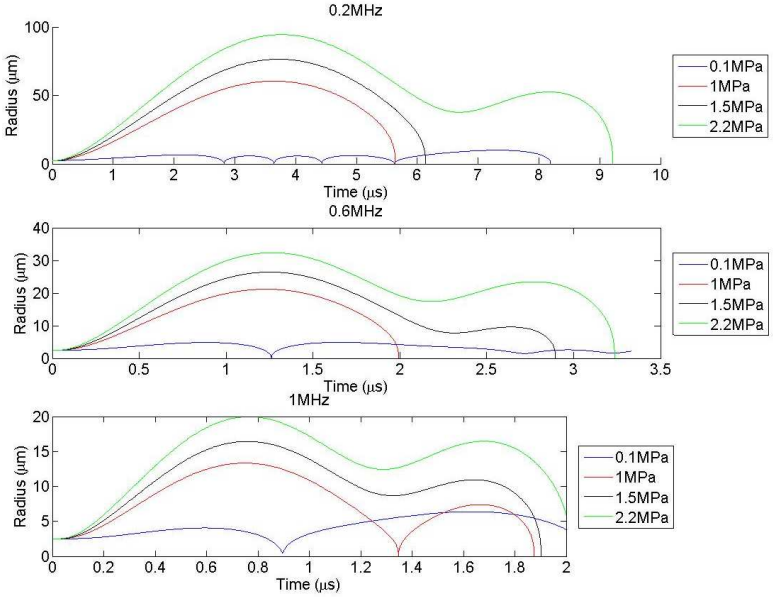

Figure 2.1: Dimensional behaviour for acoustically driven bubbles with various frequencies and various amplitudes. The length of the simulations is twice the period of acoustic forcing.

2.4 Viscous effects and shell encapsulation

As mentioned earlier in the chapter, further physical effects may be included through appropriate modifications to the boundary conditions on the bubble surface. Viscous effects for example, may be included through consideration of the stress tensor [16, 41]. Using the dimensionless regime introduced previously, the non-dimensional constant dynamic viscosity is expressed as $\bar{\mu}_l = \mu_l R_{max}\sqrt{\Delta_p \rho_1}$, where μ_l is the dimensional viscosity of the liquid. Dropping the bar for convenience, in a spherically symmetric, incompressible fluid the stress tensor is given as,

$$\begin{aligned} T_{ij} &= 0, \ i \neq j \\ T_{rr} &= -p + 2\mu_l \frac{\partial u}{\partial r} \\ T_{\theta\theta} = T_{\varphi\varphi} &= -p + 2\mu_l \frac{u}{r}. \end{aligned} \tag{2.16}$$

$p_{a\infty}(MPa)$	frequency (MHz)	0.1	0.2	1	10
0.1		2.59	2.60	3.04	2.51
1		11.50	10.17	10.73	2.60
10		119.17	60.41	13.33	3.41
14		145.47	73.48	15.86	6.39
22		187.53	94.41	19.96	9.99

Table 2.2: Maximum radii (μm) of acoustically forced bubbles with an initial radius of $2.5\mu m$, governed by the maximum pressure amplitude $p_{a\infty}$ (MPa), and frequency of acoustic forcing (MHz).

The trace of the stress tensor must equal 0 due to incompressibility, implying $T_{rr} = -(T_{\theta\theta} + T_{\varphi\varphi})$. Substituting the stress tensor (2.16) into the equation of momentum (2.1) and integrating over the liquid domain $R \leq r \leq \infty$ gives the ODE expressing the bubble radius as,

$$\ddot{R}R + \frac{3}{2}\dot{R} = \epsilon\left(\frac{R_0}{R}\right)^{3\gamma} - 1 - p_{a\infty}\sin(-\omega t) - 2\sigma\frac{1}{R} - \int_R^\infty \frac{T_{rr}}{r}dr \tag{2.17}$$

$$= \epsilon\left(\frac{R_0}{R}\right)^{3\gamma} - 1 - p_{a\infty}\sin(-\omega t) - 2\sigma\frac{1}{R} - 4\mu_l\frac{\dot{R}}{R}. \tag{2.18}$$

From this it is immediately apparent that for small bubbles, $R_{max} \sim O(\mu m)$, such as those typical of sonochemistry and medical procedures, surface tension and viscosity will have an effect, particularly during the late stages of bubble collapse and the early stages of bubble rebound. In contrast for large bubbles, $R_{max} \sim O(m)$, typical of an underwater explosion, the effect of these forces will be negligible. Gravity effects scale inversely to these (see Chapter 3) and so are of negligible effect to tiny bubbles, yet greatly affect large cavities. Surface tension will dominate during the very late rebound phase over viscosity, which will factor out due to its dependence on velocity. This is demonstrated in figure 2.2, showing a bubble with an initial radius of $2.5\mu m$ oscillating in water, driven by an acoustic wave with a frequency of $1MHz$ and a peak pressure amplitude of $p_{a\infty} = 1MPa$. The simulation here is performed with and without surface tension and viscosity. Surface

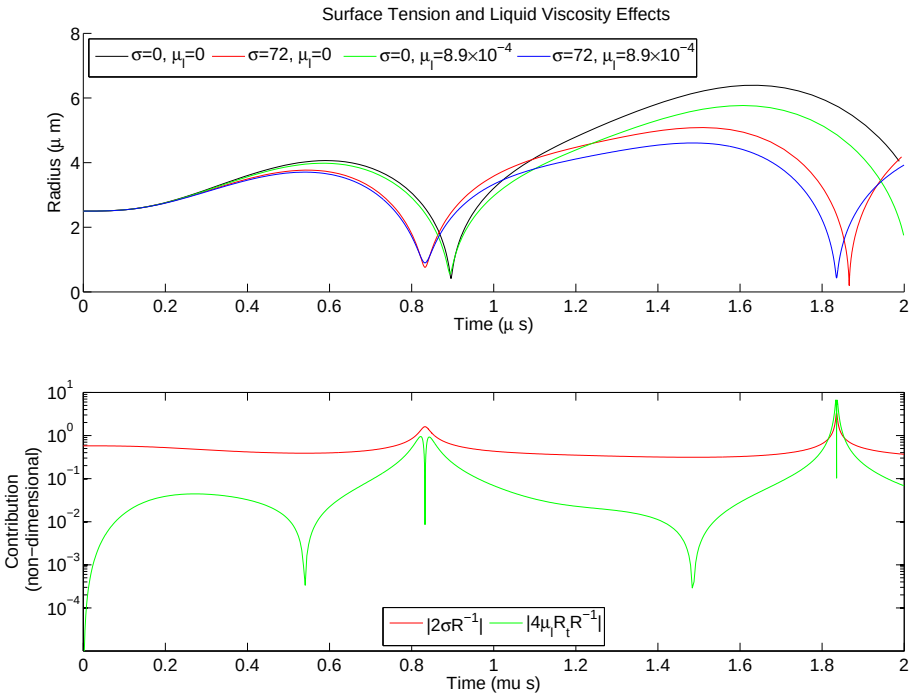

Figure 2.2: Spherical simulation of a bubble with initial radius $2.5\mu m$ being driven by an acoustic wave with frequency $1MHz$ and dimensional peak pressure $p_{a\infty} = 1MPa$. Surface tension is in $\frac{dyne}{cm}$ and viscosity is in $Pa.s$. The lower image shows the absolute non-dimensional contribution of the surface tension and viscosity terms in equation (2.17) throughout the simulation.

tension appears to be the greater factor in this particular case, as can be seen in the lower image showing the absolute contributions to the velocity form the respective terms in equation (2.17).

Elastic shells may also be incorporated via the surface stress. Here one includes the derivation of the equations governing a hard shell, such as Albunex [26, 41]. One considers a linearly visco-elastic shell constructed from an incompressible material. As in the derivation of the Rayleigh-Plesset equation, continuity of mass gives the velocity in the shell as $u_r = R^2\dot{R}r^{-2}$. Taking the shell thickness $d(t) \ll R(t)\ \forall\ t$ allows the shell inertia to be neglected due to its relatively tiny mass. This gives the equation of momentum for the shell as,

$$0 = \frac{\partial p_s}{\partial r} + \frac{\partial T_{rr}}{\partial r} + \frac{3}{r} T_{rr}. \tag{2.19}$$

Following Church [26], the stress tensor T_{rr} for an incompressible visco-elastic material may be given as,

$$T_{rr} = -4 \left(\frac{(R(t) - d(t))^2}{r^3} \right) \left(G_s(R(t) - d(t) - R_e) + \mu_s \dot{R(t)} \right),$$

where R_e is the equilibrium bubble radius where there is zero stress in the shell, G_s is the non-dimensional modulus of rigidity and μ_s is the non-dimensional dynamic viscosity of the shell. This is only applicable to small amplitude oscillations, and at high driving frequencies and pressures one may expect the shell to suffer a far more non-linear elastic, and indeed plastic, behaviour. Integrating (2.19) over the width of the shell gives,

$$f(t) = [p_s + T_{rr}]_{R-d}^{R} + 4(R-d)^2 \left(G_s(R - d - R_e) + \mu_s \dot{R} \right) \left(\frac{R^3 - (R-d)^3}{R^3 (R-d)^3} \right),$$

where $f(t)$ is a spatial constant. This is incorporated into the Rayleigh-Plesset equation using the stress balance conditions on either side of the shell, with p_b the pressure inside the bubble, and $p_l + T_l$ the total stress inside the liquid [26]. Taking surface tension to be constant on both interfaces provides the equations of stress balance as,

$$p_b = p_s(R-d) + \frac{2\sigma_{int}}{R-d} + T_{rr}(R-d)$$
$$p_l(R) + T_l(R) = p_s(R) + \frac{2\sigma}{R} + T_{rr}(R).$$

Application of these conditions leads to the modified Rayleigh-Plesset equation,

$$\begin{aligned}\ddot{R}R+\frac{3}{2}\dot{R}^2 &= \epsilon\left(\frac{R_0}{R}\right)^{3\gamma}-1-p_{a\infty}\sin(-\omega t)-4\mu_l\frac{\dot{R}}{R}-2\sigma\frac{1}{R}\\ &\quad -\frac{2\sigma_{int}}{R-d}-4\left(G_s(R-d-R_e)+\mu_s\dot{R}\right)\left(\frac{R^3-(R-d)^3}{R^3(R-d)}\right).\end{aligned}$$

As the shell is incompressible, it also holds that,

$$R(t)^3-(R(t)-d(t))^3=R_e^3-(R_e-d_e)^3=\hat{V}_s, \tag{2.20}$$

where $\hat{V}_s=\frac{3}{4\pi}V_s$ and V_s is the constant volume of the shell. Equation (2.20) naturally leads to the identity,

$$d(t)=R(t)-(R(t)^3-\hat{V}_s)^{\frac{1}{3}}. \tag{2.21}$$

Substitution of the shell thickness (2.21) allows the shell contribution to be expressed as,

$$-4\left(G_s\left((R(t)^3-\hat{V}_s)^{\frac{1}{3}}-R_e\right)+\mu_s\dot{R(t)}\right)\frac{\hat{V}_s}{R(t)^3(R(t)^3-\hat{V}_s)^{\frac{1}{3}}}, \tag{2.22}$$

and the final ODE is therefore given by,

$$\begin{aligned}\ddot{R}R+\frac{3}{2}\dot{R}^2 &= \epsilon\left(\frac{R_0}{R}\right)^{3\gamma}-1-p_{a\infty}\sin(-\omega t)-4\mu_l\frac{\dot{R}}{R}-2\sigma\frac{1}{R}\\ &\quad -\frac{2\sigma_{int}}{(R^3-\hat{V}_s)^{\frac{1}{3}}}-4\left(G_s\left((R^3-\hat{V}_s)^{\frac{1}{3}}-R_e\right)+\mu_s\dot{R}\right)\frac{\hat{V}_s}{R^3(R^3-\hat{V}_s)^{\frac{1}{3}}}.\end{aligned} \tag{2.23}$$

The equilibrium radius R_e can be determined by setting $\dot{R}=\ddot{R}=0$ at $t=0$, given the volume of the shell and the pressure in the bubble. Alternatively, the equilibrium radius may be given as the reference radius R_{ref}, with the strength parameter ϵ found accordingly.

Under the assumption that $d(t) \ll R(t)\ \forall\ t$, one may use a Taylor series expansion to simplify the $(R-d)^{-1}$ factors for the interior surface tension and the shell contributions. This then leads to the ODE,

$$\begin{aligned} \ddot{R}R + \frac{3}{2}\dot{R}^2 &= \epsilon\left(\frac{R_0}{R}\right)^{3\gamma} - 1 - p_{a\infty}\sin(-\omega t) - 4\nu\frac{\dot{R}}{R} - 2\tilde{\sigma}\frac{1}{R} \\ &\quad -4\left(G_s\left((R^3-\hat{V}_s)^{\frac{1}{3}} - R_e\right) + \mu_s\dot{R}\right)\frac{\hat{V}_s}{R^4}. \end{aligned} \tag{2.24}$$

Here the term $\tilde{\sigma} = \sigma_{int} + \sigma$ may be viewed as the effective surface tension, which for SonoVue UCA's has been experimentally determined to be roughly $51\frac{dyne}{cm}$, and is in general lower than the surface tension of water [54, 24]. The modulus of rigidity and dynamic viscosity have also been experimentally estimated, and for SonoVue and similar UCA's have been approximated as $G_s \sim O(70MPa)$ and $\mu_s \sim O(1Pa.s)$ respectively [41, 24]. Figure 2.3 contains simulations of equation (2.24) using such parameters whilst varying the shell thickness. A cavity with an equilibrium radius of $R_e = 2.5\mu m$ is used, driven by an acoustic wave with frequency $2MHz$ and dimensional peak amplitude $p_{a\infty} = 0.4MPa$. It is immediately apparent that with this linearly elastic model, the thickness of the UCA shell is of critical importance, as there is severe retardation of the oscillations even with an equilibrium shell thickness of $0.025R_e$.

2.5 Spherical approximation to the two fluid problem

In various situations, and particularly at large standoff distances, the sphericity of a cavitation bubble may be maintained throughout several oscillations, or at least until late in the collapse phase of the first oscillation. Equally at a sufficient standoff distance, the fluid-fluid interface will remain almost flat. One may use these assumptions to develop an approximation to the flow field based on a point source approximation for a single bubble.

Considering incompressible, irrotational and inviscid flow, the velocity potential in

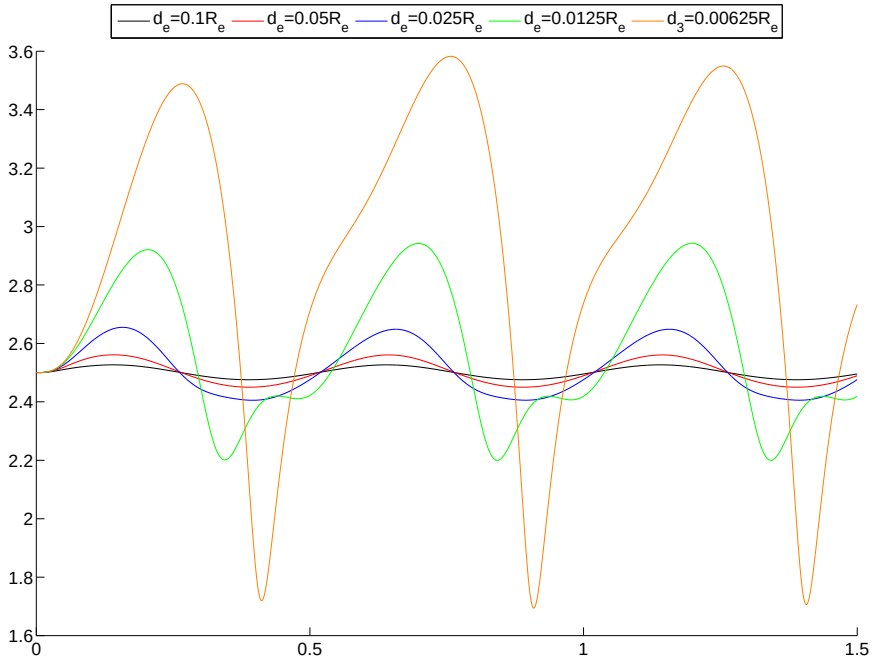

Figure 2.3: The oscillations of a linearly elastic SonoVue UCA under high frequency ($2MHz$), low amplitude ($p_{a\infty} = 0.4Mpa$) forcing. The equilibrium shell thickness is varied through $d_e \in \{0.1R_e 2^{-x} | x = 0, \ldots, 4\}$. The dimensional liquid and shell parameters used are $\mu_l = 8.9 \times 10^{-4} Pa.s,\ \mu_s = 1.2Pa.s,\ G_s = 73MPa$ and $\tilde{\sigma} = 51 \frac{dyne}{cm}$.

each fluid layer satisfies Laplace's equation, (2.25) due to the continuity of mass.

$$\nabla^2 \phi = 0. \tag{2.25}$$

As will be shown in Chapter 3, this equation may be solved using Green's integral formula, equation (3.26), in terms of the velocity potential and normal velocity on each interface. For the spherical bubble approximation, the potential and normal velocity on the bubble surface, (**b**), are,

$$\begin{aligned} \phi_1(\mathbf{b}) &= -R(t)\dot{R}(t), \\ \frac{\partial \phi_1(\mathbf{b})}{\partial n} &= -\dot{R}(t). \end{aligned}$$

On the fluid-fluid interface, (**p**), the linearised Bernoulli equation yields,

$$\frac{\partial \phi_1(\mathbf{p})}{\partial t} = \rho \frac{\partial \phi_2(\mathbf{p})}{\partial t}, \tag{2.26}$$

where $\rho = \frac{\rho_2}{\rho_1}$ is the ratio of liquid densities. The leading order flatness of the interface also gives the continuity of normal velocity across the interface as,

$$\frac{\partial \phi_1(\mathbf{p})}{\partial z} = \frac{\partial \phi_2(\mathbf{p})}{\partial z}. \tag{2.27}$$

The potential vanishes at infinity in both fluids. The location of the bubble centroid is taken to be in fluid layer 1, at $\mathbf{x}_0 = (0, \theta, -h)$, where h is the non-dimensional standoff distance and $r \in [0, \infty)$, $\theta \in [0, 2\pi)$ are the radial and azimuthal cylindrical co-ordinates.

Following Lighthill [43], one takes a Taylor series expansion of the potential as given

by Green's integral formula,

$$\begin{aligned} c(\mathbf{r})\phi(\mathbf{r}) &= \int_S \left(G(\mathbf{r},\mathbf{r}_0)\frac{\partial\phi(\mathbf{r}_0)}{\partial n} - \frac{\partial G(\mathbf{r},\mathbf{r}_0)}{\partial n}\phi(\mathbf{r}_0) \right) dS \\ &\approx \frac{1}{|\mathbf{r}|}\int_S \frac{\partial\phi(\mathbf{r}_0)}{\partial n} dS + \frac{\mathbf{r}}{|\mathbf{r}|^3}\cdot\int_S \left(-\mathbf{n}\phi(\mathbf{r}_0) + \mathbf{r}_0\frac{\partial\phi(\mathbf{r}_0)}{\partial n} \right) dS + O\left(\frac{1}{|\mathbf{r}|^3}\right) \end{aligned} \quad (2.28)$$

The coefficient $c(\mathbf{r})$ will be 4π in the fluid domain and 2π on any boundaries due to the smooth surface shapes. The first integral acts as a source of strength $4\pi R^2\dot{R}$ for a single spherical bubble. The second integral is a higher order dipole contribution of effect only if the bubble is allowed to translate significantly. As will be seen in Chapter 6, bubbles at greater standoff distances, and particularly bubbles which retain a high degree of sphericity, do not translate to a significant extent under the influence of a two fluid interface. Hence the neglect in this work of this dipole contribution is acceptable.

Fluid 2 does not contain the bubble, and hence the potential across the flat interface may be given immediately by that generated by an exterior source point, multiplied by an as yet unknown constant $K_2 \in \mathbb{R}$ to account for the change in density [8].

$$2\pi\phi_2 = 4\pi K_2 R^2\dot{R}\frac{1}{\sqrt{(z-h)^2+r^2}},\ z=0. \quad (2.29)$$

The potential function in fluid 1 requires an image source term to be reflected in the interface to counter the source point, again multiplied by an unknown constant $K_1 \in \mathbb{R}$ [8].

$$2\pi\phi_1 = 4\pi R^2\dot{R}\left(\frac{1}{\sqrt{(z-h)^2+r^2}} + \frac{K_1}{\sqrt{(z+h)^2+r^2}}\right),\ z=0. \quad (2.30)$$

Applying the boundary conditions (2.26,2.27) now gives the following two equations and

subsequently the unknowns as,

$$\begin{aligned} & (1+K_1) = \rho K_2,\ 1-K_1 = K_2 \\ \Rightarrow \quad & K_2 = \frac{2}{1+\rho},\ K_1 = \frac{\rho-1}{\rho+1}. \end{aligned} \tag{2.31}$$

Substituting the constants from (2.31) into equations (2.29) and (2.30) provides the leading order approximations of the potentials at the two fluid interface ∂I as,

$$\phi_1(\mathbf{r} \in \partial I) = 2R^2\dot{R}\left(\frac{1}{\sqrt{(z-h)^2+r^2}} - \frac{At}{\sqrt{(z+h)^2+r^2}}\right), \tag{2.32}$$

$$\phi_2(\mathbf{r} \in \partial I) = \frac{4}{1+\rho}\frac{R^2\dot{R}}{\sqrt{(z-h)^2+r^2}}. \tag{2.33}$$

Here one defines $At = \frac{1-\rho}{1+\rho}$ as the Atwood number. This maps the entire range of density ratios to the interval $\rho \in [0,\infty) \rightarrow At \in (-1,1]$, where $At = -1$ corresponds to a rigid boundary, $At = 1$ corresponds to a free surface and $At = 0$ corresponds to an infinite fluid. Using the approximations (2.32) and (2.33), one may calculate an approximation to the field potential by integrating (2.25) over the disk ($0 \leq r < \infty, 0 \leq \theta < 2\pi, z = 0$). This can potentially be performed analytically, although this would require the evaluation of complete elliptic integrals whose kernels are also elliptic integrals. Indeed, the elliptic integrals over θ form the kernels used in the axisymmetric boundary integral method described in Chapter 3. Further analytic results may however be gained using (2.32) and (2.33) without performing this evaluation.

An estimate to the higher order interfacial deformation can be made using this approximation. Taking the deformation to be $z = \eta(r,t)$, one may state that the rate of change in deformation is equal to the velocity at the interface. Calculating the velocity

using ϕ_2 (2.33) one therefore has,

$$\frac{\partial \eta}{\partial t} = \left.\frac{\partial \phi_2}{\partial z}\right|_{z=\eta} = \frac{1}{1+\rho} R^2 \dot{R} \frac{\eta + h}{((\eta - h)^2 + r^2)^{\frac{3}{2}}}.$$

This demonstrates that for $r \gg h$, the velocity along the two fluid interface decays as $O(|\mathbf{r}|^{-3})$. Re-arranging presents an analytically integrable differential equation,

$$\int \frac{d\eta}{dt} \frac{((\eta - h)^2 + r^2)^{\frac{3}{2}}}{h - \eta} dt = \frac{4}{1+\rho} \int R^2 \frac{dR}{dt} dt \tag{2.34}$$

$$\Rightarrow \quad \int d\eta \left(\frac{((\eta - h)^2 + r^2)^{\frac{3}{2}}}{h - \eta} \right) = \frac{4}{1+\rho} \frac{R^3}{3} + \chi(r)$$

$$= \quad r^3 \ln \left(\frac{2r(r + (\eta + h)^2 + r^2)^{\frac{1}{2}}}{\eta - h} \right) - \frac{((\eta - h)^2 + r^2)^{\frac{3}{2}}}{3} - r^2((\eta + h)^2 + r^2)^{\frac{1}{2}} \tag{2.35}$$

Solving this equation for η is impossible. However as in this approximation $\eta << h$, one may take a Taylor expansion in powers of $\frac{\eta}{h}$. This provides,

$$-\frac{1}{3}(h^2 + r^2)^{\frac{3}{2}} - r^2(h^2 + r^2)^{\frac{1}{2}} + r^3 \ln \left(-\frac{2r(r + (h^2 + r^2)^{\frac{1}{2}})}{h} \right) + \eta \left(\frac{(h^2 + r^2)^{\frac{3}{2}}}{h} \right)$$
$$= \frac{4R^3}{3(1+\rho)} + \chi(r) + o\left(\frac{\eta}{h}\right).$$

Ignoring higher order terms and re-arranging for η, one acquires,

$$\eta = \frac{4hR^3}{(3+3\rho)(r^2 + h^2)^{\frac{3}{2}}} - \frac{h(h^2 + 4r^2)}{3(h^2 + r^2)} + hr^3 \frac{\ln\left(\frac{2r(r+\sqrt{h^2+r^2})}{h}\right)}{(h^2 + r^2)^{\frac{3}{2}}} + \frac{\chi(r)}{(h^2 + r^2)^{\frac{3}{2}}}. \tag{2.36}$$

By necessity, $\eta \to 0$ as $r \to \infty$. Taking this limit gives,

$$0 = \frac{h^2 + 4r^2}{3(h^2 + r^2)} - \frac{r^3}{(h^2 + r^2)^{\frac{3}{2}}} \ln \left(-\frac{2r(r + (h^2 + r^2)^{\frac{1}{2}})}{h} \right) + \frac{\chi(r)}{(h^2 + r^2)^{\frac{3}{2}}},$$

and so $\chi(r)$ must be chosen to eliminate the $O(1)$ and $O(\ln(r))$ terms in equation (2.36),

particularly the complex terms arising from $\ln(-1)$. This gives the approximation to the surface deformation as,

$$\eta = \frac{4hR^3}{3(1+\rho)(r^2+h^2)^{\frac{3}{2}}} = \frac{Vh}{\pi(1+\rho)(r^2+h^2)^{\frac{3}{2}}}. \tag{2.37}$$

Using this leading order approximation, the surface deformation on the axis is therefore constrained by $\eta(r=0,t) \in (0, \frac{1}{\pi}\frac{V}{h^2})\ \forall\ \rho$, with the maximum deformation occurring for $\rho = 0$ at the time of maximum bubble volume, the bubble half life.

2.6 Approximating the Kelvin impulse

The Kelvin impulse has been widely used in the cavitation bubble dynamics field as a measure of the inertia in the fluid due to any bubbles. It allows for general aspects of the flow field to be approximated, such as the gross movement of the bubble centroid and the direction of a threading jet should one develop. The impulse is defined as,

$$\mathbf{I} = \int_{\partial S} \phi \mathbf{n} dS. \tag{2.38}$$

The time integration of the Bernoulli equation in the presence of gravity yields the impulse as,

$$\mathbf{I} = \mathbf{I}_0 + \int_0^t \left(\delta V(\tau)\mathbf{e}_z + \int_S \left(\frac{|\nabla\phi|^2}{2}\mathbf{n} - \frac{\partial\phi}{\partial n}\nabla\phi \right) dS \right) d\tau. \tag{2.39}$$

Here $\mathbf{I}_0$ is the initial impulse and S is the surface of a control volume of fluid surrounding the bubble, which in this context consists of the two fluid interface and a hemisphere with infinite radius [8, 12]. From this the direction of movement of the bubble centroid over one oscillation can be determined by considering the z component of the impulse. Following Blake [8], for a two fluid interface, assuming a zero initial impulse, implementing the point

source approximation (2.30) reduces this to,

$$\begin{aligned}\mathbf{I}_z &= \bar{\delta}\frac{4\pi}{3}\int_0^{T_c} R^3 dt + \frac{1}{4}\int_0^{T_c} R^4\dot{R}^2 \int_0^{2\pi}\int_0^{\infty} \frac{r}{(h^2+r^2)^{\frac{3}{2}}}\left(r^2(At-1)^2 - h^2(At+1)^2\right) dr d\theta dt \\ &= \bar{\delta}\frac{4\pi}{3}\int_0^{T_c} R^3 dt - \frac{At\pi}{2h^2}\int_0^{T_c} R^4\dot{R}^2 dt. \end{aligned} \tag{2.40}$$

The modified buoyancy parameter $\bar{\delta}$ =sign$(At)\delta$ is used here to prohibit Rayleigh-Taylor instabilities forming at the two fluid interface, effectively maintaining the denser fluid at the base. In cases where the bubble contains incondensable gas, this must be solved numerically. However for pure vapour bubbles, the above expression may be evaluated analytically. Given $\dot{R} = \sqrt{\frac{2}{3}\left(\frac{1}{R^3}-1\right)}$,

$$\begin{aligned}\mathbf{I}_z &= \frac{\bar{\delta}4\pi}{3}\int_0^1 R^3\left(\frac{1}{R^3}-1\right)^{-\frac{1}{2}} dR - \frac{At\pi}{h^2}\int_0^1 R^4\left(\frac{1}{R^3}-1\right)^{\frac{1}{2}} dR \\ &= \bar{\delta}\left(\frac{2}{3}\right)^{\frac{3}{2}}\int_0^1 \tau^{\frac{5}{6}}(1-\tau)^{-\frac{1}{2}} d\tau - \frac{At\pi}{6h^2}\sqrt{\frac{2}{3}}\int_0^1 \tau^{-\frac{1}{6}}(1-\tau)^{\frac{1}{2}} d\tau \\ &= \left(\frac{2}{3}\right)^{\frac{3}{2}}\pi\bar{\delta}\beta\left(\frac{11}{6},\frac{1}{2}\right) - \frac{At\pi}{6h^2}\sqrt{\frac{2}{3}}\beta\left(\frac{7}{6},\frac{3}{2}\right) \end{aligned} \tag{2.41}$$

In zero gravity cases, one may immediately deduce from equation (2.40) that the sign of the impulse in the z direction correlates to the negative of the sign of the Atwood number, as the remaining integral is necessarily positive. Hence one expects the gross movement of the bubble to be toward the interface for $\rho > 1$, and away from the interface for $\rho < 1$. This of course corresponds to the behaviour at the extremes $\rho \to \infty$, solid boundary behaviour, and $\rho = 0$, free surface behaviour [12]. For $\rho = 0$, $\mathbf{I}_z = 0$ and there is therefore no attraction or repulsion, a situation commonly known as the null-impulse state.

Under the action of gravity, it is possible to find for given ρ and δ the null impulse standoff distance. Interesting phenomena occur for bubbles in such an environment near free surfaces and rigid boundaries, including horizontal bubble pinching [74, 9]. For a vapour bubble this state is found using equation (2.41), and occurs when,

$$\begin{aligned} 2\bar{\delta}\beta\left(\frac{11}{6},\frac{1}{2}\right) &= \frac{At}{h^2}\beta\left(\frac{7}{6},\frac{3}{2}\right) \\ \Rightarrow h^2 &= \frac{At}{2\delta}\frac{\beta\left(\frac{7}{6},\frac{3}{2}\right)}{\beta\left(\frac{11}{6},\frac{1}{2}\right)} \\ \Rightarrow h &\approx 0.4417\sqrt{\frac{At}{\delta}} \end{aligned} \tag{2.42}$$

Figure 2.4 shows the null impulse state calculated for a bubble with $\epsilon = 100$, $\gamma = 1.4$ and $\sigma = 0$ over a range of buoyancy parameters and the complete range of Atwood numbers. The black lines indicate the null impulse states for $\delta = 0.0147$ and $\rho = 0.76$, their intersection corresponding to the water/white spirit experiments conducted by Chahine and Bovis [23]. The buoyancy δ has been limited to a range $\delta \geq 0.005$ as the null impulse standoff distance increases as δ^{-1}.

2.7 Chapter summary

This chapter has summarised the behaviour of a spherical bubble model in an infinite fluid, and how this can be used to find a leading order approximation to the two-fluid interface problem of interest in this thesis. This approximation is only valid for sufficiently large standoff distances, where the deformation of the interface is small. However for the applications illustrated in Chapter 1, it is essential to examine the dynamics when bubbles are created much closer to the fluid-fluid interface, and deformations in both surfaces are substantial. A numerical investigation is essential for this, and the following chapter provides a detailed account of the techniques used, namely the boundary integral method for incompressible, potential flow around a cavitation bubble near a two-fluid interface.

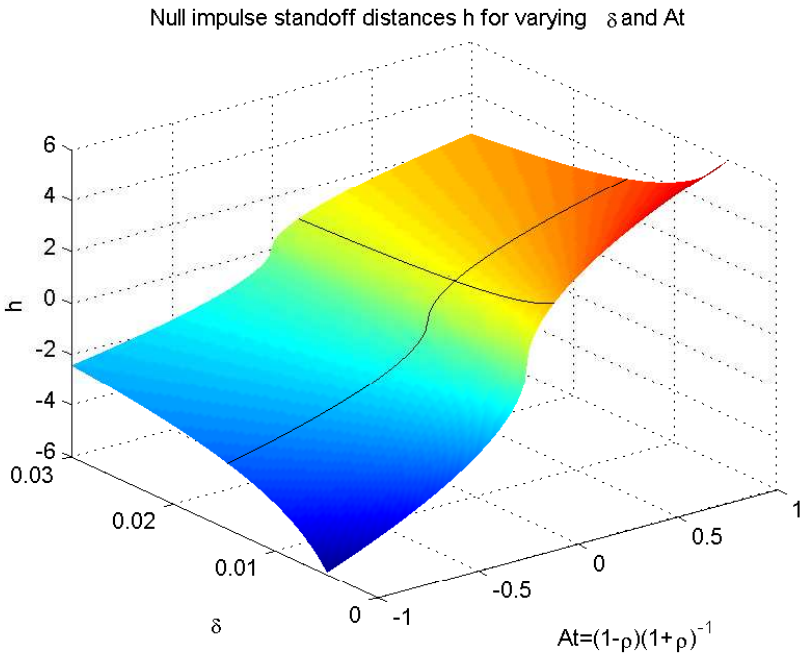

Figure 2.4: The null impulse standoff distance h for a varying range of δ and At. The black lines indicate $\delta = 0.0147$ and $\rho = 0.76$, with their crossing point applicable to the experiments in Chahine and Bovis [23].

Chapter 3

The Boundary Integral Method for Cavitation Bubbles Collapsing Near a Fluid-Fluid Interface

The techniques used to produce the results in this thesis extend the work of Taib [81] among others. The primary extension made is the inclusion of an infinite fluid-fluid interface at the shared boundary of two Newtonian fluids of different densities, ρ_1 and ρ_2. This chapter will provide a detailed description of the numerical procedures necessary to model the fluid motions up to the point where the exterior flow fields become doubly connected. The incorporation of the vortex ring method for doubly connected toroidal bubbles is given in the following chapter.

The flow fields in both external fluids initially have zero velocity and pressure gradient everywhere. No external forces other than gravity are affecting the system, and so it can be presumed that the flow remains irrotational. One presumes all velocities are sufficiently below the speed of sound in the fluid so that the compressibility of the liquid may be neglected. The equation for the continuity of mass may thereby be expressed as $\nabla \cdot \mathbf{u}_i = 0$ in liquids $i = 1, 2$. As in Chapter 2, viscosity does not enter through the

Navier-Stokes equations as $\nabla^2 \mathbf{u}_i = \nabla(\nabla \cdot \mathbf{u}_i) - \nabla \times (\nabla \times \mathbf{u}_i) = 0$. Therefore, viscosity can only enter through the boundary conditions, although in this work it is neglected. These assumptions may not fully hold within the thin boundary layers separating the fluid phases at the bubble surfaces and the two liquid interface. However, the impact this has on the bulk of the flow is likely to be negligible, as the dominant contribution to the fluid behaviour will be through inertia. An axisymmetric model is developed, and any complex external geometry is also not considered.

To initiate the simulation, one or more spherical cavities are inserted into each liquid layer along the axis of symmetry. Their initial radii are either the minimum radius attainable for a high pressure bubble, or the reference radius for an equilibrium pressure, acoustically driven bubble. In the case of the acoustically driven bubble, the oscillating pressure field is also initiated. A stylised example of the axisymmetric flow field is given in figure 3.1, illustrating the axisymmetric plane for a single value of θ.

One considers velocity potentials in each liquid layer, satisfying $\mathbf{u}_i = \nabla \phi_i$. The evaluation of the continuity equation demonstrates that they satisfy Laplace's equation,

$$0 = \nabla \cdot \mathbf{u}_i = \nabla \cdot \nabla \phi_i = \nabla^2 \phi_i, \tag{3.1}$$

and hence the solution to Laplace's equation may be used to calculate the velocity of the flow field. A boundary integral approach is therefore utilised, given appropriate kinematic and dynamic boundary conditions. This algorithmic procedure reduces the three dimensional problem over the fluid volumes to a one dimensional problem over the axisymmetric surfaces. These surfaces are discretised into a set of nodes connected through interpolating splines. A discretised version of Green's integral formula is then employed, allowing an approximation of the unknown potentials and normal velocities to be determined given various known quantities. The ODEs associated with the kinematic and dynamic bound-

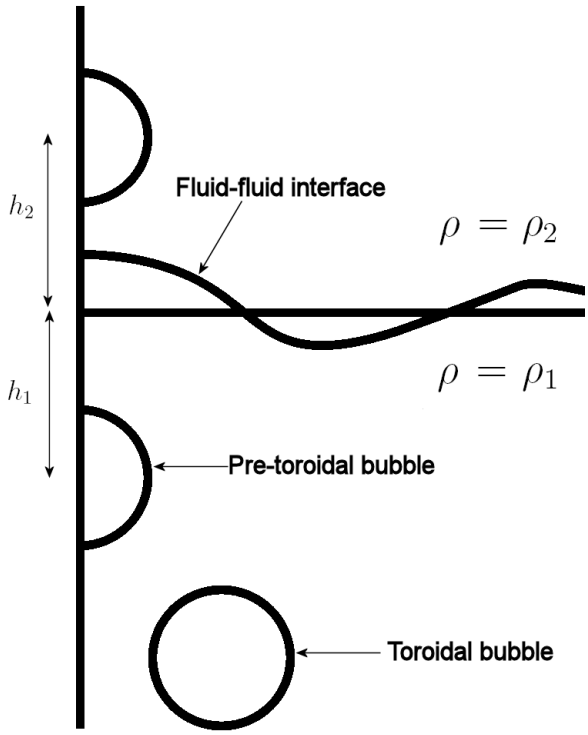

Figure 3.1: A stylised example of a single axisymmetric plane during a simulation.

ary conditions can then be explicitly advanced forward in time, providing the required information on boundary locations and velocity potentials to repeat the procedure.

3.1 Boundary value problem

As the velocity potentials satisfy Laplace's equation in each exterior liquid layer, these potentials may be found everywhere using Green's integral formula with only the potential and its normal derivative on the surfaces of the fluid domains. For the two fluid case under investigation, there are two types of surface to consider, that of the bubbles in fluid i, ∂B_i, and the fluid-fluid interface itself, ∂I.

As will be seen later, this integral approach provides the potential at a surface point $\mathbf{x}_0$ in terms of an integral over the rest of the surface, described by the points $\mathbf{x}$. To clarify the points in question, the following convention is used. The surface of bubbles in fluid 1 is described by the set $\mathbf{x} = \mathbf{c}$ and the nodes relating to this surface are at locations $\mathbf{x}_0 = \mathbf{b}$. For bubbles in fluid 2 one similarly has $\mathbf{x} = \mathbf{e},\ \mathbf{x}_0 = \mathbf{d}$, and for any point on the fluid-fluid interface $\mathbf{x}_0 = \mathbf{p},\ \mathbf{x} = \mathbf{q}$. Additionally, as in certain circumstances multiple unknown functions require identical numerical treatment in the integral equations, the function χ will be utilised as a general purpose unknown.

3.1.1 Surface interpolation using splines

The position of the surfaces, and any known functional variables along the surfaces, are only known explicitly in the numerical implementation at a discrete set of n distinct collocation points or nodes. However, the location and functional behaviour between the nodes is also required, and must therefore be interpolated. Polynomial spline interpolation is the preferred method in this work, although other methods such local overlapping polynomial interpolation are also viable.

Polynomial spline interpolation, regarded henceforth as spline interpolation, involves

approximating each section between two adjacent nodes by distinct polynomials, each of order $\hat{n}$. The coefficients of these are determined using the function values at the collocation points, as well as the values of the unknown derivatives. These are determined by solving a set of linear equations generated from the continuity of the first $\hat{n}-1$ derivatives at the n nodes. Using higher order polynomials increases the accuracy, albeit at the expense of computational time and memory. This expense is however minimal in comparison to the calculation of the coefficient matrices. Although linear splines can be used, the lowest order employed here is a cubic spline. This is to allow the evaluation of the surface curvature directly from the polynomial coefficients, as this requires the computation of the second derivatives. The smoothness of the surfaces also removes the requirement to calculate the coefficients $c(\mathbf{x}_0)$ in equation (3.26), a computationally intensive task.

Figure 3.2 illustrates the splining of a unit semicircle using linear, cubic and quintic splines through three nodes. In practice many more nodes are required for an accurate approximation, yet this is useful to visualise the improvement in accuracy as the spline order increases.

Cubic splines

Cubic splines are the lowest order spline interpolates which provide continuous second order derivatives at collocation points. These have linearly varying second order derivatives through the interpolated regions between the collocation points, named herein as spline segments. For each segment, four polynomial coefficients must be determined and therefore four variables are required. Continuity of the functions and derivatives allows these to be determined using $2n$ variables, of which n are known a priori as the discrete function values. This leaves n unknowns to be determined in order to create the spline, leading to good computational efficiency. However if higher derivatives are required, or the linear approximation for the second derivative is deemed insufficient, a higher order interpolation is clearly required.

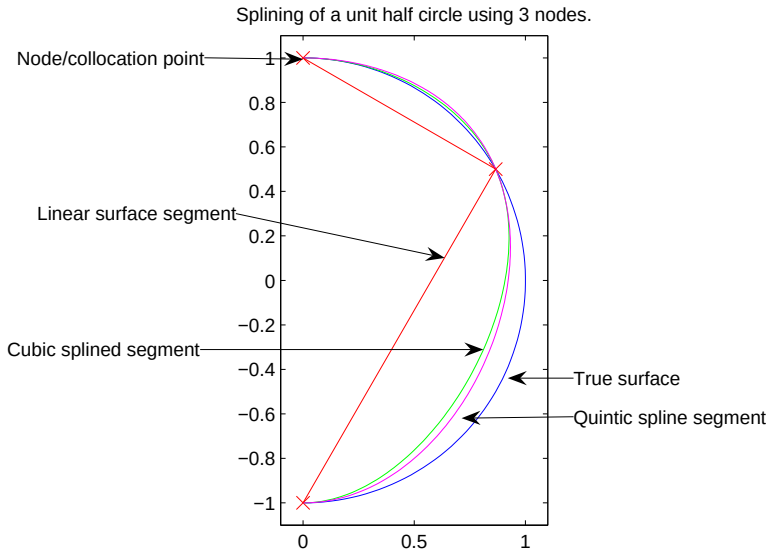

Figure 3.2: Demonstration of the approximation of a unit semi-circle using first, third and fifth order splining. Three nodes are used to emphasise the difference between the actual and approximated surfaces. Many more nodes are used in practice.

Let one first consider the arc length dependent spline given by,

$$c_i = \sum_{k=0}^{3} b_{i,k}\xi^k, \;\; i = 1, \ldots, n-1. \tag{3.2}$$

Using the second derivatives at the collocation points labeled i, $c_i''(\xi_i) = N_i$, the interpolation of this derivative between the nodes may immediately be expressed as,

$$c_i''(\xi) = \frac{N_i(\xi_{i+1} - \xi) + N_{i+1}(\xi - \xi_i)}{\xi_{i+1} - \xi_i}.$$

Integrating twice now returns the spline segment as,

$$c_i(\xi) = \frac{N_i(\xi_{i+1} - \xi)^3 + N_{i+1}(\xi - \xi_i)^3}{6(\xi_{i+1} - \xi_i)} + A_i(\xi - \xi_i) + B_i(\xi_{i+1} - \xi).$$

The coefficients A_i and B_i are readily determined by substitution of the nodal function

values, C_i and C_{i+1}. Using $\Delta_i = (\xi_{i+1} - \xi_i)$ for clarity, this gives the spline segment as the cubic polynomial,

$$c_i = \frac{N_i(\xi_{i+1} - \xi)^3 + N_{i+1}(\xi - \xi_i)^3}{6\Delta_i} + \left(6C_i - N_i\Delta_i^2\right)\frac{(\xi_{i+1} - \xi)}{6\Delta_i} + \left(6C_{i+1} - N_{i+1}\Delta_i^2\right)\frac{(\xi - \xi_i)}{6\Delta_i}.$$

The coefficients $b_{i,k},\ i = 1, ..., n,\ k = 0, ..., 3$ in (3.2) are hence given as,

$$\begin{aligned}
b_{i,3} &= \frac{N_{i+1} - N_i}{6\Delta_i}, \\
b_{i,2} &= \frac{\xi_{i+1}N_i - \xi_i N_{i+1}}{2\Delta_i}, \\
b_{i,1} &= \frac{\xi_i^2 N_{i+1} - \xi_{i+1}N_i}{2\Delta_i} + \frac{C_{i+1} - C_i}{\Delta_i} + \frac{(N_i - N_{i+1})\Delta_i}{6}, \\
b_{i,0} &= \frac{\xi_{i+1}^3 N_i - \xi_i^3 N_{i+1}}{6\Delta_i} + \frac{\xi_{i+1}\left(6C_i - N_i\Delta_i^2\right) - \xi_i\left(6C_{i+1} - N_{i+1}\Delta_i^2\right)}{6\Delta_i}.
\end{aligned} \tag{3.3}$$

Continuity of the first derivatives provides the required equations for the $n - 2$ unknowns $N_i,\ i = 2, ..., n - 1$. This gives the set of equations,

$$\begin{aligned}
& N_i\left(\frac{\Delta_{i-1}}{3}\right) + N_{i-1}\left(\frac{\Delta_{i-1}}{6}\right) + \frac{C_i - C_{i-1}}{\Delta_{i-1}} = -N_i\left(\frac{\Delta_i}{3}\right) - N_{i+1}\left(\frac{\Delta_i}{6}\right) + \frac{C_{i+1} - C_i}{\Delta_i} \\
\Rightarrow\ & \frac{C_{i+1} - C_i}{\Delta_i} + \frac{C_{i-1} - C_i}{\Delta_{i-1}} = N_i\left(\frac{\Delta_i + \Delta_{i-1}}{3}\right) + N_{i-1}\left(\frac{\Delta_{i-1}}{6}\right) + N_{i+1}\left(\frac{\Delta_i}{6}\right).
\end{aligned}$$

Either the first or second derivative may be given as the remaining two unknowns at the end nodes. Given, for example, the first derivative at the first node and the second derivative at the final node, the system may be written in matrix form as,

$$
T1\mathbf{N} = \begin{bmatrix}
-\frac{\Delta_2}{6} & -\frac{\Delta_2}{3} & & & & \\
\frac{\Delta_{i-1}}{6} & \frac{\Delta_i - \Delta_{i-1}}{3} & \frac{\Delta_i}{6} & & & \\
& \ddots & \ddots & \ddots & & \\
& & \frac{\Delta_{i-1}}{6} & \frac{\Delta_i - \Delta_{i-1}}{3} & \frac{\Delta_i}{6} & \\
& & & & 1
\end{bmatrix}
\begin{bmatrix} N_1 \\ \\ \vdots \\ \\ N_n \end{bmatrix}
$$

$$
= \begin{bmatrix}
\frac{1}{\Delta_2} & -\frac{1}{\Delta_2} & & & & \\
\frac{1}{\Delta_{i-1}} & -\frac{1}{\Delta_{i-1}} - \frac{1}{\Delta_i} & \frac{1}{\Delta_i} & & & \\
& \ddots & \ddots & \ddots & & \\
& & -\frac{1}{\Delta_{i-1}} - \frac{1}{\Delta_i} & \frac{1}{\Delta_i} & & \\
& & & & 0
\end{bmatrix}
\begin{bmatrix} C_1 \\ \\ \vdots \\ \\ C_n \end{bmatrix}
+ \begin{bmatrix} C_1' \\ 0 \\ \vdots \\ 0 \\ N_n \end{bmatrix}
= T2\mathbf{C} + \mathbf{D}. \quad (3.4)
$$

The matrix $T1$ is tri-diagonal and hence the unknowns $\mathbf{N}$ may be found rapidly using the Thomas algorithm or other suitable solver.

Quintic splines

Quintic splines provide a significant increase in accuracy of cubic splines. This is demonstrated in Chapter 5 over a variety of test cases. The increase in accuracy does however require approximately twice the computational time of the cubic variant to determine the polynomial coefficients due to the requirement to determine a further n unknown variables. Furthermore, the time required to calculate the coefficient block matrices required in the equation (3.40). This is due to the need to calculate the fourth and fifth powers of the splining parameter ξ, which requires a further two multiplications per integration point. The derivation is included here in depth.

A general quintic polynomial between nodes i and $i+1$ is given as,

$$q_i(\xi) = a_{i,0} + \sum_{k=1}^{5} a_{i,k}(\xi)^k. \tag{3.5}$$

By differentiating, it is clear that the fourth derivatives vary linearly between adjacent nodes, as the second derivatives behaved using cubic splines. Using the nomenclature $q_i^{iv}(\xi_i) = M_i$ for the values of the nodal fourth derivatives, one has,

$$q_i^{iv}(\xi) = \frac{M_i(\xi_{i+1} - \xi) + M_{i+1}(\xi - \xi_i)}{\Delta_i}.$$

In an analogous manner to constructing the cubic spline, integrating twice gives the second derivative of the quintic spline as,

$$q_i''(\xi) = \frac{M_i(\xi_{i+1} - \xi)^3 + M_{i+1}(\xi - \xi_i)^3}{6\Delta_i} + A_i(\xi - \xi_i) + B_i(\xi_{i+1} - \xi). \tag{3.6}$$

The constants A_i and B_i can now be determined in terms of the as yet unknown values of the second derivatives at the nodes. Substitution of the second derivative N_i at $\xi = \xi_i$, yields B_i as,

$$N_i = \frac{M_i\Delta_i^2}{6} + B_i\Delta_i \Rightarrow B_i = \frac{6N_i - M_i\Delta_i^2}{6\Delta_i}.$$

Similarly using the second derivative at $\xi = \xi_{i+1}$, N_{i+1}, A_i may be found as,

$$A_i \;=\; \frac{6N_{i+1} - M_{i+1}\Delta_i^2}{6\Delta_i}.$$

Integrating twice again gives the equation for each quintic spline segment as,

$$\begin{aligned} q_i(\xi) &= \frac{M_i(\xi_{i+1}-\xi)^5 + M_{i+1}(\xi-\xi_i)^5}{120\Delta_i} + \left(\frac{6N_{i+1} - M_{i+1}\Delta_i^2}{36\Delta_i}\right)(\xi-\xi_i)^3 \\ &+ \left(\frac{6N_i - M_i\Delta_i^2}{36\Delta_i}\right)(\xi_{i+1}-\xi)^3 + C_i(\xi-\xi_i) + D_i(\xi_{i+1}-\xi). \end{aligned}$$

The coefficients C_i and D_i can now be expressed using the known values $q_i(\xi_i) = Q_i$ and $q_i(\xi_{i+1}) = Q_{i+1}$. This gives,

$$\begin{aligned} D_i &= \frac{Q_i}{\Delta_i} - \frac{N_i\Delta_i}{6} + \frac{7M_i\Delta_i^3}{360}, \\ C_i &= \frac{Q_{i+1}}{\Delta_i} - \frac{N_{i+1}\Delta_i}{6} + \frac{7M_{i+1}\Delta_i^3}{360}. \end{aligned}$$

Substitution of these values then provides the spline segment as,

$$\begin{aligned} q_i(\xi) &= \frac{M_i(\xi_{i+1}-\xi)^5 + M_{i+1}(\xi-\xi_i)^5}{120\Delta_i} \\ &+ \frac{(6N_{i+1} - M_{i+1}\Delta_i^2)(\xi-\xi_i)^3 + (6N_i - M_i\Delta_i^2(\xi_{i+1}-\xi)^3)}{36\Delta_i} \\ &+ \left(\frac{Q_{i+1}}{\Delta_i} - \frac{N_{i+1}\Delta_i}{6} + \frac{7M_{i+1}\Delta_i^3}{360}\right)(\xi-\xi_i) + \left(\frac{Q_i}{\Delta_i} - \frac{N_i\Delta_i}{6} + \frac{7M_i\Delta_i^3}{360}\right)(\xi_{i+1}-\xi). \end{aligned}$$

Thus, the coefficients $a_{i,k}$ of the spline segment are given by,

$$\begin{aligned}
a_{i,5} &= \frac{M_{i+1}-M_i}{120\Delta_i},\\
a_{i,4} &= \frac{M_i\xi_{i+1}-M_{i+1}\xi_i}{24\Delta_i},\\
a_{i,3} &= \frac{M_{i+1}\xi_i^2-M_i\xi_{i+1}^2}{12\Delta_i}+\frac{6(N_{i+1}-N_i)+\Delta_i^2(M_i-M_{i+1})}{36\Delta_i},\\
a_{i,2} &= \frac{M_i\xi_{i+1}^3-M_{i+1}\xi_i^3}{12\Delta_i}+\frac{\xi_{i+1}(6N_i-M_i\Delta_i^2)-\xi_i(6N_{i+1}-M_{i+1}\Delta_i^2)}{12\Delta_i},\\
a_{i,1} &= \frac{M_{i+1}\xi_i^4-M_i\xi_{i+1}^4}{24\Delta_i}+\frac{\xi_i^2(6N_{i+1}-M_{i+1}\Delta_i^2)-\xi_{i+1}^2(6N_i-M_i\Delta_i^2)}{12\Delta_i}\\
&\quad+\left(\frac{Q_{i+1}}{\Delta_i}-\frac{N_{i+1}\Delta_i}{6}+\frac{7M_{i+1}\Delta_i^3}{360}\right)-\left(\frac{Q_i}{\Delta_i}-\frac{N_i\Delta_i}{6}+\frac{7M_i\Delta_i^3}{360}\right),\\
a_{i,0} &= \frac{M_i\xi_{i+1}^5-M_{i+1}\xi_i^5}{120\Delta_i}+\frac{-\xi_i^3(6N_{i+1}-M_{i+1}\Delta_i^2)+\xi_{i+1}^3(6N_i-M_i\Delta_i^2)}{36\Delta_i}\\
&\quad+\xi_{i+1}\left(\frac{Q_i}{\Delta_i}-\frac{N_i\Delta_i}{6}+\frac{7M_i\Delta_i^3}{360}\right)-\xi_i\left(\frac{Q_{i+1}}{\Delta_i}-\frac{N_{i+1}\Delta_i}{6}+\frac{7M_{i+1}\Delta_i^3}{360}\right).
\end{aligned}$$

It now remains to find the $2n$ unknowns $\{N_i, M_i | i = 1, ..., n\}$. The continuity of the first and third derivatives give $2n-4$ equations involving the unknowns associated with the proceeding and following collocation points. Hence the remaining four unknowns must be imposed at nodes 1 and n. From the third derivative of equation (3.5), for the nodes $i = 2, \ldots, n-1$ one acquires,

$$60a_{i,5}\xi_i^2+24a_{i,4}\xi_i+6a_{i,3}=60a_{i-1,5}\xi_i^2+24a_{i-1,4}\xi_i+6a_{i-1,3},$$

and hence half of the simultaneous equations to be solved for the unknown derivatives are given by,

$$\begin{aligned}
&-\frac{(2M_i+M_{i+1})\Delta_i}{6}+\frac{N_{i+1}-N_i}{\Delta_i}=\frac{(M_{i-1}+2M_i)\Delta_{i-1}}{6}+\frac{N_i-N_{i-1}}{\Delta_{i-1}}\\
\Rightarrow\quad &0=M_i\left(\frac{\Delta_i+\Delta_{i-1}}{3}\right)+\frac{M_{i+1}\Delta_i}{6}+\frac{M_{i-1}\Delta_{i-1}}{6}+N_i\left(\frac{1}{\Delta_{i-1}}+\frac{1}{\Delta_i}\right)-\frac{N_{i-1}}{\Delta_{i-1}}-\frac{N_{i+1}}{\Delta_i}.
\end{aligned}$$

Similarly, the first derivatives of equation (3.5) at nodes $i = 2, \ldots, n-1$ give,

$$5a_{i,5}\xi_i^4 + 4a_{i,4}\xi_i^3 + 3a_{i,3}\xi_i^2 + 2a_{i,2}\xi_i + a_{i,1} = \\ 5a_{i-1,5}\xi_i^4 + 4a_{i-1,4}\xi_i^3 + 3a_{i-1,3}\xi_i^2 + 2a_{i-1,2}\xi_i + a_{i-1,1},$$

and therefore the remaining simultaneous equations are provided at these collocation points as,

$$\begin{aligned} &\frac{M_i\Delta_i^3}{45} + \frac{7M_{i+1}\Delta_i^3}{360} + \frac{Q_{i+1}-Q_i}{\Delta_i} - \frac{(2N_i+N_{i+1})\Delta_i}{6} = \\ &\qquad - \frac{M_i\Delta_{i-1}^3}{45} - \frac{7M_{i-1}\Delta_{i-1}^3}{360} + \frac{N_i\Delta_{i-1}}{3} + \frac{N_{i-1}\Delta_{i-1}}{6} + \frac{Q_i - Q_{i-1}}{\Delta_{i-1}} \\ \Rightarrow \quad &\frac{Q_{i+1}-Q_i}{\Delta_i} + \frac{Q_{i-1}-Q_i}{\Delta_{i-1}} = -\frac{M_i(\Delta_i^3+\Delta_{i-1}^3)}{45} - \frac{7M_{i+1}\Delta_i^3}{360} - \frac{7M_{i-1}\Delta_{i-1}^3}{360} \\ &\qquad + \frac{N_i(\Delta_i+\Delta_{i-1})}{3} + \frac{N_{i+1}\Delta_i}{6} + \frac{N_{i-1}\Delta_{i-1}}{6} \end{aligned}$$

These equations form a system of the type $\mathbf{Ax} = \mathbf{b}$ where $\mathbf{A}$ is a sparse banded matrix, and again may be rapidly solved. If desired, some simple algebra allows the first and third derivatives at the end points to be used if known.

Due to the axisymmetric nature of the model, it must hold that the first and third derivatives of the potential functions ϕ and the normal velocities must be zero on the axis of symmetry. This also holds for the parameterised vertical co-ordinate z. The parameterised radial position r of the surface has zero second and fourth derivatives on the axis.

When a complete closed curve is required, as is the case for vortex ring toroidal bubbles, the first node is also the last and so all derivatives must be continuous at the ends of the loop, leading to a system of $2n$ unknowns with $2n$ equations. In this case it is not necessary to enter pre-calculated derivatives at the end points, although this has been done in previous works [64, 5]. The closed spline may also be used for non-toroidal

bubbles by reflecting all non-axial nodes across the axis of rotation, and then ignoring the additional spline coefficients generated in the reflected plane. This is computationally expensive, and will not necessarily give an exactly symmetrical solution, although in some circumstances may provide a more stable arc length calculation.

The gain in accuracy from using quintic splines over cubic splines, as will be shown in Chapter 5, outweighed the additional computational expense in practice, and so quintic splines were employed predominantly.

Calculation of the arc length

Although the total surface arc length is not known initially, it can be computed iteratively to a high degree of accuracy [5, 31, 64]. The length L of any contour parameterised by ξ in the r, z plane is given by,

$$L = \int_0^{\xi_{end}} \sqrt{\left(\frac{dr}{d\xi}\right)^2 + \left(\frac{dz}{d\xi}\right)^2}\, d\xi,$$

where ξ_{end} is the value of ξ at the end of the contour. Hence in terms of the spline approximation of a contour over n nodes, the arc length is given as,

$$L = \sum_{k=1}^{n-1} \int_{\xi_k}^{\xi_{k+1}} \sqrt{\left(\frac{dr_k}{d\xi}\right)^2 + \left(\frac{dz_k}{d\xi}\right)^2}\, d\xi \qquad (3.7)$$
$$\xi_1 = 0,\ \xi_n = \xi_{end}.$$

An iterative algorithm is used, based on successive approximations to the arc length. This involves splining through the r and z co-ordinates using the previous arc length estimate, initially the straight line distance between adjacent nodes, and then re-evaluating the arc length by integrating the integrals in (3.7). Once the difference between the input and output arc lengths has reached a specified tolerance, the algorithm finishes. Any

spline based approximations for non-geometric functions are calculated using the final arc length. The aim is to equate the splining parameter to the actual arc length, so that $\sqrt{r'^2 + z'^2} = 1$, where $'$ represents differentiation with respect to ξ. In practice due to the finite order of each spline segment this is not always possible, particularly in regions of high curvature. It is however sufficiently correct in simpler regions, particularly towards the far end of the fluid-fluid interface. The algorithm is detailed in equation (3.8).

$$
\begin{aligned}
\xi_{(i)a} &= 0 \;\forall\; i = 1 \ldots_1, n \\
\xi_{(i)b} &= \sum_{k=1}^{i-1} |\mathbf{x}_{i+1} - \mathbf{x}_i| \\
\text{while} \quad & (|\xi_{(n)a} - \xi_{(n)b}| > \mathbf{tol}) \\
& \xi_{(i)a} = \xi_{(i)b}, \;\forall\; i = 1, \ldots, n \\
& r(\xi) = \mathbf{spline}(r, \xi_a) \\
& z(\xi) = \text{spline}(z, \xi_a) \\
& \xi_{ib} = \int \sum_{k=1}^{i-1} \int_{\xi_{(k)a}}^{\xi_{(k+1)a}} \sqrt{\frac{dr}{d\xi}^2 + \frac{dz}{d\xi}^2}\, d\xi \qquad (3.8) \\
\text{end} & \qquad (3.9)
\end{aligned}
$$

3.1.2 Calculation of the surface curvature

The surface curvature is needed in the calculation of normal stress balances across fluid boundaries. It may be calculated using three orders of derivatives of the spatial variables r, z as,

$$
\nabla \cdot \mathbf{n} = \begin{cases} \frac{r'z'' - z'r''}{(r'^2 + z'^2)^{\frac{3}{2}}} + \frac{z'}{r\sqrt{r'^2 + z'^2}} & r \neq 0 \\ \frac{2z''}{r'^3} & r = 0 \end{cases}. \qquad (3.10)
$$

This may be calculated directly from the splines interpolating r and z. It was found however that the inherently noisy behaviour associated with the BIM simulation could lead to significant oscillations in the second derivatives, as is shown in Chapter 5. To combat this, one employed a least squares fitted polynomial about each collocation point. Typically this was taken to be of fourth order and fitted over 10 points centered at the node in question. Higher order polynomials needed significantly more nodes to fit a stable polynomial through, whereas one required a sufficiently accurate second order approximation using the fourth order interpolants. These polynomials were constructed using the MATLAB function POLYFIT with minimal computational cost. The least squares fit created a significantly more stable approximation, albeit at the expense of the true solution given by the splines.

3.1.3 Kinematic and dynamic boundary conditions

Kinematic conditions

It is assumed that any particle located on any surface will remain on that surface. As such, it is required to move with the normal velocity of that surface. The tangential velocity of any surface particles is however arbitrary providing the necessary modifications to the dynamic conditions are performed.

On the bubble surfaces, the velocity of a surface particle is taken as the velocity of the exterior fluid, and hence the kinematic condition for a bubble in fluid 1 is given by,

$$\frac{d\mathbf{b}}{dt} = \mathbf{u}_1(\mathbf{b}). \tag{3.11}$$

The equivalent condition applies for bubbles located in fluid 2.

To prevent cavities forming between the two liquid layers the normal velocity must be continuous across the fluid-fluid interface. Therefore the relationship between the normal

derivatives of the potentials across this interface with respect to the outward normal of fluid 2 must satisfy,

$$\mathbf{u}_1 \cdot \mathbf{n}_2 = \mathbf{u}_2 \cdot \mathbf{n}_2. \tag{3.12}$$

Due to the inviscid nature of the model, there is a difference in tangential velocity across the interface, and so it is taken that any particles located on this interface will move at the average velocity of the two fluids on either side of the interface.

$$\frac{d\mathbf{p}}{dt} = \frac{\mathbf{u}_1(\mathbf{p}) + \mathbf{u}_2(\mathbf{p})}{2} = \mathbf{u}_{av}(\mathbf{p}), \tag{3.13}$$

Therefore particles on this interface move in a pseudo-Lagrangian manner. This is acceptable mathematically, as the surface evolution is governed exclusively by the normal velocity, and so the tangential velocity may be taken arbitrarily so long as the appropriate modifications are made to the dynamic condition.

It is now convenient to introduce the following notation to express the potentials at the two fluid interface and further remove any ambiguity over which potential is under reference. One defines,

$$\bar{\phi}(\mathbf{p}) = \phi_1(\mathbf{p}) + \phi_2(\mathbf{p})$$
$$\mu(\mathbf{p}) = \phi_1(\mathbf{p}) - \phi_2(\mathbf{p}).$$

$\bar{\phi}$ is effectively double the average potential, whilst μ is a measure of the tangential slip at the interface. Using these variables, the kinematic condition at the fluid-fluid interface may be written as,

$$\frac{d\mathbf{p}}{dt} = \frac{\nabla\bar{\phi}(\mathbf{p})}{2} = \mathbf{u}_{av}. \tag{3.14}$$

Dynamic conditions

Bernoulli's equation is valid everywhere in both exterior fluids, and specifically it is valid at the interfaces. In dimensional terms it is stated as,

$$\frac{\partial \phi_i}{\partial t} + \frac{|\mathbf{u}_i|^2}{2} = -\frac{p}{\rho_i} - g(z - z_0) + \frac{p_\infty(t)}{\rho_i}. \tag{3.15}$$

Given $p_\infty(t)$, it is employed to establish the normal stress balance at the interfaces, and to construct the necessary substantial derivatives for the evolution of the surface potentials. In this section harmonic forcing will be ignored for brevity, although it is included in the study of ultrasound driven cavitation in Chapter 8. The constants z_0 are the given reference co-ordinates of the system at rest. This is taken to be $z_0 = 0$ along the two fluid interface as this is always taken as the vertical centre of the flow field. For any bubbles it is taken as the the initial centroid location for all points on the surface. This would be the hypothetical limit if the bubble was initiated from a single point. The initial centroid locations are naturally the standoff distances of the bubbles, taken as negative for bubbles in layer 1 and positive for bubbles in layer 2. All terms are non-dimensionalised with respect to the maximum radius the bubble would reach in an infinite fluid for both high pressure underwater explosion (UNDEX) bubbles and equilibrium pressure acoustically driven bubbles, as described in Chapter 2. The density chosen for non-dimensionalisation is the density of liquid layer 1, ρ_1. The non-dimensional density ratio is given as $\rho = \frac{\rho_2}{\rho_1}$.

At a bubble surface in fluid 1, assuming the gases inside the bubble are ideal and behave adiabatically, one has,

$$\frac{\partial \phi_1(\mathbf{b})}{\partial t} + \frac{|\mathbf{u}_1(\mathbf{b})|^2}{2} = 1 - \epsilon \left(\frac{V_0}{V}\right)^\gamma - \delta(z - z_0) + \sigma_{b1} \nabla \cdot \mathbf{n}_{b1}, \tag{3.16}$$

and similarly for bubbles located in the second fluid layer, one has

$$\frac{\partial \phi_2(\mathbf{d})}{\partial t} + \frac{|\mathbf{u}_2(\mathbf{d})|^2}{2} = \frac{1}{\rho}\left(1 - \epsilon\left(\frac{V_0}{V}\right)^{\gamma} + \sigma_{b2}\nabla \cdot \mathbf{n}_{b2}\right) - \delta(z - z_0). \tag{3.17}$$

The buoyancy parameter δ is given as,

$$\delta = \frac{\rho_1 g R_{max}}{\Delta_p}, \tag{3.18}$$

and hence one observes that the effect of gravity on the bubble is directly proportional to the size of the bubble.

The surfaces are updated in a Lagrangian/pseudo-Lagrangian manner dependent on their type, using the surface velocities $\mathbf{u} = \frac{d\mathbf{x}}{dt}$. The substantial derivatives are therefore constructed using,

$$\frac{D}{Dt} = \frac{\partial}{\partial t} + \mathbf{u} \cdot \nabla. \tag{3.19}$$

Some elementary manipulation then yields the Lagrangian evolution of the potentials on the bubble surfaces through time as,

$$\frac{D\phi_1(\mathbf{b})}{Dt} = \frac{|\mathbf{u}_1(\mathbf{b})|^2}{2} + 1 - \epsilon\left(\frac{V_0}{V}\right)^{\gamma} - \delta(z + h_1) + \sigma_{b1}\nabla \cdot \mathbf{n}_{b1}, \tag{3.20}$$

$$\frac{D\phi_2(\mathbf{d})}{Dt} = \frac{|\mathbf{u}_2(\mathbf{d})|^2}{2} + \frac{1}{\rho}\left(1 - \epsilon\left(\frac{V_0}{V}\right)^{\gamma} + \sigma_{b2}\nabla \cdot \mathbf{n}_{b2}\right) - \delta(z - h_2). \tag{3.21}$$

These potentials may now be found at a subsequent times by numerically integrating (3.20) and (3.21), given the velocity at the bubble surface and the shape of the bubble.

At the fluid-fluid interface the pressure is not explicitly known. However, the Young-

Laplace condition does provide the pressure balance across the interface as,

$$p_1 = p_2 - \hat{\sigma}_I \nabla \cdot \mathbf{n}_1,$$

where $\hat{\sigma}_I$ is the interfacial tension.One now has,

$$\rho_1 \left(\frac{\partial \phi_1(\mathbf{p})}{\partial t} + \frac{|\mathbf{u}_1(\mathbf{p})|^2}{2} + gz \right) = \rho_2 \left(\frac{\partial \phi_2(\mathbf{p})}{\partial t} + \frac{|\mathbf{u}_2(\mathbf{p})|^2}{2} + gz \right) - \hat{\sigma}_I \nabla \cdot \mathbf{n}_1. \qquad (3.22)$$

One notes here that there will be no explicit dependence on $p_\infty(t)$ in (3.22), and so any harmonic forcing is only incorporated into (3.20) and (3.21). This is because the pressure itself is not explicitly calculated at this interface during the normal processing of the algorithm.

Manipulating (3.22) and non-dimensionalising as previously, one finds at $\mathbf{p}$,

$$\begin{aligned} \left(\frac{\partial \phi_1}{\partial t} + \frac{|\mathbf{u}_1|^2}{2} \right) - \frac{\rho_2}{\rho_1} \left(\frac{\partial \phi_2}{\partial t} + \frac{|\mathbf{u}_2|^2}{2} \right) &= \frac{g R_{max} \rho_1}{\Delta p} z \left(1 + \frac{\rho_2}{\rho_1} \right) - \frac{\hat{\sigma}_I \rho_1}{\Delta_p R_{max}} \nabla \cdot \mathbf{n}_1 \\ \Rightarrow \left(\frac{\partial \phi_1}{\partial t} + \frac{|\mathbf{u}_1|^2}{2} \right) - \rho \left(\frac{\partial \phi_2}{\partial t} + \frac{|\mathbf{u}_2|^2}{2} \right) &= \delta z \left(1 + \rho \right) + \sigma_I \nabla \cdot \mathbf{n}_2, \qquad (3.23) \end{aligned}$$

where ρ is the ratio of the liquid densities as given in (3.25). Incorporating the substantial derivative, the following is obtained.

$$\frac{D}{Dt} \left(\bar{\phi} \left(1 - \rho \right) + \mu \left(1 + \rho \right) \right) = \left(1 - \rho \right) \left(\mathbf{u}_1 \cdot \mathbf{u}_2 \right) - 2\delta z \left(1 + \rho \right) - 2\sigma_I \nabla \cdot \mathbf{n}_2. \qquad (3.24)$$

The dimensionless parameters appearing in equations (3.20) and (3.24) are the buoyancy parameter δ, the density ratio ρ, the strength parameter ϵ, the ratio of specific heats of the incondensable gases in the bubble γ, the standoff distances h_i, and the surface tension on the fluid-fluid interface and bubble surfaces, σ_I and σ_b respectively. They are

defined as follows.

$$\delta = \frac{gR_{max}\rho_1}{\Delta_p},\ \rho = \frac{\rho_2}{\rho_1},\ \sigma_{bi} = \frac{\bar{\sigma}_b}{\Delta_p R_{max}},\ \sigma_I = \frac{\hat{\sigma}_I}{\Delta_p R_{max}},\ \epsilon = \frac{p_0}{\Delta_p},\ h = \frac{h_{dim}}{R_{max}}. \quad (3.25)$$

3.1.4 Green's Integral Formula

As stated previously, Green's integral formula provides the solution to Laplace's equation, $\nabla^2\phi = 0$, in any simply connected domain D as a function of the potential and normal velocity on the boundary ∂D. For any point $\mathbf{x}_0 \in D$, with the surface co-ordinates of the fluid given as $\mathbf{x} \in \partial D$, this formula states that,

$$c(\mathbf{x}_0)\phi(\mathbf{x}_0) = \int_{\partial D} \left(G(\mathbf{x}_0, \mathbf{x}) \frac{\partial \phi(\mathbf{x})}{\partial n} - \phi(\mathbf{x}) \frac{\partial G(\mathbf{x}_0, \mathbf{x})}{\partial n} \right) dS. \quad (3.26)$$

The coefficients $c(\mathbf{x}_0)$ are the solid angles subtended from the collocation points by the surface geometry. Should linear interpolation be employed for the surface co-ordinates, these would have to be calculated at each node. However, due to the spline interpolation providing continuous first and second derivatives in the interpolated surface co-ordinates, the boundary ∂D is sufficiently smooth for the collocation coefficients to be given by,

$$c(\mathbf{x}_0) = \begin{cases} 4\pi & \mathbf{x}_0 \in D \backslash \partial D \\ 2\pi & \mathbf{x}_0 \in \partial D \end{cases}. \quad (3.27)$$

In this work $G(\mathbf{x}_0, \mathbf{x})$ is a variant of the classical free space Green's function with the factor 4π absorbed into the collocation coefficients. Therefore this Green's function is given by,

$$G(\mathbf{x}_0, \mathbf{x}) = \frac{1}{|\mathbf{x}_0 - \mathbf{x}|}.$$

In cylindrical co-ordinates, the distance between the points $\mathbf{x} = (r, \theta, z)$ and $\mathbf{x}_0 =$

(r_0, θ_0, z_0) is given as,

$$|\mathbf{x}_0 - \mathbf{x}| = \sqrt{r^2 + r_0^2 - 2rr_0\cos(\theta - \theta_0) + (z - z_0)^2}. \tag{3.28}$$

Assuming the flow to be axisymmetric, as is the case for a vertical column of bubbles perpendicular to an initially horizontal surface, θ_0 may be taken arbitrarily as 0. The free space Green's function becomes,

$$\begin{aligned} G(\mathbf{x}, \mathbf{x}_0) &= \frac{1}{\sqrt{r^2 + r_0^2 + 2rr_0 - 2rr_0(\cos(\theta) - 1) + (z - z_0)^2}} \\ &= \frac{1}{\sqrt{(r + r_0)^2 + (z - z_0)^2 - 4rr_0\cos^2(\frac{\theta}{2})}}. \end{aligned} \tag{3.29}$$

The surfaces ∂D encasing each fluid region are parameterised with respect to (ξ, θ) as $\mathbf{x} = (r(\xi), \theta, z(\xi))$. Due to the axisymmetric model all derivatives with respect to θ are taken as zero. The normals $\mathbf{n}$ on the fluid surfaces are therefore given in cylindrical polar co-ordinates by,

$$\mathbf{n} = \frac{z'\mathbf{e}_r - r'\mathbf{e}_z}{\sqrt{z'^2 + r'^2}}, \tag{3.30}$$

where $'$ again signifies differentiation with respect to ξ. The corresponding derivative of the free space Green's function (3.29) with respect to this normal vector is therefore,

$$\begin{aligned} \frac{\partial G(\mathbf{x}, \mathbf{x}_0)}{\partial n} &= \mathbf{n} \cdot \nabla \left(\frac{1}{|\mathbf{x} - \mathbf{x}_0|} \right) \\ &= -\frac{\begin{pmatrix} z' \\ -r' \end{pmatrix} \cdot \begin{pmatrix} r + r_0 - 2r_0\cos^2\left(\frac{\theta}{2}\right) \\ (z - z_0) \end{pmatrix}}{\sqrt{r'^2 + z'^2}\left((r + r_0)^2 + (z - z_0)^2 - 4rr_0\cos^2\left(\frac{\theta}{2}\right)\right)^{\frac{3}{2}}} \\ &= \frac{r'(z - z_0) - z'\left((r + r_0) - 2r_0\cos^2\left(\frac{\theta}{2}\right)\right)}{\sqrt{r'^2 + z'^2}\left((r + r_0)^2 + (z - z_0)^2 - 4rr_0\cos^2\left(\frac{\theta}{2}\right)\right)^{\frac{3}{2}}}. \end{aligned} \tag{3.31}$$

Equation (3.26) can be simplified into integrals over ξ and complete elliptic integrals of the first and second kind over θ. Consider first integrals of the form,

$$\int_{\partial D} \frac{1}{|\mathbf{x}-\mathbf{x}_0|}\chi(\mathbf{x})dS,$$

where $\chi(\mathbf{x}) = \chi(\xi)$ is some known or unknown function parameterised by ξ. Incorporating the parameterisation gives,

$$\begin{aligned}
&\int_{\partial D} \frac{1}{\left((r+r_0)^2 - 4rr_0\cos^2(\frac{\theta}{2}) + (z-z_0)^2\right)^{\frac{1}{2}}}\chi dS \\
= &\int_0^L r\chi\sqrt{r'^2+z'^2}\int_0^{2\pi} \frac{d\theta d\xi}{\left[(r+r_0)^2 + (z-z_0)^2 - 4rr_0\cos\left(\frac{\theta}{2}\right)\right]^{\frac{1}{2}}} \\
= &\int_0^L \frac{r\sqrt{r'^2+z'^2}}{\left[(r+r_0)^2+(z-z_0)^2\right]^{\frac{1}{2}}}\chi\int_0^{2\pi} \frac{d\theta}{\left(1-\frac{4r(\xi)r_0\cos^2\left(\frac{\theta}{2}\right)}{(r+r_0)^2+(z-z_0)^2}\right)^{\frac{1}{2}}}d\xi, \qquad (3.32)
\end{aligned}$$

where $r = r(\xi)$, $z = z(\xi)$ and $\chi = \chi(\xi)$. Let the elliptic parameter be defined by,

$$m^2 = \frac{4rr_0}{(r+r_0)^2+(z-z_0)^2}.$$

Then equation (3.32) becomes,

$$\int_0^L \frac{m}{2}\sqrt{\frac{r(r'^2+z'^2)}{r_0}}\chi\int_0^{2\pi} \frac{d\theta d\xi}{\left(1-m^2\cos^2\left(\frac{\theta}{2}\right)\right)^{\frac{1}{2}}}.$$

Applying $\theta = \pi - 2\psi$ one acquires,

$$\begin{aligned}
& \int_0^L \frac{m}{2}\sqrt{\frac{r(r'^2+z'^2)}{r_0}}\chi \int_{-\frac{\pi}{2}}^{\frac{\pi}{2}} \frac{2d\psi d\xi}{(1-m^2\sin^2(\psi))^{\frac{1}{2}}} \\
= & \int_0^L \frac{m}{2}\sqrt{\frac{r(r'^2+z'^2)}{r_0}}\chi \int_0^{\frac{\pi}{2}} \frac{4d\psi d\xi}{(1-m^2\sin^2(\psi))^{\frac{1}{2}}} \\
= & \int_0^L \frac{m}{2}\sqrt{\frac{r(r'^2+z'^2)}{r_0}}\chi 4K(m)d\xi \\
= & \; 2\int_0^L \chi(\xi)m\sqrt{\frac{r(r'^2+z'^2)}{r_0}}K(m)d\xi, \qquad (3.33)
\end{aligned}$$

where $K(m)$ is the complete elliptic integral of the first kind [1].

Now consider integrals of the form,

$$\int_{\partial D} \chi(\mathbf{x})\frac{\partial}{\partial n}\left(\frac{1}{|\mathbf{x}-\mathbf{x}_0|}\right) dS.$$

Using the expression given by (3.31) these are evaluated as follows.

$$
\begin{aligned}
&\int_0^L r\chi\sqrt{z'^2+r'^2}\int_0^{2\pi}\frac{r'(z-z_0)-z'(r+r_0)+2z'r_0\cos^2(\frac{\theta}{2})}{(\sqrt{z'^2+r'^2})\left((r+r_0)^2+(z-z_0)^2-4rr_0\cos^2\left(\frac{\theta}{2}\right)\right)^{\frac{3}{2}}}d\theta d\xi\\
=&\int_0^L\frac{r\chi}{((r+r_0)^2+(z-z_0)^2)^{\frac{3}{2}}}\int_0^{2\pi}\frac{r'(z-z_0)-z'(r+r_0)+2z'r_0\cos^2\left(\frac{\theta}{2}\right)}{\left(1-\frac{4rr_0}{(r+r_0)^2+(z-z_0)^2}\cos^2\left(\frac{\theta}{2}\right)\right)^{\frac{3}{2}}}d\theta d\xi\\
=&\int_0^L\frac{m^3r\chi}{(4rr_0)^{\frac{3}{2}}}\int_0^{2\pi}\frac{r'(z-z_0)-z'(r+r_0)+2z'r_0\cos^2\left(\frac{\theta}{2}\right)}{\left(1-m^2\cos^2\left(\frac{\theta}{2}\right)\right)^{\frac{3}{2}}}d\theta d\xi\\
=&\int_0^L\frac{m^3r\chi}{(4rr_0)^{\frac{3}{2}}}\int_0^{2\pi}\frac{r'(z-z_0)-z'(r+r_0)}{\left(1-m^2\cos^2\left(\frac{\theta}{2}\right)\right)^{\frac{3}{2}}}d\theta d\xi+\int_0^L\frac{m^3r\chi}{(4rr_0)^{\frac{3}{2}}}\int_0^{2\pi}\frac{2z'r_0\cos^2\left(\frac{\theta}{2}\right)d\theta d\xi}{\left(1-m^2\cos^2\left(\frac{\theta}{2}\right)\right)^{\frac{3}{2}}}\\
=&\int_0^L\frac{m^3r(r'(z-z_0)-z'(r+r_0))\chi}{(4rr_0)^{\frac{3}{2}}}\int_0^{2\pi}\frac{1}{\left(1-m^2\cos^2\left(\frac{\theta}{2}\right)\right)^{\frac{3}{2}}}d\theta d\xi\\
&-\int_0^L\frac{2mrr_0z'\chi}{(4rr_0)^{\frac{3}{2}}}\int_0^{2\pi}\frac{-1+1-m^2\cos^2\left(\frac{\theta}{2}\right)}{\left(1-m^2\cos^2\left(\frac{\theta}{2}\right)\right)^{\frac{3}{2}}}d\theta d\xi\\
=&\int_0^L\chi\left(\frac{m^3r(r'(z-z_0)-z'(r+r_0))}{(4rr_0)^{\frac{3}{2}}}+\frac{mz'}{4\sqrt{rr_0}}\right)\int_0^{2\pi}\frac{1}{\left(1-m^2\cos^2\left(\frac{\theta}{2}\right)\right)^{\frac{3}{2}}}d\theta d\xi\\
&-\int_0^L\frac{mz'\chi}{4\sqrt{rr_0}}\int_0^{2\pi}\frac{d\theta}{\sqrt{1-m^2\cos^2\left(\frac{\theta}{2}\right)}}d\xi\\
=&\int_0^L\chi\frac{\left(\frac{m^2}{r_0}(r'(z-z_0)-z'(r+r_0))+2z'\right)\frac{E(m)}{1-m^2}-2z'K(m)}{\sqrt{(r+r_0)^2+(z-z_0)^2}}d\xi. \qquad (3.34)
\end{aligned}
$$

Here the new θ integral is a special case of a complete elliptic integral of the third kind, expressible using $E(m)$, the complete elliptic integral of the second kind [1].

3.1.5 Discretisation and function interpolation

In order to proceed it is necessary to discretise equations (3.33) and (3.34) in terms of the sections of arc length between each node. For any unknown variables, a piecewise

linear approximation is employed in order to invert the integral. This approximation for an unknown χ between nodes i and $i+1$, and consequently with $\xi \in [\xi_i, \xi_{i+1}]$, is given by,

$$\chi(\xi) = \chi_i \left(\frac{\xi_{i+1} - \xi}{\Delta_i} \right) + \chi_{i+1} \left(\frac{\xi - \xi_i}{\Delta_i} \right). \tag{3.35}$$

Consider equation (3.33). For each node located at $\xi = \xi_j$ one has,

$$2 \sum_{k=1}^{n-1} \int_{\xi_k}^{\xi_{k+1}} \left(\chi_k \left(\frac{\xi_{k+1} - \xi}{\Delta_k} \right) + \chi_{k+1} \left(\frac{\xi - \xi_k}{\Delta_k} \right) \right) m_{k,j} \sqrt{\frac{r_k(r_k'^2 + z_k'^2)}{r_j}} K(m_{k,j}) d\xi.$$

The discrete nodal values are,

$$r_j = r(\xi_j), \;\; z_j = z(\xi_j),$$

whilst the continuous k^{th} spline segments are given as,

$$r_k = r_k(\xi), \;\; z_k = z_k(\xi).$$

This then leads to the elliptic parameter along the k^{th} segment with respect to the j^{th} node being,

$$(m_{k,j})^2 = \frac{4 r_k(\xi) r_j}{(r_k(\xi) + r_j)^2 + (z_k(\xi) - z_j)^2}.$$

For nodes on the axis of symmetry, in addition to the implicitly known function values of any unknown function, one also has that the function must have a local minimum or maximum. Hence one explicitly has the first derivative, $\frac{\partial \chi}{\partial \xi} = 0$. The linear interpolant does not satisfy this without forcing the functional value on the axis to be the same as the value at the adjacent node, and thereby using a piecewise constant across both nodes.

The additional information does however allow for quadratic interpolants to be employed. These are given by,

$$\begin{aligned}
\chi(\xi \in [0, \xi_2]) &\approx \chi_1 \left(1 - \frac{\xi^2}{\Delta_1^2}\right) + \chi_2 \left(\frac{\xi^2}{\Delta_1^2}\right), \\
\chi(\xi \in [\xi_{N-1}, \xi_N]) &\approx \chi_{N-1} \left(\frac{(\xi_N - \xi^2)}{\Delta_{N-1}^2}\right) + \chi_N \left(1 - \frac{(\xi_N - \xi)^2}{\Delta_{N-1}^2}\right).
\end{aligned} \tag{3.36}$$

Expression (3.36) may be separated into a linear equation for the discrete values χ_k and therefore, by utilising all the nodes located at $\xi_j,\ j = 1 \ldots n$, one may construct a system of linear equations with regards to the discrete function values. The corresponding

coefficient matrix $G_{j,k}$ is given by,

$$
\begin{aligned}
G_{j,1} &= 2\int_0^{\xi_2}\left(1-\frac{\xi^2}{\xi_2^2}\right)m_{1,j}\sqrt{\frac{r_1(r_1'^2+z_1'^2)}{r_j}}K(m_{1,j})d\xi,\\
G_{j,2} &= 2\int_0^{\xi_2}\left(\frac{\xi^2}{\xi_2^2}\right)m_{1,j}\sqrt{\frac{r_1(r_1'^2+z_1'^2)}{r_j}}K(m_{1,j})d\xi\\
&\quad +2\int_{\xi_2}^{\xi_3}\left(\frac{\xi_3-\xi}{\Delta_2}\right)m_{2,j}\sqrt{\frac{r_2(r_2'^2+z_2'^2)}{r_j}}K(m_{2,j})d\xi,\\
G_{j,k} &= 2\int_{\xi_{k-1}}^{\xi_k}\left(\frac{\xi-\xi_{k-1}}{\Delta_{k-1}}\right)m_{k-1,j}\sqrt{\frac{r_{k-1}(r_{k-1}'^2+z_{k-1}'^2)}{r_j}}K(m_{k-1,j})d\xi\\
&\quad +2\int_{\xi_k}^{\xi_{k+1}}\left(\frac{\xi_{k+1}-\xi}{\Delta_k}\right)m_{k,j}\sqrt{\frac{r_k(r_k'^2+z_k'^2)}{r_j}}K(m_{k,j})d\xi,\\
G_{j,n-1} &= 2\int_{\xi_{n-2}}^{\xi_{n-1}}\left(\frac{\xi-\xi_{n-2}}{\Delta_{n-2}}\right)m_{n-2,j}\sqrt{\frac{r_{n-2}(r_{n-2}'^2+z_{n-2}'^2)}{r_j}}K(m_{n-2,j})d\xi\\
&\quad +2\int_{\xi_{n-1}}^{\xi_n}\left(\frac{(\xi_n-\xi)^2}{\Delta_{n-1}^2}\right)m_{n-1,j}\sqrt{\frac{r_{n-1}(r_{n-1}'^2+z_{n-1}'^2)}{r_j}}K(m_{n-1,j})d\xi,\\
G_{j,n} &= 2\int_{\xi_{n-1}}^{\xi_n}\left(1-\frac{(\xi_n-\xi)^2}{\Delta_{n-1}^2}\right)m_{n-1,j}\sqrt{\frac{r_{n-1}(r_{n-1}'^2+z_{n-1}'^2)}{r_j}}K(m_{n-1,j})d\xi \quad (3.37)
\end{aligned}
$$

Analogously, equations of the type evaluated in (3.34) may be given linear approximations with regards to the attached potentials.

If however, the function χ is known a priori, then the spline approximations for the functions may be used immediately. For example, using n nodes located at ξ_j as above, one may create a vector of the following type.

$$
DG\chi_j=\sum_{k=1}^{n-1}\left(\int_{\xi_k}^{\xi_{k+1}}\frac{m_{k,j}\chi_k}{(r_kr_j)^{\frac{1}{2}}}\left(z_k'+\frac{m_{k,j}^2[z_k'(r_k-r_j)-r_k'(z_k-z_j)]}{2r_j}\right)\frac{E(m_{k,j})}{1-m_{k,j}^2}d\xi-\int_{\xi_k}^{\xi_{k+1}}\frac{z_k'm_{k,j}\chi_k}{(r_kr_j)^{\frac{1}{2}}}K(m_{k,j})d\xi\right).
$$

This may lead to some gain in accuracy, and is employed when calculating field quantities where all surface functions have already been found. Additionally it conserves memory, as there is no need to explicitly store the full coefficient matrix before multiplication with the vector of discrete function values. In calculations where only one of ϕ and $\frac{\partial \phi}{\partial n}$ are unknown, this may be used directly in calculating the unknown surface quantities [65]. In the normal running of the algorithm in this work however, linear interpolation is used for the known and unknown non-geometric functions for simplicity in calculating the discretised matrix equations shown in the following sections.

3.1.6 The integral formula in the context of the two fluid interface

From equation (3.26), the potential ϕ_i in each fluid layer i containing NB_i bubbles satisfies,

$$\begin{aligned} 2\pi\phi_i(\mathbf{x}_0) &= \int\limits_{\partial I} \left(G(\mathbf{x},\mathbf{x}_0)\frac{\partial \phi_i(\mathbf{x})}{\partial n_i} - \frac{\partial G}{\partial n_i}(\mathbf{x},\mathbf{x}_0)\phi_i(\mathbf{x}) \right) dS(\mathbf{x}) \\ &\quad + \sum_{k=1}^{NB_i} \int\limits_{\partial B_{i,k}} \left(G(\mathbf{x},\mathbf{x}_0)\frac{\partial \phi_i(\mathbf{x})}{\partial n_i} - \frac{\partial G}{\partial n_i}(\mathbf{x},\mathbf{x}_0)\phi_i(\mathbf{x}) \right) dS(\mathbf{x}). \end{aligned}$$

After discretisation additional bubble surfaces in each fluid merely increase the size of the bubble coefficient blocks. Therefore for clarity the summation over individual bubble surfaces will be considered as a single bubble in each fluid layer.

The normal velocity balance at the fluid-fluid interface before toroidal bubble formation is given by,

$$\frac{\partial \phi_1}{\partial n_2} = \frac{\partial \phi_2}{\partial n_2}.$$

This allows the integrals in each exterior fluid to be coupled. Consider the potential sum $\bar{\phi}(\mathbf{p})$, and the interfacial quantity $F(\mathbf{p}) = \bar{\phi}(\mathbf{p})(1-\rho) + \mu(\mathbf{p})(1+\rho)$. Some algebraic

manipulation on the potentials along the two fluid interface shows the following holds,

$$\phi_1 = \bar{\phi}\frac{\rho}{1+\rho} + F\frac{1}{2(1+\rho)},$$
$$\phi_2 = \bar{\phi}\frac{1}{1+\rho} - F\frac{1}{2(1+\rho)}.$$

Now using normals orientated with regards to the outward normal of liquid layer 2, and using the normal potential derivative from liquid layer 2 on the fluid-fluid interface, equation (3.26) can be split into four coupled blocks of linear equations.

The equations for the potential on the bubble surface in fluid 1 satisfy,

$$\begin{aligned} 2\pi\phi_1(\mathbf{b}) &= \int_{\partial B_1} \left(G(\mathbf{b},\mathbf{c})\frac{\partial\phi_1(\mathbf{c})}{\partial n_1} - \phi_1(\mathbf{c})\frac{\partial G(\mathbf{b},\mathbf{c})}{\partial n_1} \right) dS(\mathbf{c}) \\ &\quad + \int_{\partial I} \left(-G(\mathbf{b},\mathbf{q})\frac{\partial\phi_2(\mathbf{q})}{\partial n_2} + \frac{\partial G(\mathbf{b},\mathbf{q})}{\partial n_2} \left(\bar{\phi}(\mathbf{q})\frac{\rho}{1+\rho} + F(\mathbf{q})\frac{1}{2(1+\rho)} \right) \right) dS(\mathbf{q}). \end{aligned}$$

Similarly for the bubble surface potentials in fluid 2 one has,

$$\begin{aligned} 2\pi\phi_2(\mathbf{d}) &= \int_{\partial B_2} \left(G(\mathbf{d},\mathbf{e})\frac{\partial\phi_2(\mathbf{e})}{\partial n_2} - \frac{\partial G(\mathbf{d},\mathbf{e})}{\partial n_2}\phi_2(\mathbf{e}) \right) dS(\mathbf{e}) \\ &\quad + \int_{\partial I} \left(G(\mathbf{d},\mathbf{q})\frac{\partial\phi_2(\mathbf{q})}{\partial n_2} - \frac{\partial G(\mathbf{d},\mathbf{q})}{\partial n_2} \left(\bar{\phi}(\mathbf{q})\frac{1}{1+\rho} - F(\mathbf{q})\frac{1}{2(1+\rho)} \right) \right) dS(\mathbf{q}). \end{aligned}$$

On the fluid-fluid interface the following two equations occur.

$$
\begin{aligned}
2\pi\bar{\phi}(\mathbf{p}) &= \int_{\partial B_1}\left(G(\mathbf{p},\mathbf{c})\frac{\partial\phi_1(\mathbf{c})}{\partial n_1}-\frac{\partial G(\mathbf{p},\mathbf{c})}{\partial n_1}\phi_1(\mathbf{c})\right)dS(\mathbf{c}) \\
&\quad+\int_{\partial B_2}\left(G(\mathbf{p},\mathbf{e})\frac{\partial\phi_2(\mathbf{e})}{\partial n_2}-\frac{\partial G(\mathbf{p},\mathbf{e})}{\partial n_2}\phi_2(\mathbf{e})\right)dS(\mathbf{e}) \\
&\quad+\int_{\partial I}\left(\frac{\partial G(\mathbf{p},\mathbf{q})}{\partial n_2}\left(-F(\mathbf{q})\frac{1}{1+\rho}+\bar{\phi}(\mathbf{q})\frac{1-\rho}{1+\rho}\right)\right)dS(\mathbf{q}), \\
2\pi\left(\frac{F(\mathbf{p})}{1+\rho}-\bar{\phi}(\mathbf{p})\frac{1-\rho}{1+\rho}\right) &= \int_{\partial B_1}\left(G(\mathbf{p},\mathbf{c})\frac{\partial\phi_1(\mathbf{c})}{\partial n_1}-\frac{\partial G(\mathbf{p},\mathbf{c})}{\partial n_1}\phi_1(\mathbf{c})\right)dS(\mathbf{c}) \\
&\quad-\int_{\partial B_2}\left(G(\mathbf{p},\mathbf{e})\frac{\partial\phi_2(\mathbf{e})}{\partial n_2}-\frac{\partial G(\mathbf{p},\mathbf{e})}{\partial n_2}\phi_2(\mathbf{e})\right)dS(\mathbf{e}) \\
&\quad+\int_{\partial I}\left(-2G(\mathbf{p},\mathbf{q})\frac{\partial\phi_2(\mathbf{q})}{\partial n_2}+\frac{\partial G(\mathbf{p},\mathbf{q})}{\partial n_2}\bar{\phi}(\mathbf{q})\right)dS(\mathbf{q}).
\end{aligned}
$$

Now one discretises the system using,

$$\int_{\partial D}\phi(\mathbf{x})\frac{\partial G(\mathbf{x}_0,\mathbf{x})}{\partial n_i}dS(\mathbf{x})\approx DG_{x_0,x}\boldsymbol{\phi}(x_0), \tag{3.38}$$

$$\int_{\partial D}G(\mathbf{x}_0,\mathbf{x})\frac{\partial\phi}{\partial n_i}(\mathbf{x})dS(\mathbf{x})\approx G_{x_0,x}\frac{\partial\boldsymbol{\phi}(x_0)}{\partial n_i}. \tag{3.39}$$

where G and DG represent the coefficient matrices accounting for the interpolation of the known and unknown functions along the surfaces. The vectors $\boldsymbol{\phi}$ and $\boldsymbol{\phi}_{ni}$ contain the discrete values of the potentials and normal normal potential derivatives at the collocation points, and are hence referred to using the source location $\mathbf{x}_0$.

Using this discretisation leads to the following matrix equations for the unknown

potentials and corresponding normal derivatives given the required known variables.

$$\begin{bmatrix} G_{bc} & 0 & -G_{bq} & \frac{\rho}{1+\rho}DG_{bq} \\ 0 & G_{de} & G_{dq} & \frac{-1}{1+\rho}DG_{dq} \\ G_{pc} & G_{pe} & 0 & \frac{\rho-1}{\rho+1}DG_{pq} - 2\pi I_{pq} \\ G_{pc} & -G_{pe} & -2G_{pq} & DG_{pq} + 2\pi\frac{1-\rho}{1+\rho}I_{pq} \end{bmatrix} \begin{bmatrix} \frac{\partial\phi_1(b)}{\partial n_1} \\ \frac{\partial\phi_2(d)}{\partial n_2} \\ \frac{\partial\phi_2(p)}{\partial n_2} \\ \bar{\phi}(p) \end{bmatrix}$$

$$= \begin{bmatrix} 2\pi I_{bc} + DG_{bc} & 0 & \frac{-1}{2+2\rho}DG_{bq} \\ 0 & 2\pi I_{de} + DG_{de} & \frac{-1}{2+2\rho}DG_{dq} \\ DG_{pc} & DG_{pe} & \frac{-1}{1+\rho}DG_{pq} \\ DG_{pc} & -DG_{pe} & 2\pi\frac{1}{1+\rho}I_{pq} \end{bmatrix} \begin{bmatrix} \phi_1(b) \\ \phi_2(d) \\ F(p) \end{bmatrix} \tag{3.40}$$

Whilst coefficient matrices corresponding to G only appear on the left hand side, the coefficient matrices corresponding to DG for variables along the two fluid interface appear on both the left and right hand sides of (3.40). This is in contrast to previous works where only the normal velocity needed to be found through the inversion of the coefficient matrices as the pressure at all interfaces was explicitly known [10, 89, 65, 6, 88]. It is also a significantly different approach to that of Klaseboer and Khoo [45], who use a geometric argument to remove the normal potential derivative along the fluid-fluid interface in their simulations involving a single pre-toroidal bubble.

The left hand side has dimension $(2N_p + N_{b1} + N_{b2}, 1)$, matching the right hand side, and so the unknowns on the left may be found using any suitable solver. The maximum dimension of the coefficient matrices is $\sim O(100)$ and so even direct matrix inversion is not a computationally intensive task, at least in comparison to the evaluation of the coefficient matrices. At this stage all the required variables for calculating the components of the kinematic and dynamic conditions are known, and so these may be advanced forward in time in an explicit manner.

3.1.7 Initial conditions

It is assumed that the two fluids are initially at rest and that all bubbles begin as spherical cavities instantaneously created at standoff distances h_i from the initially level fluid-fluid interface. Where the gaseous content of the bubble behaves adiabatically ($\epsilon \neq 0$), zero potential is prescribed everywhere in both fluids, the flow being driven from rest by the pressure in the bubble.

In cases where the strength parameter $\epsilon = 0$, the initial surface potential of the bubble is given as the Rayleigh potential for the pre-assigned initial radius and time as stated in Chapter 2. For the potential function F along the two fluid interface, the initial value prescribed is that calculated from the leading order spherical approximations (2.32) and (2.33).

3.1.8 Time-stepping

Once all potentials and normal derivatives are known for time t_k, it is necessary to advance the solution forward. This is done using well known time-stepping techniques, summarised here for completion. Whichever technique is used, all surface locations $\mathbf{b}, \mathbf{d}$ and $\mathbf{p}$ must be advected forward, as well as the bubble surface potentials $\phi_1(\mathbf{b})$, $\phi_2(\mathbf{d})$, and the solution to equation (3.24), $F(\mathbf{p})$.

Given the time derivative of a function y at time t,

$$\frac{dy}{dt} = f(y(t), t),$$

the value of y at time $t + dt$ is given exactly as,

$$y(t + dt) = y(t) + \int_t^{t+dt} f(y(\tau), \tau) d\tau. \tag{3.41}$$

The time stepping procedures approximate the above integral in order to find the subsequent solution.

First order explicit Euler time step

The Euler time step is the simplest to implement, and also the least computationally intensive per step. It evaluates the integral in (3.41) using a constant approximation for the derivative f between time steps. Therefore this explicit time stepping procedure is given by,

$$y(t + dt) = y(t) + dtf(y, t).$$

Second order Runge-Kutta time step

A second order Runge-Kutta (RK2) method is also implemented. The error in the calculation in velocity is of this order due to its linear interpolation, and so the best error one may achieve throughout the simulations will be second order. This method allows for increased stability should the velocities switch from positive to negative rapidly, as happens around jet impact and minimum bubble volume.

The time derivative in (3.41) is approximated by,

$$\frac{dy}{dt} = \frac{f(y, t) + f(y + dy, t + dt)}{2} = \frac{f(y, t) + f(y + dtf(y, t), t + dt)}{2},$$

and hence the solution at time $t + dt$ is approximated as,

$$y(t + dt) = y(t) + \frac{dt}{2}(f(y, t) + f(y + dtf(y, t), t + dt)).$$

It is necessary to use an explicit sub-step to approximate $f(y + dy, t + dt)$, differentiating this procedure from the implicit trapezium method.

Fourth order Runge-Kutta time step

A fourth order Runge-Kutta (RK4) time step is implemented for more accurate computations, at the cost of computation time. Four sub-steps are used in calculating one step, with the result over time being being fourth order accurate at most[1]. In previous works this method has demonstrated greater stability than lower order techniques, despite the error in the normal velocity calculation being at best second order [64, 31]. The sub-steps are given by,

$$\begin{aligned} s_1 &= f(y,t),\ s_2 = f\left(y + \frac{s_1}{2}, t + \frac{dt}{2}\right), \\ s_3 &= f\left(y + \frac{s_2}{2}, t + \frac{dt}{2}\right),\ s_4 = f\left(y + s_3, t + dt\right), \end{aligned}$$

and the final approximation is computed as,

$$y(t+dt) = y(t) + \frac{dt}{6}\left(s_1 + 2s_2 + 2s_3 + s_4\right).$$

At each sub-step, all surfaces, potentials and normal derivatives must be calculated, leading to the quadrupling of the computational time per step with respect to the Euler method. These must all be done explicitly given the previous sub-step estimates. However, the increased stability allows for larger steps to be taken, reducing the accumulation of error associated with the numerical approximations.

[1]Due to the necessity to approximate the velocity at each sub-step using a lower order explicit integration scheme, the theoretical accuracy of the RK4 procedure may not be realised.

3.1.9 The calculation of the time interval dt

In many previous works, the approach of Gibson and Blake [37] has been used. In essence, this places a bound on dt found from the maximum change in potential over the surface,

$$dt = \frac{\triangle\phi}{\max\limits_{S} \frac{D\phi}{Dt}},$$

where $\triangle\phi$ is a user chosen constant determined through experimentation. In this work however, the change in potentials on either side of the fluid-fluid interface is not explicitly calculated at each time step. Instead the maximum change in F is used as this is dependent upon the maximum change in both normal and tangential velocities on either side of the interface. A maximum bound is also placed on dt to prevent the solution exploding near the maximum bubble volume. Hence dt is found via,

$$dt = \min\left(\frac{\triangle\phi}{\max\left(\max\left|\frac{D\phi_1(\mathbf{b})}{Dt}\right|, \max\left|\frac{DF(\mathbf{p})}{Dt}\right|\right)}, dt_{max}\right). \tag{3.42}$$

It is worth noting that the greatest change is usually associated with the bubble potentials, with the fluid-fluid interface satisfying maximum change only when the bubbles are near maximum volume.

For the greater part of the bubble lifetime, when dt is deemed sufficiently large, the Eulerian time step is used. Once the change in maximum surface potential forces dt below a set threshold, determined through numerical experimentation to be in the range $10^{-4} < dt < 10^{-2}$ the RK2 or RK4 method is employed. This allowed for rapid calculation of the stable behaviour near the maximum bubble radius, and accurate time stepping for the more intricate portions of the bubbles lifetime, typically when bubble jetting is occurring and when the volume of the bubble is small.

No minimum is prescribed on dt. However should it remain below a certain threshold,

typically set at $dt < 10^{-6}$, for a prolonged period, usually about 200 steps, the simulation is stopped. The result becomes unreliable when such short time steps are employed, due to numerical noise, and the increasing influence of smoothing effects. Additionally, when the potential change is this rapid for such a long time it is also often the case that two surfaces are becoming increasingly close to one another. Should any interfaces cross then the numerical scheme is immediately invalidated. An example of where this may happen is given in Chapter 5. It is not efficient to check this has not happened at every time step, as most likely any interfacial collisions will occur along the interpolated sections of the surface, and not at a collocation point.

Care must be taken in choosing $\triangle\phi$, particularly when using the higher order RK4 method. The interval dt is chosen during the first intermediate stage. Yet this may not satisfy the same stability requirements at the latter stages, especially toward the end of a collapse where velocities increase rapidly. In practice, $\triangle\phi$ is determined on a case by case basis, although a value in the range of $10^{-3} < \triangle\phi < 0.03$ was found to be sufficient in most instances. Smaller values lead to excessive smoothing as there will be more timesteps taken to reach a certain time. Larger values lead to excessive numerical noise, as the error in the calculation of surface velocity and potential will be magnified by the greater timestep, particularly when using the explicit Euler scheme.

3.1.10 The evaluation of surface integrals with singular integrands

Integrable singularities occur in both the G and DG integrands as the surface co-ordinates $(r(\xi), z(\xi))$ approach and leave the collocation points (r_0, z_0). The distance between the surface locations $\mathbf{x}$ and the nodal locations $\mathbf{x}_0$ approaches zero and the values of $\frac{1}{|\mathbf{x}-\mathbf{x}_0|}$ and $\frac{\partial}{\partial n}\left(\frac{1}{|\mathbf{x}-\mathbf{x}_0|}\right)$ approach infinity. In the axisymmetric geometry used here, these singularities appear in the evaluation of the complete elliptic integrals for nodes not located on the axis.

This leads to unacceptable errors in using standard Gaussian quadrature in evaluating the ξ integral over the elliptic integrals, affecting the contribution from the segments on each side of the node in question. From the properties of elliptic integrals, these may be shown to be log type singularities, and are thereby integrable.

One uses the commonly adapted approach originally used by Taib in the context of bubble dynamics [81]. This employs a Taylor expansion of (r, z) in the neighbourhood of (r_0, z_0) in the evaluation of polynomial/logarithmic approximations to the elliptic integrals. The highly accurate approximations as tabulated in Pearson [64] are used, in which the complete elliptic integrals are approximated as 12^{th} order polynomials of the form,

$$K(m) = p_K(1-m^2) - q_K(1-m^2)\ln(1-m^2), \tag{3.43}$$

$$E(m) = 1 + p_E(1-m^2) - q_E(1-m^2)\ln(1-m^2). \tag{3.44}$$

Here p_K, p_E, q_K and q_E are all polynomials. From the definition of m^2 given previously, as $\mathbf{x} \to \mathbf{x}_0$, $1-m^2 \to 0$. It is noted that the approximation for $E(m)$ has an order 0 term with respect to $1-m^2$ and therefore $E(m)$ remains regular as all logarithmic terms are multiplied by $1-m^2$. However, in the numerical implementation it is still treated in the same manner as the singular $K(m)$ kernels, to combat any unwanted computational errors. Substituting (3.43) and (3.44) into the the surface integrals (3.33) and (3.34) gives integrals of the form,

$$\int_a^b f(x)(p(x) - q(x)\ln(1-m^2))dx, \tag{3.45}$$

where x is a parameter for the surface co-ordinates and a and b are the values of x at adjacent collocation points. As stated, one begins by Taylor expanding $1-m^2$ about the singularity, and then removing the singularity from the surface integral. For $x \in [a, b]$ the

following holds for $1 - m^2$.

$$1 - m^2 \approx (x-c)^2 \frac{r'^2 + z'^2}{4r_0^2} + O\left((x-c)^3\right). \tag{3.46}$$

Substituting (3.46) into (3.45) gives the following integrals to represent the behaviour about a singular point.

$$\int_a^b f(x)\left(p(x) - q(x)\ln\left(\frac{(1-m^2)\Delta_a^2}{(x-c)^2}\right)\right)dx + \int_a^b f(x)q(x)\left(\ln\left(\frac{\Delta_a^2}{(x-c)^2}\right)\right)dx, \tag{3.47}$$

where $\Delta_a = (b-a)$.

As can be seen, in this approach the integrand in (3.46) is split into a regular component and a singular component, where the singular contribution comes from the factor of $\ln(\Delta_a^{-2}(x-c)^2)$. By using the transformation $x \in [a,b] \rightarrow y \in [0,1]$, these singular integrals can be written in terms of a regular function multiplied by $\ln(y)$, for which a Gaussian quadrature may be generated.

By the definition of the splines and the linear interpolants, the singularities will only occur at the start or end of each segment, and hence there are two cases to consider. The first case occurs when $c = a$, and $\mathbf{x} \rightarrow \mathbf{x}_0^+$. In this case the integral may be re-written as,

$$\int_a^b f(x)q(x)\ln\left(\frac{\Delta_a^2}{(x-a)^2}\right)dx = 2\Delta_a \int_0^1 f(\Delta_a y + a)q(\Delta_a y + a)\ln\left(\frac{1}{y}\right)dy. \tag{3.48}$$

Similarly, in the second case where $c = b$, and $\mathbf{x} \rightarrow \mathbf{x}_0^-$, one may manipulate the

integrals as,

$$\int_a^b f(x)q(x)\left(\ln\left(\frac{\Delta_a^2}{(b-x)^2}\right)\right)dx = 2\Delta_a\int_0^1 f(\Delta_a y+a)q(\Delta_a y+a)\ln\left(\frac{1}{1-y}\right)dy$$
$$= -2\Delta_a\int_1^0 f(\Delta_a(1-w)+a)q(\Delta_a(1-w)+a)\ln\left(\frac{1}{w}\right)dw$$
$$= 2\Delta_a\int_0^1 f(\Delta_a(-w)+b)q(\Delta_a(-w)+b)\ln\left(\frac{1}{w}\right)dw. \tag{3.49}$$

Along panels adjacent to the collocation point in question, both the regular and logarithmic integrals are calculated using appropriate Gaussian quadrature techniques, with 20 and 32 points respectively. For non-adjacent panels, the number of Gauss points used depends on the distance from the end points to the node. Should this be below 0.05 maximum bubble radii 20 Gauss points are used, otherwise 8 points are sufficient. Indeed some authors have used far less, particularly in three dimensional simulations [87].

3.1.11 Far field approximations

The surface separating the two fluids theoretically extends to infinity. However only a finite portion can be interpolated numerically. The loss of accuracy associated with this truncation may lead to the introduction of a saw tooth instability in the potential at the far nodes, which may cause the simulations to fail. As such it is necessary to introduce a mechanism to prevent this from happening.

As stated in Chapter 2, in the far field the bubbles act as sources in the Taylor expansion of (3.26). In the approximations formed for the potentials (2.29) and (2.30), both ϕ_1 and ϕ_2 decay as $O\left(\frac{1}{|\mathbf{r}_0|}\right)$, where $\mathbf{r}_0$ is the distance from any bubbles. Therefore it is apparent that F, $\bar{\phi}$ and μ will also decay in this manner as they are linear functions of ϕ_1 and ϕ_2.

From these approximations, the normal velocity can be shown to decay as $\sim O\left(\frac{1}{|\mathbf{r}_0|^3}\right)$, in agreement with the results shown in Robinson *et al* [74] for a free surface. Moreover, the interfacial deformation was shown in equation (2.37) to decay in a similar manner. Given this knowledge of the decay rates of the various far field unknowns, a least squares approximation is developed to allow the surface integral to be taken to infinity. An additional node is interpolated on the infinite surface, node N_{p+1}. The r value of this node is fixed, and the values of F, $\bar{\phi}$, $\frac{\partial \phi_2}{\partial n_2}$ and z are approximated. It is assumed the behaviour of these functions follows $\chi \approx \frac{a}{R} + \frac{b}{R^3}$, where $R = \sqrt{r^2 + (z - z_c)^2}$ with $(0, z_c)$ the location of the bubble centroid. This approximation therefore includes the first two powers of the Taylor expansions for ϕ. The presence of the $O \sim (R^{-1})$ term in the velocity and surface deformation is not however problematic, as the least squares fit will find a suitably small factor a in these cases. Where multiple bubbles are present, this least squares fit is repeated for each bubble, and then averaged over the number of bubbles. By performing this averaging, the necessity to explicitly incorporate ρ into the potential approximation is negated as it will already be accounted for implicitly.

The least squares fit through α surface nodes for the unknowns a and b minimises,

$$\sum_{k=N_p-\alpha}^{N_p} \left(\chi(R_k) - \left(\frac{a}{R_k} + \frac{b}{R_k^3} \right) \right)^2 . \tag{3.50}$$

To find the values of a and b, the least squares sum is partially differentiated with respect to each factor, and these derivatives are set to zero. This gives the following system of simultaneous equations,

$$\begin{aligned} 0 &= \sum_{k=Np-\alpha}^{Np} \left(\frac{a}{R_k^2} + \frac{b}{R_k^4} - \frac{\chi_k}{R_k} \right), \\ 0 &= \sum_{k=Np-\alpha}^{Np} \left(\frac{b}{R_k^6} + \frac{a}{R_k^4} - \frac{\chi_k}{R_k^3} \right). \end{aligned} \tag{3.51}$$

Solving (3.51) gives a and b as,

$$
\begin{aligned}
b\left(\frac{\sum_{k=Np-\alpha}^{Np}\frac{1}{R_k^4}}{\sum_{k=Np-\alpha}^{Np}\frac{1}{R_k^2}}-\frac{\sum_{k=Np-\alpha}^{Np}\frac{1}{R_k^6}}{\sum_{k=Np-\alpha}^{Np}\frac{1}{R_k^4}}\right) &= \frac{\sum_{k=Np-\alpha}^{Np}\frac{\chi_k}{R_k}}{\sum_{k=Np-\alpha}^{Np}\frac{1}{R_k^2}}-\frac{\sum_{k=Np-\alpha}^{Np}\frac{\chi_k}{R_k^3}}{\sum_{k=Np-\alpha}^{Np}\frac{1}{R_k^4}}, \\
a\left(\frac{\sum_{k=Np-\alpha}^{Np}\frac{1}{R_k^2}}{\sum_{k=Np-\alpha}^{Np}\frac{1}{R_k^4}}-\frac{\sum_{k=Np-\alpha}^{Np}\frac{1}{R_k^4}}{\sum_{k=Np-\alpha}^{Np}\frac{1}{R_k^6}}\right) &= \frac{\sum_{k=Np-\alpha}^{Np}\frac{\chi_k}{R_k}}{\sum_{k=Np-\alpha}^{Np}\frac{1}{R_k^4}}-\frac{\sum_{k=Np-\alpha}^{Np}\frac{\chi_k}{R_k^3}}{\sum_{k=Np-\alpha}^{Np}\frac{1}{R_k^6}}.
\end{aligned}
\tag{3.52}
$$

Using (3.50) , the z co-ordinate of node N_{p+1} is given by,

$$
z_{N_{p+1}} = \frac{a}{\sqrt{r_{N_{p+1}}^2+(z_{N_{p+1}}-z_c)^2)}}+\frac{b}{(r_{N_{p+1}}^2+(z_{N_{p+1}}-z_c)^2)^{\frac{3}{2}}}.
$$

And hence by substituting $\chi = z$ into (3.52) one observes that $z_{N_{p+1}}$ is a function of $r_{N_{p+1}}$ and itself. However due to the small size of $z_{N_{p+1}}$, it may be found iteratively at minimal computational expense. Once $z_{N_{p+1}}$ is known, the calculation of the remaining approximated functions is done by directly using (3.52), and then substituting a and b back into (3.50).

The surface integral beyond node N_{p+1} is parameterised by $\xi = r$ and hence the arc length integrand is given by $\sqrt{1+z_r^2} \neq 1$. From the above expression for z it is trivial to show that z_r is given by,

$$
\frac{dz}{dr} = -r\left(\frac{a}{R^3}+\frac{3b}{R^5}\right)\left(1+(z-z_c)\left(\frac{a}{R^3}+\frac{3b}{R^5}\right)\right)^{-1}. \tag{3.53}
$$

Using the quotient rule for derivatives then gives z_{rr} as,

$$
\frac{d^2z}{dr^2} = \frac{vu_r-uv_r}{v^2}, \tag{3.54}
$$

where,

$$\begin{aligned} u &= -r\left(\frac{a}{R^3}+\frac{3b}{R^5}\right), \\ v &= \left(1+(z-z_c)\left(\frac{a}{R^3}+\frac{3b}{R^5}\right)\right), \\ u_r &= -\left(\frac{a}{R^3}+\frac{3b}{R^5}\right)+(r+z_r(z-z_c))\left(\frac{3a}{R^5}+\frac{15b}{R^7}\right), \\ v_r &= z_r\left(\frac{a}{R^3}+\frac{3b}{R^5}\right)-(r+z_r(z-z_c))\left(\frac{3a}{R^5}+\frac{15b}{R^7}\right). \end{aligned}$$

As this section of the surface is not parameterised with respect to ξ, it remains to determine the derivatives for the spline at node N_{p+1}. This can be done as the arc length with respect to ξ can be assumed to satisfy $\sqrt{r_\xi^2+z_\xi^2}=1$. Using the chain rule repeatedly, the unknown derivatives with respect to ξ are found as follows. The first derivative of z with respect to ξ satisfies,

$$\frac{dz}{d\xi}=\frac{dz}{dr}\frac{dr}{d\xi}. \tag{3.55}$$

Substituting (3.55) into the arc length then gives the first derivative of r with respect to ξ as,

$$1=\frac{dr}{d\xi}^2\left(\frac{dz}{dr}^2+1\right)\Rightarrow\frac{dr}{d\xi}=\frac{1}{\sqrt{1+\frac{dz}{dr}^2}}. \tag{3.56}$$

Differentiating (3.55) with respect to ξ then gives,

$$\frac{d^2z}{d\xi^2}=\frac{d}{d\xi}\left(\frac{dr}{d\xi}\frac{dz}{dr}\right)=\frac{dr}{d\xi}\frac{d}{dr}\left(\frac{dr}{d\xi}\frac{dz}{dr}\right)=\left(\frac{dr}{d\xi}\right)^2\frac{d^2z}{dr^2}+\frac{dr}{d\xi}\frac{dz}{dr}\frac{d}{dr}\left(\frac{dr}{d\xi}\right),$$

which implies the second z derivative satisfies,

$$\frac{d^2z}{d\xi^2} = \left(\frac{dr}{d\xi}\right)^2 \frac{d^2z}{dr^2} + \frac{dz}{dr}\left(\frac{d^2r}{d\xi^2}\right). \tag{3.57}$$

Differentiating (3.56) with respect to ξ shows that the second r derivative satisfies,

$$\frac{d^2r}{d\xi^2} = -\frac{\frac{dz}{d\xi}\frac{d^2z}{d\xi^2}}{\frac{dr}{d\xi}}. \tag{3.58}$$

Substituting (3.58) into (3.57) implies that,

$$\frac{d^2z}{d\xi^2} = \left(\frac{dr}{d\xi}\right)^2 \frac{d^2z}{dr^2} - \frac{\frac{dz}{dr}\frac{dz}{d\xi}\frac{d^2z}{d\xi^2}}{\frac{dr}{d\xi}},$$

and hence the second derivative of z with respect to ξ is,

$$\frac{d^2z}{d\xi^2} = \frac{\frac{dr}{d\xi}\frac{d^2z}{dr^2}}{\frac{dr}{d\xi} + \frac{dz}{dr}\frac{dr}{d\xi}}, \tag{3.59}$$

and by substituting (3.59) into (3.58) one has that the second r derivative is given by,

$$\frac{d^2r}{d\xi^2} = -\frac{\frac{dz}{d\xi}\frac{d^2z}{dr^2}}{\frac{dr}{d\xi} + \frac{dz}{d\xi}\frac{dz}{dr}}. \tag{3.60}$$

In order to numerically integrate the far field surface integrals, Gaussian quadrature is again employed. Due to the semi-infinite domain however the integration scheme uses Laguerre polynomials for the points of integration and e^{-x} for the weight function as described in Abramowitz and Stegun [1]. The interval of integration is $[0, \infty)$ and as such a final remapping $\bar{r} \rightarrow r - r_{N_{p+1}}$ is required.

As stated in the least squares approximation, the functions $\bar{\phi}$ and $\frac{\partial \phi_2}{\partial n_2}$ in the far field are linear summations of the potential summations and normal velocities of α previous nodes. This is incorporated into the integral equations by adding the surface integrals

corresponding to nodes $N_p - \alpha, \ldots, N_p$ in the matrices $G_{p,q}$, $G_{b,q}$, $DG_{p,q}$ and $DG_{b,q}$ for each source node.

3.1.12 Nodal re-gridding and surface smoothing

The surfaces in simulations of this type become highly locally deformed. The potential and velocity along the interfaces will also become very uneven. As such the location of the collocation points from which the surfaces are formed is of critical importance. Moreover, these points will be advected with the fluid velocity, and so if left to evolve will cluster together in regions of high curvature and high velocity. This can create issues with the splining algorithm, as calculation of the arc length may become erroneous. In order to combat these factors, the surface must be re-gridded to maintain both the stability and accuracy of the surface interpolation, and hence also the simulation.

Various different methods were deployed in order to facilitate this with varying levels of success. The simplest method was to re-grid each surface with a sufficiently high, constant number of nodes, equidistant from adjacent nodes. Whilst this was sufficient for toroidal bubbles, issues involved with the axial nodes in the simply connected phase caused some simulations to fail, and in some cases caused unphysical waves to form along the threading jets. Along the two fluid interface, this was not computationally efficient, as the concentration of nodes about the axis needed to maintain accuracy is much higher than that needed throughout the bulk of the interface.

More advanced methods involved weighting the distribution of nodes with respect to some function, either the curvature, the potential or the velocity at the surface. Originally this was performed by comparing the function values between adjacent nodes, and should the difference be below a pre-set threshold an additional node would be interpolated in the center of the segment. This was coupled with minimum and maximum separation distances to enforce stability. This was later abandoned for the simpler brute force scheme

of interpolating five nodes between all original nodes, and then removing nodes along the arc length parameter as the thresholds were exceeded. Using curvature in this manner was unsuccessful, as only the tip of the high speed jets would become heavily populated with nodes. The use of the potential, and on the two fluid interface the known function F, gave greater success and was used through many simulations. The use of the surface speed, calculated as $|\mathbf{u}|$, was only developed and employed later in the evolution of the numerical code. However this proved to be most successful, particularly in the acoustically driven simulations in Chapter 8, and in general in simulations where the toroidal bubble jet has a significant interaction with the two fluid interface. This was also efficient in the pre-toroidal jetting phase, as it more accurately captured the behaviour of the threading jet through the incorporation of both the normal and tangential velocities.

All surfaces were also explicitly smoothed using an irregular spaced version of the five point star approach of Longuet-Higgins and Cokelet [52]. This is deployed to remove noise associated with the interpolation of surfaces and potentials, which if left untreated can lead to unwanted waves forming on the surface. The use of this is especially important in cases where surface tension dominates, as unwanted changes in the sign of the curvature will result in the surface being pulled apart.

It must be stated however that explicitly smoothing the interface in this manner can remove fine detail behaviour, such as the onset of Rayleigh-Taylor instabilities. Whilst these are physically expected, one makes the assumption that they will not propagate sufficiently and that the fluid inertia will always dominate. Similarly excessive smoothing can inhibit the formation of surface jets which one clearly expects to be formed. Additionally it was observed that about the bubbles minimum volume, especially when in the toroidal state, smoothing may result in a significant mass loss typically as two surfaces are approaching one another. This was another reason for limiting the number of consecutive time steps below a given threshold.

3.1.13 Field solutions and the calculation of physical quantities

Although the numerical scheme is dependent only on information along the boundaries of each exterior liquid layer, it is of great use to be able to calculate various physical characteristics in the main body of the fluids. Several such characteristics, including the pressure and the velocity, may be calculated by using the potential in the field. This is directly calculable from equation (3.26), taking $c(\mathbf{x}_0) = 4\pi$. Spatial and time derivatives may then be found using finite difference approximations. However complications arise near the boundaries as each domain is continually evolving in time.

It is necessary to determine the domain in which the field point in question resides, and to verify that all local field points used in the numerical differentiations lie in the same domain at the appropriate time. This was done automatically in MATLAB, effectively by creating a polygon using all the surface co-ordinates skirting the bounded region under investigation and calculating the relevant winding numbers[2].

Field points in close proximity to the boundaries showed the highest error in calculation, and so any point within a given distance of any boundary are abandoned. This locus was typically taken as 0.015 maximum bubble radii. The distance between the boundary and field point was calculated directly from the spline coefficients used in the surface interpolation, and also ensured that any points mis-located by the polygonal approximation to the surface were removed. The selection of field points is illustrated in figure 3.3 for a two step application.

Once the field locations were verified, the field velocities were calculated using finite difference approximations of the field potentials. Pressure can then be calculated using finite differences to approximate the derivative of the potential with respect to time, in either a Lagrangian or Eulerian manner. The calculation of the difference approximations,

[2]The winding number of a point $\chi_0 = r_0 + iz_0$ with respect to a closed curve ∂C in the complex plane encompassing C is defined as, $w = \frac{1}{2\pi i} \oint_C \frac{d\chi}{\chi - \chi_0}$. $w \in \mathbb{I} iff \chi \in C$.

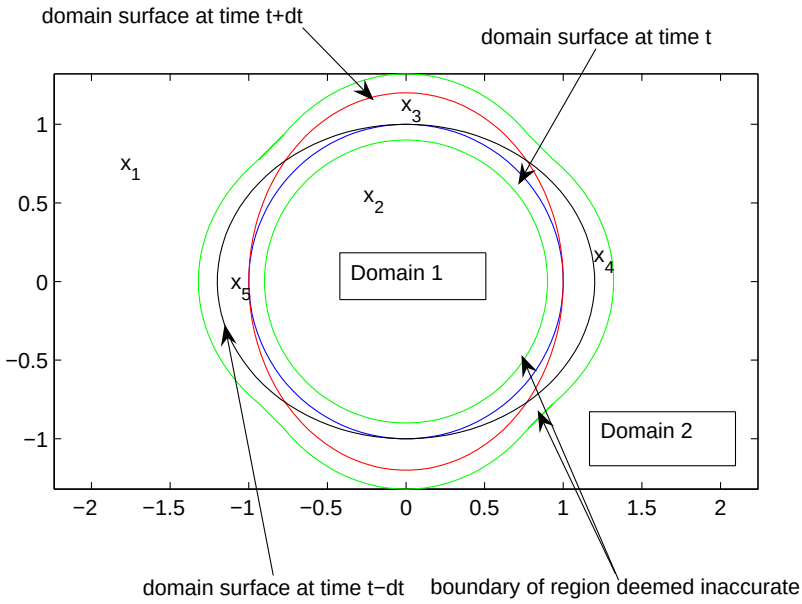

Figure 3.3: Illustration of the selection of field points where domain boundaries are time dependent. Points 1 and 2 are accepted. Points 3 and 5 are rejected as both lie in different domains at times $t \pm dt$ to where they lie at time t. Point 4 is rejected as it lies too close to the boundary of the domain at least once in the time interval $[t - dt, t + dt]$ and so the evaluation of the potential at this point may be inaccurate.

both spatially and temporally, use the five point formula given in (3.61). For simplicity dt was fixed at the value calculated in the first of the time steps. The interpolating formula may be readily found by fitting a polynomial through the five values and differentiating, resulting in,

$$\frac{d\chi(t_0+2dt)}{dt} \approx \frac{(\chi(t_0)-\chi(t_0+4dt)+8(\chi(t_0+3dt)-\chi(t_0+dt)))}{12dt}. \tag{3.61}$$

In the Lagrangian case, the field locations are advected forward in time using the field velocity in an appropriate manner. For N field locations, this requires $37N$ evaluations of the potential from (3.26) if the field is advected using an Eulerian time step, and $133N$ evaluations if the field is advected using an RK4 scheme. After the field has been advected to t_0+4dt, the finite difference approximation gives $\frac{D\phi}{Dt}$. Pressure is then calculated from the non-dimensional Bernoulli equation as,

$$\begin{aligned} p_1(\mathbf{x}_1) &= 1+\frac{|\mathbf{u}_1(\mathbf{x}_1)|^2}{2}-\frac{D\phi_1(\mathbf{x}_1)}{Dt}-\delta z_1, \\ p_2(\mathbf{x}_2) &= 1+\rho\left(\frac{|\mathbf{u}_2(\mathbf{x}_2)|^2}{2}-\frac{D\phi_2(\mathbf{x}_2)}{Dt}-\delta z_2\right). \end{aligned} \tag{3.62}$$

If an Eulerian approach is used, the field locations are fixed, and so it becomes necessary to re-check in which exterior fluid the field locations lie. However, there is no need to calculate the field velocity of every particle at time t_0, t_0+dt and t_0+3dt to advect the field, and as such only the field velocities at time t_0+2dt are required. Substituting ϕ into (3.61) then provides $\frac{\partial\phi}{\partial t}$. Pressure is then calculated as,

$$\begin{aligned} p_1(\mathbf{x}_1) &= 1-\frac{|\mathbf{u}_1(\mathbf{x}_1)|^2}{2}-\frac{\partial\phi_1(\mathbf{x}_1)}{\partial t}+\delta z_1 \\ p_2(\mathbf{x}_2) &= 1-\rho\left(\frac{|\mathbf{u}_2(\mathbf{x}_2)|^2}{2}+\frac{\partial\phi_2(\mathbf{x}_2)}{\partial t}+\delta z_2\right) \end{aligned} \tag{3.63}$$

This presents a considerable computational saving over the Lagrangian approach, as

only $13N$ evaluations of (3.26) are required. However, the Lagrangian approach allows one to track the paths taken by the fluid particle should it be required.

A further method for calculating field pressures is provided through the differentiation of Laplace's equation with respect to time. Clearly one has,

$$\frac{\partial}{\partial t}\nabla^2\phi_i = \nabla^2\frac{\partial\phi}{\partial t} = 0. \tag{3.64}$$

The value of $\frac{\partial\phi_i}{\partial t}$ on the bubble surfaces may be found using Bernoulli's equation given the bubble pressures and surface velocities already calculated. At the two fluid interface however one is again presented with no explicit method of calculation. It is therefore again necessary to exploit the normal derivatives. This is valid as on the interface,

$$\begin{aligned}\phi_1 = \phi_2 + \chi_1(\xi,t) \quad &\Rightarrow \quad \frac{\partial\phi_1}{\partial t} = \frac{\partial\phi_2}{\partial t} + \chi_2(\xi,t) \\ &\Rightarrow \quad \frac{\partial^2\phi_1}{\partial t\partial n_2} = \frac{\partial^2\phi_2}{\partial t\partial n_2} + 0 \Rightarrow \frac{\partial}{\partial n_2}\frac{\partial\phi_1}{\partial t} = \frac{\partial}{\partial n_2}\frac{\partial\phi_2}{\partial t}.\end{aligned}$$

Resultantly, a similar expression to equation (3.40) may be used, and so the field potential time derivatives may be found without the need for additional time steps to be taken, drastically increasing computational efficiency. Moreover, once the bubble becomes toroidal as described in the following chapter, there is no need for additional coefficient matrices as the time derivatives of the vortex ring potential are necessarily constant over time. A comparison between field pressures calculated using the three different methods is given in Chapter 5.

It is also of interest to calculate the pressure along the interfaces. The pressure inside any bubble is explicitly known, and hence the pressure on the exterior bubble surfaces is

given by,

$$p = \epsilon \left(\frac{V_0}{V} \right)^{\gamma} - \sigma_b \nabla \cdot \mathbf{n}_b. \tag{3.65}$$

The pressure p_i on either side of the fluid-fluid interface may be calculated from Bernoulli's equation once a time derivative of the potential is known. For example, this may be calculated in a pseudo-Lagrangian manner using (3.61) as,

$$p_i = 1 - ((i-1)\rho + 2 - i) \left(\frac{D\phi_i}{Dt} - \mathbf{u}_{av} \cdot \mathbf{u}_i + \frac{|\mathbf{u}_i|^2}{2} + \delta(z) \right). \tag{3.66}$$

Alternatively, the partial time derivatives calculated from (3.64) may be used in conjunction with a non-dimensional variant of equation (3.15).

This can be used to check the accuracy of the pressure calculation, as the Young-Laplace condition must also be satisfied at the interface. It is worth noting that in order to calculate the surface pressures using a finite difference approach, the surfaces may not be re-gridded during the time steps from which the data is taken. If re-gridding does occur, the recorded location of the nodes will not be that to which the nodes were advected to and hence will not be usable in the calculation of the Lagrangian/pseudo-Lagrangian time derivatives. As such, to acquire the data used in the field calculations, a single recorded time step is taken at t_0 as an initial reference, and no smoothing or re-gridding is performed during the evolution to $t_0 + 4dt$.

In the images produced herein, one typically adopts the standard of the pressure field on the right hand side, and the velocity field reflected on the left. In previous works the tendency has been to use variable length arrows alone for the velocity field, often scaled to fit into a preset frame. Whilst this has demonstrated the flow field about the axis during the toroidal phase well, it is often the case that the slower motions away from the impact sight are difficult to observe easily. An alternative visualisation method has

been used herein, with the velocity fields typically constructed as a field surface plot of the absolute velocity, coupled with directional arrows of equal length, coloured differently for each layer. This proved very useful in identifying several key features in the slower moving liquid, such as the translation of stagnation points along domain boundaries, and the high levels of tangential slip associated with more extreme density ratios.

3.2 Chapter summary

A boundary integral scheme for solving the problem in question has been given in this chapter. Detailed analysis of the integral equations, splines, kinematic and dynamic boundary conditions has been presented. This information has been used to create a highly accurate numerical code which will be used to investigate the impact of the density jump on a rapidly evolving bubble. The following chapter contains a detailed description of the extension to the toroidal phase, using the vortex ring method initially developed by Lundgren and Mansour [53]. The subsequent chapter provides test cases for this numerical implementation. The benefit of using quintic as opposed to cubic splines is clearly demonstrated. Later the code is shown to behave correctly under surface tension via perturbations to a spherical incompressible droplet. Further validation is drawn from accurate solutions to the Rayleigh-Plesset equation for the solution over just the bubble surface, and with the fluid-fluid interface included with the density ratio $\rho = 1$. Finally the code is verified in both the pre and post toroidal regimes against free surface and rigid boundary experiments at the extremes of the density ratio, and also against the water/white spirit experiments of Chahine and Bovis [23].

Chapter 4

Toroidal bubble model

In many circumstances high speed liquid jets may form about the axis, threading the bubbles under consideration and impacting on the opposing side. Once this happens the fluid domain becomes doubly connected, and as a result equation (3.26) no longer has a unique solution. The flow gains a circulation around the bubble torus which must be conserved to maintain the Kelvin impulse. As mentioned in Chapter 1, several methods have been developed to account for such a jet impact, allowing the simulation to continue further into the lifetime of the bubbles.

4.1 Vortex ring bubbles

The axial jet impact method employed herein, is the vortex ring method. This was introduced by Lundgren and Mansour [53] and has been utilised since for both axisymmetric and fully three dimensional simulations [89, 87, 88, 92]. The advantage of this method over the others mentioned in Chapter 1, is that no vortex sheet or dynamic cut needs to be tracked in time, nor does one need to be integrated over at every time step. This allows for high computational efficiency, a significant advantage as the post toroidal behaviour will in general involve the high speed propagation of a surface perturbation about the toroid. Resultantly, this requires significantly smaller time steps than the pre-toroidal

behaviour, even when compared to the formation of the threading jet. As an additional consequence of the removal of the domain cut, the surfaces of integration remain analytical everywhere. Therefore, there are no points along any surface where either the normal or tangential derivatives become undefined, as there are in the method of Best [5]. Furthermore, there will be no curvature singularities remaining after jet impact, and so there is no requirement to evaluate a hyper-singular boundary integral equation as in Zhang *et al* [91].

In the method employed here, the circulation is accounted for by introducing a vortex ring inside the bubble toroid at impact, and decomposing the potential on all relevant surfaces into that caused by the vortex ring, and a continuous remnant potential. The velocity field is maintained after jet impact, constructed from the gradient of the remnant potential and the vortex ring velocity as,

$$\mathbf{u} = \nabla\psi + \mathbf{v}_{vr}. \tag{4.1}$$

Here the location of the vortex ring generating the velocity field $\mathbf{v}_{vr}$ is along the ring (r_{vr}, θ, z_{vr}) inside the bubble toroid, and thereby outside the exterior liquid layers. The corresponding potential decomposition is,

$$\phi = \psi + \psi_{vr} \tag{4.2}$$

where ψ_{vr} is the potential generated by the vortex ring and ψ is the continuous remnant potential. Additional toroidal bubbles are introduced in an identical manner, resulting in

$$\mathbf{u} = \nabla\psi + \sum_j \mathbf{v}_{vr_j}, \tag{4.3}$$

$$\phi = \psi + \sum_j \psi_{vr_j}. \tag{4.4}$$

From here, the sum of vortex ring velocities and potentials from bubbles in a single exterior layer will be treated as a single quantity to avoid confusion. It is noted however that a toroidal bubble in fluid 1 does not result in a doubly connected domain in fluid 2, and so vortex ring decompositions only affect the potential of the exterior fluid in question. As will be seen later however, this directly affects the coupling of the boundary integral equations at the two fluid interface. This is in contrast to previous implementations over free surfaces and rigid boundaries, where the decomposition has only affected the kinematic and dynamic conditions [89, 87, 88].

4.1.1 Numerical toroidalisation procedure

Once the axial nodes on a pre-toroidal bubble, numbered 1 and N, are within a pre-described distance of one another, typically of $|z_1 - z_N| \sim O(10^{-3})$, a time-step dt is chosen so that the two nodes will coincide, in essence jet impact occurs. Regardless of the value of dt, an Eulerian time step is used, to avoid the possibility of the bubble surface at a sub-step forming a continuous cycle in the (r, z) plane. Upon jet impact, nodes 1 and N are removed from the bubble surface, and a circulation of strength $\Gamma = \phi(\xi_N) - \phi(0)$ is generated in the flow field. The surface shape of the resulting toroid is then found by splining through remaining nodes labelled $2, ..., N-1$ [1], although once interpolated more nodes may be added as required. Care must be taken to ensure that nodes 2 and $N-1$ are close enough to nodes 1 and N to minimise the loss in bubble volume, and hence potential energy, during this numerical transition.

The vortex ring velocity satisfies the continuity of mass everywhere except at the vortex ring source, and as such the exact location of the vortex ring is irrelevant so long as it is inside the toroid. In order to maximise stability, it is placed at the furthest point

[1] In practice, more nodes maybe removed to find a stable solution. Typically the removal ensures that no non-adjacent nodes are within 10^{-2} maximum bubble radii of each other. The Gaussian integration routines involved in calculating the coefficient matrices are non-adaptable, and so may give erroneous results for the influence of non-adjacent nodes as the separating distance becomes very small.

inside the toroid from the toroid wall. This location is found heuristically to sufficient accuracy with minimal effort. The potential is then decomposed, and in the future of the simulation the velocity generated by the ring is taken into account, as shown in equation (4.1). As will be seen, once the decomposition is taken there is no requirement to calculate the discontinuous potential, except if the location of the vortex ring inside the toroid must be changed.

The velocity field at a point $\mathbf{x}_0 = (r_0, 0, z_0)$ caused by a vortex ring located at $\mathbf{x}_{vr} = (r_{vr}, \theta, z_{vr})$ with circulation Γ, is given by the Biot-Savart law as follows.

$$\begin{aligned}
\frac{4\pi}{\Gamma}\mathbf{v}_{vr}(\mathbf{x}_0) &= \oint_{vr} d\mathbf{x}_{vr} \times \frac{(\mathbf{x}_0 - \mathbf{x}_{vr})}{|\mathbf{x}_0 - \mathbf{x}_{vr}|^3} \\
&= \int_0^{2\pi} \frac{r_{vr}\mathbf{e}_\theta \times (r_0\cos(\theta) - r_{vr}), \theta, (z_0 - z_{vr}))}{\left((r_0 + r_{vr})^2 + (z_0 - z_{vr})^2 - 4r_0 r_{vr}\cos^2\left(\frac{\theta}{2}\right)\right)^{\frac{3}{2}}} d\theta \\
&= \int_0^{2\pi} \frac{r_{vr}(z_0 - z_{vr})\mathbf{e}_r + r_{vr}(r_{vr} - r_0\cos(\theta))\mathbf{e}_z}{R^3\left(1 - m^2\cos^2\left(\frac{\theta}{2}\right)\right)^{\frac{3}{2}}} d\theta, \qquad (4.5)
\end{aligned}$$

where $R^2 = (r_0 + r_{vr})^2 + (z_0 - z_{vr})^2$ and $m^2 = 4r_{vr}r_0R^{-2}$. As in Chapter 3, the integrals in question may now be readily evaluated using complete elliptic integrals of the first and second kind using the identities,

$$\int_0^{2\pi} \frac{1}{\left(1 - m^2\cos^2\left(\frac{\theta}{2}\right)\right)^{\frac{3}{2}}} = 4\frac{E(m)}{1 - m^2}, \qquad (4.6)$$

and,

$$\int_0^{2\pi} \frac{\cos(\theta)}{\left(1-m^2\cos^2\left(\frac{\theta}{2}\right)\right)^{\frac{3}{2}}}d\theta = \int_0^{2\pi} \frac{2\cos^2\left(\frac{\theta}{2}\right)-1}{\left(1-m^2\cos^2\left(\frac{\theta}{2}\right)\right)^{\frac{3}{2}}}d\theta$$

$$= -\frac{2}{m^2}\int_0^{2\pi} \frac{\left(1-m^2\cos^2\left(\frac{\theta}{2}\right)\right)+\left(-1+\frac{1}{2}m^2\right)}{\left(1-m^2\cos^2\left(\frac{\theta}{2}\right)\right)^{\frac{3}{2}}}d\theta$$

$$= \frac{1}{m^2}\left[-8K(m)+(8-4m^2)\frac{E(m)}{1-m^2}\right]. \tag{4.7}$$

As required there is no velocity in the direction of $\mathbf{e}_\theta$, and for $\mathbf{v}_{vr} = u_{vr}\mathbf{e}_r + w_{vr}\mathbf{e}_z$ one has,

$$u_{vr} = \frac{\Gamma r_{vr}(z-z_{vr})}{\pi R^3 m^2}\left((2-m^2)\frac{E(m)}{1-m^2}-2K(m)\right), \tag{4.8}$$

$$w_{vr} = \frac{\Gamma r_{vr}}{\pi R^3}\left(r_{vr}\frac{E(m)}{1-m^2}-\frac{r_0}{m^2}\left((2-m^2)\frac{E(m)}{1-m^2}-2K(m)\right)\right). \tag{4.9}$$

The vortex potential ψ_{vr} is calculated on most surfaces using the method of Zhang *et al* [92] based on the result in Milne and Thompson [60] using the solid angle formula,

$$\psi_{vr}(\mathbf{x}) = \frac{\Gamma}{4\pi}\int_{S_c}\frac{\partial G(\mathbf{x},\mathbf{x}_{S_c})}{\partial n}dS(\mathbf{x}_{S_c}). \tag{4.10}$$

S_c is any surface enclosed by the vortex ring, and for simplicity is taken to be the disk of radius r_{vr} in the z_{vr} plane. Hence $S_c = \{(r,\theta,z_{vr})|0 \le r \le r_{vr},\ 0 \le \theta < 2\pi\}$ and for the point $\mathbf{x}_0$ located on any surface one has,

$$\psi_{vr}(\mathbf{x}_0) = \frac{\Gamma}{4\pi}\int_0^{r_{vr}} r\int_0^{2\pi}\frac{\partial}{\partial z}\frac{1}{|\mathbf{x}_{vr}-\mathbf{x}_0|}d\theta dr$$

$$= \frac{-(z_{vr}-z_0)\Gamma}{\pi}\int_0^{r_{vr}}\frac{r}{R^3}\frac{E(m)}{(1-m^2)}dr \tag{4.11}$$

This has a discontinuity across the disk S_c, and so using this directly leads to unacceptable errors when employed on the toroidal bubble in question at nodes close to or on the discontinuity. Instead for this bubble the potential is found by an integration over the vortex ring velocity field. However unlike in previous works, including Wang *et al* [89, 88] where an integration from infinity is used to calculate the potential at a start point on the ring, the properties of (4.11) are exploited. It is immediately apparent that on the side of the torus furthest from the axis, the potential level with the vortex ring core, $\psi_{vr}(r_{ex}, z_{vr})$ is exactly equal to zero, where $r_{ex} = r_k(\xi_{ex})$ and ξ_{ex} is the root of $z_k(\xi) - z_{vr} = 0$, on the appropriate segment k of the bubble toroid surface. As such a temporary node is introduced at (r_{ex}, z_{vr}) After re-ordering the nodes on the bubble such that (r_{ex}, z_{vr}) is the first, the potential at nodes $j > 1$ may be found consecutively from,

$$\psi_{vr}(r_j, z_j) = \int_{\xi(j-1)}^{\xi(j)} (u_{vr}r' + w_{vr}z')\sqrt{r'^2 + z'^2}d\xi - \psi_{vr}(r_{j-1}, z_{j-1}). \tag{4.12}$$

This will result in the jump in potential being located at (r_{ex}, z_{vr}), and so it remains to subtract the circulation Γ from the potential of all nodes satisfying $z_j > z_{vr}$. This then maps the jump in potential to (r_{S_c}, z_{vr}), the intersection of S_c and the toroid surface. It is then necessary to remap the discontinuity in the original potential ϕ to this location, which may be done without loss of generality.

It was shown by Best that the location of the discontinuity in potential was arbitrary when using the domain cut technique [7]. This is not strictly valid in the vortex ring method, as the velocity potential at infinity generated by the vortex ring must be zero, and hence the potential jump must be located on the axial side of the vortex ring source. This is only an issue when decomposing the potentials initially, and when repositioning the vortex ring location should it become to close to the bubble wall, which is itself a rare event. As stated at all other times only the vortex ring velocity is needed, which is

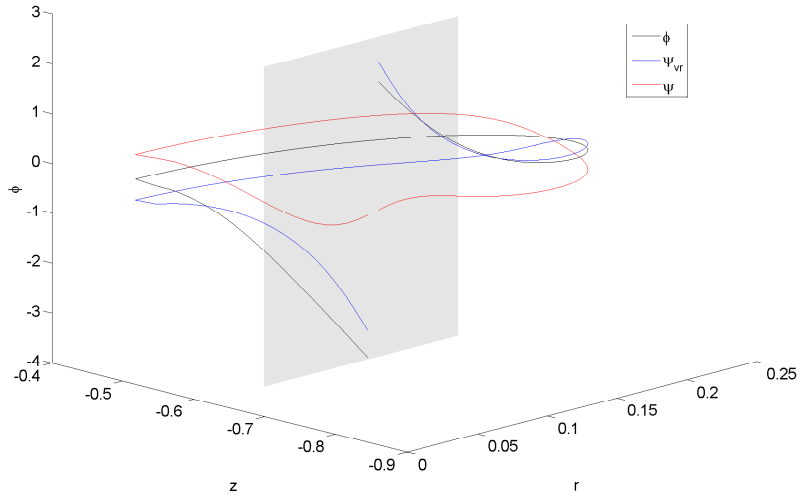

Figure 4.1: Potential decomposition of a toroidal bubble showing ϕ (black), ψ (red) and ψ_{vr} (blue). The gray rectangle represents the disk S_c.

continuous everywhere in the exterior fluid domain.

Once the vortex ring potentials are known, the remnant potential at nodes $2, ..., N-1$ is found via,

$$\psi(r_j, z_j) = \phi(r_j, z_j) - \psi_{vr}(r_j, z_j). \tag{4.13}$$

An example decomposition is shown in figure 4.1.

Any other surfaces in the same fluid layer have their surface potential decomposed using (4.11). On the fluid-fluid interface, the quantity $F = \bar{\phi}(1-\rho)+\mu(1+\rho) = 2\phi_1 - 2\rho\phi_2$ is decomposed in the obvious manner, resulting in the decomposed surface quantities,

$$\begin{aligned}
\bar{\psi} &= \psi_1 + \psi_2 = \phi_1 + \phi_2 - \psi_{vr_1} - \psi_{vr_2}, \\
\bar{\mu} &= \psi_1 - \psi_2 = \phi_1 - \phi_2 - \psi_{vr_1} + \psi_{vr_2}, \\
\bar{F} &= \bar{\psi}(1-\rho) + \bar{\mu}(1+\rho) - 2\psi_{vr_1} + 2\rho\psi_{vr_2}.
\end{aligned} \tag{4.14}$$

4.1.2 Decomposed surface boundary conditions

The resulting decomposed potentials obey the far field conditions imposed by the model, as well as Laplace's equation. It is now necessary to create boundary conditions on the bubble surfaces and two fluid interface to allow a boundary integral method to be used in their calculation.

Firstly, the vortex ring potentials ψ_{vr} are constant in time. It must therefore be true that after jet impact,

$$\frac{\partial \phi}{\partial t} = \frac{\partial \psi}{\partial t}.$$

However, the vortex ring velocity does provide contributions when evaluating the substantial derivatives.

On the bubble surfaces, it is correct to state,

$$\frac{D\phi_i}{Dt} = \frac{\partial \psi_i}{\partial t} + \mathbf{u}_i \cdot (\nabla \psi_i) + \mathbf{u}_i \cdot \mathbf{v}_{vr_i} \Rightarrow \frac{D\psi_i}{Dt} = \frac{D\phi_i}{Dt} - \mathbf{u}_i \cdot \mathbf{v}_{vr_i}. \tag{4.15}$$

Substituting this into (3.20) then gives the evolution equation for ψ on the surface of the bubbles as,

$$\frac{D\psi_i}{Dt} = \frac{|\nabla \psi_i|^2}{2} - \frac{|\mathbf{v}_{vr_i}|^2}{2} + \left(\frac{i-1}{\rho} + 2 - i\right)\left(1 - \epsilon\left(\frac{V_0}{V}\right)^{\gamma} + \sigma_{bi}\nabla \cdot \mathbf{n}\right) - \delta(z - z_0) \tag{4.16}$$

In a similar manipulation, on the fluid-fluid interface the substantial derivative of F satisfies,

$$\frac{DF}{Dt} = \frac{D\bar{F}}{Dt} + 2\mathbf{u}_{av} \cdot (\mathbf{v}_{vr_1} - \rho \mathbf{v}_{vr_2}). \tag{4.17}$$

This thereby creates the evolution of $\bar{F}$ from (3.24) as,

$$\frac{D\bar{F}}{Dt} = (1-\rho)(\mathbf{u}_1 \cdot \mathbf{u}_2) - 2\mathbf{u}_{av} \cdot (\mathbf{v}_{vr_1} - \rho \mathbf{v}_{vr_2}) + 2\sigma_I \nabla \cdot \mathbf{n}_2 - 2(1+\rho)\delta z. \quad (4.18)$$

The kinematic conditions as described in Chapter 3 are unaffected, albeit with a different method of calculation.

4.1.3 Coupled boundary integral equations

The normal derivatives of the decomposed potentials no longer equal the normal velocity, as the continuity of normal velocity is expressed using the normal vortex ring components along the two fluid interface as well. One may state,

$$\frac{\partial \psi_1(\mathbf{p})}{\partial n_2} = \frac{\partial \psi_2(\mathbf{p})}{\partial n_2} + vr_{2n_2}(\mathbf{p}) - vr_{1n_2}(\mathbf{p}), \quad (4.19)$$

where vr_{in_2} is the normal scalar component of $\mathbf{v}_{vr_i}$ in fluid layer i with respect to $\mathbf{n}_2$.

Let the integrals over the bubble surfaces be denoted as,

$$I_{Bi}(\mathbf{x}_0) = \int_{\partial B_i} \left[G(\mathbf{x}_0, \mathbf{x}) \frac{\partial \psi_i(\mathbf{x})}{\partial n_i} - \psi(\mathbf{x}) \frac{\partial G(\mathbf{x}_0, \mathbf{x})}{\partial n_i} \right] dS(\mathbf{x}).$$

Again using normals orientated to be outward of liquid layer 2, the potential sum $\bar{\psi}$, the normal potential derivative of fluid 2 and the decomposed $\bar{F}$, the decomposed potential in fluid 1 now satisfies,

$$\begin{aligned} 2\pi\psi_1(\mathbf{b}) = & -\int_{\partial I} G(\mathbf{b}, \mathbf{q}) \left(\frac{\partial \psi_2(\mathbf{q})}{\partial n_2} + vr_{2n_2}(\mathbf{q}) - vr_{1n_2}(\mathbf{q}) \right) dS(\mathbf{q}) \\ & + \int_{\partial I} \frac{\partial G(\mathbf{b}, \mathbf{q})}{\partial n_2} \left(\bar{\psi}(\mathbf{q}) \frac{\rho}{1+\rho} + \bar{F}(\mathbf{q}) \frac{1}{2(1+\rho)} \right) dS(\mathbf{q}) + I_{B1}(\mathbf{b}). \end{aligned}$$

Similarly for the bubble surface potential in fluid 2 one has,

$$2\pi\psi_2(\mathbf{d}) = \int_{\partial I}\left(G(\mathbf{d},\mathbf{q})\frac{\partial\psi_2(\mathbf{q})}{\partial n_2} - \frac{\partial G(\mathbf{d},\mathbf{q})}{\partial n_2}\left(\bar{\psi}(\mathbf{q})\frac{1}{1+\rho} - \bar{F}(\mathbf{q})\frac{1}{2(1+\rho)}\right)\right)dS(\mathbf{q}) + I_{B2}(\mathbf{d}).$$

On the fluid-fluid interface the following two equations occur.

$$\begin{aligned}
2\pi\bar{\psi}(\mathbf{p}) &= -\int_{\partial I} G(\mathbf{p},\mathbf{q})\left(vr_{2n_2}(\mathbf{q}) - vr_{1n_2}(\mathbf{q})\right)dS(\mathbf{q}) \\
&\quad + \int_{\partial I}\frac{\partial G(\mathbf{p},\mathbf{q})}{\partial n_2}\left(-\bar{F}(\mathbf{q})\frac{1}{1+\rho} + \bar{\psi}(\mathbf{q})\frac{1-\rho}{1+\rho}\right)dS(\mathbf{q}) + I_{B1}(\mathbf{p}) + I_{B2}(\mathbf{p}), \\
2\pi\left(\frac{\bar{F}(\mathbf{p})}{1+\rho}\right) &+ 2\pi\left(\bar{\psi}(\mathbf{p})\frac{(\rho-1)}{\rho+1}\right) = -\int_{\partial I} G(\mathbf{p},\mathbf{q})\left(2\frac{\partial\psi_2(\mathbf{p})}{\partial n_2} + vr_{2n_2}(\mathbf{q}) - vr_{1n_2}(\mathbf{q})\right)dS(\mathbf{q}) \\
&\quad + \int_{\partial I}\frac{\partial G(\mathbf{p},\mathbf{q})}{\partial n_2}\bar{\psi}dS(\mathbf{q}) + I_{B1}(\mathbf{p}) - I_{B2}(\mathbf{p}),
\end{aligned}$$

Using the same discretisation as in Chapter 3, the following matrix equation is realised to find the unknown potentials and corresponding normal derivatives.

$$\begin{aligned}
&\begin{bmatrix} G_{bc} & 0 & -G_{bq} & \frac{\rho}{1+\rho}DG_{bq} \\ 0 & G_{de} & G_{dq} & \frac{-1}{1+\rho}DG_{dq} \\ G_{pc} & G_{pe} & 0 & \frac{\rho-1}{\rho+1}DG_{pq} - 2\pi I_{pq} \\ G_{pc} & -G_{pe} & -2G_{pq} & DG_{pq} + 2\pi\frac{1-\rho}{1+\rho}I_{pq} \end{bmatrix}\begin{bmatrix} \frac{\partial\psi_1(b)}{\partial n_1} \\ \frac{\partial\psi_2(d)}{\partial n_2} \\ \frac{\partial\psi_2(p)}{\partial n_2} \\ \bar{\psi}(p) \end{bmatrix} \\
&= \begin{bmatrix} 2\pi I_{bc} + DG_{bc} & 0 & \frac{-1}{2+2\rho}DG_{bq} & G_{bq} \\ 0 & 2\pi I_{de} + DG_{de} & \frac{-1}{2+2\rho}DG_{dq} & 0 \\ DG_{pc} & DG_{pe} & \frac{-1}{1+\rho}DG_{pq} & G_{pq} \\ DG_{pc} & -DG_{pe} & \frac{2\pi}{1+\rho}I_{pq} & G_{pq} \end{bmatrix}\begin{bmatrix} \psi_1(b) \\ \psi_2(d) \\ \bar{F}(p) \\ vr_{2n_2}(p) - vr_{1n_2}(p) \end{bmatrix}.
\end{aligned} \tag{4.20}$$

One notes here that additional coefficient matrices multiply the vortex ring velocities after jet impact and are essential in maintaining the velocity balance across the fluid-fluid

interface. This also introduces block coefficient matrices involving G into the right hand side of equation (4.20), in contrast to the pre-toroidal matrix equation (3.40).

4.2 Chapter summary

This chapter has detailed the transition from a simply connected geometry to a doubly connected (toroidal) geometry. The incorporation of the vortex ring approach has been realised, including the decomposition of fluid potentials and velocities along with the corresponding dynamic conditions for decomposed variables, and the necessary modifications to the Laplace solver to maintain the balance in normal velocity across the two fluid interface. The following chapter illustrates the verification of the numerical implementation, including comparisons to the water/white spirit experiments in Chahine and Bovis [23].

Chapter 5

Boundary integral method verification and comparison with experiments

There are multiple aspects of the numerical implementation which must be verified before the numerical results can be trusted. This includes the interpolation routines, and the accuracy of the associated derivatives, the calculation of the unknown potentials and velocities using the solution to Laplace's equation, and the explicit forward time-stepping utilising these. Further the numerical transition to the toroidal phase requires verification of both its accuracy, and of the consequent behaviour of the toroidal bubbles.

The surface interpolation is verified by comparison with analytic surfaces. Accurate surface interpolation is essential as the bubble surfaces and fluid-fluid interface cannot intersect each other without violating the mathematical formulation, and yet as will be seen in the subsequent chapters, they do come into very close proximity. The calculation of the unknown quantities and time evolution is verified by comparison with existing analytic and experimental investigations. These unknowns govern the future solution and hence accuracy is paramount in order to prolong the simulation, particularly for cases where the

solution requires small time intervals due to rapid jetting and surface deformations.

5.1 Spline verification

The spline routines were tested against various analytic functions. This was done to verify both the accuracy and the adaptability of the routines to non-uniform meshes.

The system of equations (5.1) was constructed as a test case for the spline routines. It allowed for two variables x, y to be parameterised with respect to ξ in such a way that $\sqrt{x_\xi^2 + y_\xi^2} = 1$ at every point. As stated in Chapter 3, this is the theoretical target of the spline routines, ensuring that the parameterising variable is in fact the arc length along the surfaces. The system allows the interpolated function and derivatives to be compared directly to the corresponding analytic solutions. The function and derivatives as functions of ξ and of x are shown in figure 5.1. The derivatives with respect to x are singular at $x = 0,\ \xi = 0$ and $x = 0.25,\ \xi = 0.5$, and so the interval interpolated is restricted to $\xi \in [0.01, 0.49]$.

$$\begin{aligned}
x &= \xi^2 \\
1 &= \sqrt{\left(\frac{dy}{d\xi}\right)^2 + \left(\frac{dx}{d\xi}\right)^2} \\
\Rightarrow y &= \frac{\xi\sqrt{1-4\xi^2}}{2} + \frac{\sin^{-1}(2\xi)}{4} \\
\Rightarrow y &= \frac{\sqrt{x}\sqrt{1-4x}}{2} + \frac{\sin^{-1}(2\sqrt{x})}{4} \\
\Rightarrow \frac{dy}{dx} &= \frac{\sqrt{1-4x}}{2\sqrt{x}} \\
\Rightarrow \frac{d^2y}{dx^2} &= -\frac{1}{4\sqrt{1-4x}x^{3/2}} = \frac{d^2y}{d\xi^2}\left(\frac{dx}{d\xi}\right)^{-2} - \frac{1}{2x(\xi)}\frac{dy}{d\xi}.
\end{aligned} \tag{5.1}$$

As seen in figure 5.2, when using quintic splines the absolute error in the interpolation of y, $\frac{dy}{dx}$ and $\frac{d^2y}{dx^2}$ decay proportionally to N^{-6}, N^{-5} and N^{-4} respectively, where N is the number of collocation points. Interpolation using cubic splines results in error decay in

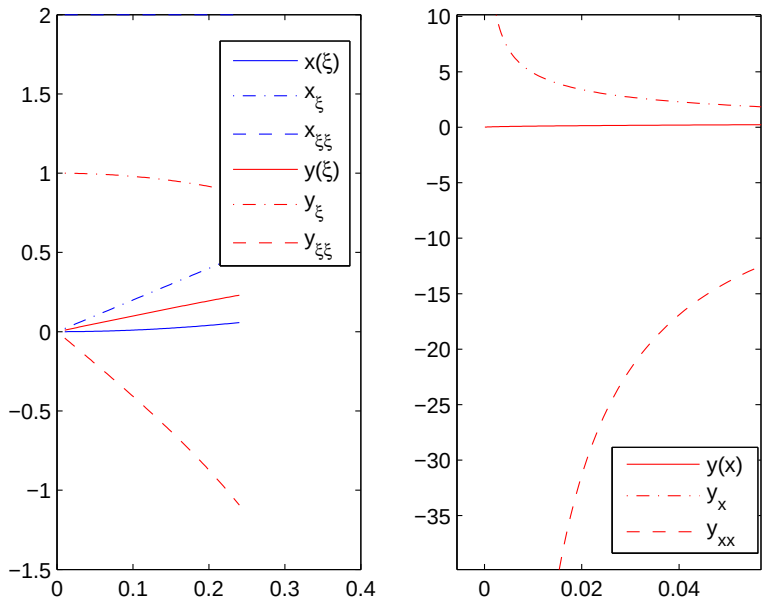

Figure 5.1: Graphical presentation of the spline test function (5.1) with respect to ξ (left) and x (right). By the definition of the test function, $x_{\xi\xi} = 2$ in the left graph.

these functions proportional to N^{-4}, N^{-3} and N^{-2} respectively. The error in all cubic cases is several orders of magnitude greater than the corresponding quintic cases. However round off errors take effect at $N \approx 30$ when interpolating with quintic splines, leading to the loss of accuracy seen in both the function and its derivatives. The separation distance between nodes with respect to ξ is $\Delta_k \approx 0.016$. Such a degradation does not occur with cubic interpolation with this range of N, implying that the cubic spline may be more stable as the distance between nodes becomes very small.

The interpolation of a half unit circle, the initial condition for the bubble shape in the BIM algorithm, is investigated in figure 5.3. With uniform nodal spacing, again one observes the error in the first, second and third derivatives decreasing proportionally to N^{-6}, N^{-5} and N^{-4} using quintic interpolation and proportionally to N^{-4}, N^{-3} and N^{-2} using cubic interpolation. Round off error did not affect the quintic interpolation

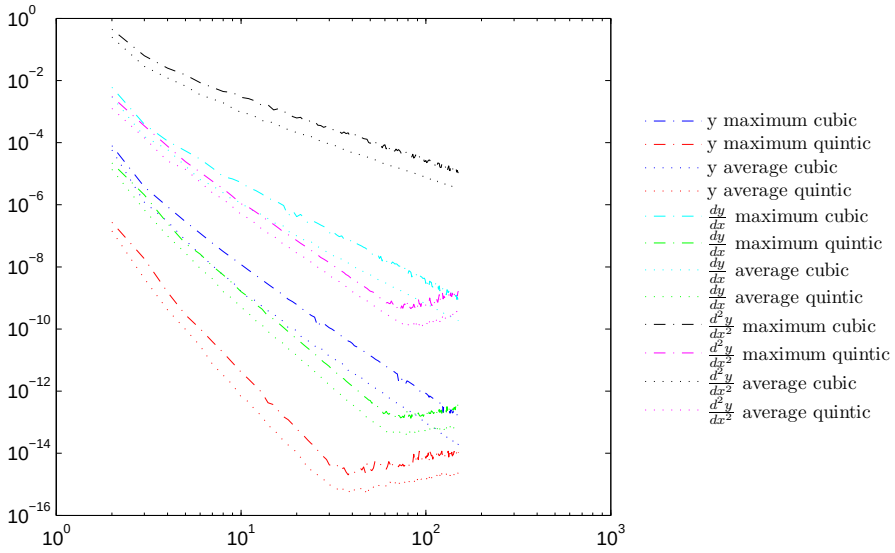

Figure 5.2: Comparison of the absolute error gained though cubic and quintic spline interpolation of (5.1) with even node spacing.

until $N \sim O(100)$, and began to affect the cubic interpolation when $N \sim O(800)$. Even at $N = 1000$ however, the error in the second derivatives was two orders of magnitude greater using cubic interpolation over quintic interpolation.

The effect of a non-uniform node distribution is illustrated in the second (right) and third (base) graphs. In the second the node spacing is determined by a geometric series with common ration $r = 1.005$. The scale factor α is taken so that,

$$\sum_{0}^{N-1} \alpha r^k = \pi.$$

Hence α becomes increasingly smaller as N increases. The behaviour of the absolute error initially decreases in line with the uniform grid as expected, levelling out as N further increases past 100.

The third graph illustrates the effect of randomly distributing the nodes throughout the interval. This is important, as the dynamic node placement during the BIM simulations

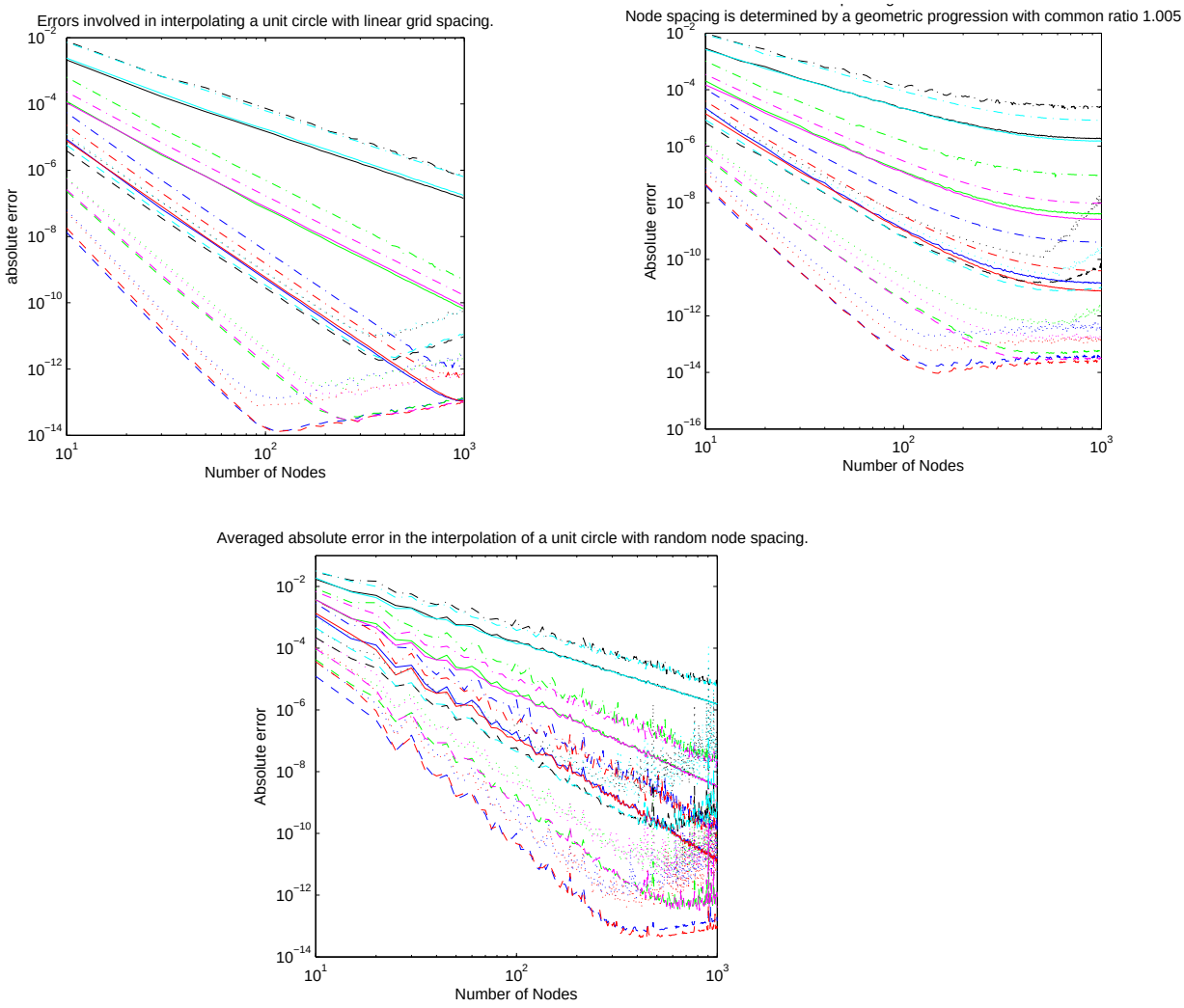

Figure 5.3: Comparison of the absolute error in the interpolation of a unit half circle and its derivatives, parameterised as $(x, y) = (\sin(\theta), \cos(\theta)),\ \theta \in [0, \pi]$. The error in the functions x, y, x', y', x'', y'' are displayed via the red, blue, magenta, green, cyan and black lines respectively. The maximum and average errors using quintic and cubic splines are displayed as dashed, dotted, solid and alternating dash-dot respectively.

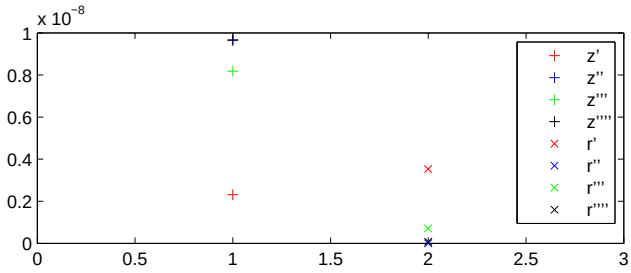

Figure 5.4: Graph illustrating there is no connection point sensitivity in the calculation of the r (x) and z (+) derivatives along a toroidal spline. The plotted values are $|1 - \frac{d(0)}{E(d)}|$, where $d(0)$ is the derivative calculated using a spline originating from the connection point and $E(d)$ is the mean of the derivatives calculated using splines calculated with 25 randomly determined connection points.

may produce irregular nodal distributions. For each N, this was repeated 10 times and the mean average taken. It is clear that although the error no longer decreases monotonically, the trend for the functions and the first and second derivatives still behaves comparably to the uniform case, albeit with greater error on all counts. It is also apparent that round off error may have a drastic impact on the interpolation as N becomes large and node spacing is not smooth.

The toroidal splining routine is essentially the same as the non-toroidal, except for a difference in end conditions. One examines the validity of this extension by comparing the derivatives at the end nodes to those found elsewhere in the spline for a randomly perturbed circle. Fifty nodes are used, with the first co-ordinate randomly selected. The derivatives were then calculated for the same node using splines calculated with twenty five different randomly selected connection points. This comparison is given in figure 5.4, showing the initially calculated derivatives divided by the mean of the corresponding derivatives from the other splines. The derivatives in both the r and z co-ordinates clearly differ only by numerical noise below the tolerance of the splining function, and hence the continuous derivatives condition at the connection point is implemented correctly.

5.1.1 Curvature calculations

Here one illustrates the difficulty in accurately calculating the surface curvature as numerical noise begins to affect the solution. One takes a sphere of radius 0.1, where curvature is already high, interpolated with 50 evenly spaced nodes. To this one adds a small amount of random distortion, $O(10^{-4})$, to the z co-ordinate. Figure 5.5 shows the first and second derivatives calculated with cubic splines, quintic splines and least squares fitted fourth order polynomials. One observes little difference between the first derivatives in the three cases. This is crucial, as it supports the use of the splines in calculating the surface integrals in the coefficient matrices which do not require higher order derivatives. The second derivatives are however, much more susceptible to the random perturbations. One observes quite considerable oscillations using the splines. Both splining methods appear to find a similar solution, as is evidenced by the sharp peaks occurring at the same nodes, although the solution using the cubic splines is generally further from the intended solution. In either case it is not the splines which are at fault, it is the difficulties associated with differentiating noisy data which unfortunately will occur during the evolution of the numerical solution. The fitted polynomials provide a much smoother curve, significantly closer to the solution one would expect from an unperturbed sphere. The impact this has on curvature is shown in figure 5.6 comparing the three cases. One can immediately see how even with this level of perturbation, the 'true' curvature calculated from the splines supports errors on the order of 1 significant figure from the value actually required. This may result in significant errors in the evolution of the surface potentials, particularly in cases where surface tension can become a dominant factor. In particular, this has a severely detrimental effect on the simulation of ultrasonically driven UCA's, where the early surface velocities have a significantly lower contribution to the potential time derivatives than the high surface tension forces. This is also a severe restriction on the performance of the method about the the axial nodes, where jet formation is expected

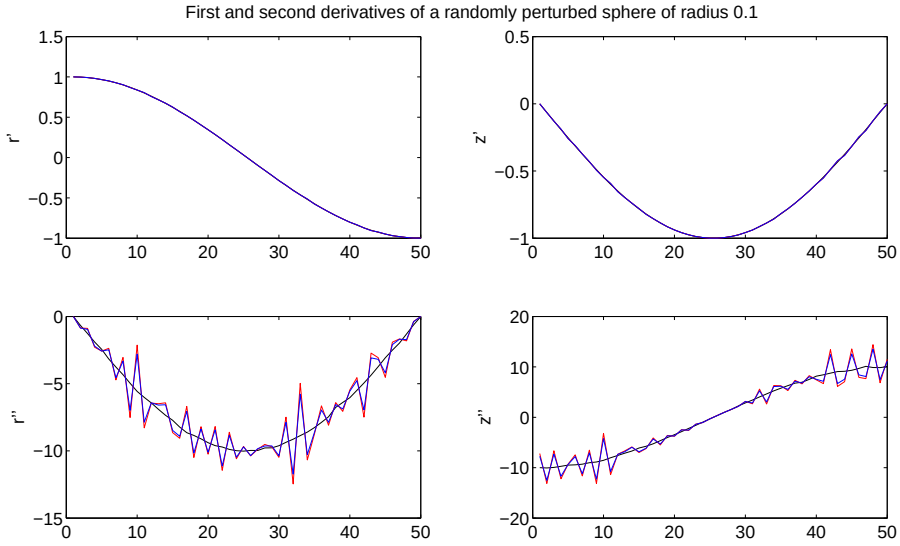

Figure 5.5: First (top) and second (base) r (left) and z (right) derivatives of a slightly perturbed sphere of radius $R_0 = 0.1 + O(10^{-4})$ calculated using cubic splines (red), quintic splines (blue) and least squares fitted polynomials (black).

and the error in the curvature calculation is of a higher order of magnitude due to the dependence on the second z derivative. The smoothed polynomial fit however provides a much smoother curvature, and as such one expects this to provide a more stable solution.

It is also feasible to approximate the axial curvature by interpolating over the curvature of the near axis nodes. This can give a better estimate when the bubble is spherical and the difference in curvature is expected to be small. On the contrary it can give much lessened curvature estimates when the bubble is jetting and one expects a substantially higher curvature at the tip than along the sides of the jet. As such this was not implemented in general.

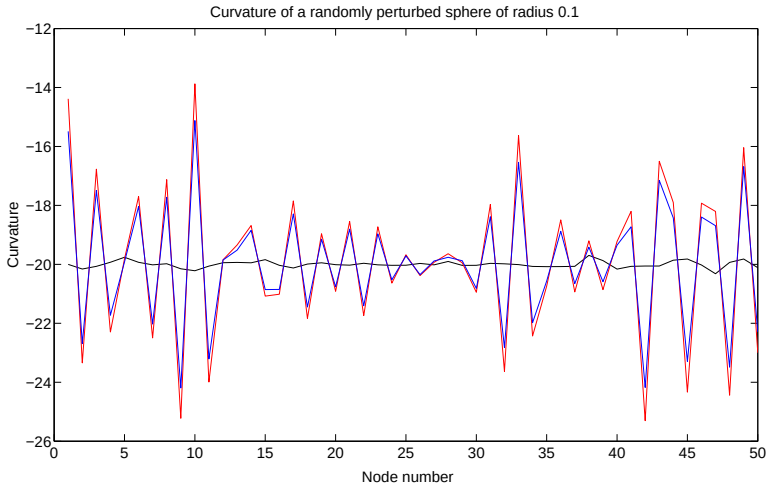

Figure 5.6: Curvature of a randomly perturbed sphere of radius ≈ 0.1 against node number. Calculation performed using cubic splines (red), quintic splines (blue) and least squares fitted polynomials (black).

5.2 Comparison with analytic solutions

5.2.1 Incompressible spherical droplet

The oscillation of a incompressible fluid sphere in a zero gravity vacuum, and perturbed by a Legendre polynomial of order n, P_n, is used to validate the BIM under the action of surface tension. It can be shown that for a such a droplet, with perturbed radius $R = (1 + \epsilon P_n(\cos(\theta)))\cos(\omega t)$, the frequency of oscillation will be $\omega = \sqrt{n(n-1)(n+2)}$ as $\epsilon \to 0$ [48].

In order to simulate this, the governing equations are non-dimensionalised to eliminate σ. At the surface of the droplet, assuming the curvature to be positive the Young-Laplace condition states,

$$\rho\left(\frac{\partial\bar{\phi}}{\partial\bar{t}} + \frac{|\nabla\bar{\phi}|^2}{2}\right) = -\sigma\nabla\cdot\mathbf{n}.$$

Hence appropriate scalings are $\bar{R} = LR,\ \bar{\phi} = \sqrt{\frac{L\sigma}{\rho}}\phi,\ \bar{t} = \sqrt{\frac{L^3\rho}{\sigma}}$, with the pressure scaled as $\bar{p} = \frac{\sigma}{L}p$. With this non-dimensionalisation, the kinematic and dynamic conditions on the droplet surface are,

$$\begin{aligned} \frac{D\phi}{Dt} &= \frac{|\nabla\phi|^2}{2} - 2 + \nabla\cdot\mathbf{n}, \\ \frac{d\mathbf{x}}{dt} &= \nabla\phi. \end{aligned}$$

The constant 2 appears as the curvature is given via $nabla \cdot \mathbf{n} = -2 + O(\epsilon)$ in this framework. As in the method described in Chapter 3, the surface node locations are updated through the time stepping of the ODE governing the surface velocity, $\mathbf{x}_{t+dt} = \mathbf{x}_t + \int_t^{t+dt} \frac{d\mathbf{x}}{d\tau} dt\tau$.

The initial conditions in cylindrical co-ordinates parameterised with respect to arc length are,

$$\begin{aligned} r &= \sin(\xi) + \epsilon\sin(\xi)P_n(\cos(\xi)) \\ z &= \cos(\xi) + \epsilon\cos(\xi)P_n(\cos(\xi)) \\ \phi(\xi) &= 0. \end{aligned}$$

At initiation, $\xi = \theta$ is used, as the arc length along the surface will be $1 + O(\epsilon^2)$, and so this approximation will have minimal effect.

Simulations using mode P_2 oscillations are shown in figure 5.7. The top image compares the Euler and RK4 time stepping routines with $\Delta\phi = 0.01$. Using this liberal time step, the Euler stepping routine fails during the first oscillation, introducing large high frequency disturbances in the solution. The RK4 technique remains stable throughout. The second graph shown illustrates an Euler stepping simulation, with a high node number of $N_b = 60$ and a very conservative time step of $\Delta\phi = 0.0005$. At this resolution, the

Euler technique remains stable, however the computational cost is very large, with 30000 time steps required to reach three oscillations.

Figure 5.8 demonstrates the stability of the RK4 stepping procedure using 15, 30 and 60 droplet surface nodes with $\Delta\phi = 0.01$. Using 15 nodes the simulation has lost phase accuracy with the expected oscillation time, yet unlike the unstable Euler simulation in figure 5.7, it does not exhibit the large high frequency disturbances. The 30 node simulation is also loosing phase, yet at a much slower rate. Even after 15 oscillations, the 60 node simulation remained in phase with the expected solution. As may be seen in the lower image, the first order Euler method required the considerably smaller time step of $\Delta\phi = 0.0005$ to retain accuracy through the first 7 oscillations, again at a very high computational cost.

Figure 5.9 shows the stability of the curvature for modes P_3 and P_4 using the high resolution Euler time stepped simulations. In both cases, the evolution of the curvature on the droplet surface behaves in the expected manner, with no formation of unwanted spurious peaks. The curvature evolution of mode P_3 using 15 nodes and a low temporal resolution RK4 routine is also shown, illustrating the stability of this regime despite some loss of phase accuracy.

A comparison of the stability of the three methods is shown in figure 5.10. This shows the curvature along an droplet perturbed by a P_3 polynomial with $\epsilon = 0.01$, constructed with 50 equally spaced nodes. Smoothing was further reduced to once every 100 timesteps, with the timestep controlled by $\Delta\phi = 0.005$. As can be seen the Euler stepping procedure failed during the first oscillation, after approximately $t = 0.1$. The RK2 case survived considerably longer, up to about $t = 0.4$. The RK4 procedure remained stable beyond $t = 3$, greatly in excess of the other two routines. After $t = 4$, the RK4 method did begin to deteriorate, as the effect of smoothing gradually affected the volume of the bubble. Nevertheless, this case clearly demonstrates the benefit in using the higher order methods

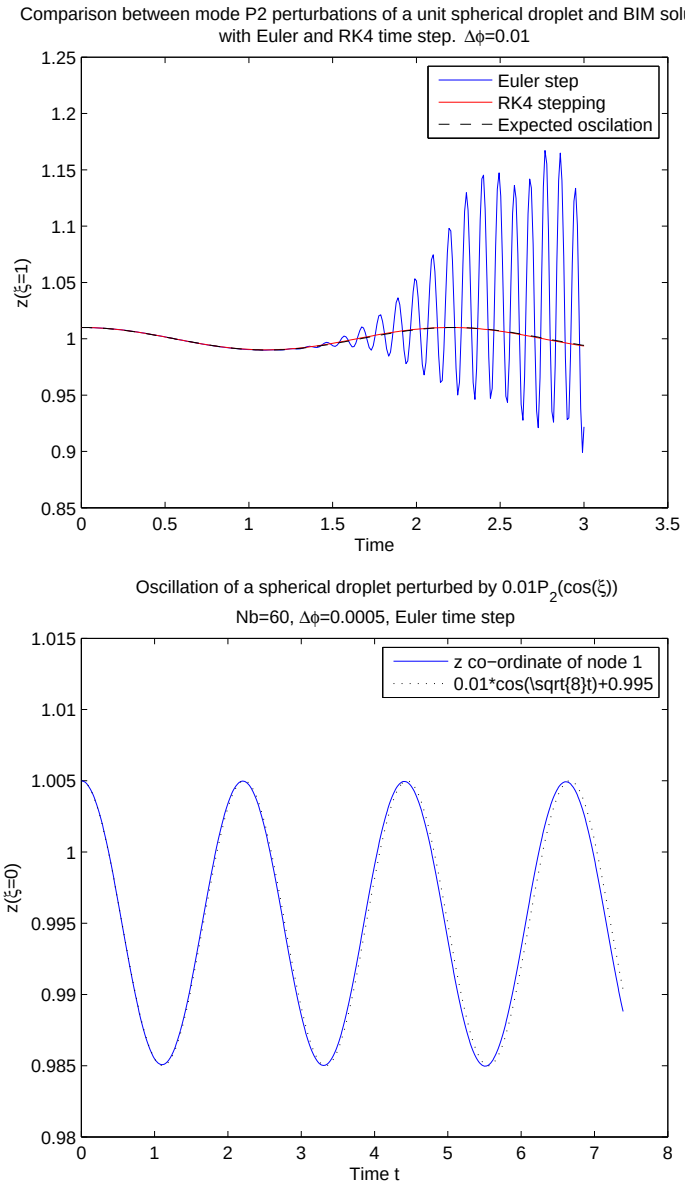

Figure 5.7: Mode P_2 oscillations of an incompressible spherical droplet. The top image shows comparison between RK4 and Euler time stepping procedures with $\Delta\phi = 0.01$. The lower image shows stable evolution using the Euler stepping procedure, with high resolution given by $N_b = 60$ nodes on the bubble surface and $\Delta\phi = 0.0005$.

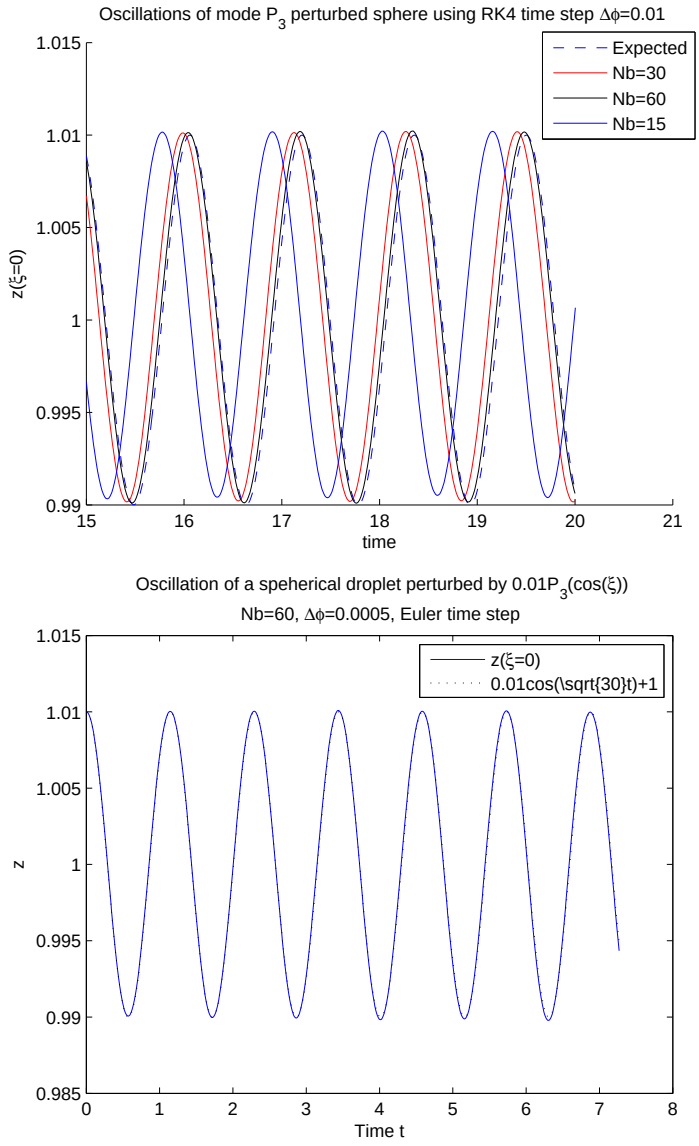

Figure 5.8: Mode P_3 oscillations of an incompressible spherical droplet. The top image shows the effect of increasing the surface resolution whilst using the fourth order $RK4$ stepping routine with $\Delta\phi = 0.01$. The lower image shows stable evolution using the Euler stepping procedure, with high resolution given by $N_b = 60$ nodes on the bubble surface and $\Delta\phi = 0.0005$.

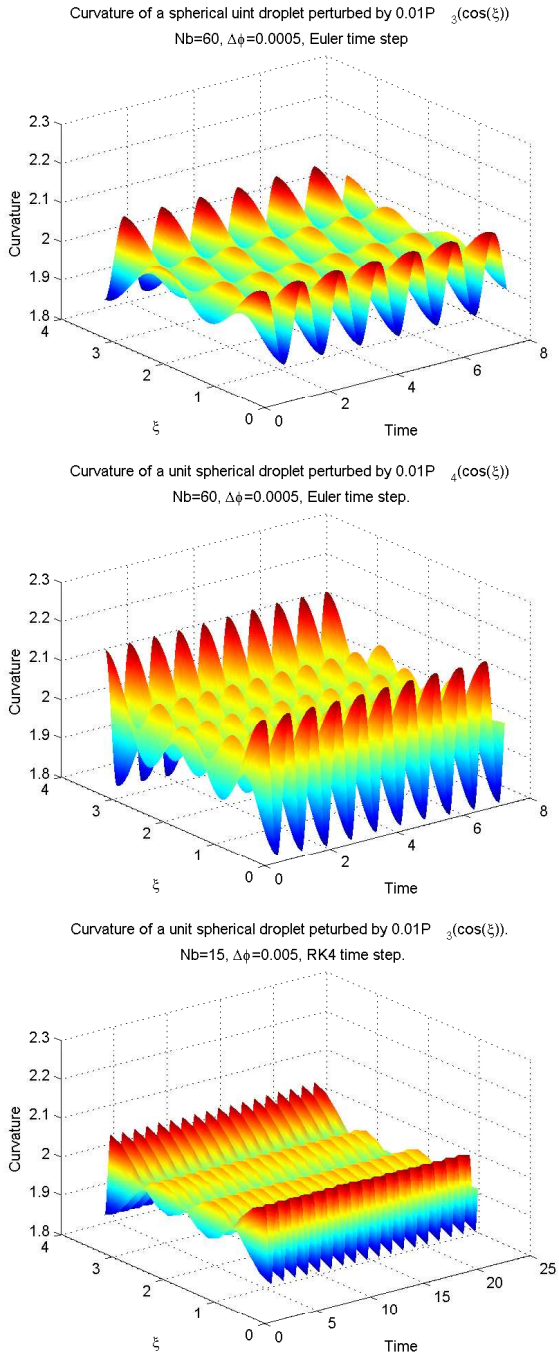

Figure 5.9: Curvature evolution of mode P_3 (top) and P_4 (middle) oscillations of an incompressible spherical droplet using Euler time stepping procedure with high spatial and temporal resolution. The lower image is a low resolution RK4 simulation of mode P_3, through 17 oscillations, loosing phase accuracy yet remaining stable.

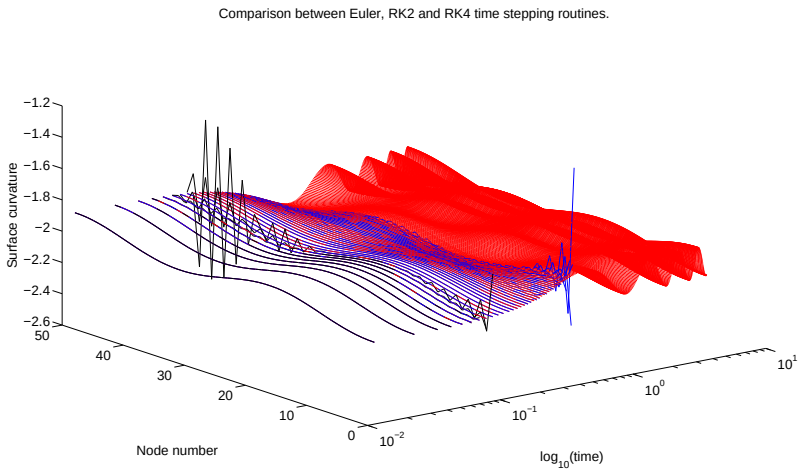

Figure 5.10: Curvature of a droplet of radius $R = 1$, perturbed with a $0.01 \times P_3(\cos(\theta))$. The timestepping parameter is $\Delta\phi = 0.005$, with smoothing restricted to once every 100 timesteps. The solutions are created using the Euler timestep (black), RK2 timestep (blue), and RK4 timestep. Stability clearly increases with the increase in the order of the timestepping routine.

over the Euler time step, especially with the restriction in smoothing frequency. It also clearly shows the benefit in using the fourth order routine over the second order routine, despite the second order errors associated with the velocity calculation.

5.2.2 Comparison with Rayleigh-Plesset equations

As shown in Chapter (2), the Rayleigh-Plesset equations provides an ODE solutions for the potential in an infinite fluid for a radially oscillating bubble. This allows for a direct verification between the BIM solution with both a single bubble, and with an infinite fluid-fluid interface supporting a density ratio of $\rho = 1$. A comparison may therefore be taken both with the potential and normal velocity on the bubble surface, and also the potential and normal velocity on the two fluid interface, which can be any singly connected surface, continuous over $0 \leq r < \infty$.

Figure 5.11 illustrates excellent agreement between the BIM and the ODE solution without the fluid-fluid interface. Using an RK4 time-stepping routine allowed for stable

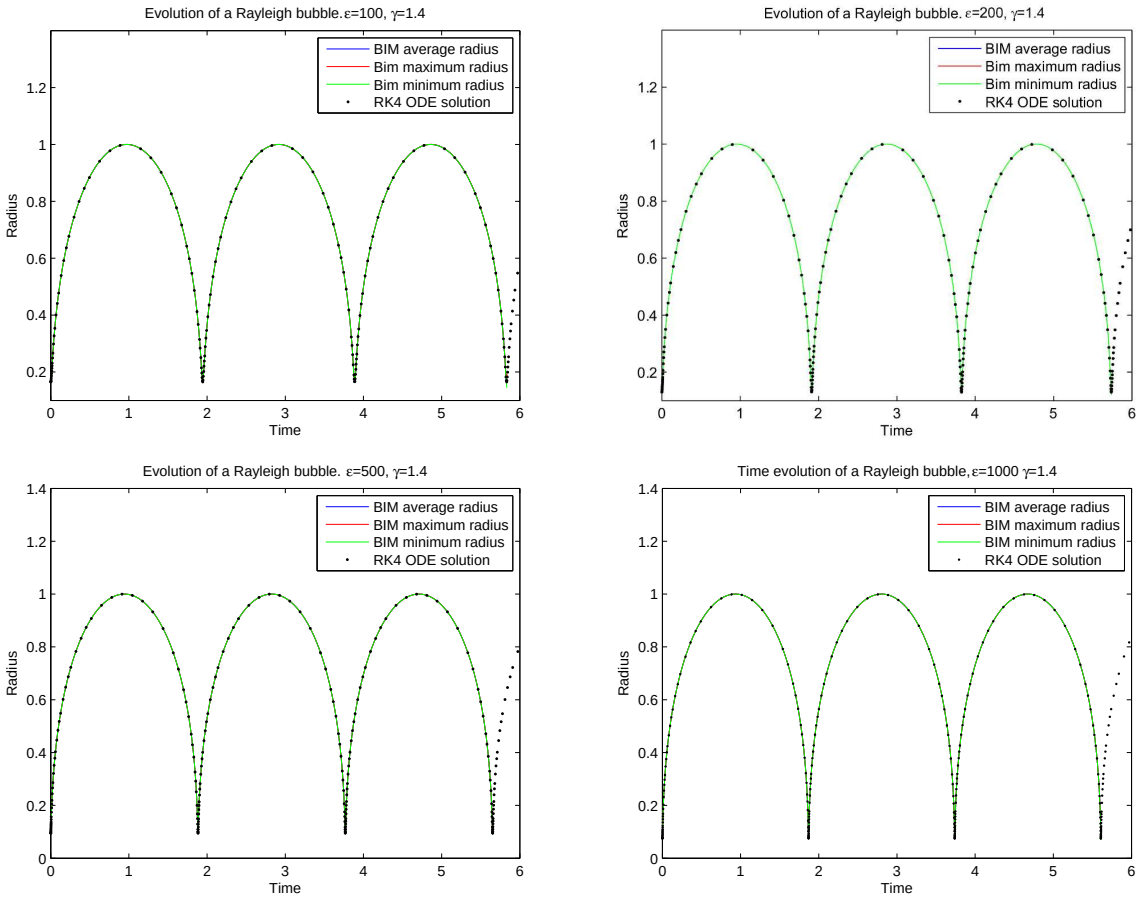

Figure 5.11: Comparison between spherical bubble radii calculated using an RKCK fourth order ODE solution and a RK4 stepped boundary integral solution, in the absence of an additional interface. Near perfect agreement is found for the strength parameters $\epsilon = 100$ (top left), $\epsilon = 200$ (top right), $\epsilon = 500$ (bottom left), and $\epsilon = 1000$ (bottom right).

solutions for 3 oscillations with various strength parameters up to $\epsilon = 1000$. In each simulation the bubble remained very spherical throughout, as is evidenced by the average, minimum and maximum nodal distances from the bubble centre falling nearly exactly atop one another. Indeed any discrepancy is invisible to the naked eye.

The normal on the bubble surface used in the BIM simulations is exactly the negative of the normal taken in the Rayleigh-Plesset equation, and so comparison between the normal velocities is trivial. Similarly as the potential field is known, direct comparison between the true and calculated normal velocities of any given material surface is also

readily applicable, the true normal velocity being given by,

$$\frac{\partial \phi}{\partial n} = \mathbf{n}_i \cdot \nabla \phi = \frac{(-rz' + r'(z+h))R^2\dot{R}}{(r^2 + (z+h)^2)^{\frac{3}{2}}\sqrt{r'^2 + z'^2}}. \tag{5.2}$$

The simplest of these comparisons is that of the constant pressure spherical vapour bubble. Figure 5.12 illustrates the accuracy of the BIM in calculating the radius of the cavity compared to the ODE solution. Both are calculated using fourth order Runge-Kutta methods with adaptive time stepping. The fluid-fluid interface includes the least squares far field conditions as detailed in Chapter 3. The differences between the radii are indistinguishable. The lower image shows both the fluid-fluid interface and the bubble at regular intervals throughout the evolution of the cavity. The blue side is calculated using the BIM with a standoff of $h = 1$ with 30 interpolated nodes on both the interface and the bubble. The red side is calculated using the ODE solution for the bubble, restricted to the time steps used in the BIM simulation. The fluid-fluid interface in the ODE simulation was tracked in a Lagrangian manner given the calculated velocity from the bubble using a first order Euler stepping method. As is clearly visible there is excellent agreement between the two sides. Agreement in the bubble shapes is indistinguishable to the naked eye. However there is a slight variation in the interfacial position, most likely due to the tracking mechanism employed in the ODE solution and the relatively low resolution used in the BIM. The bubble oscillation period is also in agreement with that of the analytical bubble as given by the solution of equation (2.11).

The equations governing this example indicate that the fluid-fluid interface should have no influence on the bubble surface potential or velocity. However, this is not the case in the numerics due to the finite truncation of the infinite free surface, and indeed the second order accuracy of the calculation of potentials and normal velocity. The effect of truncation is investigated in figure 5.13, showing the oscillation of a high pressure bubble

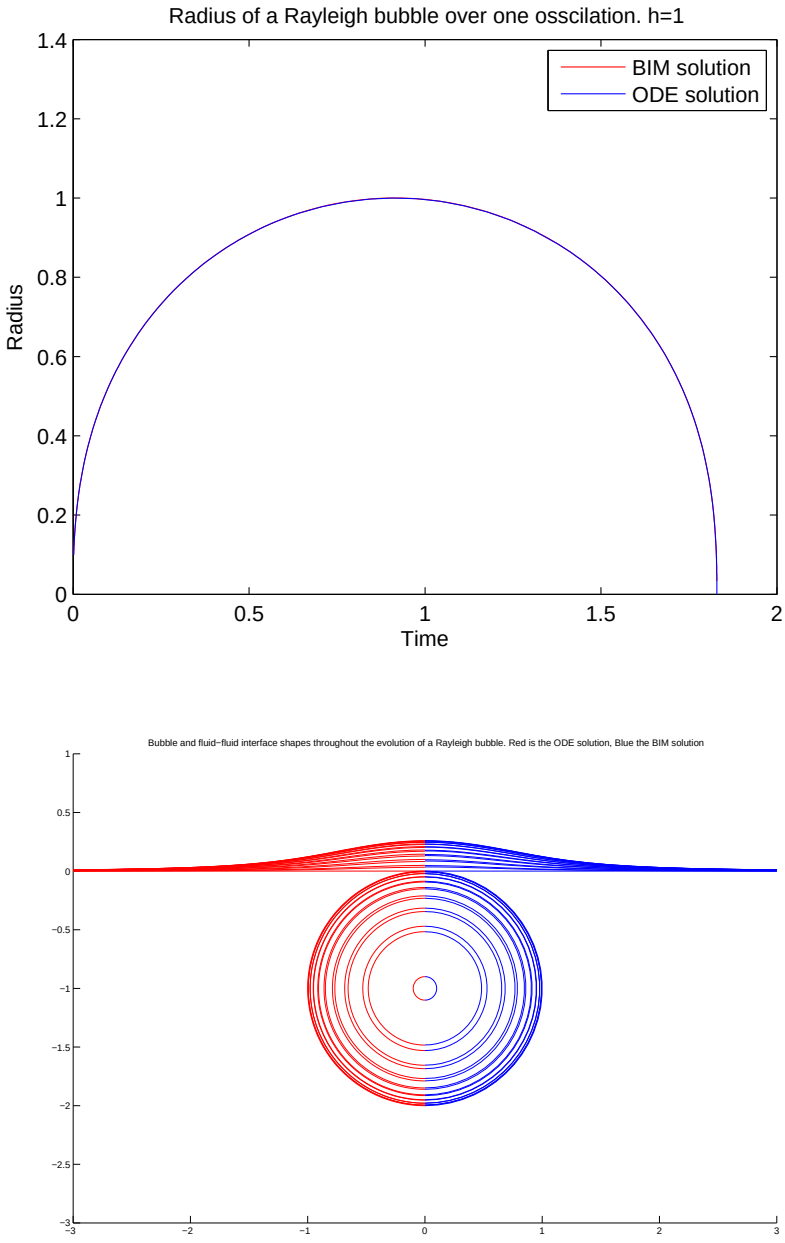

Figure 5.12: Comparison between the ODE solution for the Rayleigh equation and the BIM solution with $\rho = 1$. The top figure shows the bubble radius calculated with each method over time. The lower figure shows the bubble and fluid-fluid interface shapes at intervals of $\Delta_t \approx 0.1$. Excellent agreement is immediately apparent.

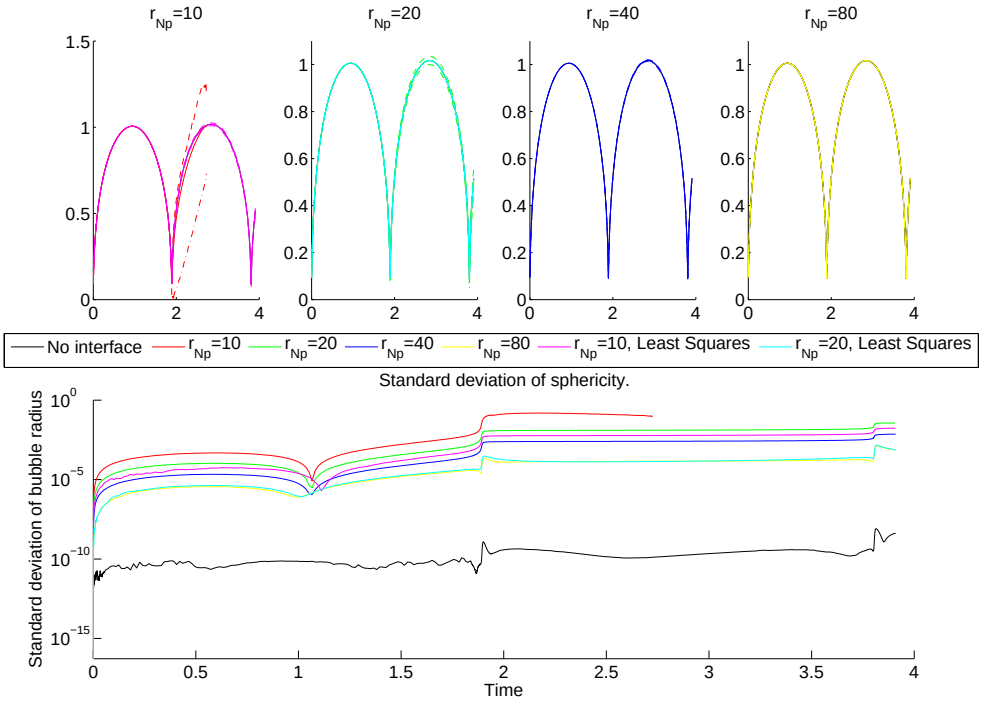

Figure 5.13: The first two oscillations of a spherical bubble initiated at $h = 1$ with $\epsilon = 100$, $\gamma = 1.4$ near an infinite fluid-fluid interface with $\rho = 1$ extending to various different truncation distances r_{Np} with the maximum (dashed), minimum (dot-dash) and mean (solid) bubble radius (top). The standard deviation of the distances of the bubble surface nodes from the initial bubble centroid (base).

at a standoff distance of $h = 1$ near a numerically infinite two fluid interface supporting a density ratio $\rho = 1$. The numerical truncation is taken at $r_{Np} \in \{10, 20, 40, 80\}$, with additional simulations using the least squares far field approximation taken for $r_{Np} = 10, 20$. The standard deviation of the distance of the bubble surface nodes from the initial bubble centroid is also shown throughout the timespan of the simulation. This is a measure of the sphericity of the bubble, and therefore indicates the overall accuracy of the BIM implementation. To eliminate the dependency of the solutions on nodal density, in each case the fluid-fluid interface was initially populated using an identical geometric progression up to $r = 10$, with the remaining surface nodes implemented with a maximum separation of 0.75 maximum bubble radii. The adaptable surface re-griding routine was then used throughout the simulation, stripping and introducing nodes in a similar way in each simulation.

The common choice of a numerical infinity of 10 maximum bubble radii [89, 45] was found to be insufficient. In this case, the second oscillation of the bubble displayed a severe loss of sphericity as well as a loss of temporal and radial accuracy. This resulted in the premature failure of the routine. Setting $r_{Np} = 20$ allowed the simulation to complete the second oscillation, although again during this oscillation the bubble suffered a fair loss of sphericity. Further increasing the truncation of the two-fluid interface to $r_{Np} = 50$ greatly lessened this loss, whilst extending the interface to $r_{Np} = 80$ further decreased the nodal distance standard deviation by another order of magnitude. All cases including the interface suffered a distinct jump in the standard deviation at the point of minimum bubble volume, most likely due to the small amount the bubble centroid will have translated through the action of numerical noise. Including the least squares fitted infinite extension gave a significant performance increase to the cases $r_{Np} = 10$ and $r_{Np} = 20$. In the first case it allowed the simulation to complete the second oscillation, and gave a standard deviation superior to that of the case $r_{Np} = 20$ without the least

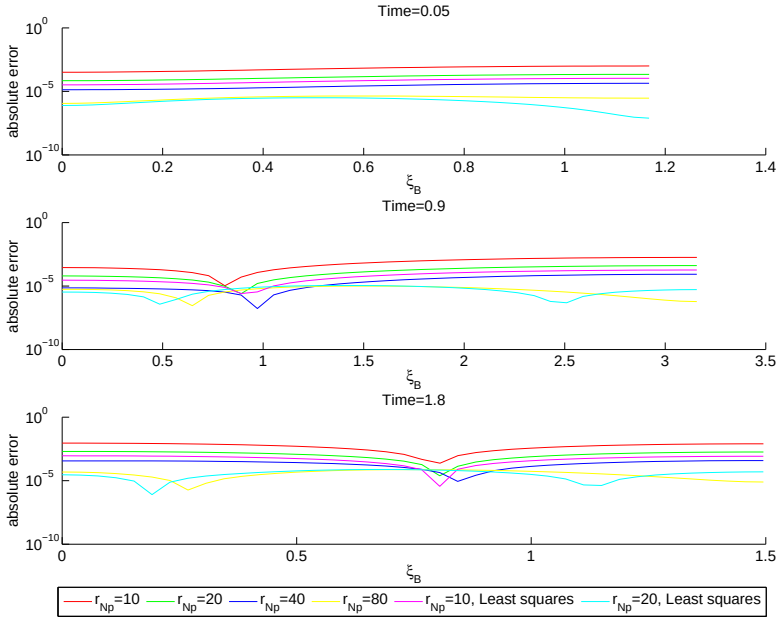

Figure 5.14: Sample surface potential variation due to varying the truncation distance. Comparisons are taken at $t = 0.05$, $t = 0.9$ and $t = 1.8$ for a bubble characterised by $\epsilon = 100, \gamma = 1.4$, at a standoff distance of $h = 1$.

squares extension. Including the extension in the case $r_{Np} = 20$ gave a further considerable improvement, resulting in a comparable standard deviation to the unextended $r_{Np} = 80$ simulation.

In all cases, sphericity was affected to some extent. This is evidenced by the simulation without an interface having a nodal distance standard deviation superior by four orders of magnitude throughout the simulation. This does not however significantly effect the gained results as is shown by the excellent agreement most cases provided with regards to bubble radius, where the respective simulation curves are indistinguishable. This difference is also shown in figure 5.14, showing the absolute difference between potential along the bubble surface calculated using the BIM with and without the two fluid interface. Nodal placement is fixed to 50 evenly spaced nodes about the bubble, and so this comparison should be sufficiently accurate. One again observes the improvement associated with increasing the numerical truncation, on an order of magnitude as the truncation

distance doubles. The superior performance of the least squares fitted far field is also again seen, with the case with $r_{Np} = 20$ consistently giving the best agreement with the test simulation.

The effect of truncation on the surface velocity is seen in figure 5.15. This compares the initial bubble surface normal velocity of a Rayleigh bubble to that calculated with various truncation distances without the least squares extension. In this simulation the standoff distance was $h = 1.5$, with the initial conditions on the bubble surface given as $R = 0.1,\ \phi_0 = -2.5806976,\ \epsilon = 0$ at an initial time of $t_0 = 0.0015527$ [5]. Along the infinite interface, the potential functions $\phi_1(\mathbf{p})$ and $\phi_2(\mathbf{p})$ are identical as $\rho = 1$, and as such the function $F(\mathbf{p}) \equiv 0$ always. This simulation used 30 nodes along the bubble surface, with 100 nodes distributed using a geometric progression along the two fluid interface. In order to gain a velocity accuracy to the same order as a simulation without the interface, a value of $r_{Np} = 100$ was required. Even so, setting $r_{Np} = 20$ gave a difference of $O(10^{-5})$, which would most likely be sufficient for most simulations at this standoff distance.

Finally, a comparison is taken using a material surface exterior to the bubble, given by $z = \cos(r)e^{-r^2},\ r \in [0, 10]$ and using the least squares far field approximation. The standoff distance is $h = 0.5$ from the $z = 0$ plane, with the bubble behaving as a vapour bubble, $p_b = p_v$. Figure 5.16 demonstrates the accuracy of this approach as the number of nodes on the interface increases, with the nodes on the bubble set to 40. The absolute error between the two velocities is displayed on both the fluid-fluid interface, and the bubble surface. The effect on the bubble of increasing the number of nodes on the fluid-fluid interface is very clear, with considerable improvement each time N_p doubles. As expected the error in the normal velocity on the fluid-fluid interface also decreases with N_p increasing, as can be seen by the decrease in error in the heavily perturbed region of this material surface. At $N_p = 160$ this region displays the same level of error as the much

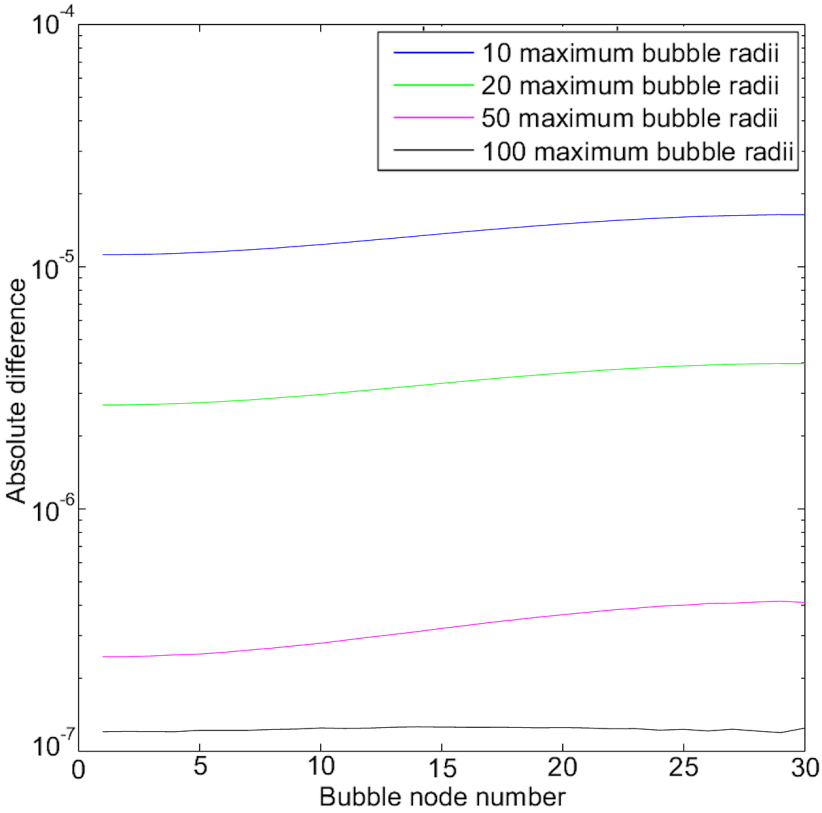

Figure 5.15: Comparing the effect of different truncation distances of the fluid-fluid interface for a Rayleigh bubble. The absolute error found in the potential on the bubble surface is shown, with the error only reaching the same magnitude as the BIM simulation without the interface when the interface is interpolated to 100 maximum radii.

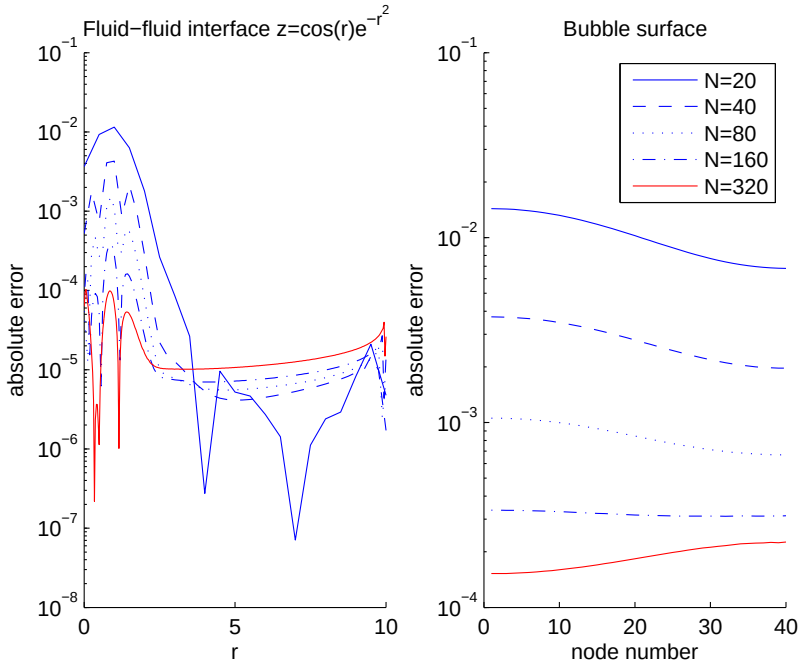

Figure 5.16: Absolute errors in normal velocities on both the fluid-fluid interface (left) and bubble surface (right), where $\rho = 1$ and the fluid-fluid interface is located at $z = cos(r)e^{-r^2}$. The number of nodes on the bubble is fixed at $N_b = 40$ whereas the number on the interface Np increases from 20 to 320. All nodes are evenly spaced. It is clear that an insufficient number of nodes on the fluid-fluid interface results in discrepancies in the normal velocities on both surfaces, and that the far field ($r > 4$) of the fluid-fluid interface remains stable even with low nodal density.

less perturbed region. It is also clear that in the region $r > 4$, the error is sufficiently small for all N_p tested, showing that the nodal density away from the active region can be kept low, which is of great benefit to the computational cost of the simulations.

5.2.3 Infinite surface verification

In order to verify the evaluation of the normal velocity along the numerical infinite surface, a point source solution is employed. The code is used to solve for the normal velocity along the surface of an infinite half-space defined by $\{(r, \theta, z)|0 < r < \infty, 0 > z > -\infty, 0 < \theta < 2\pi\}$ given a point source of strength 1 located at $(0, \theta, 1)$. The analytic solution is

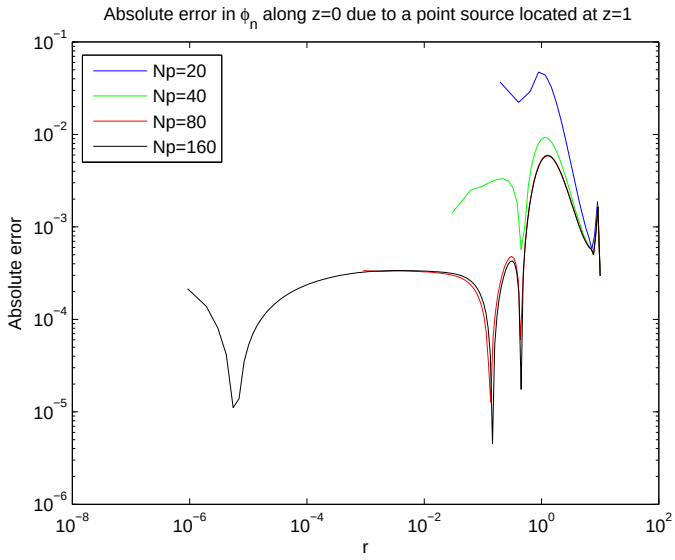

Figure 5.17: Absolute error in normal velocity along the surface of a half-space under the influence of a unit point source at $(r, z) = (0, 1)$. Excellent agreement is observed near the origin for 80 and 160 nodes along the surface. Far field agreement is worse, yet still acceptable due in part to the very small potential.

immediately given as,

$$\phi = \frac{1}{\sqrt{r^2 + (z+1)^2}},$$
$$\frac{\partial \phi(r,\theta,0)}{\partial n} = \frac{\partial \phi(r,\theta,0)}{\partial z} = -\frac{1}{(r^2+1^2)^{3/2}}.$$

Figure 5.17 shows the absolute error in $\frac{\partial \phi}{\partial n}$ in comparison to the expected value for $N_p \in \{20, 40, 80, 160\}$, with nodes geometrically progressing from $r = 0$ to numerical truncation at $r = 10$. The point source least squares approximation is then used for the remaining surface. Near the origin where nodal density is greatest and the influence of the source is most predominant, agreement is excellent. However little improvement is visible between the use of 80 and 160 nodes. As the nodal density decreases and the potential approaches zero, the solution is less accurate. However, this region is sufficiently far away for this error to have negligible influence on the interesting behaviour about the origin.

As a result of these and other investigation not shown here, it was decided to employ both the least squares fitted far field estimate, and a substantial truncation distance for the infinite interface. In the most aggressive simulations, typically those at very shallow standoff distances and those with multiple bubbles on either side of the interface, truncation is taken at $r_{Np} = 100$. The nodal density along the interface actively varied according to the interfacial velocity, with an increasing minimum nodal separation distance as r increases.

5.3 Pressure field comparisons

Three methods were forwarded in Chapter 3 for the evaluation of the pressure field away from the bubble. Here one will compare the results gained with the three methods for a selection of bubble simulations in both the simply and doubly connected phases. Firstly, figure 5.18 shows a selected pressure field for the simulation $\rho = 2,\ \epsilon = 100,\ h = 0.7$ at the non-dimensional time $t = 2.0$. At this point the bubble is about to form a threading jet, driven by the higher pressure region above. The three dimensional images are constructed using 1500 randomly selected points in the set $\{(r, z)|r \in [0, 2),\ z \in (-1, 2)\}$, whilst the flat coloured pressure fields are generated from a 300 by 500 regular grid whose associated values are cubically interpolated from the random points. All three show excellent agreement with one another, as well as with the pressure calculated along the fluid boundaries.

The pressures shown in figure 5.19 illustrate the failings of the finite difference schemes. These are taken during the rapid dynamics in the toroidal phase following jet impact. The simulation is that of a single high pressure bubble characterised by $\epsilon = 500, \gamma = 1.4$, at a standoff distance of $h = 1$ from a two liquid interface supporting a density ratio of $\rho = 2$ and $\sigma_I = 0$. The pressure fields are interpolated over 2000 randomly positioned particles using a regularly spaced 300×500 grid. The clearest error in the

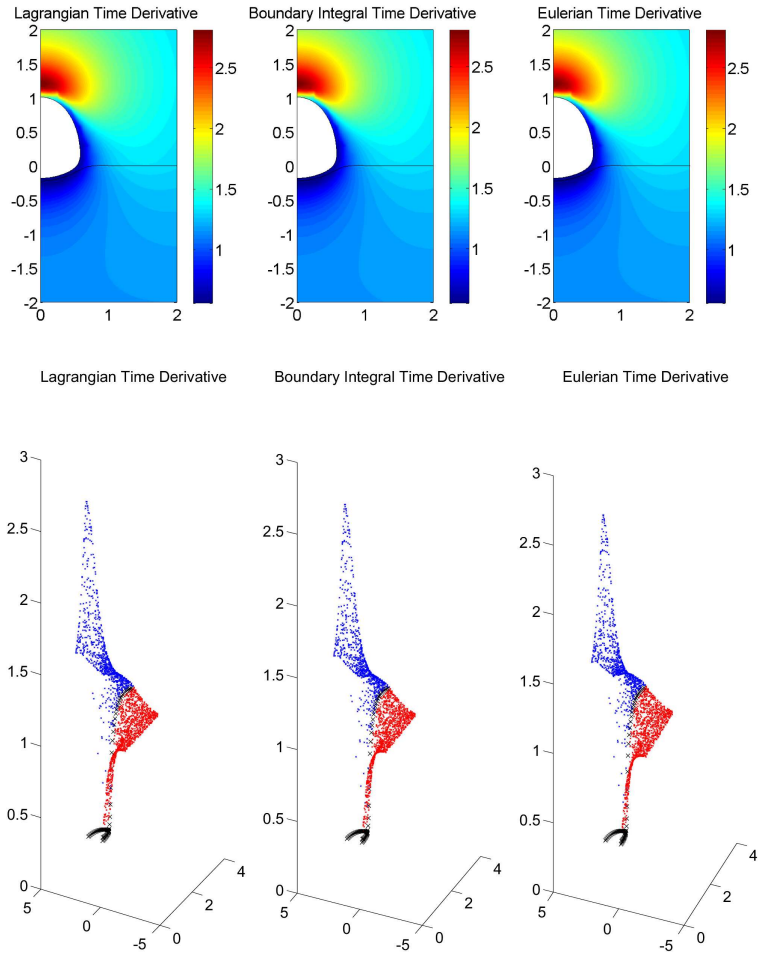

Figure 5.18: Pressure fields for $\rho = 2.5,\ h = 0.7$ before jet impact occurs, with the time derivative of the potential field calculated using the Lagrangian (left), Eulerian (right) and direct BIM (centre) approaches. Lower row shows the corresponding field particle solutions, with layer 1 (blue), layer 2 (red) and the interfaces (black).

pressure fields is the apparent discontinuity across the two fluid interface. Obviously this is incorrect as in this case there is no surface tension. By examining the three dimensional particle plots, calculated with identical particle velocities, it is clear this error is due to the numerical differentiation through time of the field potentials. In both the Lagrangian and Eulerian cases, there is a distinct discontinuity between the field pressure and the pressure calculated along the interface. This is most pronounced in the toroidal domain, yet is also present to a lesser extent in the second liquid layer. As the Eulerian time derivative is calculated in an identical manner to the pre-toroidal phase, and is in very close agreement with the Lagrangian time derivative which requires modification to include the vortex ring advection, one has that the numerical differentiation must be insufficient. In order to improve this, it was found that an extremely high resolution both spatially and temporally was required throughout the entire BIM simulation, which in itself lead to stability issues as detailed in Chapter 3. The central images however use time derivatives calculated by direct differentiation of the BIM equations (3.26). Therefore, these are subject to less error as the time derivative of a field particle is calculated though the evaluation of a numerical surface integral and not through the numerical derivative of multiple numerical surface integrals. As can be seen these show excellent agreement with the interfacial pressure in both liquid domains, without the discontinuity observed for the Eulerian and Lagrangian cases.

Due to this apparent improvement in accuracy, most of the pressure calculations herein are performed using the direct differentiation of the BIM equations. As mentioned in Chapter 3, this is also by far the most computationally efficient method of the three.

5.4 Failure due to surface intersection

As mentioned previously, should any surfaces cross the solution is invalidated. One demonstrates how this may happen in figure 5.20, illustrating why it is important to limit the

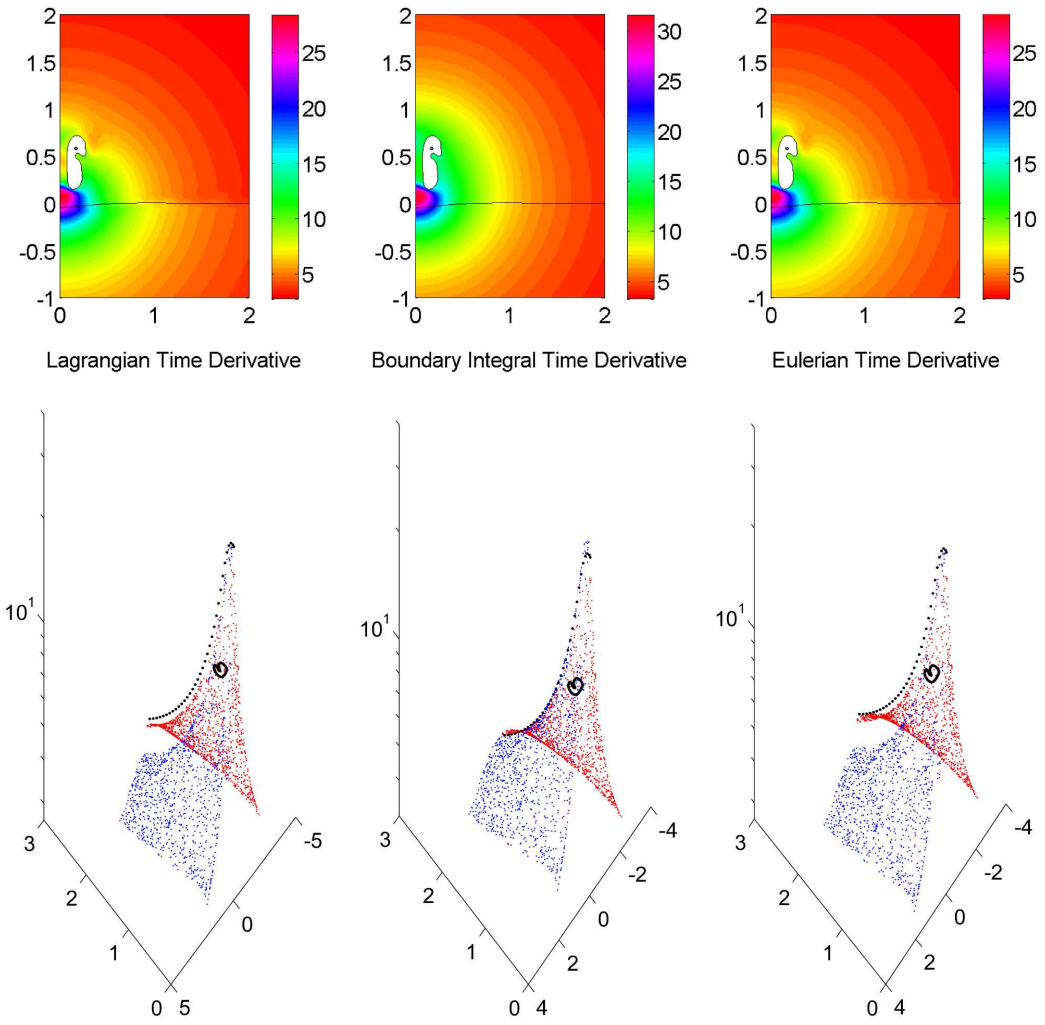

Figure 5.19: Example pressure field calculations using time derivatives calculated using the Lagrangian method (right), direct BIM method (centre), and the Eulerian method (right). The top row shows the interpolated pressure fields, whilst the lower row shows the particle fields upon which the top row is interpolated over.

number of time steps allowed below the minimum threshold. This contains time frames taken during the toroidal phase of a high pressure bubble collapse in very close proximity to the two fluid interface. The system parameters where $h = 0.5,\ \epsilon = 100,\ \gamma = 1.4,\ \rho = 1.5,\ \delta = \sigma_b = \sigma_I = 0$, with the liberal $\Delta\phi = 0.03$. Before the bubble and two fluid interface collide, there is a distinctly high region of the decomposed potential ψ, corresponding to the high speed pinching ring jet. At collision, a small increase in this potential is observed directly over the offending area, as can be seen in the third frame at time $t = 1.9593$. Further progress is highly erroneous, as can be seen by the complete eradication of the high potential spike by $t = 1.9594$ in the fourth frame. Approximately 1000 time steps separated these frames, and as such this collapse in potential is significantly influenced by explicit surface smoothing as well as the incorrect surface velocity calculation. By the sixth frame shown here, the section of the bubble surface which crossed the boundary has grown quite substantially, as the incorrectly calculated surface potential in this region continues to grow rapidly.

5.4.1 Existing methods for increasing stability

The above results have shown that in some cases, the boundary integral method can produce inaccurate results, particularly as the simulation reaches more extreme situations involving approaching boundaries. Various methods have been developed to compensate for this, often involving grid refinement of some sort. In Beale *et al.* [3], the simulation of overturning water waves was achieved through greatly increasing the nodal concentration about the wave tip, even beyond the analytically proven convergence threshold they provided. Similar approaches have also been deployed in inviscid droplet pinch-off simulations, by smoothly increasing node concentrations about the centre of the indentation [51, 63]. Other authors have employed h, p and $h - p$ refinement methods, where the mesh is refined locally by either halving the mesh separation (h), increasing the order of

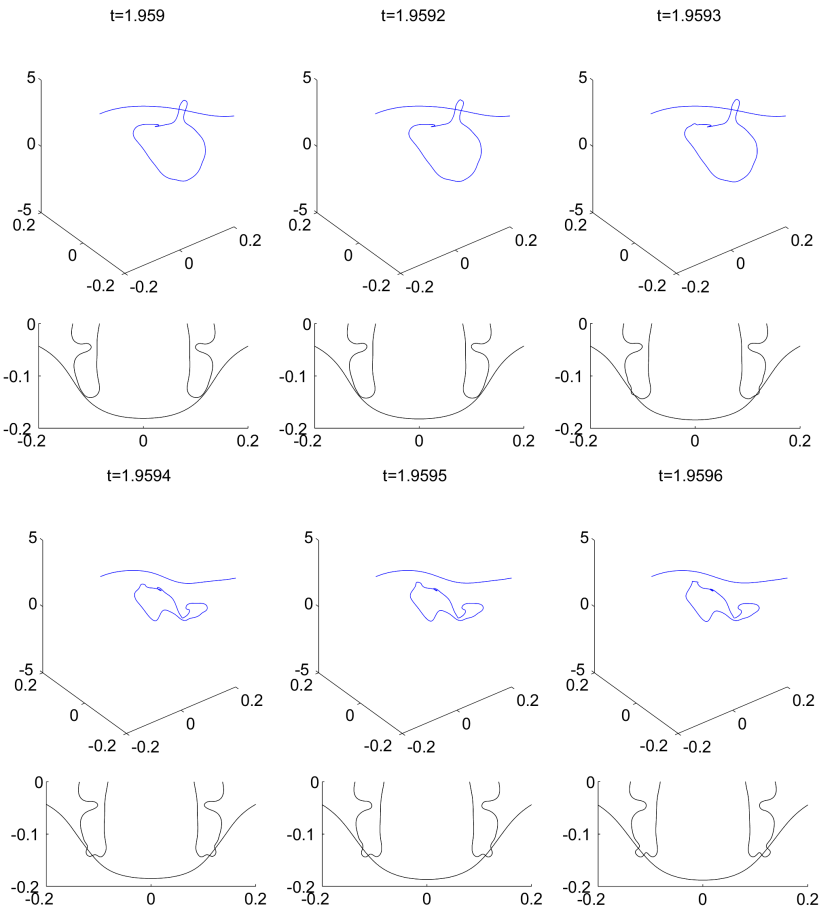

Figure 5.20: Failure of the numerical scheme due to surface intersection during the toroidal stage of a simulation in close proximity to the two fluid interface.

the interpolating polynomials over a mesh section (p), or a combination of the two. These compare the solution over coarser and finer grids, with refinement being initiated only if the two solutions are beyond some convergence threshold, such as the relative error in an energy norm [22]. Such an approach requires a significant increase in computation, as it requires each step to be re-evaluated several times using successively denser meshes.

5.5 Comparison with experimental solutions

5.5.1 Free surface comparison

Bubbles collapsing near free surfaces have been extensively studied both experimentally [36, 74, 23] and numerically [64, 89, 74]. The standoff distance has been shown to be a very significant factor in this situation, with the bubble dynamics showing great variation dependent upon it. The key features with very shallow standoff distance experiments with $h \approx 0.5$, are the formation of slender threading jets in comparison to the bubble radius, coupled with drastic free surface spiking. In contrast for $h > 1$ broad threading jets are formed, potentially resulting in a non-axial impact on the opposing bubble wall. The deformation to the surface is also drastically different, with no spike formation evident above a critical standoff distance.

Free surface behaviour may be simulated using the two fluid model by setting the density ratio $\rho = 0$. The cavitation free layer will then in effect have no associated inertia, and from the evaluation of the field and surface pressure, equations (3.63) and (3.66), it is immediately apparent that this layer will have constant pressure everywhere with a magnitude of $p_2 = 1$. The evolution of $F(\mathbf{p})$ on the fluid-fluid interface will now be comparable to the evolution of the potential $2\phi_1(\mathbf{p})$. In contrast to the previous works above, in this implementation the surface particles still behave in a pseudo-Lagrangian manner, as the algorithm will continue to calculate a slip in tangential velocities at the interface. This is of course totally arbitrary and will have no effect on the fluid dynamics

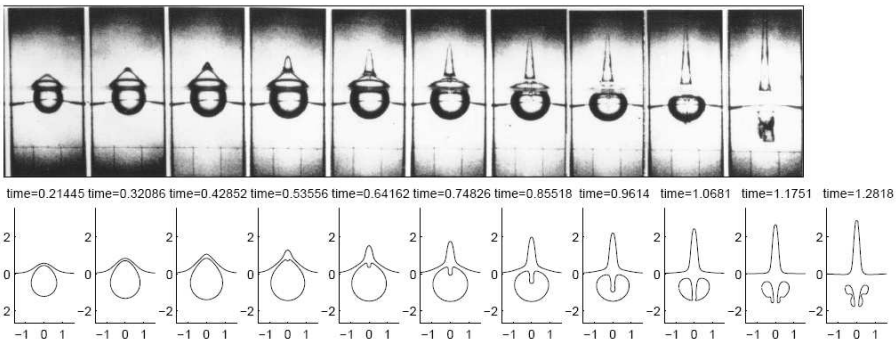

Figure 5.21: Comparison between an experiment by Gibson and Blake [36] of behaviour near a free surface at $h = 0.56$ and a numerical simulation with $\rho = 0$, continuing into the toroidal phase.

in layer 1, nor the pressure in layer 2. It does however allow for some information to be gained about the fluid dynamics in the zero density layer, as is shown in figure 6.7.

Comparison is taken against the experiments of Gibson and Blake [36] in figure 5.21 for a bubble initiated at the close standoff of $h = 0.56$. The simulation continues into the toroidal phase beyond the final experimental frame. The toroidal behaviour is in excellent agreement with simulations by Wang [89] and Pearson *et al* [64, 65]. This also illustrates a toroidal effect that is encountered later in more complex settings, the splitting of the bubble by a horizontally acting fluid ring. In this case the simulation is stopped as the bubble sides became very close, as the bubble is still collapsing. In other cases this may be avoided through the bubble re-expansion, which can be seen for example in Chapter 7.

5.5.2 Rigid boundary comparison

In the opposing density ratio extreme, as $\rho \to \infty$, the potential in the secondary fluid will approach zero everywhere permanently. Hence this fluid will remain motionless in the limit and the cavitated fluid will thereby behave as if in the presence of a rigid wall. This is demonstrated in figure 5.22 with a ratio $\rho = 10000$. Excellent agreement is seen between the numerical solution and the experiments of Brujan *et al.* [66] for $\rho = 0.9$ about the pre-

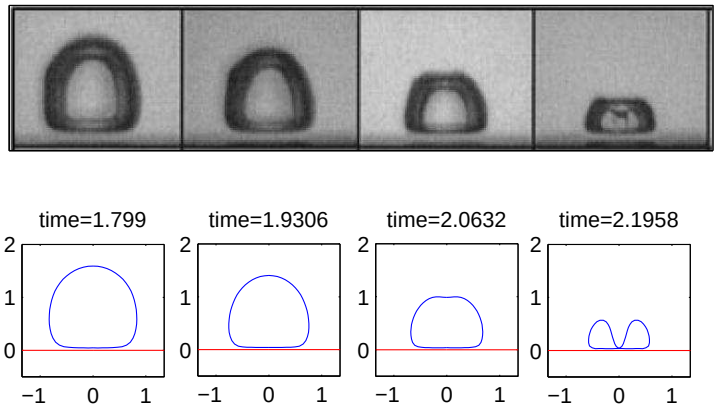

Figure 5.22: Experimental (top) and numerical (bottom) bubble collapse near a rigid boundary for $h = 0.9$. The rigid boundary is simulated using the two-fluid model with a density ratio of $\rho = 10000$.

toroidal jetting stage. Each experimental time frame is separated by $17.7\mu s$ corresponding to a non-dimensional time of approximately $t = 0.13$. The experimental bubble is of size $R_{max} \sim O(1mm)$ and so buoyancy may be neglected.

Additionally one may exploit the properties of Laplace's equation to find further comparisons to the rigid boundary behaviour. As has been used by many previous authors, a rigid boundary may be implemented using an image Green's function. This is essentially the same as simulating two bubbles in an infinite fluid with a separation distance of twice the comparable standoff distance. One uses this property in figure 5.23, with a comparison to the high speed photography in Brujan *et al* [17]. In this a laser generated bubble is formed at a standoff distance $h = 1.1$ from a metal plate. The strength parameter is calculated to be 40246 using the radius and velocity data given. The simulations performed in the aforementioned paper used a different initial condition on the bubble surface, and

so were able to use a considerably lower strength parameter, whereas in this work high pressure cavities are assumed to start at minimum volume.

The late collapse phase for these cases is shown in figure 5.23 with $\rho = 100$ used to approximate $\rho = \infty$ in the single bubble case. Excellent agreement is seen, although there is some disparity between bubble volumes at impact, with the radius of the experimental images being approximately 0.25 maximum bubble radii, and numerical images being approximately 0.3 maximum bubble radii. This is most likely attributable to discrepancies in the initial conditions, as the strength parameter $\epsilon = 40246$ is substantial. There is also a slight temporal shift between the single and multiple bubble numerical cases of approximately $t_s \approx 0.005$. Further in this specific example, the bubble jets in the two bubble system should theoretically impact at the same moment. This cannot be achieved in the current implementation, as the build up of numerical error in the calculations before jet impact will result in a slight discrepancy in jet tip velocities and bubble shapes.

5.5.3 Comparisons with existing research involving fluid-fluid interfaces and the null impulse state

Experiments studying cavitation near a two fluid interface have been conducted by Chahine and Bovis [23]. In these a water/white spirit interface, with a density ratio of $\rho = 0.76$, is examined, with spark generated centimetre sized bubbles formed in the water layer. Figure 5.24 compares two of these experiments with BIM simulations acting under gravity with a buoyancy parameter of $\delta = 0.0147$. With the shallow standoff of $h = 0.87$, the simulation is halted after one oscillation as a non-axial jet impact occurs. The velocity and pressure fields at the end of this simulation are shown in figure 5.25. These clearly demonstrate that the observed shape is not a result of the electrical filaments in the experiments, and that a high speed ring of fluid flows down around an axial bubble stalk. In the deeper standoff case of $h = 2.2$, a buoyancy driven jet forms, leading to an axial

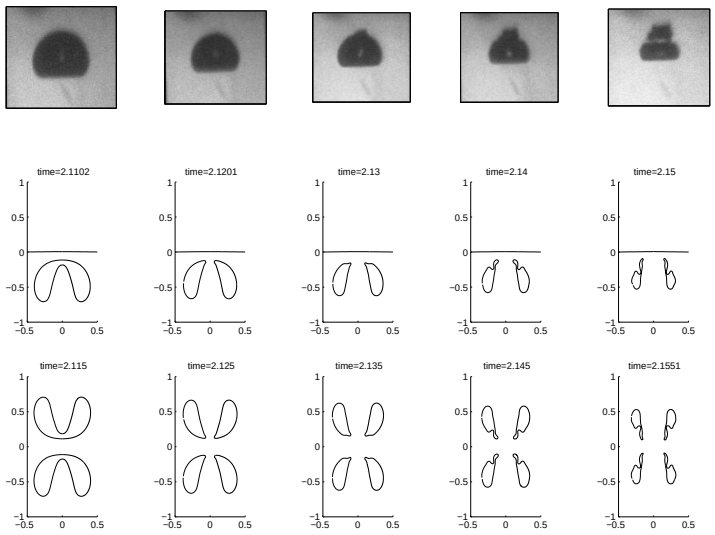

Figure 5.23: Comparison between experimental and numerical results for $h = 1.1$ in the vicinity of a rigid boundary. Experiment [17] (top), $\rho = 100$ (centre) and an infinite fluid containing 2 bubbles at $h = \pm 1.1$ (base)

.

jet impact and is hence simulated further using the toroidal bubble model above. In both cases excellent agreement is seen between the experiment and the simulation.

These experimental observations are also in line with the Kelvin impulse approximation given in equation (2.42). In this case the null impulse standoff distance is approximately $h = 1.27$, and the impulses calculated for the two experimental standoff distances have different signs. Further evidence that the upward jetting bubble migration for $h = 2.2$ is buoyancy driven is shown in figure 5.26, comparing the BIM simulation of the experiment with $\delta = 0.0147$, to a zero buoyancy simulation with all other parameters identical. In this $\delta = 0$ simulation bubble jet formation begins in the early rebound state of the bubble, resulting in a downward jet which does not impact before the bubble re-expands.

In figure 5.27 the behaviour near the null impulse state is examined, with a bubble

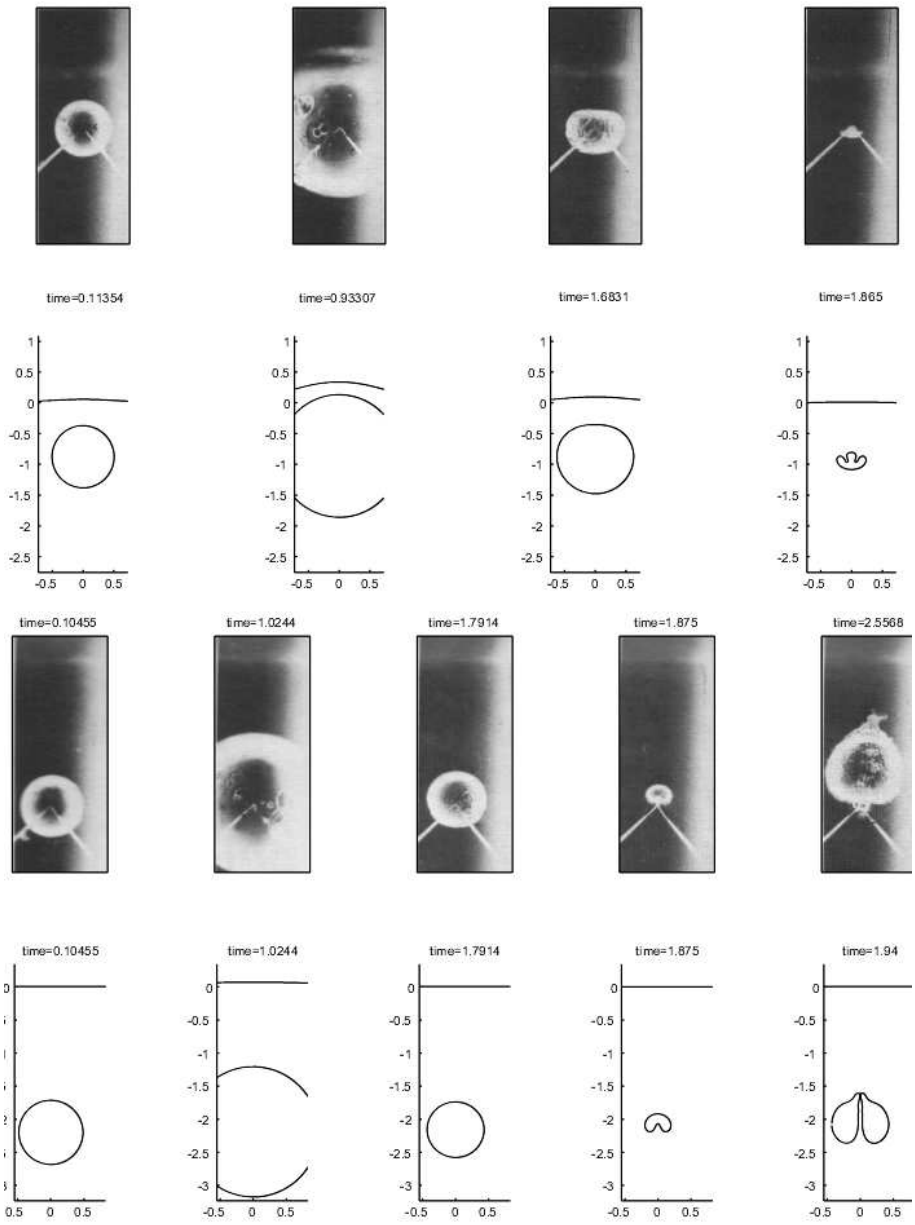

Figure 5.24: Comparisons between experiments near a water/white spirit interface $\rho = 0.76, \delta = 0.0147$ by [23], used with permission, and the numerical code for $h = 0.87$ (top) and $h = 2.2$ (base). The final frames in both cases are where the simulation ends due to either non-axial jet impact (top) or jet disconnection (base), and resultantly the time of the final frames for $h = 2.2$ are not at the same time. Other parameters are estimated as $\epsilon = 100,\ \sigma_b = 0.001$

.

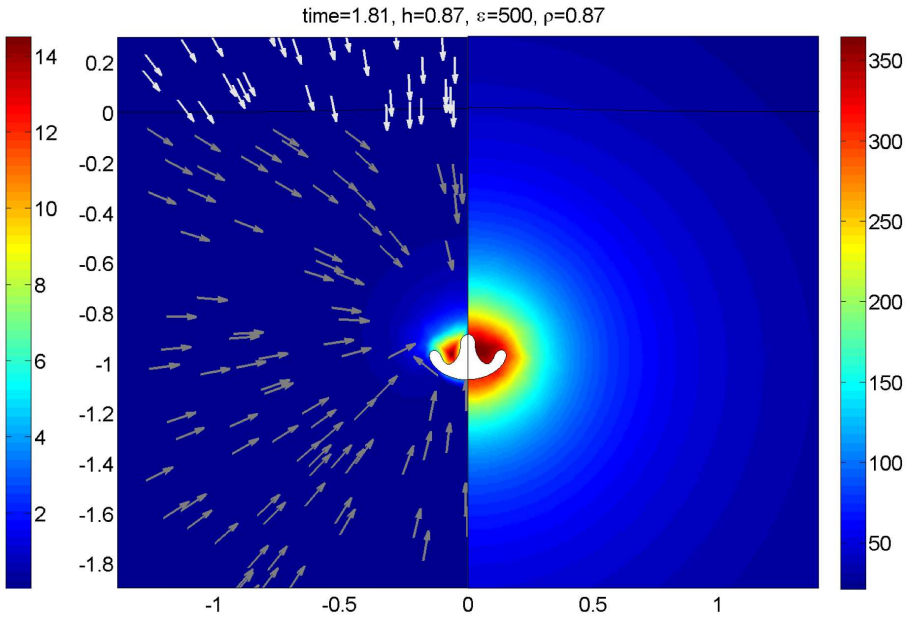

Figure 5.25: Pressure and velocity fields at the end of the first collapse for $\rho = 0.76$, $\epsilon = 100$ at the standoff distance $h = 0.87$.

.

simulated at a standoff distance of $h = 1.27$. The time frames shown for the bubble shapes occur during the late collapse and early rebound phases, whilst the pressure and velocity fields demonstrate the magnification in perturbations just after the bubble rebounds. Prior to these time frames, the bubble remains predominantly spherical, with a very slight oblation occurring toward the end of the first collapse. During the early stages of the bubble rebound, the slight perturbations present on the bubble surface are magnified, and a ring deformation is observed to occur slightly above the vertical center of the bubble. A small indentation also occurs at the base of the bubble, indicative of the early stages of a buoyancy driven jet. However from the velocity fields shown, it is apparent this indentation in the base is in fact magnified by the bubble further from the axis expanding quicker than the centre, as opposed to a jet forming upward as would be expected in a buoyancy dominated simulation. The far more prominent deformation to the bubble shape is however the observed inward radial jet. Again from the first velocity

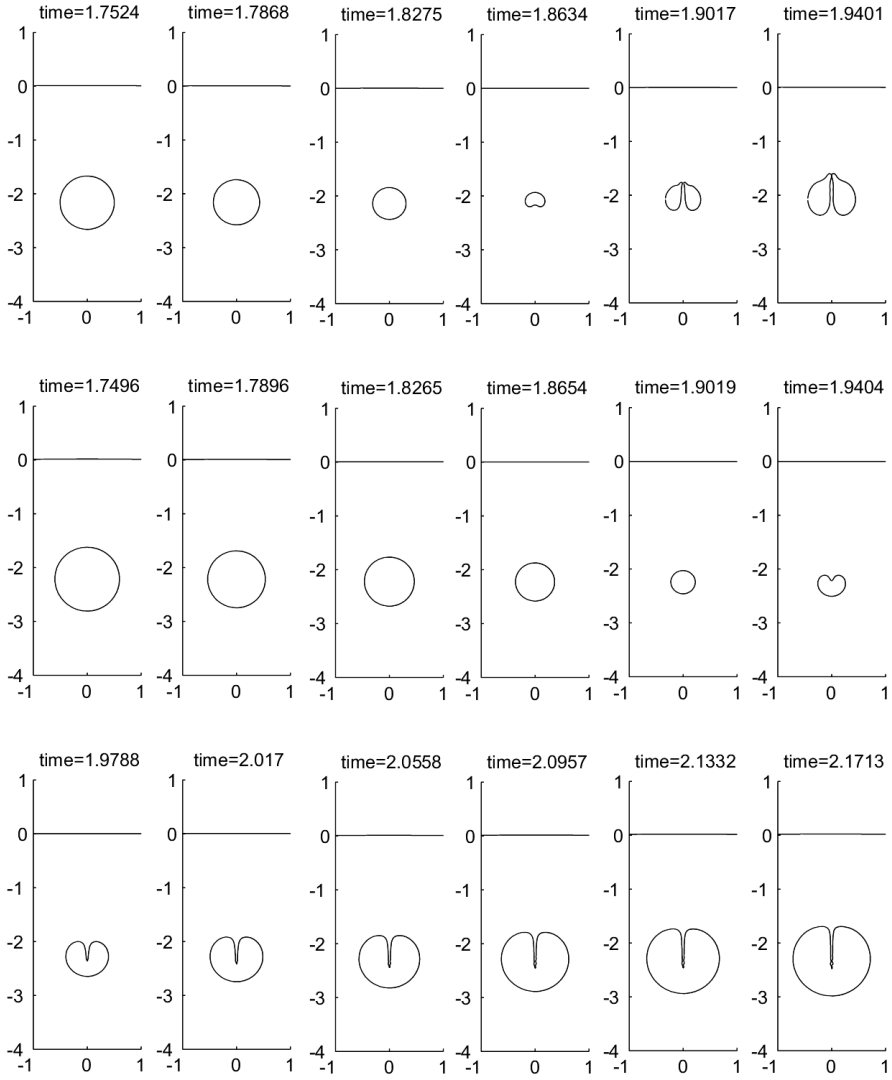

Figure 5.26: Demonstration of buoyancy effects for $\rho = 0.76, h = 2.2$. The first 5 figures show the rebound of the bubble with $\delta = 0.0147$ showing a buoyancy driven jet treading the bubble. The central row show the behaviour at the same times for the corresponding zero buoyancy case, with the final row showing the rebound of this case with no bubble jet impact.

field shown, whilst this may form to a very small degree during the bubble collapse, it is the faster re-expansion of the upper and lower bubble domes that exacerbate its presence. Indeed it is most likely that as the bubble expands the radial jet will not retract sufficiently fast back into the fluid bulk, resulting in a thin annulus of liquid breaking off inside the bubble core. As such this may present a mechanism for small amounts of liquid to enter a predominantly spherical bubble, beneficial for thermally driven chemical reactions. After this happens, the bubble surface perturbations will diminish greatly as the bubble again reaches maximum volume, and will therefore be significantly spherical in shape. It is however unclear as to whether the remaining surface perturbations will be magnified during the subsequent collapse, and if so whether this will be sufficient to cause a significant topological change in the bubble, either through horizontal pinching or vertical jetting.

Increasing the density ratio towards the rigid boundary case leads to vertical elongation with horizontal splitting. This is demonstrated in figures 5.28 and 5.29. For these simulations the density ratio is $\rho = 2$, equivalent to a bubble in carbon-tetra-chloride near a layer of bromine. The bubbles are driven by an initial internal pressure of $\epsilon = 98.49$,and a $\gamma = 1.4$, with zero surface tension on both surfaces and the buoyancy parameter $\delta = 0.05$. The simulations illustrate the transition through the null impulse state, calculated from the spherical model (2.42) to be $h \approx 1.08$. The standoff distances of the bubbles shown are $h = 0.7$, $h = 0.9$ and $h = 1.11$, where the case $h = 0.9$ is in agreement with the similar bubble modelled in [45][1]. For the case $h = 0.7$, the top half of the bubble is initially broader than the lower half due to the effects of buoyancy. However the attractive nature of the denser fluid layer prohibits the movement of the lower half of the bubble, and as such the top half is compressed faster than the lower half. Eventually, the top of the bubble collapses sufficiently for the formation of a bubble jet toward the interface.

[1]In this work, the ratio of specific heats was $\gamma = 1.25$, compared to $\gamma = 1.4$ here.

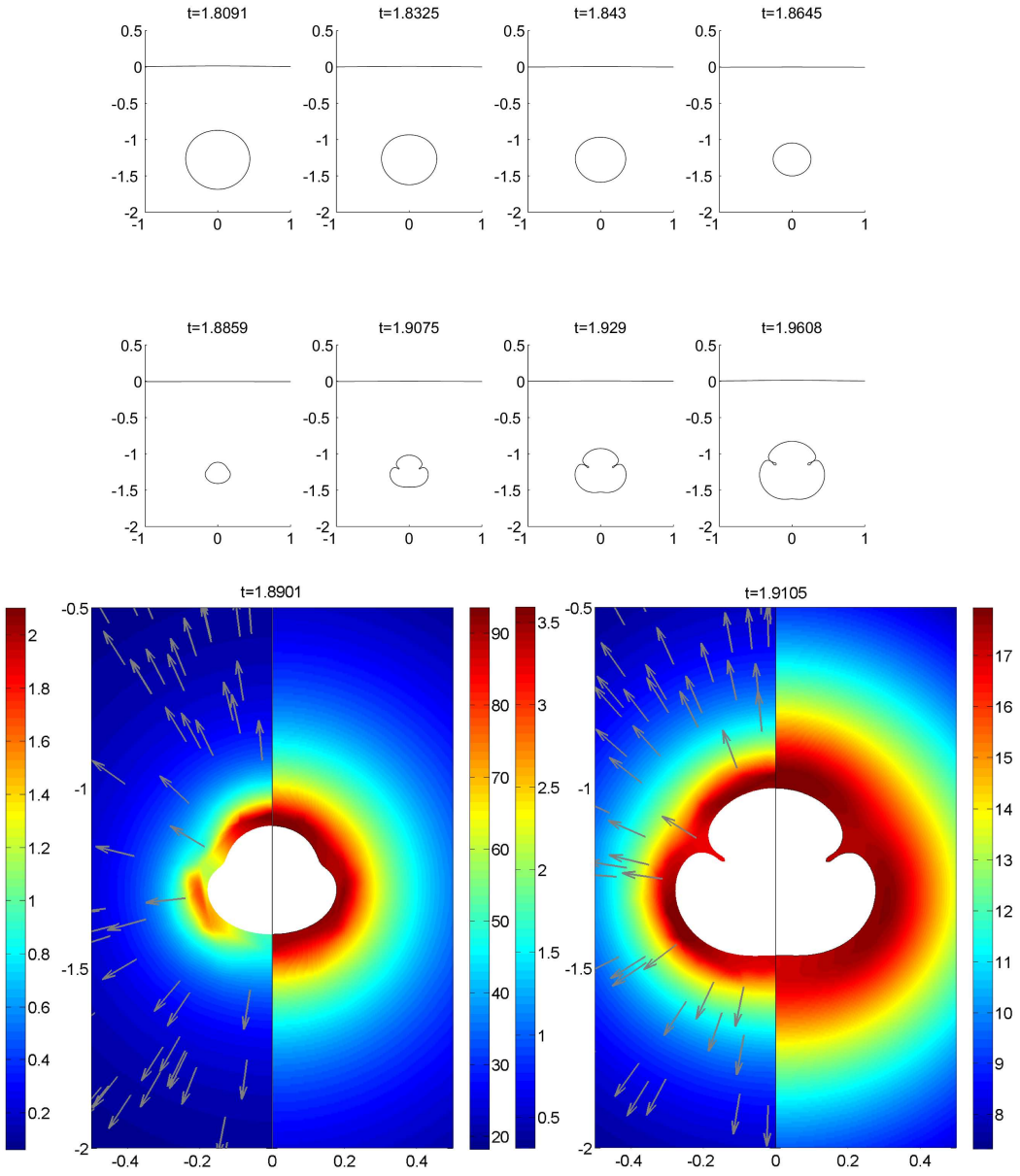

Figure 5.27: Behaviour near the null impulse state for $\rho = 0.76,\ \delta = 0.0147$ at a standoff distance $h = 1.27$ for a bubble characterised by $\epsilon = 100,\ \gamma = 1.4$ and $\sigma_b = 0$. Top images show the bubble shapes throughout the second bubble oscillation. Lower images show the pressure fields near minimum bubble volume at the beginning of the second expansion phase

The collapse behaviour for $h = 1.11$ is initially complementary, with both bubbles having similar shapes at time $t = 1.9$. However the greater distance between the bubble and the denser layer does not drag the lower bubble surface down sufficiently to prohibit the formation of an upwardly directed jet through the action of buoyancy. Nearer the null impulse state at $h = 0.9$, the observed behaviour at the end of the oscillation is significantly different . Instead of forming an axial jet as in the other two cases, the bubble pinches horizontally, with a high pressure ring forming about the bubble and contracting toward the axis. Interestingly, at the time frame shown this bubble is expanding, with the top and base being pulled apart. As can be seen from the velocity directional arrows, the liquid forced away from the poles is being drawn back into the pinching ring, although the speed at the poles is significantly lower. This re-expansion behaviour is in direct contrast to both the case $h = 0.7$ and $h = 1.11$, where the velocity field is seen to be in the collapse phase. The maximum speed of the fluid being pumped inward by the ring is an order of magnitude lower than that observed in the axial jets, which may have an impact on the mixing performance. Should the bubble pinch fully very slender high speed jets may form in opposing axial directions through the two daughter bubbles, as has been observed in some previous experiments and simulations [18, 9].

The pressure fields presented show no increased pressure regions along the axis, and the resultant lack of jetting is as expected about the null impulse. Significantly high pressures arise in the vicinity of the pinch, triple the pressure of the bubble at initiation. Clearly the bubble does not remain spherical, nor the fluid-fluid interface unperturbed at these standoff distances, yet the the spherical model still roughly predicted the migration of the bubble.

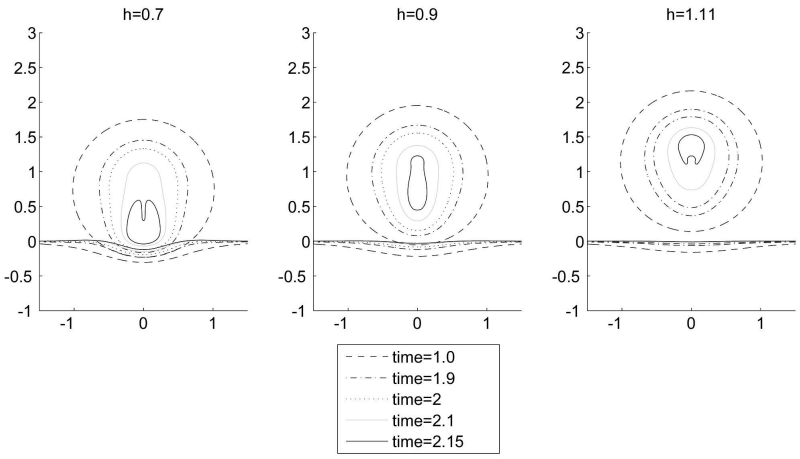

Figure 5.28: Shapes of bubbles characterised by $\epsilon = 98.56,\ \gamma = 1.4,\ \sigma_b = 0,\ \sigma_I = 0$, with buoyancy $\delta = 0.05$ and at standoff distances $h = 0.7$ (left), $h = 0.9$ (centre) and $h = 1.11$ (right). The central case shows the null impulse pinching behaviour, in agreement with the results in [45].

5.6 Chapter summary

This chapter has compared the implementation of the boundary integral method detailed in Chapter 3 against both analytic and experimental test cases. Evaluation of the interpolation of the surfaces has shown clear benefit in using quintic splines over cubic splines. Curvature calculation through noise loaded data has been shown to be best performed using least squares fitted polynomials and not either the quintic or cubic splines due to the tendency of these methods to amplify small perturbations as the derivative order is increased.

Comparison with spherical droplet perturbations has shown the RK4 time-stepping regime to be more stable than the Eulerian method, although the Eulerian method has been shown to be stable with sufficiently small time steps. Comparisons with the Rayleigh-Plesset equation with and without the fluid-fluid interface have also shown excellent agreement.

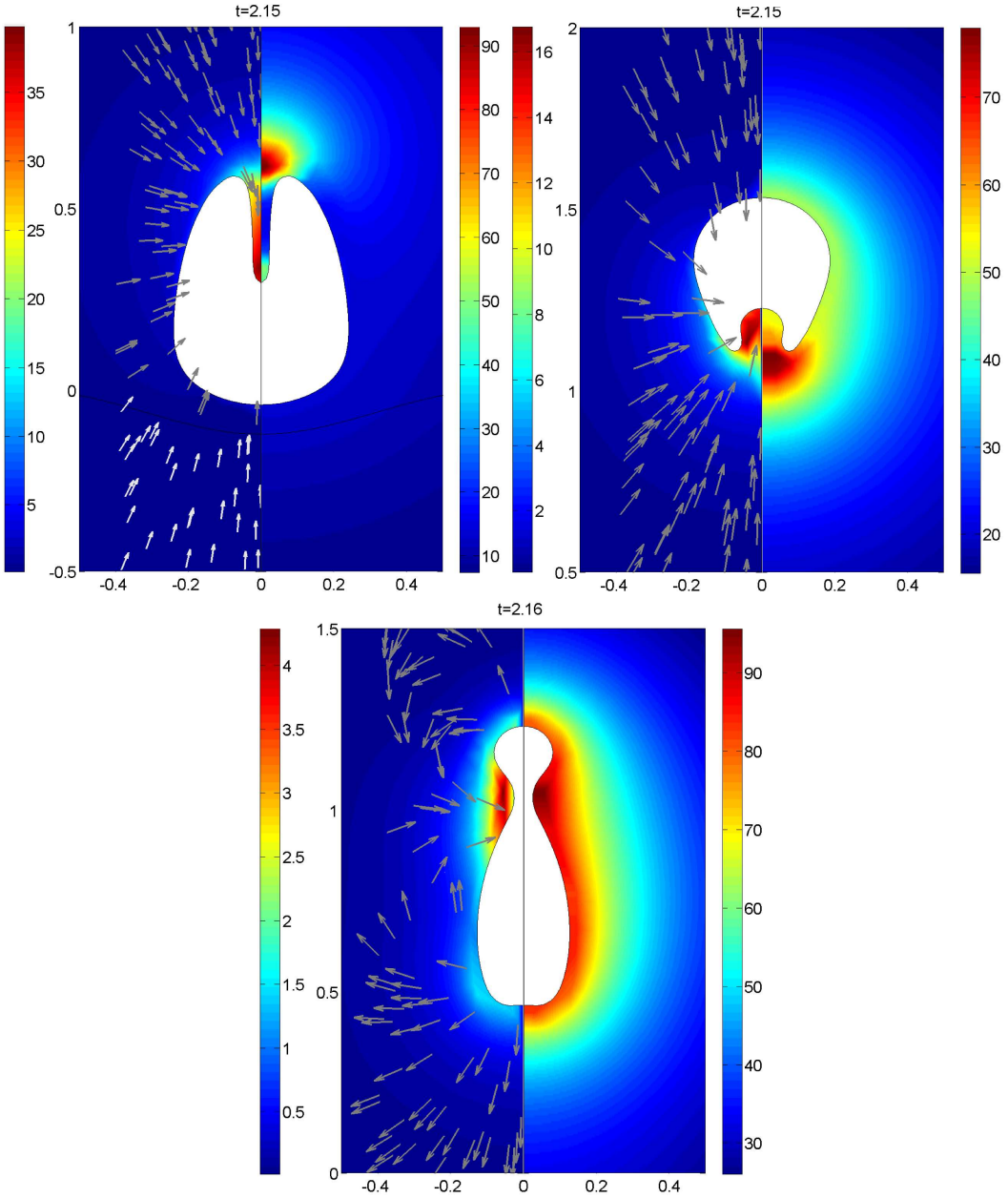

Figure 5.29: Pressure and speed fields with velocity directed arrows for bubbles characterised by $\epsilon = 98.56$, $\gamma = 1.4$, $\sigma_b = 0$, $\sigma_I = 0$, with buoyancy $\delta = 0.05$ and at standoff distances $h = 0.7$ (top left), $h = 1.11$ (top right) and $h = 0.9$ (lower).

BIM simulations with $\rho = 0, \rho \to \infty$ and $\rho = 0.76$ are also in excellent agreement with experiments involving free surfaces, rigid boundaries and a water/white spirit interface at appropriate standoff distances respectively. They have also been shown to be in agreement with previous works regarding bubble interactions with two fluid interfaces. As such it is safe to conclude the numerical implementation is accurate and correct and may be used to examine the flow dynamics as the parameter space is investigated. This is done throughout the following chapters in a variety of meaningful situations.

Chapter 6

Single bubble interactions with the two fluid interface

This chapter will investigate the behaviour of a single cavitation bubble in close proximity to the two fluid interface. A variety of moderate standoff distances are investigated first to gain insight into the potential variations in non-spherical bubble behaviour. Shallow standoff distances are then chosen as these may lead to significant surface deformations, crucial in both biomedical and industrial applications. The bubbles investigated are initiated with high internal gas pressure, $\epsilon \gg 1$, and as such are representative of the type generated using laser or spark based methods. The strength parameter $\epsilon = 100$ is chosen in most examples to allow for extended simulations of the toroidal phases. Larger values have also been tested, although the minimum volumes associated with these can create numerical issues, and may cause the toroidal bubble to reconnect at a comparably earlier time. The dimensional length scales are presumed large enough to ignore surface tension, although a small amount is included for the period immediately after jet impact. The bubbles are also considered to be small enough to ignore the influence of gravity, or may be considered to be in a free fall environment. A typical bubble radius would therefore be $R_{max} \sim O(mm)$, as in this scale in water, both $\sigma_b \sim O(10^{-4})$ and $\delta \sim O(10^{-4})$. These

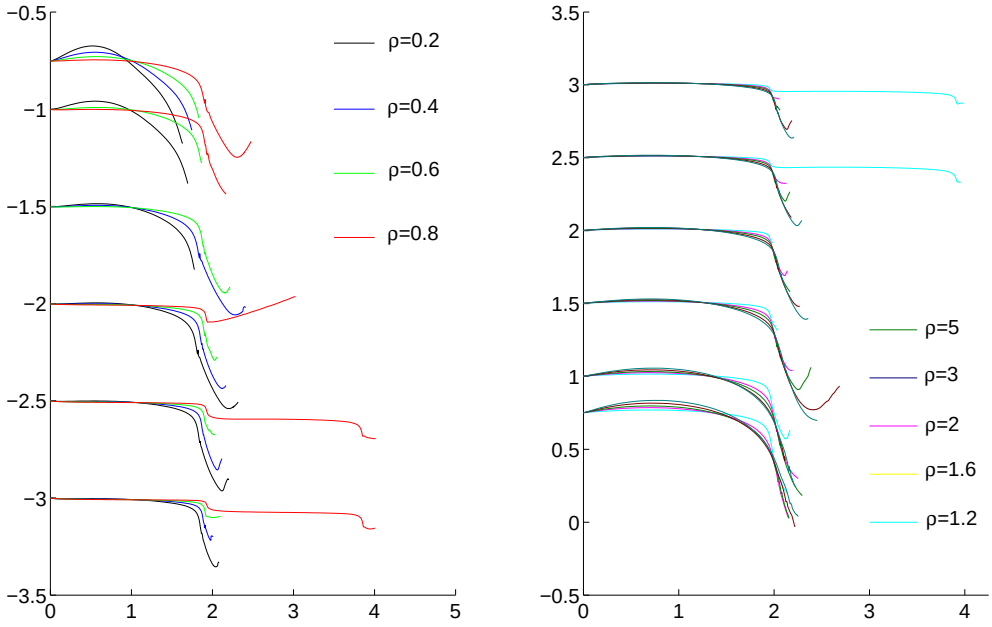

Figure 6.1: The location of the bubble centroid as the standoff distance and density ratio are altered. The left image shows repulsion from the interface for $\rho < 1$, whereas the right image shows attraction to the interface for $\rho > 1$.

assumptions are made as one seeks to investigate the influence of the fluid-fluid interface on the bubble, and not the influence of any exterior forces.

6.1 Standoff distance effects on bubble behaviour

The effect variations in standoff distance can have on the behaviour of both a bubble and a free surface have been well documented in the literature. In the context of the two fluid interface this may have a significant impact, particularly in the context of mixing applications where the level of surface deformation can greatly affect reaction rates.

Figure 6.1 shows the location of the bubble centroid through time, for the density ratios $\rho \in \{0.2, 0.4, 0.6, 0.8, 1.2, 1.6, 2, 3, 5\}$, at the standoff distances $h = 0.75,\ 1,\ 1.5,\ 2,\ 2.5$ and 3. The two graphs have been orientated so that the denser fluid layer is at the base, and hence the interface is above the bubble for $\rho < 1$ and below the bubble for $\rho > 1$. The

simulations are stopped when either the time step is below the set threshold of 10^{-6} for 2000 steps, or a time of $t = 4$ is reached. Additionally the simulations may be stopped if any two surfaces cross, or a non-axial bubble jet impact occurs. From the Kelvin impulse analysis in Chapter 2, one expects the centroid to be repelled and attracted in accordance with the sign of the Atwood number. This is indeed in general the case, at least over an entire oscillation before toroidal effects become apparent. However, it can be observed that the centroid behaves in the opposite manner to that anticipated from the spherical analysis during the first expansion of the bubble, particularly at shallower standoff distances as the density ratio approaches the extremes of the Atwood number.

The displacement of the bubble centroid is primarily affected by the non-spherical jetting phenomena. This is apparent in all simulations, evidenced by the sudden alteration to the centroid location during the collapse phase of the bubble. The effect the density ratio has on the time to jetting may also be readily observed by this behaviour, with simulations with density ratios closest to unity displaying a prolonged existence before this onset. During the toroidal phase in several simulations, there is a late change in the direction of the movement of the bubble centroid. This is due to the rear of the bubble expanding more spherically than the front, as the front is dragged into an elongated shape by the threading jet as is clearly demonstrated in figures 6.2 and 6.3. These show the bubble shapes at various time intervals for $\rho \in \{0.2, 0.4, 0.6\}$ and $\rho \in \{1.6, 2, 5\}$ respectively, with the image mapped so that the initial location of the centroid is (0,0).

It is of particular interest to observe the difference in toroidal behaviour displayed as the standoff distance and density varies. For example, the bubble toroid with $\rho = 0.2,\ h = 3$ forms a more slender snout than at shallower standoff distances. This is repeated for $\rho = 0.4$, yet for $\rho = 0.6$ the bubble jet failed to impact on the opposing wall in the standoff case $h = 3$.

In the simulations contained in figure 6.3, one observes more variation in both the

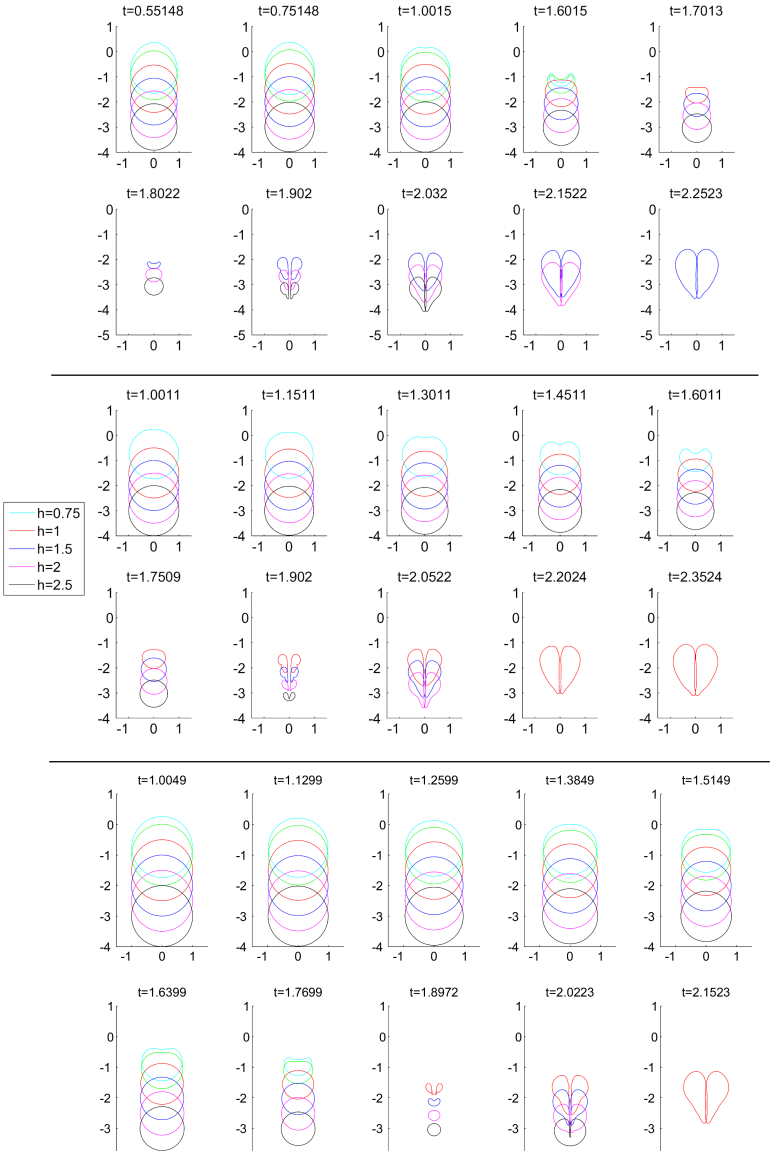

Figure 6.2: Bubble shapes at various times for $\rho = 0.2$ (top two rows), $\rho = 0.4$ (central two rows) and $\rho = 0.6$ (lower two rows). All bubbles have $\epsilon = 500$, with zero tension on both the bubble surfaces and two fluid interface (not shown). Standoff distances are $h = 0.75$ (cyan), $h = 1$ (green), $h = 1.5$ (red), $h = 2$ (blue), $h = 2.5$ (magenta) and $h = 3$ (black).

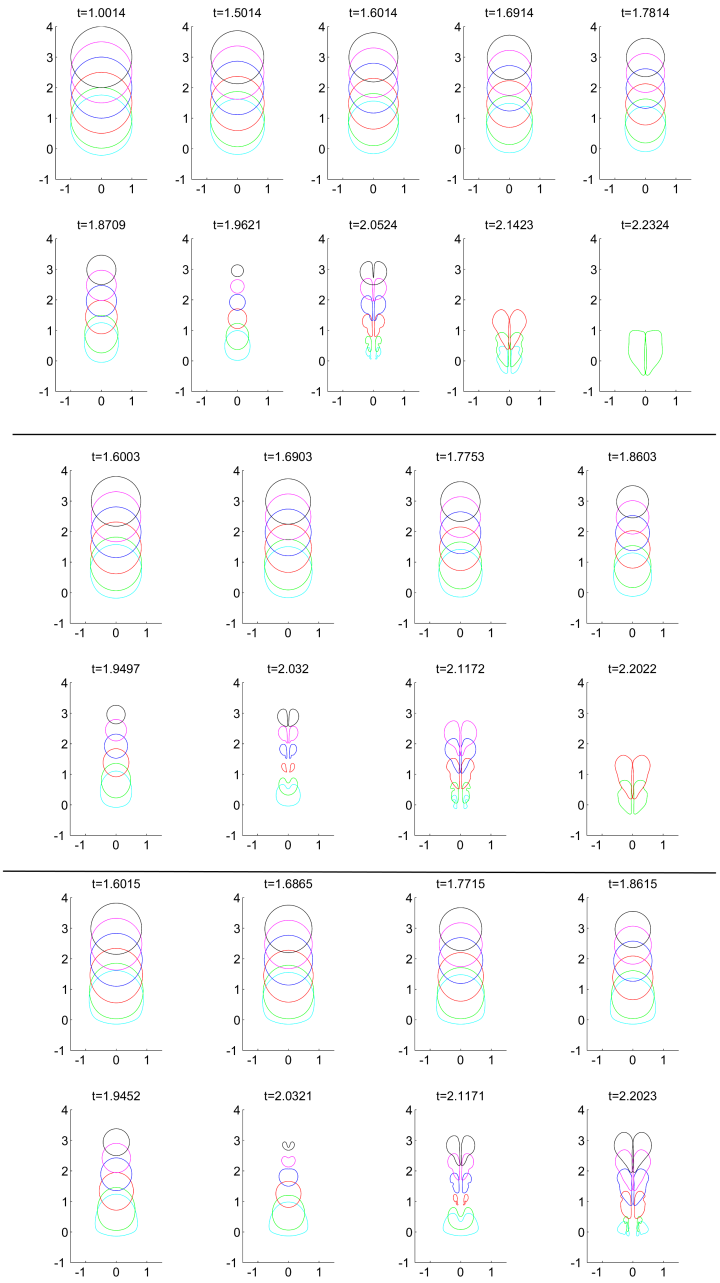

Figure 6.3: Bubble shapes at various times for $\rho = 1.6$ (top two rows), $\rho = 2$ (central two rows) and $\rho = 5$ (lower two rows). All bubbles have $\epsilon = 500$, with zero tension on both the bubble surfaces and two fluid interface (not shown). Standoff distances are $h = 0.75$ (cyan), $h = 1$ (green), $h = 1.5$ (red), $h = 2$ (blue), $h = 2.5$ (magenta) and $h = 3$ (black).

singly and doubly connected phases. Unlike the simulations in figure 6.2, the bubbles acting under the influence of $\rho \in \{1.6, 2, 5\}$, at standoff distances below 1.5 maximum radii, migrate sufficiently far to become entrained into the interface. Such entrainment results in the flattening of the lower side of the bubble, and a subsequent delay in the time to jet formation. This flattening increases with ρ as anticipated by the known behaviour near a rigid wall. Such behaviour then impacts on the toroidal phases, with bubbles at greater standoff distances developing a slender protrusion at the fore, whilst at lower standoff distances the development of the frontal lobe is inhibited, and a disturbance is seen to propagate about the bubble toward the rear. As mentioned the attraction toward the interface is significantly accelerated during the jetting phase, as may be seen in figure 6.1. Indeed the translation in the centroids in the shallower standoff cases end below the initial location of the two fluid interface.

As the density ratio nears unity, and particularly as the standoff distance increases, one expects the bubbles to behave in a more spherical manner. This is the case for $\rho = 0.8$ and $\rho = 1.2$ at sufficient standoff distances. From figure 6.1, one observes that for both these density ratios, at a standoff distance greater than two maximum bubble radii, the bubbles are able to rebound throughout two complete oscillations. Non-spherical effects are still apparent however, as at the end of the first oscillation the centroid locations are shifted away and toward the interface respectively. This is however by a significantly smaller amount than that observed for other density ratios, and over a shorter time period. As may be seen in figure 6.4, in these cases jet impact does not occur. Jet formation does occur at $h = 2$ with $\rho = 0.8$ very late in the collapse phase, although the bubble rebounds too rapidly to become toroidal. During the re-expansion phase, this jet continues to elongate, becoming progressively thinner and less stable. At the greater standoff distances, the rebound of the bubble is almost spherical. Any non-spherical perturbations at the end of the first oscillation almost disappear as the bubble re-expands

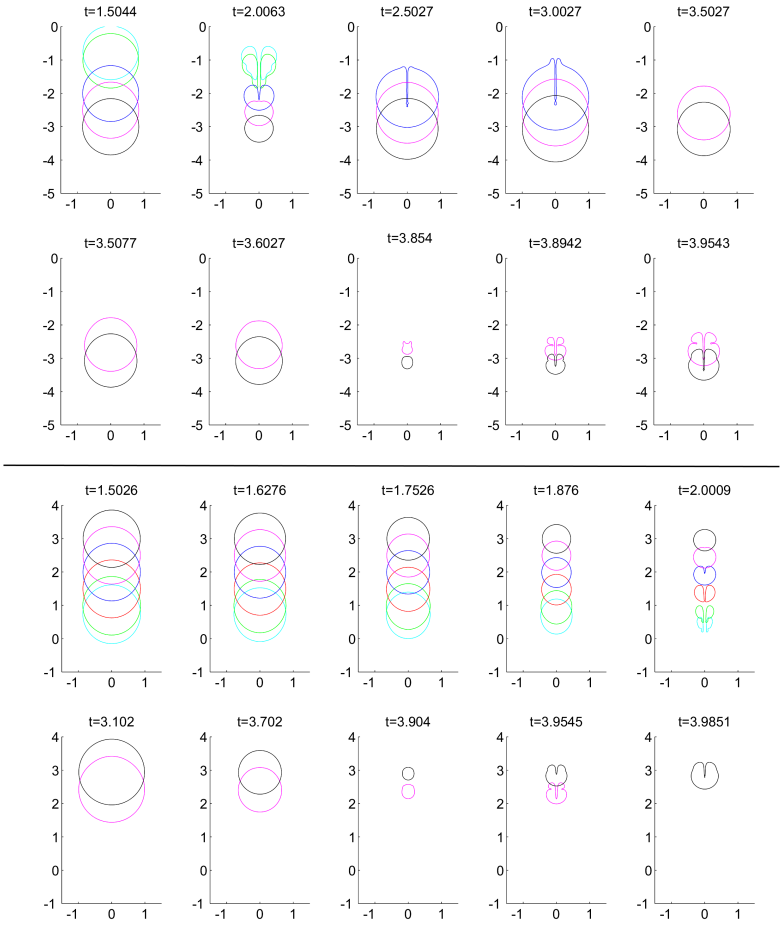

Figure 6.4: Bubble shapes during the first and second collapse for $\rho = 0.8$ (top two rows), and $\rho = 1.2$ (lower two rows). All bubbles have $\epsilon = 500$, with zero tension on both the bubble surfaces and two fluid interface (not shown). Standoff distances are $h = 0.75$ (cyan), $h = 1$ (green), $h = 1.5$ (red), $h = 2$ (blue), $h = 2.5$ (magenta) and $h = 3$ (black).

to maximum volume. In the second collapse however, these perturbations are magnified. Axial jet formation is observed, as well as a pinching motion in toward the jet. Again in both cases visualised here, the primary axial jet does not impact, and the bubble re-expands into a third oscillation. In contrast, the simulations for $h \leq 1.5$ all became toroidal during the first oscillation, and rebounded in a very aspherical manner.

In the case $\rho = 1.2$, at standoff distances greater than 2, no significant jet formation is seen during the first oscillation. Even during the second collapse phase jet formation only

occurs near minimum bubble volume, and does not impact on the opposing bubble side. Additionally, a ring deformation appears, pinching inwards toward the jet. In both cases shown here this does not impact with the jet, and the bubble is able to rebound again in a connected manner. It may be postulated that in subsequent rebounds this may be magnified, and resultantly one may envisage this bubble splitting into smaller fragments. The ability to maintain sphericity throughout two oscillations is important, particularly for sonochemical processes. It allows for greater temperatures to be obtained in the centre of the bubble, as energy is not dissipated through both jet formation and impact. However if the aim is to mix the two fluids, it may be more important to maximise the perturbation to the fluid-fluid interface. This is greatest in this case for the lower standoff distances, both through the initial expansion of the bubble, and through the interaction of the interface with the toroidal bubble jet.

The curves in figure 6.5 represent the z co-ordinate of the axial node on the fluid-fluid interface for the same simulations. The most substantial factor affecting this during the first oscillation is the standoff distance, as the expansion of the bubble toward maximum volume and consequently maximum surface deformation, is roughly spherical at standoff distances of unit order, even at the extremes of both free surface ($\rho = 0$) and rigid boundary ($\rho \to \infty$) simulations. In all the simulations shown here, it is apparent that a denser second layer will retard the deformation of the interface, again as one may expect as the density ratio increases towards solid boundary behaviour. Whilst the behaviour during the first oscillation is in agreement with what one may expect from spherical models, in some cases the behaviour as the bubble begins to rebound is not. In particular, when the bubble is in the less dense layer at shallower standoff distances, one observes a drastic increase in the surface deformation. This is due to the threading jet of the bubble flowing up into the interface as opposed to away from it. In contrast however, it is known that at very shallow standoff distances, a free surface will form a significant counter jet to the

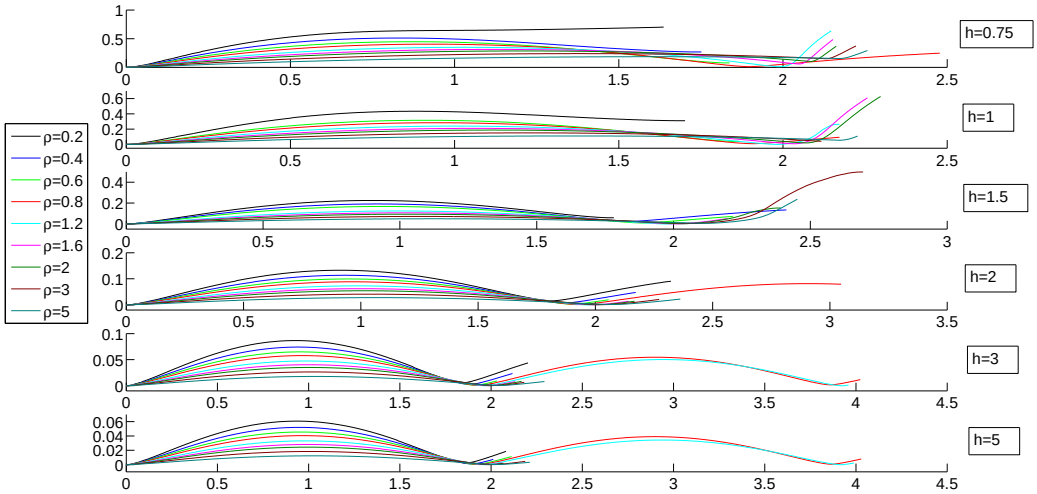

Figure 6.5: The z co-ordinate of the axial fluid-fluid interface node as influenced by a single cavitation bubble at various density ratios for standoff distances (from top to base) $h = 0.75, 1, 1.5, 2, 2.5, 3$.

bubble jet. It is therefore worth investigating which type of jetting behaviour is most efficient at disturbing the fluid-fluid interface.

6.2 Interfacial spiking at low density ratios

The experiments of Gibson and Blake [36], as shown in figure 5.21, show the distinct formation of a surface spike generated by a single bubble at a standoff distance of $h = 0.56$. Should this behaviour be repeated for greater sub-unity density ratios, it would provide an effective mixing mechanism. From the following results, one demonstrates that this only occurs for $0 \leq \rho \lesssim 0.4$ at $h \approx 0.5$. Figure 6.6 illustrates the evolution of this spike as the density ratio is increased. It is most pronounced in the well known free surface case, $\rho = 0$, where a tall slender spike is formed in the opposing direction to the bubble jet. At the initiation of the bubble jet, the fluid-fluid interface forms a spike at the axis, with the bubble itself becoming entrained and ovoidal in shape. The bubble jet formed is also thin, with the tip of the bubble jet moving considerably faster than the tip of

the fluid-fluid interface spike. Jet formation occurs during the expansion phase of the bubble, at a non-dimensional time $t \approx 0.4$. The collapsing bubble and the repulsiveness of the free surface allow for the substantially raised interface to fall everywhere except the spike, which continues unabated. Jet impact on the opposing bubble wall occurs when the bubble is still largely inflated. The corresponding impact time is in fact close to the half life of a spherical bubble at $t = 1.1$. The high curvature of the slender bubble jet results in an axial impact, and so this simulation is continued into the toroidal phase. The anticipated forward lobe of the bubble is generated, with the circular disturbance rolling up the sides of the bubble. This pinches the bubble into two toroids at $t \approx 1.3$, at which point the subsequent fluid motion can not be modelled using this approach due to the formation of a definite vortex sheet. The surface spike grows continually, with a final height approaching four maximum bubble radii.

By increasing the density ratio toward $\rho = 0.2$, applicable to a bromine-butane or iodine-water interface, it is immediately clear that increasing the density of the second layer has a negative effect on the surface spike. The first new feature is that the two fluid interface does not become as hyperbolic as the free surface case. This creates a broader spike tip as the bubble jet begins to form, although the width of the jet itself is comparable at the same time frame. This spike formation again happens during the expansion phase of the bubbles, at the later time of $t \approx 0.6$ for $\rho = 0.1$. As jetting continues, the height of the spike is substantially decreased compared to the free surface example, with the formation of a bulbous head as liquid is pumped upward. The speed at which the spike increases in height also decreases with ρ increasing. The curvature of the bubble jet tip lessens as ρ increases, although in both these cases it is still sufficiently high in comparison to the lower bubble wall to impact along the axis. This occurs at $t \approx 1.25$ for $\rho = 0.1$, and at $t \approx 1.45$ for $\rho = 0.2$. The remaining simulated toroidal behaviour matches that of the free surface qualitatively, with the formation of the advancing lobe. The bubble volume

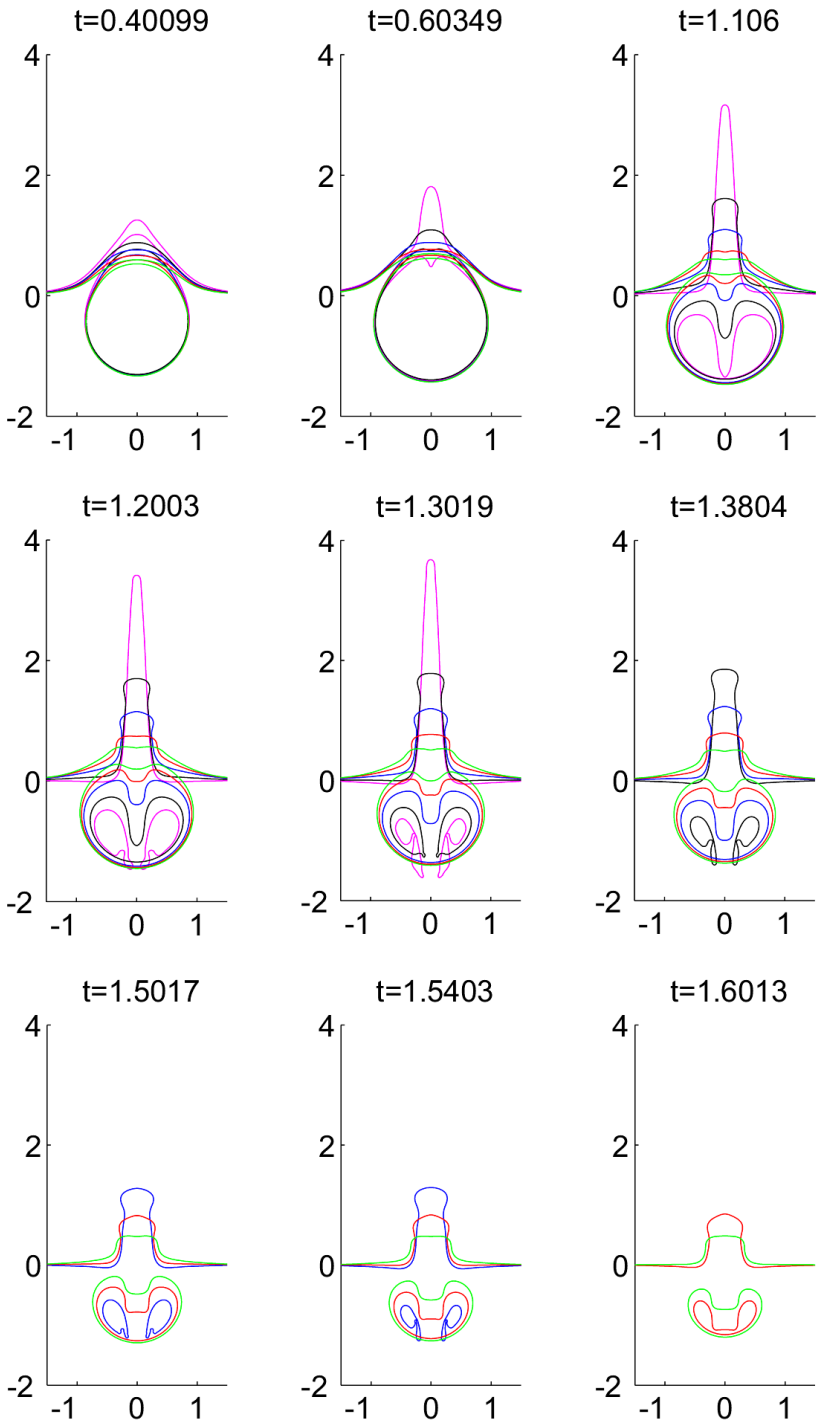

Figure 6.6: The evolution of the bubble and fluid-fluid interface for density ratios in the region where surface spiking is observed ($h = 0.5$). Magenta corresponds to $\rho = 0$, black to $\rho = 0.1$, blue to $\rho = 0.2$, red to $\rho = 0.3$ and green to $\rho = 0.4$.

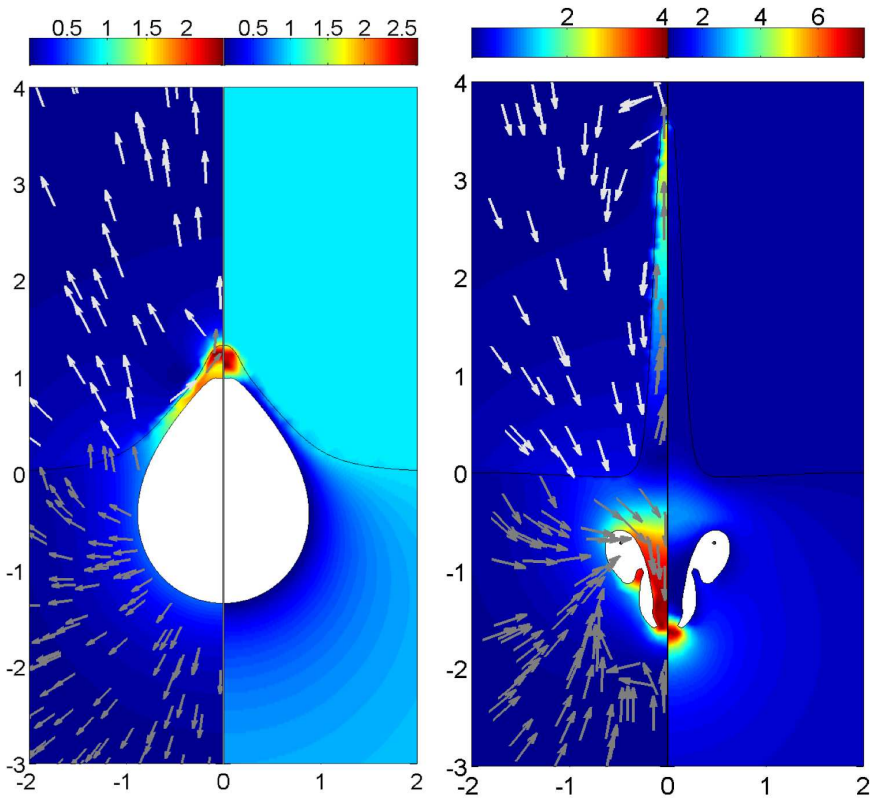

Figure 6.7: Pressure and velocity fields for a bubble simulation with $\epsilon = 100$, $\gamma = 1.4$, $\sigma_b = \sigma_I = 0$, $\rho = 0$, with a standoff distance $h = 0.5$. Time frames are taken at jet initiation $t = 0.4$ (left) and nearing toroidal bubble pinching $t = 1.26$ (right).

is markedly less during this period as it occurs later in the collapse phase. The pinching into two toroids occurs at $t \approx 1.38$ for $\rho = 0.1$ and $t \approx 1.54$ for $\rho = 0.2$, implying the time interval between the first and second toroidal formations decreases with increasing ρ. The height of the spike throughout in both cases is also continually increasing.

Further to this, the behaviour of fluid inside the spike provides some insight into the mixing potential of spike formation. Whilst in the absolute limit no incompressible liquids could obtain this density ratio, the behaviour of the second fluid layer is still of interest as a comparative base to the subsequent results at higher density ratios. Specifically, as is observed in the toroidal time frames in figures 6.7 and 6.8, the spike may contain a stagnation point, with fluid at the tip and base of the spike flowing in different directions. This may eventually lead to jet breakup, with a droplet of the denser fluid snapping off inside the lighter fluid. As well as this, one observes that the jump in speed across the two fluid interface can be significant. By necessity, this is due entirely to the difference in tangential velocities, and implies that at these low density ratios one would expect additional hydrodynamic instabilities to form along the separating vortex sheet. This jump in tangential velocity is dampened by increasing the density ratio toward unity, as one would expect. These images also show that the tangential velocity can be much higher than the normal velocity, particularly along the sides of the spike, and also when the bubble is near maximum volume. This observation implies that the non-linear terms present in equation (3.24) will play a significant role when the bubble is at a close standoff distance, and should in these cases not be neglected as in [45] where only greater standoff distances were investigated.

This trend continues somewhat as ρ increases towards $\rho = 0.4$. The level of ovoidicity decreases further, with the increasing density of the lighter layer causing the top edge of the bubble to be flatter. The onset of bubble jetting is delayed further, and now occurs during the collapse phase. The threading jets are broader than at lower ratios, with flatter

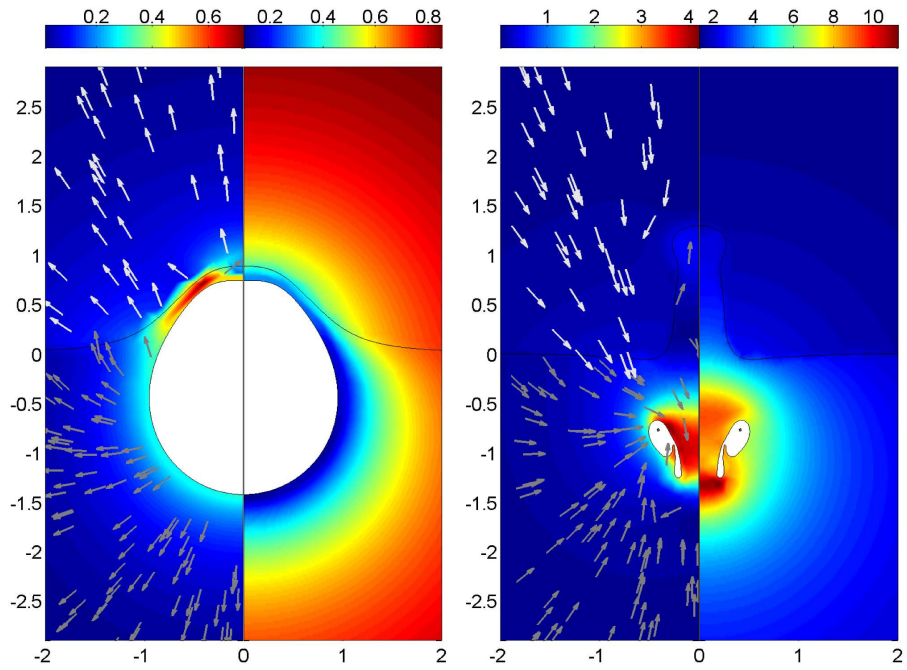

Figure 6.8: Pressure and velocity fields for a bubble simulation with $\epsilon = 100$, $\gamma = 1.4$, $\sigma_b = \sigma_I = 0$, $\rho = 0.2$, with a standoff distance $h = 0.5$. Time frames are taken near to jet initiation $t = 0.6$(left) and nearing toroidal bubble pinching $t = 1.56$ (right).

tips. This increased tip flatness is sufficient in the case $\rho = 0.4$ to cause an impact over an annular region, and not at a single point located upon the axis of symmetry. It is therefore possible that subsequently, the bubble will be split into a toroidal and a simply connected component. The simply connected component would most likely be forced further away by the bubble jet, and so the bubble may not be able to re-connect during the expansion phase. This in turn would further retard the deformation of the fluid-fluid interface through the action of bubble expansion during future oscillations.

It is debatable as to whether spike formation occurs for these instances, at least in the same manner as for lower ρ values. The inflation of the bulbous head is again observed for $\rho = 0.3$, yet for $\rho = 0.4$, applicable to a bromine-propanol interface, this does not appear to happen. As can be observed by the velocity field in the later frame of figure 6.9, the speed about the top of the incursive jet is near zero. In contrast the velocity around the

bend in the interface deformation is closer to 1.5 non-dimensional units in the direction of the bubble. This implies that as opposed to lower density ratios, the surface spike here is formed by fluid collapsing about the deformation at maximum bubble volume, and not through the pumping of fluid into the lighter layer by the counter jet.

6.3 Interfacial indentation

Once the density ratio is great enough to prohibit spike formation, the regime of surface mounding and indentation occurs. Shape profiles for this behaviour are seen in figure 6.10 for the density ratios $\rho = 0.5, 0.6, 0.7$ and 0.8, relevant to the mixing of a large number of liquids. In each case the fluid-fluid interface falls from its maximum elevation as the bubble collapses, unlike in the previous spiking behaviour. The formation of the bubble jet occurs after the bubble half-life during the collapse phase. The bubble jets are all broad, with a decreasing jet thickness corresponding to the bubble volume at the time of jet formation. The tip curvature in all cases is flatter than the approaching lower bubble surface, and so in each case the bubble impacts over an annulus and not at the axis, as occurred for $\rho = 0.4$.

As the bubble jets, the centre of the fluid-fluid interface is dragged downwards. As can be seen in figure 6.11 showing the pressure and velocity in the second layer for $\rho = 0.5$, a higher pressure region forms at the axis, forcing fluid into the center of the deformation. The fluid to the sides then falls inwards as the bubble contracts in volume, leaving the stump shape with a high pressure region at its base. The velocity field also shows how liquid flowing downwards along the axis is forced sideways by the denser liquid, which may accelerate the collapse of the sides.

This indentation behaviour is coupled with a progressive widening of the bubble jet. In figure 6.12, this is due to the transference of the region of highest pressure from above the two fluid boundary, to below it. The initially fastest part of the threading jet is the jet

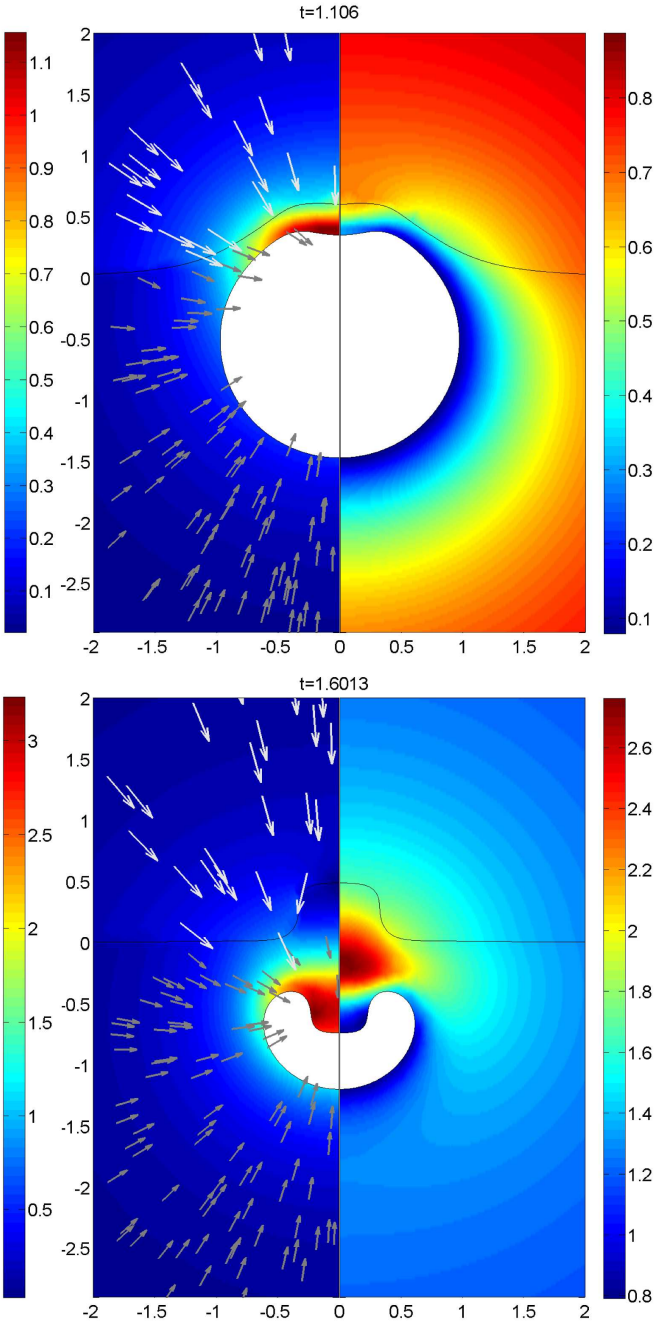

Figure 6.9: Pressure and velocity fields for a bubble characterised by $\epsilon = 100$, $\gamma = 1.4$, $\sigma_b = 0$, at a standoff distance of $h = 0.5$ from a two fluid interface with density ratio $\rho = 0.4$. Frames are taken near maximum bubble volume, $t = 1.1$, and during bubble jetting, $t = 1.6$.

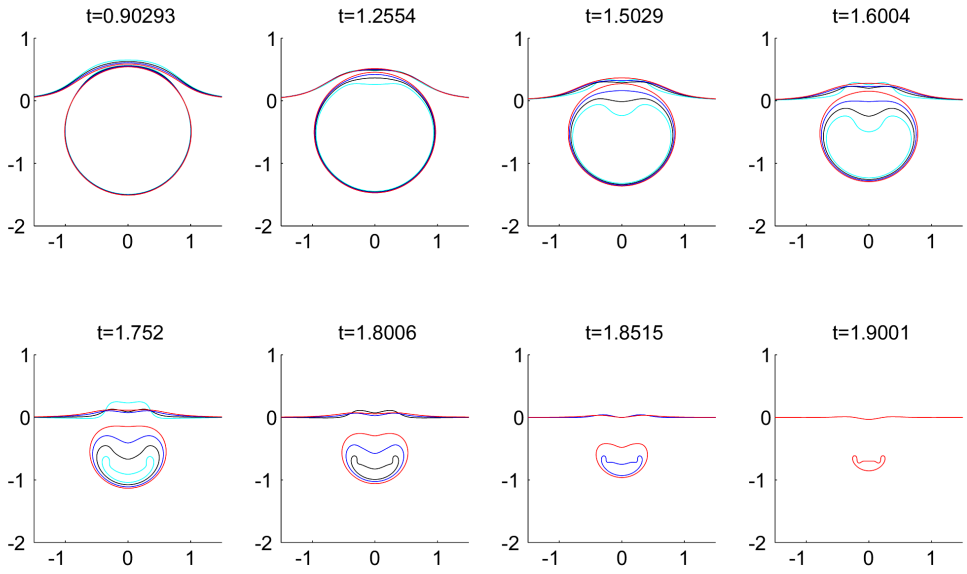

Figure 6.10: Single bubble behaviour in the surface mounding region. The bubble is characterised by $\epsilon = 100$, $\gamma = 1.4$, with zero surface tension and is initiated at $h = 0.5$. The density ratios supported by the interface are $\rho = 0.5$ (cyan), $\rho = 0.6$ (black), $\rho = 0.7$ (blue) and $\rho = 0.8$ (red).

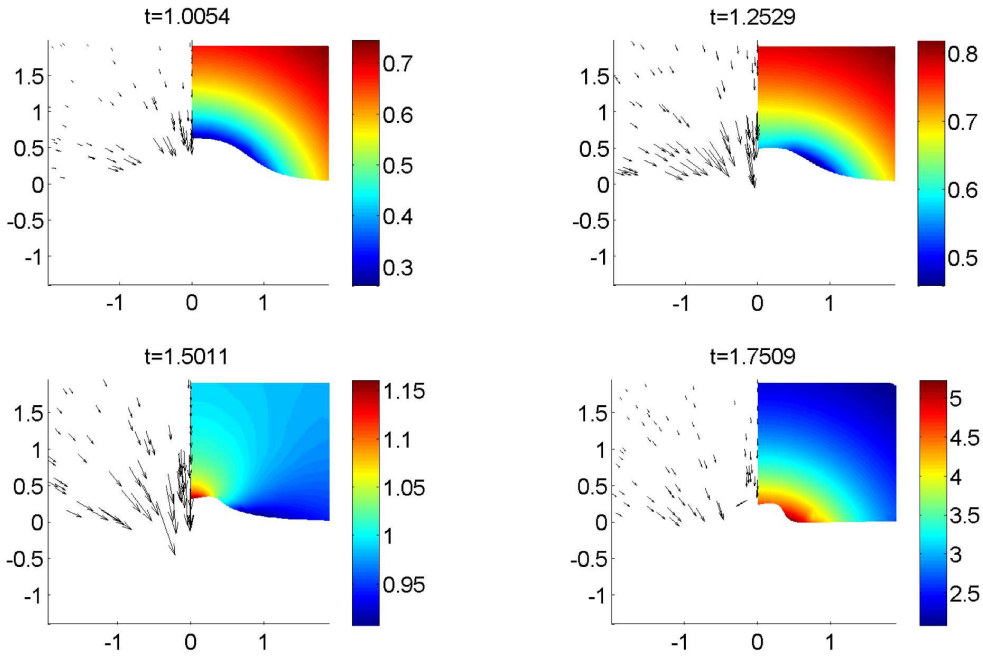

Figure 6.11: Pressure and velocity fields in the second fluid layer during the collapse phase for a bubble initiated at $h = 0.5$ from a two fluid interface with density ratio $\rho = 0.5$. The bubble is characterised by, $\epsilon = 100$, $\gamma = 1.4$ with zero surface tension.

tip. This is driven by the raised pressure region above the indentation with a magnitude of approximately 1.2. As the bubble collapses, this region of high pressure translates downward into the denser liquid layer. This causes the side of the jet to gain a slightly higher velocity, approximately 0.4 non-dimensional units faster than the jet tip. As the widening continues, this difference in velocity increases to the case where the edge of the jet is moving 33% faster than the jet tip. The region of highest pressure is now also found about a ring above the highest point of the bubble and not at the axis. This is due partly to the greater mass of fluid above the side of the bubble than the centre resultant of the surface mounding. Naturally, this will now continue to drive the edge of the jet faster than the centre, and it is due to this that the jet does not impact at a single point.

6.4 Behaviour as the density ratio approaches unity

As the density ratio approaches 1, directly relevant to the behaviour of many liquids with water, the fluid dynamics should approach that of a bubble in an infinite fluid. The remaining non-spherical behaviour can still cause significant deviation from this, particularly as toroidal effects become apparent. Figure 6.13 shows the bubble shapes associated with the density ratios $\rho \in \{0.9, 0.95, 1\}$, from a non-dimensional time $t = 1.88$, approaching the spherical bubble lifetime. The dynamics before this time are nearly identical as would be expected, with minimal centroidal displacement and surface perturbation in the non-unity cases. As expected however, the case $\rho = 0.9$ shows the greatest deviation from the spherical bubble in the first oscillation, as may be seen in the first frame shown where the onset of non-spherical effects is at a more advanced stage than for the case $\rho = 0.95$. The shapes corresponding to these ratios are of particular interest as they demonstrate how jet impact may occur after the bubble has rebounded. In both cases, the jet in the collapsing bubble suffers an axial concavity, as occurred for $\rho = 0.8$. Before this impacts on the opposing bubble wall, they enter the second expansion phase. One may clearly

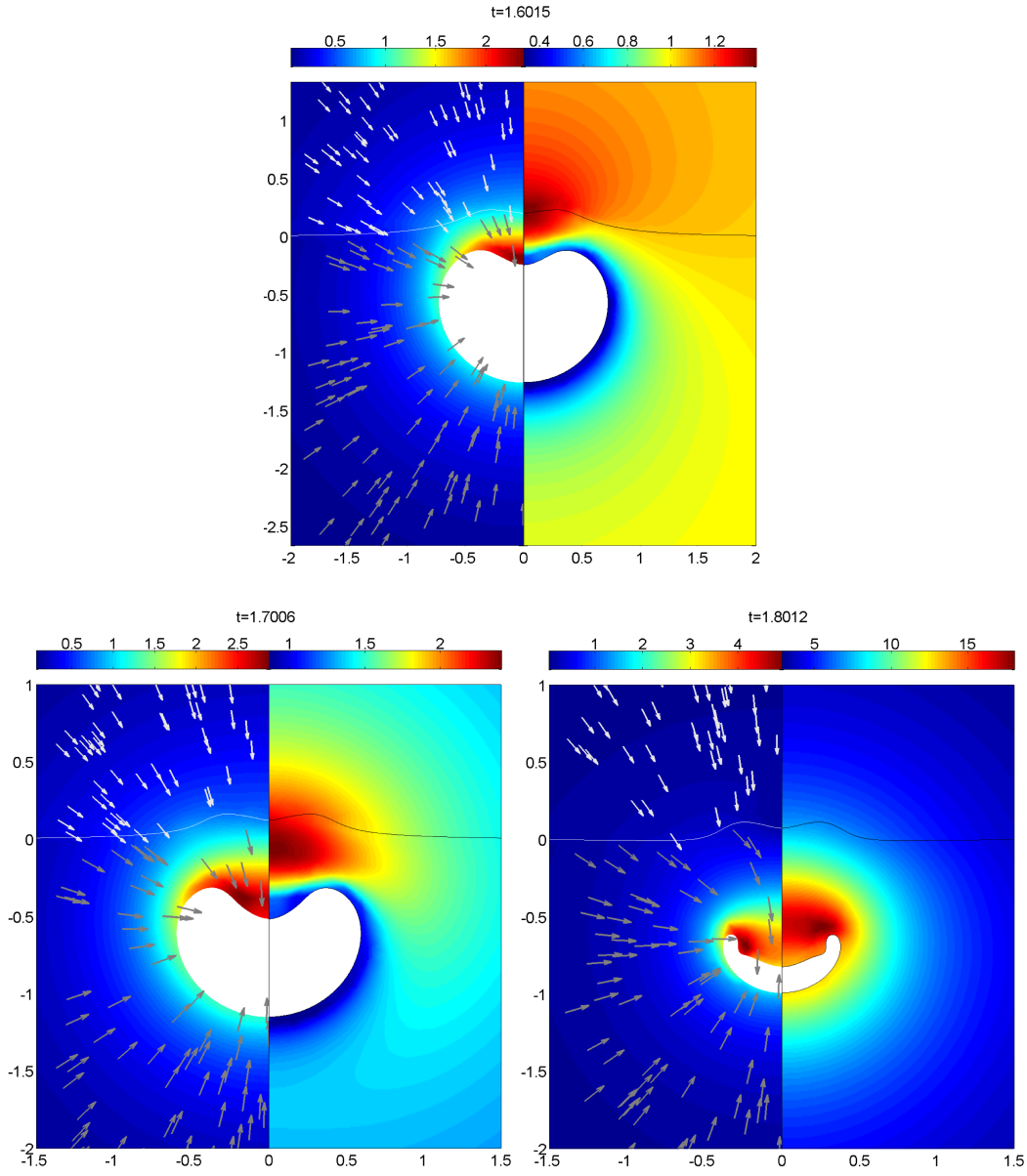

Figure 6.12: The collapse phase of a high pressure bubble at a standoff distance of $h = 0.5$ from a two liquid interface supporting a density ratio of $\rho = 0.6$.

observe this in figure 6.14, showing the velocity and pressure fields in both layers during the shift from compression to expansion. As the bubble jet forms initially, it still takes a convex form. The highest velocity in the surrounding fluid is however not located directly upon the axis. This forces the fluid slightly away from the axis to descend into the bubble core faster, resulting in the concave jet tip. As the bubble rebounds however, the highest pressure region is in fact axially located, and a stagnation point also forms at $z \approx 0.6$. This naturally forces the centre of the jet downwards, and in the two cases investigated here, this is sufficiently faster than the re-expanding base of the bubble to cause an axially located impact.

The toroidal aspects that follow jet impact are potentially detrimental to mixing applications, whereas it may increase free radical production. As the jet direction is away from the interface, there will not be any direct mechanical interaction. Moreover, this jet drags the bubbles away from the interface, which combined with the non-spherical re-inflation of the bubble hinders further surface deformation in comparison to the equal density case. Again towards the end of these simulations, the bubble jets appear to pinch at either end. This may deposit a droplet inside the bubble core, whilst the bubble itself will regain sphericity as the expansion continues. Additionally as the bubble will have translated away from the interface, the subsequent collapse may remain spherical for a longer period, allowing this droplet to be subjected to the higher gas temperatures associated with a spherical collapse.

6.5 Bubble attraction and toroidal jetting for $\rho > 1$

As was shown in Chapter 2, the Kelvin impulse in the absence of gravity indicates that the bubble will migrate toward the interface if the bubble is located in the less dense layer. The high speed jet will form in this direction as well, as was demonstrated in the simulations shown in figures 6.1, 6.3 and 6.4. This does present some difficulties

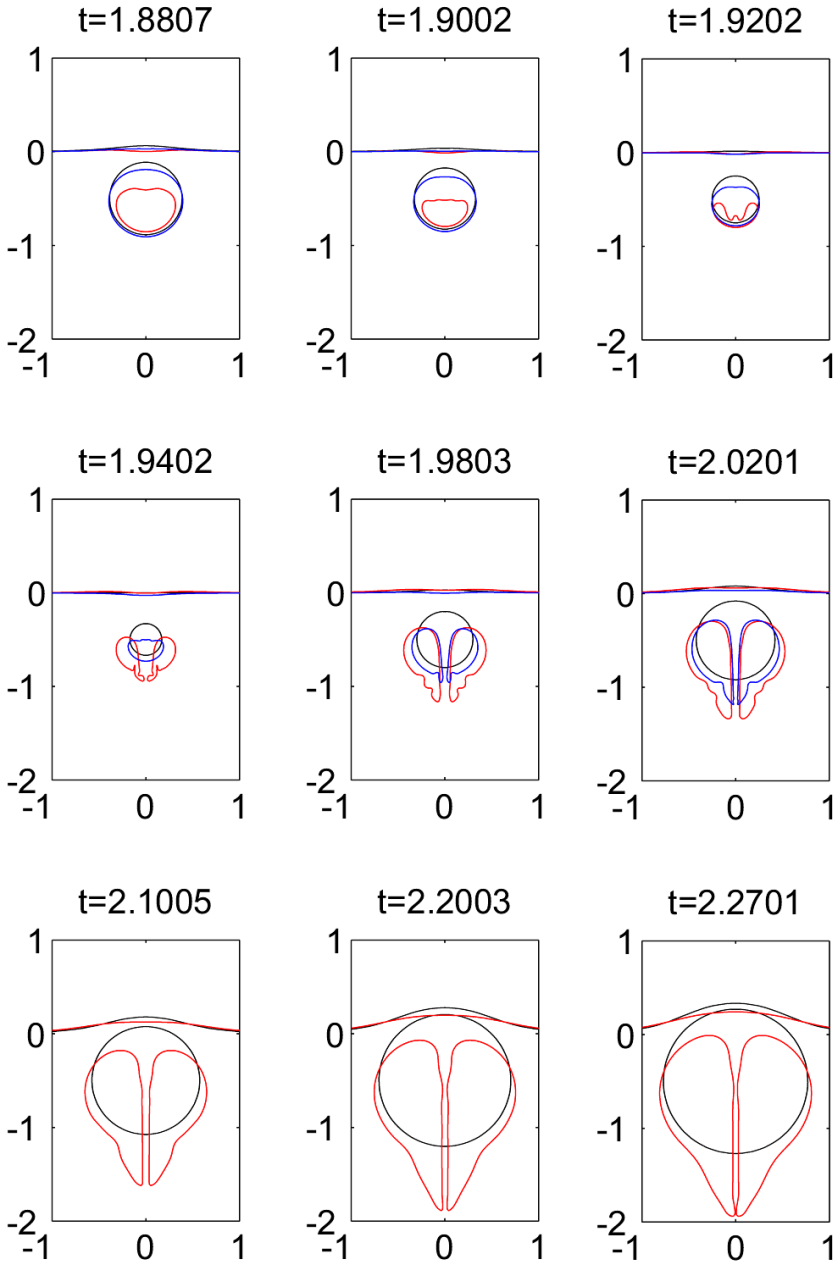

Figure 6.13: The rebound of bubbles characterised by $\epsilon = 100$, $\gamma = 1.4$ and $\sigma_b = 0$ at a standoff distance of $h = 0.5$ from a two fluid interface. The density ratios are $\rho = 0.9$ (red), $\rho = 0.95$ (blue) and $\rho = 1$ (black).

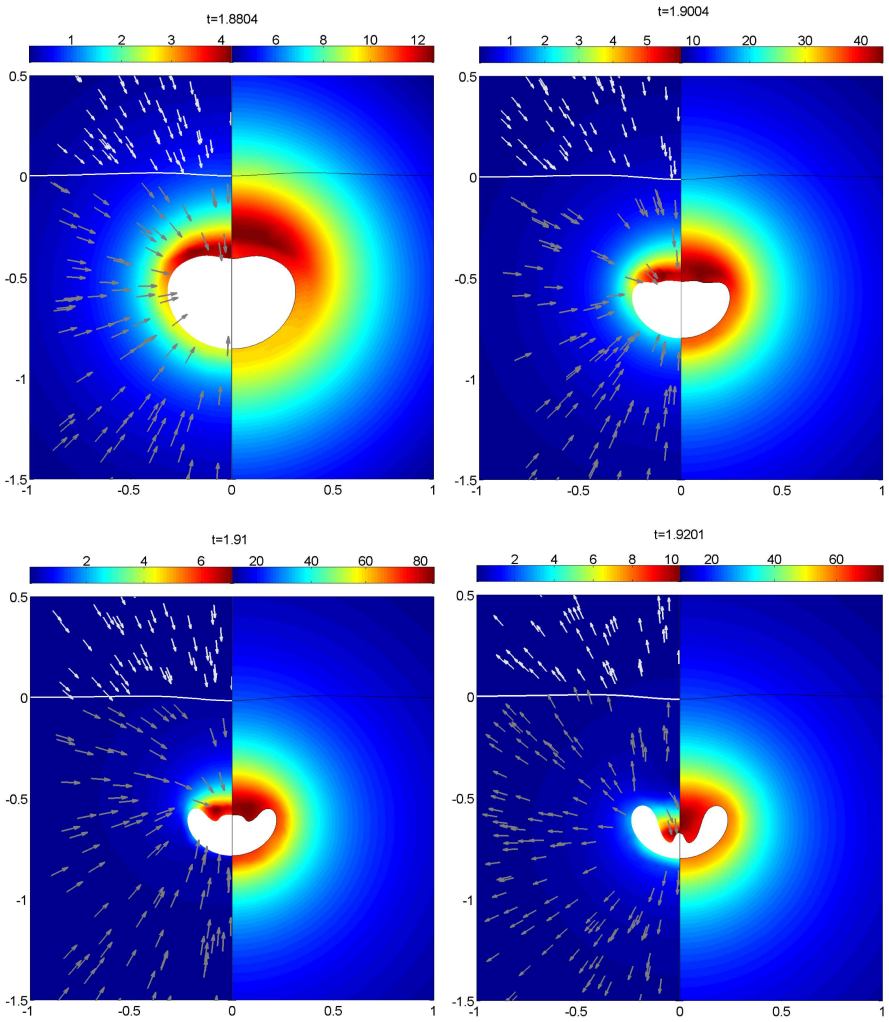

Figure 6.14: Velocity and pressure fields during the late pre-toroidal phase of a high pressure bubble with $\epsilon = 100$, $\gamma = 1.4$ and $\sigma_b = 0$, initiated at a standoff distance of $h = 0.5$ from a fluid-fluid interface supporting a density ratio of $\rho = 0.9$.

from a computational aspect at very close standoff distances, especially as ρ is increased and the velocity field in the second layer decreases toward zero. Previous research into the rigid boundary case, $\rho \to \infty$, has used image systems and explicit velocity criterion to overcome this [17, 64, 10, 91]. In this work this cannot be done, as the interface is deformable and the velocity is not known a priori. As such a larger standoff distance $h = 0.7$ is used instead of $h = 0.5$. This is still sufficiently small to draw comparison to the previous results, and allows the bubble freedom to rebound to varying degrees. From the previous results, one also does not expect any surface spike formation to occur, which was motivational in deciding on the standoff distance $h = 0.5$. Indeed as is apparent from the maximum surface deformations from bubbles at greater standoff distances in figure 6.5, increasing the density ratio adversely affects the amount the interface is distorted during the first oscillation. Contrasting to this is the significant increase in deformation observed for $h = 0.75$ and $h = 1$, where the highly non-spherical properties of the toroidal evolution of the bubbles take effect.

One also includes a small amount of surface tension as an additional smoothing mechanism, on the order of $\sigma_b \sim O(10^{-4})$. This is due to the very high curvatures observed in some situations immediately after jet impact, which if left unchecked may cause the splining routines to fail and the simulation to stop prematurely. This will only have an influence when jet impact occurs, as the curvature of the bubble jet tip will in general be $\nabla \cdot \mathbf{n}_b \sim o(10^3)$, and so the evolution of the surface potential will be more significantly affected by the surface velocity.

With the ratio $\rho = 1.2$, the re-expansion of the bubble and the influence of the high speed jet cause significant deformation to the interface. Figure 6.15 shows the initial collapse behaviour of the bubble. Deformation to the interface is smooth throughout this phase, and is due to the bubble volume only. What is more the difference in tangential velocity is small, as the density ratio is near unity. Impact occurs as the bubble approaches

its minimum volume and so the interface is close to its initial flat position. The bubble has migrated toward the interface as predicted by the Kelvin impulse, and as occurred for the slightly greater standoff distances in figure 6.1. The pressure fields in the primary fluid layer exhibit similar behaviour to those in a rigid boundary case, with a distinct region of high pressure building at the opposing bubble pole. The pressure in the second layer is more akin to that expected in an infinite fluid, with a near spherical pattern of decreasing pressure as the distance from the bubble increases. The jet tip is similarly rounded, and impacts on the axis first at a time slightly greater than one spherical bubble oscillation.

When the bubble enters the toroidal phase, the subsequent deformation to the surface is significantly different to the pre-toroidal oscillation. In figure 6.16 this is demonstrated by comparing the early toroidal behaviour with the initial expansion stage of a bubble initiated at a standoff distance of $h = 0.34$, corresponding to the z location of minimum bubble volume. The most prominent features are associated with the high speed jet. This causes severe disruption to the interface though direct mechanical interaction. Moreover, it drags the bubble further toward the interface, and allows for the volume of the bubble to increase dramatically through the formation of the two lobed structure, causing further interfacial deformation The newly created bubble on the other hand causes a much more rounded perturbation to the interface as it expands almost spherically. Due to the lack of a flow field flowing toward the interface, this bubble does not translate a great deal during this time period, and so the interfacial deformation is significantly less. This clearly demonstrates the importance of the jet interaction with the fluid-fluid interface, and illustrates the potential for non-spherical bubble effects in mixing phenomena.

Figure 6.17 contains velocity and pressure time frames taken during the re-expansion of this bubble. Throughout these frames, the velocity of the bubble jet is high, with fluid flowing rapidly toward the second layer. As the simulation continues, the elongated

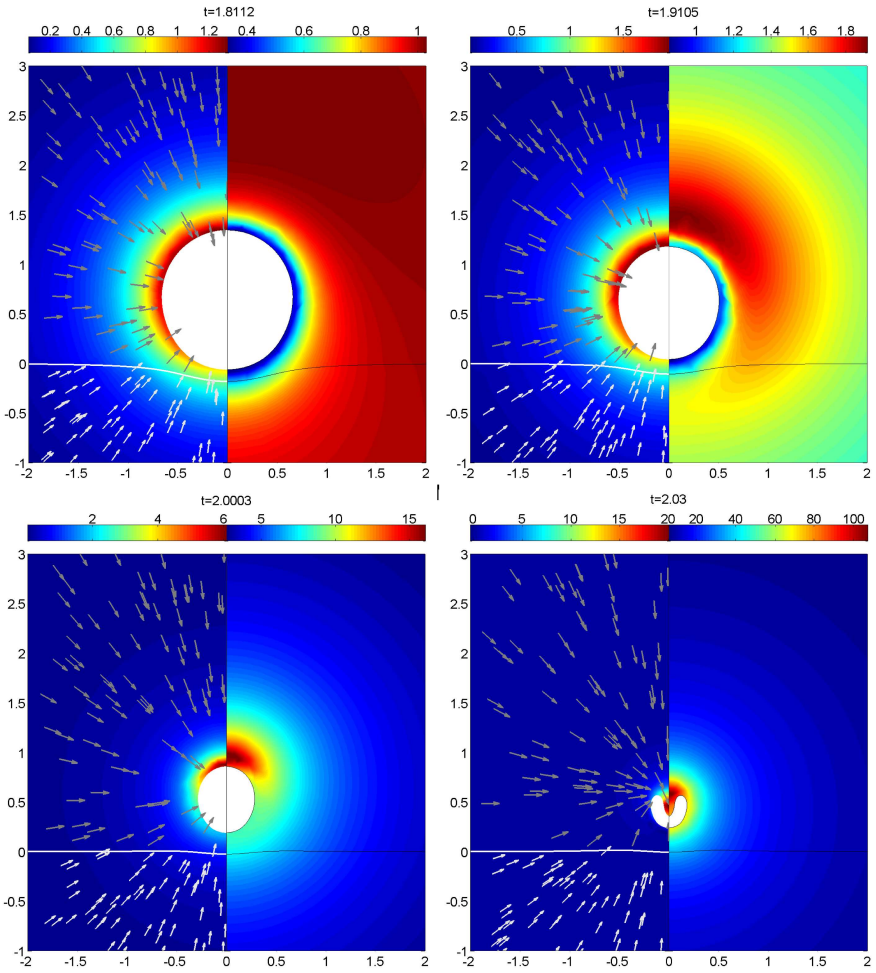

Figure 6.15: Behaviour of a high pressure bubble characterised by $\epsilon = 100$, $\gamma = 1.4$, at a standoff distance of $h = 0.7$ from a two fluid interface suporting the density ratio $\rho = 1.2$. Time frames are taken during the first bubble collapse, demonstrating bubble attraction and jetting toward the interface.

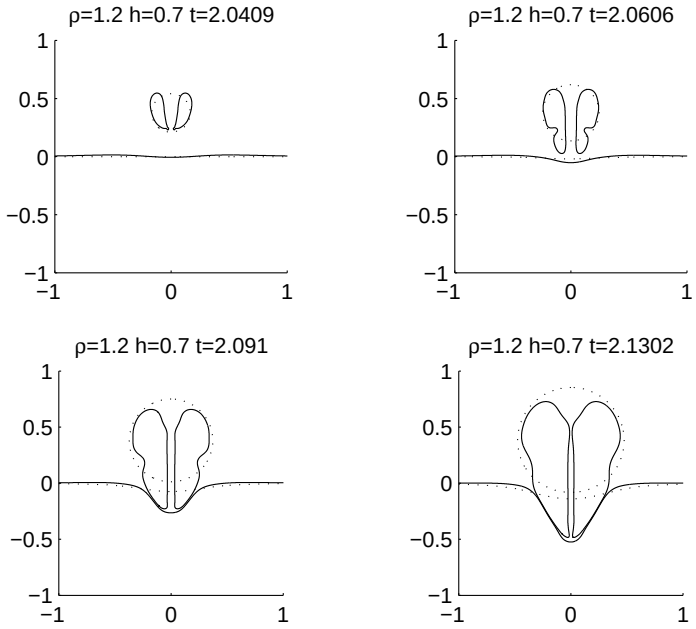

Figure 6.16: Toroidal behaviour for $\rho = 1.2, h = 0.7$ (solid line) compared to the initial expansion of an equivalent bubble at $h = 0.34$ (dotted line). Surface deformation at jet re-attachment is significant.

bubble becomes entrained into the interface, and it is likely that physically the thin layer of less dense fluid between the bubble and interface will disappear through diffusion and vapourisation. The high pressure region at the end of the jet remains throughout, and translates the two-fluid interface between the first and second time frames. The re-inflation of the bubble forces liquid away into the field. This has the side effect of causing a stagnation point to form at the rear of the bubble jet, with the jet taking fluid toward the interface and the volume re-expansion forcing fluid away. One observes in the final frame the pinching motion caused by this phenomena, which may separate the bubble jet from the surrounding fluid inside the bubble core. At the opposing pole, a different pinching mechanism is occurring, as the inflating bubble is funnelled toward the axis by the denser layer. Several possibilities now remain as to what happens next. It is likely that the pinching at both ends will result in a droplet of fluid 1 being deposited inside the bubble, which would be beneficial for thermally activated reactions associated with the high temperatures at the bubble core. The forward pinch may also act as a cannon for depositing a droplet of the lighter fluid into the denser layer, as the fluid velocity at the front of the jet is still significantly high.

Figures 6.18 and 6.19 contain shape profiles for the ratio set $\rho \in \{1.4, 1.6, 1.8\}$, and $\rho \in \{2.5, 5\}$ respectively, from the time $t = 1.5$ to the end of the simulation. Several key features appear as the the density ratio increases, predominantly as a result of the decrease in deformability. One begins to observe splashing phenomena at $\rho = 1.4$. This is caused be the retardation of the advancement of the frontal lobe by the denser layer. The re-expansion of the bubble combined with the threading jet, forces a surface perturbation around the bubble, which then acts to collapse the rear lobe. The re-inflation of the bubble is thereby restricted to a more ovoidal shape than for $\rho = 1.2$. The behaviour of the splash varies somewhat as the density increases, with the disturbance being forced into the bubble more severely at $\rho = 2.5$ and $\rho = 5$. During these simulations, the bubble is

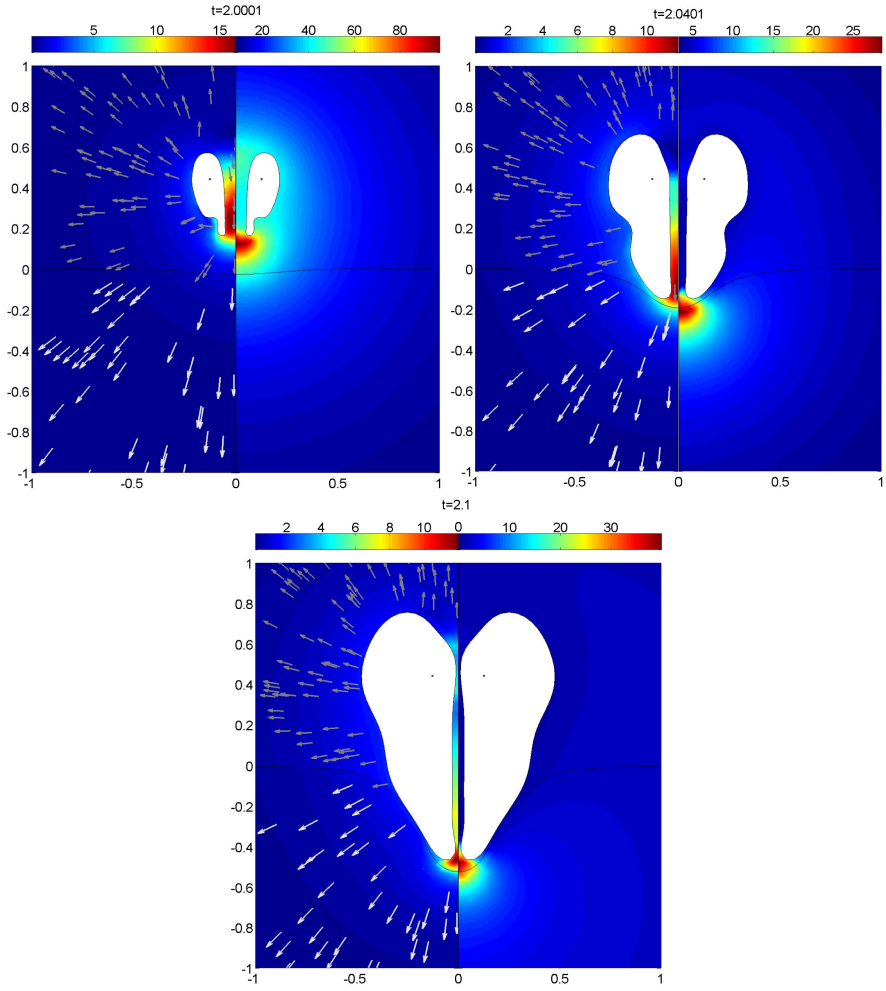

Figure 6.17: Pressure fields during the toroidal stage of the re-expansion a high pressure bubble ($\epsilon = 100,\ \gamma = 1.4$) initiated at $h = 0.7$ from a two fluid interface with density ratio $\rho = 1.2$.

also seen to slide into the pit formed by the advancing liquid jet, with the bubble centroid actually below the initial line of the two fluid interface. This will result in the bubble re-expanding in a very non-spherical manner, as the denser layer may force it outward.

The jet tip velocity at impact[1] is also seen to decrease as ρ increases, as shown in figure 6.20. This is in part due to the increasing bubble volume at impact as ρ increases, and in some cases impact actually occurs while the bubble is re-expanding. The inertia and kinetic energy of the jet will therefore be further lessened relative to the density of the second layer, as it is both lighter and moving slower. This is complimentary to what has been observed as the standoff distance is increased in a rigid boundary case, with bubbles which can advance forward more at greater standoff distances having greater momentum than bubbles collapsing close to the wall [65].

6.6 Summary

This chapter has investigated the collapse of a single cavitation bubble near a fluid-fluid interface supporting a discontinuity in liquid densities. The standoff distance was initially varied to give an indication into the applicability of the spherical models in Chapter 2, and has shown that even at moderate standoff distances the non-spherical behaviour is critical. In particular it has illustrated that the threading jets formed due to the presence of the interface cause the bubble to translate significantly more than a purely spherical alternative. It has also been demonstrated that at moderate standoff distances with density ratios greater than unity, the toroidalisation of the bubbles caused additional surface deformation.

Various different ρ have also been investigated at close standoff distances. Different modes of behaviour have been observed as ρ increases. Surface spiking has only been observed for $\rho < 0.4$, and is believed to occur when bubble jet formation begins in the

[1] In these cases this is taken as the velocity in the z direction of the final node on the bubble at the time-step where the proximity criteria is met for toroidalisation.

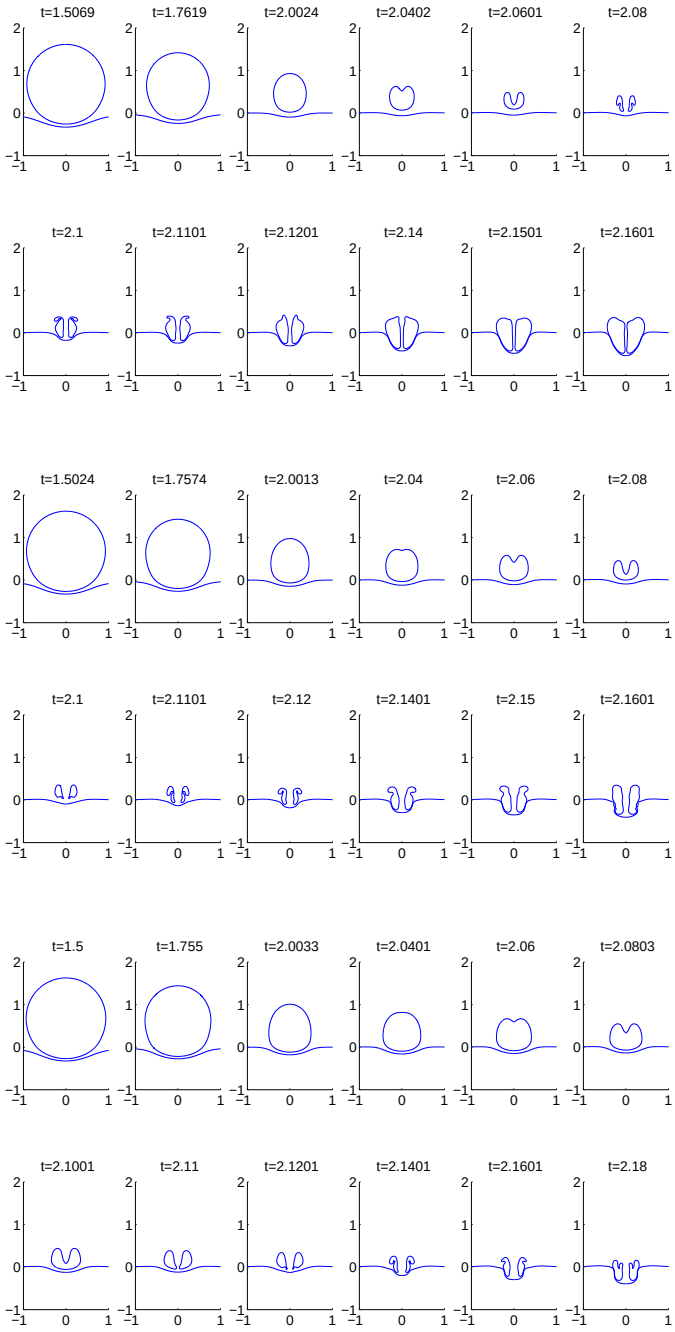

Figure 6.18: Bubble shapes during the collapse and re-expansion of a high pressure bubble initiated at a standoff distance of $h = 0.7$ from a two fluid interface with density ratios $\rho = 1.4$ (top), 1.6 (centre), and $\rho = 1.8$ (base).

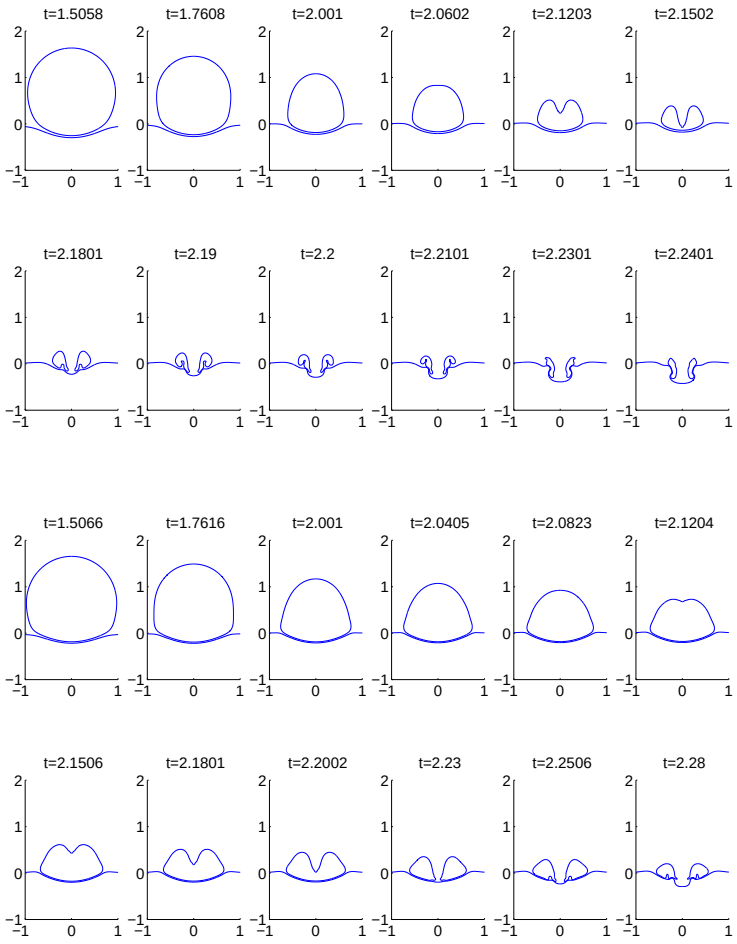

Figure 6.19: Bubble shapes during the collapse and re-expansion of a high pressure bubble initiated at a standoff distance of $h = 0.7$ from a two fluid interface with density ratios $\rho = 2.5$ (top) and $\rho = 5$ (base).

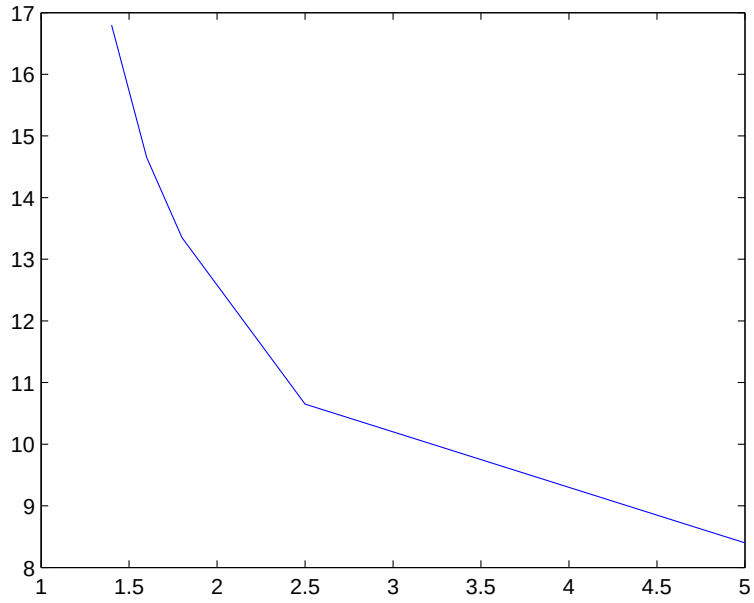

Figure 6.20: Jet tip velocities (vertical axis) at impact as ρ increases (horizontal axis).

late expansion phase and not the collapse phase. For $\rho \in (0.4, 1)$ the fluid-fluid interface is seen to become indented at the top of the mound, with no stagnation point formation inside the less dense liquid layer. The bubble jet is also seen to impact at a non-axial location for some $\rho < 0.9$, although for $\rho = 0.9$, the re-expansion of the bubble can cause an axial impact.

For $\rho > 1$ bubble migration toward, and entrainment into the fluid-fluid interface is observed. Bubble jet direction occurs only in the direction of the denser fluid. The subsequent toroidal motion demonstrates how the jet and enlarging bubble interacts with the interface, with the deformation lessening as ρ increases. It has also shown that the toroidal behaviour may create droplets of the less dense liquid both inside the bubble, and inside the denser layer. Splashing around the bubble has also been observed for $\rho > 1.4$.

The following chapter concerns the interactions of multiple initially high pressure bubbles near a density jump. This is of importance to bubble assisted mixing phenomena, as

in such an application multiple bubbles will be present, and their impact on the behaviour observed in this chapter for single bubbles may be significant.

Chapter 7

Multi-bubble behaviour near a density jump

The results in this chapter demonstrate the behaviour of high pressure cavities in two and three bubble configurations with a variety of density ratios. The location of the bubbles may be in a single fluid layer uniquely, a homogeneous configuration, or may be on opposing sides of the interface, a heterogeneous configuration. Depending on the configuration, it may be possible to either magnify or repress the behaviour observed in Chapter 6.

It is useful first to re-address the behaviour in the test case $\rho = 1$. Here, providing the fluid-fluid interface carries no tension, the dynamics of a two bubble configuration are exactly equivalent to those of a single bubble near a rigid boundary. As was illustrated in figure 5.23, this entails the jetting of both bubbles towards each other identically, with both bubbles becoming multi-lobed after jet impact has occurred given a sufficient separating distance. There should also be no deformation to the interface at all, although in simulations numerical noise will cause some error to occur, particularly through the transition to toroidal geometries. An example three bubble simulation is included in figures 7.11 and 7.13.

7.1 Two bubbles in a homogeneous configuration

The behaviour in homogeneous configurations can show qualitative similarities to the infinite fluid case. This is illustrated well in figures 7.1 and 7.2, containing bubble shapes from the simulations of two bubbles in either the denser layer or lighter layer respectively. The ratio of densities in both cases is 2:1, implying that the density ratio is $\rho = 2$ for the first case and $\rho = 0.5$ for the second case. In these simulations the separating distance of the two bubble centroids at initiation is 3 maximum bubble radii, whereas the standoff distance of the bubble closest to the interface is $h = 1.5$.

In the denser primary layer case, the combination of the interfacial repulsion and bubble-bubble attraction accelerates the jetting of the bubble closest to the interface. The farther bubble begins jetting slightly later. Both bubble jets are directed toward the other bubble, with bubble migration also occurring in this direction. The two liquid interface remains relatively flat during the lower volume jetting behaviour, and is only significantly deformed by the bubbles when they first approach maximum volume. The simulation in this case is stopped when the bubbles begin to directly interact. At this point, the forward protrusion of the larger bubble furthest from the interface appears to be forcing its way inside the threading jet of the smaller, closer bubble. Neither jet is showing signs of collapse, although the farther bubble jet is significantly thinner than the near bubble jet. The opposing ends of the jets are still broad, indicating the pinch off entrapment of a fluid droplet inside these bubble may not occur here, at least until much later into the evolution. It is postulated that over the subsequent oscillations of the bubbles, the influence of the density jump will be lessened by the increased distance, and that the two bubbles will coalesce into a larger entity.

For the case $\rho = 2$, one observes an initial elongation of the closer bubble to the interface. The lower bubble deforms axially first, with a jet directed toward the other

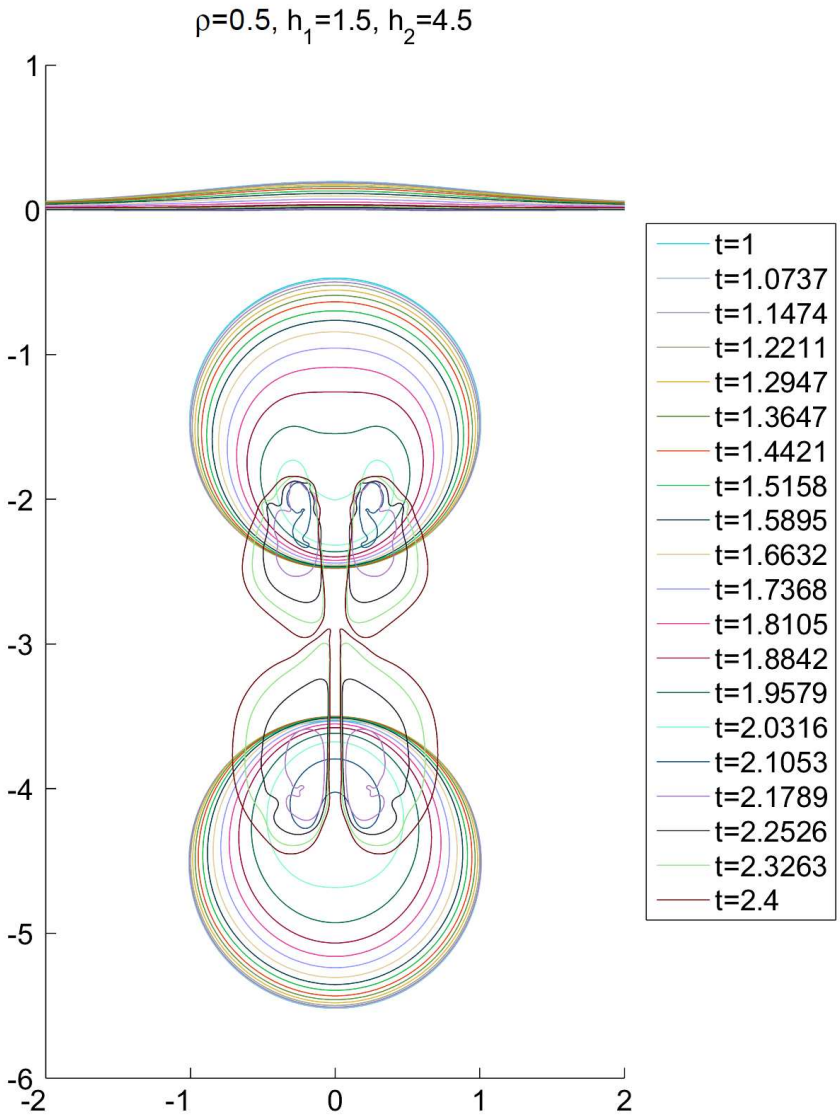

Figure 7.1: Collapse and re-expansion of two bubbles characterised by $\epsilon = 100$, $\gamma = 1.4$, below an interface with density ratio $\rho = 0.5$. The bubble standoff distances are $h_1 = 1.5$ and $h_2 = 4.5$.

bubble and the interface. This is similar to a four bubble case in an infinite fluid, or the equivalent case of two bubbles near a rigid boundary (the limit as $\rho \to \infty$). Attraction of the farther bubble dominates the attraction of the interface, and as a result the closer bubble forms a jet toward the farther bubble. This jet is considerably thinner than the closer bubble jet in the case $\rho = 0.5$, due to the elongation of the closer bubble. Again in similarity to the above mentioned cases, the bubbles move toward each other, against the behaviour observed for a single bubble near a denser fluid layer. As with the first case, there is no significant interaction between the high speed jet and the interface, again in contrast to the single bubble behaviour. At the end of this simulation, one observes again the fore-lobe of the second toroidal bubble appearing to encroach into the threading jet of the first bubble. Unlike in the previous simulation however, the thinner appears to pinch at both the fore and aft, implying a fluid droplet may pinch off in this case. One may again expect the two bubbles to merge during the subsequent rebound, with the remnant bubble migrating back toward the fluid-fluid interface.

The counteraction of the interfacial attraction by the presence of a second bubble leads to the assumption that there should be a range of standoff distances where the behaviour of the closer bubble switches between jetting toward the interface to jetting away from the interface. In effect this would be a null impulse state in the absence of gravity. This is indeed the case with $\rho = 2$, as is demonstrated in figure 7.3. Here the bubbles are characterised identically by $\epsilon = 100$, $\gamma = 1.4$ and $\sigma_b = 0$, with the closer bubble initiated at $h_1 = 1$. The initiation of the second bubble varies through the set $h_2 \in \{3.5, 4.25, 5\}$. At the smaller of these, the Bjerknes attraction of the second bubble dominates that of the density jump. The closer bubble is initially elongated vertically by the two entities, before the near side contracts inwards and eventually forms a very fine jet toward the second bubble. As can be seen from the pressure and velocity field in figure 7.4, this jet is driven by an extremely concentrated pressure peak, and achieves a correspondingly high

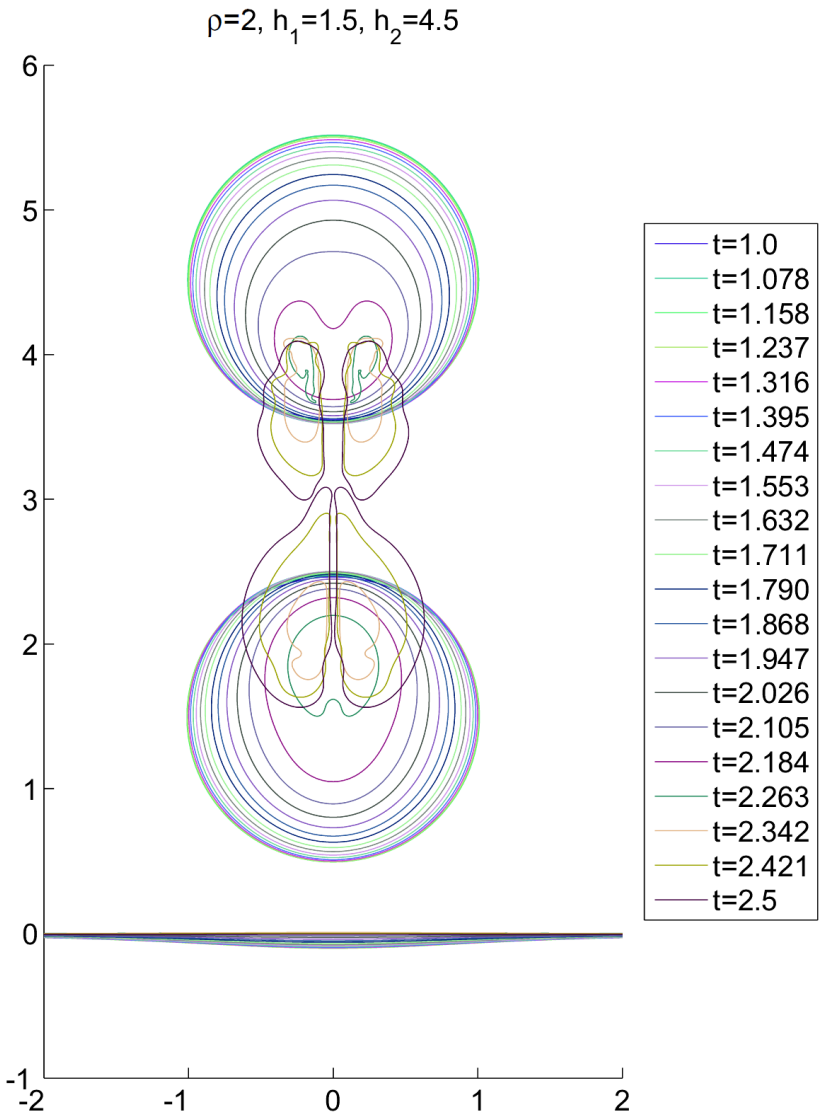

Figure 7.2: Collapse and re-expansion of two bubbles characterised by $\epsilon = 100$, $\gamma = 1.4$, above an interface with density ratio $\rho = 2$. The bubble standoff distances are $h_1 = 1.5$ and $h_2 = 4.5$.

velocity. The velocity of the toroidal jet in the second bubble is significantly slower than this, although it is approximately equivalent to those seen in single bubble cases.

Increasing the standoff distance of the second bubble to $h_2 = 5$ illustrates the opposite effect, although it is not necessarily entirely due to the Bjerknes attraction of the density jump overcoming the Bjerknes attraction of the second bubble. The additional mechanism in this case arises from the far bubble becoming toroidal at an earlier time than for the case $h_2 = 3.5$. This naturally pumps fluid down toward the near pole of the closer bubble, further building the pressure in this region.

The state where the two forces are in balance occurs when $h_2 \approx 4.25$. In this case the jetting of the closer bubble is delayed longer, and subsequently the entire bubble is under a much higher pressure. The behaviour observed is unlike that of a buoyancy/interface interaction in that the bubble does not pinch or rebound before becoming toroidal. Instead very high speed jets form at both bubble poles, jetting toward one another at tremendous velocity. One may observe from the pressure and velocity before this occurs that this is driven by a significant build up of pressure over either pole. Interestingly, in all three cases shown here the fluid-fluid interface is not heavily perturbed during the jet formation. Neither was it heavily perturbed during the first oscillations, and only in the case $h_2 = 5$ did the bubble translate toward it. This leads to the conclusion that should bubbles be arranged in a homogeneous configuration, ample space must separate them in order for significant jet/interface interactions to occur. Alternatively of course, should one wish to minimise the disruption to the interface in a biomedical application, then using a smaller separation distance would be advisable.

7.2 Two bubbles in a heterogeneous configuration

Figure 7.5 shows how this behaviour may be disrupted by the presence of the density discontinuity. Due to the nature of the two bubble system in question, this illustrates

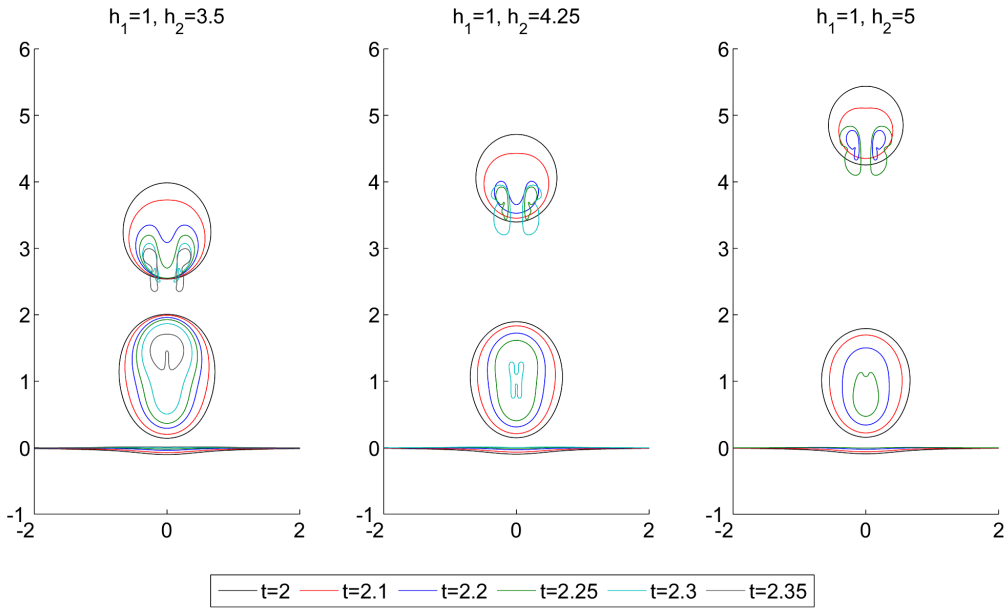

Figure 7.3: Bubble shapes through the final stages of the collapse of the closer bubble for $\rho = 2$, given varying standoff distances for the further bubble.

the behaviour of both $\rho = 2$ and the reciprocal density ratio $\rho = 0.5$, albeit with a different time scale. In these cases, the bubbles are characterised with the parameters $\epsilon = 100, \gamma = 1.4$ and $\sigma_b = 10^{-4}$, with the fluid-fluid interface located 1.5 maximum radii away from each bubble centroid. As in some simulations in Chapter 6, surface tension is included as an additional smoothing mechanism only effective at jet impact. One observes the global pre-toroidal behaviour to be primarily governed by the denser layer, as the interface is forced into the less dense layer by the slower expansion of the denser layer bubble. This is expected as the denser layer will necessarily have greater inertia. This dominance continues until after the bubble in the less dense layer has jetted and becomes toroidal. This bubble forms a jet towards the denser layer, with significantly high pressures surrounding the impact region, of magnitude $30\Delta_p$. The high speed jet then continues downwards with velocities as high as 8 non-dimensional units, with sufficient force to deflect the centre of the interfacial mound. This, combined with the re-expansion

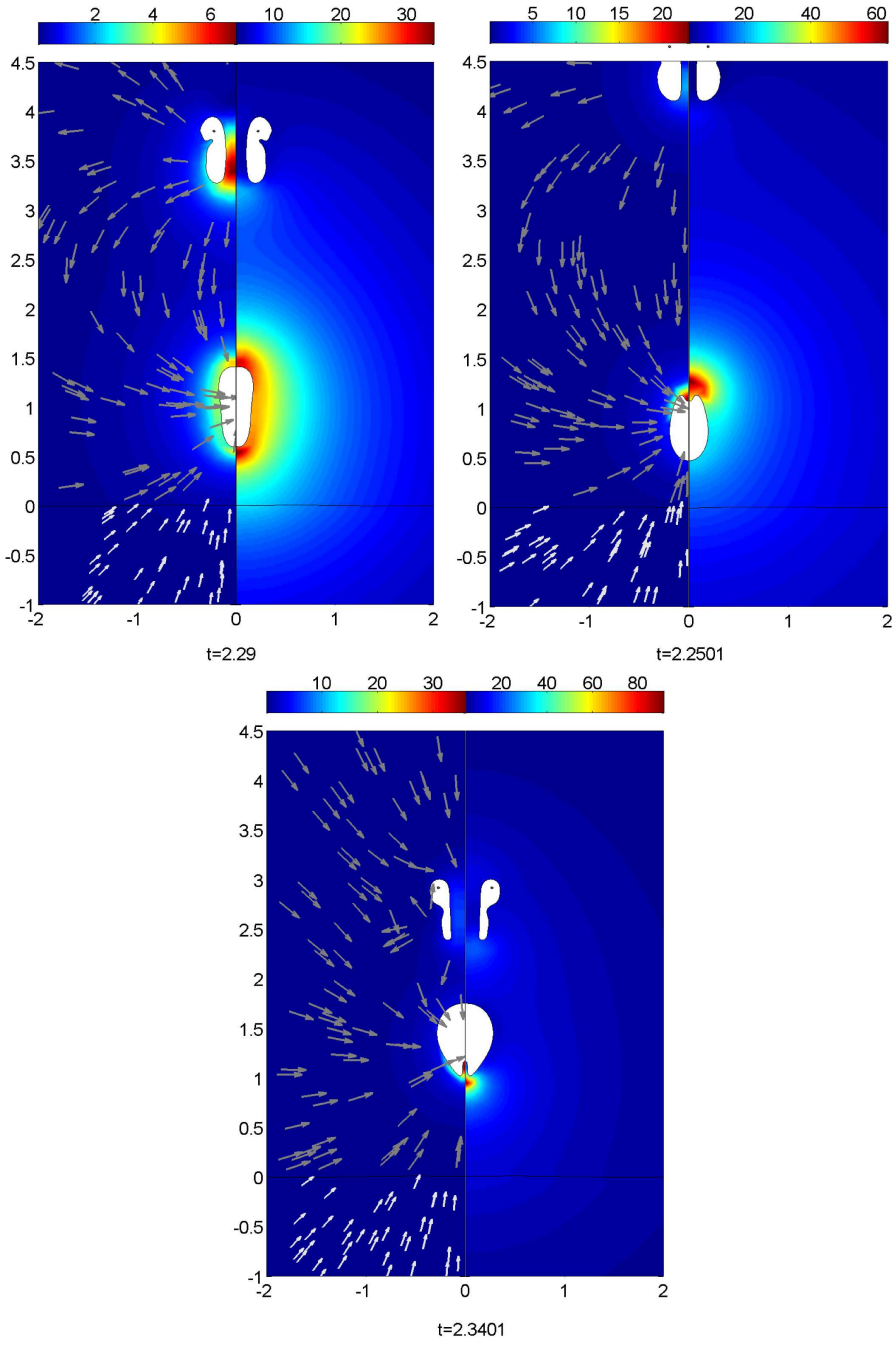

Figure 7.4: Pressure and velocity fields at time frames taken near the onset of the second bubble jetting for $\rho = 2,\ h_1 = 1$ and $h_2 = 3.5$ (base), $h_2 = 4.25$ (top left) and $h_2 = 5$ (top right).

of the bubble, causes a raised pressure region on the axis near to the bubble tip. In turn this then causes significant flattening of the near side of the opposing bubble. This may then lead to the second bubble jetting away from the interface instead of toward it as in the infinite fluid case, although the simulation here is halted due to the increasing proximity of the upper bubble to the fluid-fluid interface.

Also of interest is the re-expansion phase of the toroidal bubble. The lower lobe formed after impact is allowed to grow in a much less constrained manner than that near a rigid boundary due to the deformability of the interface. This is to such an extent that the newer lobe becomes the largest as the bubble expands. The bubble also remains toroidal for a prolonged time period, with the interior jet not being restrained by the bubble re-expansion. This increased jet stability is significant in mixing phenomena as fluid injection between layers could contribute significantly. It will also promote the onset of Richtmyer-Meshkov disturbances at the interface in real systems, as the lighter fluid is forced into the denser layer. The velocity and pressure of the jet are seen to decrease with time as expected. As in some single bubble simulations, one also observes a stagnation point forming at the top of the jet, indicating that as the expansion phase continues the jet top will eventually close off.

It has been shown that the direction of the jet in the denser layer may be affected by the jetting motion in the less dense layer. One therefore predicts there to be a choice of ρ for a given symmetrical standoff distance, where the attraction of the two cavities is in balance with the force of the initial jet. As the first bubble jet is in fact the cause of the jet deflection, and not the expansion of the bubble, a spherical approximation similar to that used for the null impulse state would be meaningless. Instead one proceeds to investigate this numerically. Figure 7.6 illustrates the transition through this equilibrium point with the late collapse and re-expansion phases for $\rho = 1.1,\ \rho = 1.3$ and $\rho = 1.5$, with the denser layer at the base of the image and each bubble at an initial standoff distance of $h_i = 1.5$.

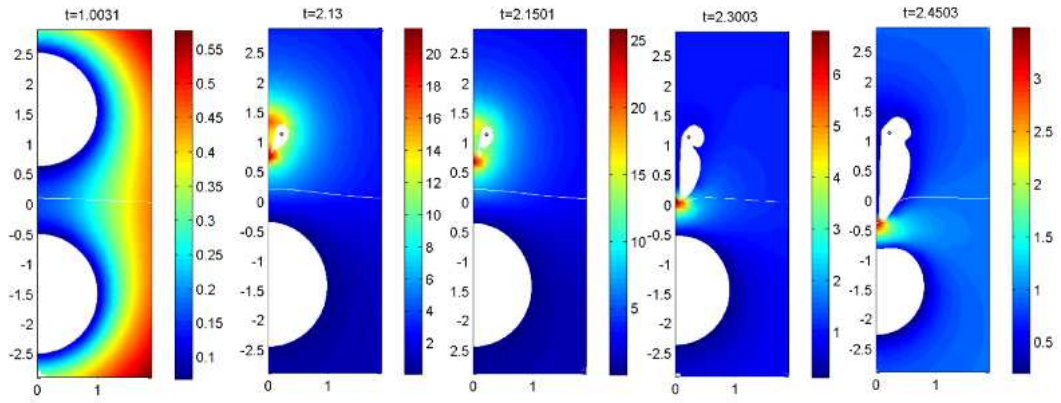

Figure 7.5: Pressure fields for $\rho = 2, h_1 = 1.5, h_2 = -1.5, \epsilon = 100, \delta = 0, \sigma_b = 0.0001$. Frames show maximum bubble volume (left), toroidal jet impact (centre left and centre), during jet flow (centre right) and lower bubble deflection (right).

The first is in the mode of the reference infinite fluid case, with the second bubble jetting in the direction of the first. The second case, $\rho = 1.3$, is near the point of equal deflection, and one observes both upward and downward jet formation and not horizontal pinching or the three-point perturbation seen in Chapter 5 for buoyancy driven cases. The case $\rho = 1.5$ has a broad, downward jet significantly driven by the jetting and re-expansion of the primary bubble, as can be seen by the severe downward perturbation of the two fluid interface. The secondary bubble has not decreased in volume sufficiently for the Bjerknes jetting to form upward, and so it is suggested that in this case the downward jet will impact first.

Varying the standoff distances of the bubbles from the interface can also have a significant effect on the subsequent behaviour. This is shown in figure 7.7 for the density ratio $\rho = 1.3$, the case above that demonstrated jet deflection.

The first of these simulations decreases the standoff distance in the denser fluid to $h = 0.75$. The dominating factor here is again the second bubble and not the density jump. During the first expansion, the bubble in the denser fluid becomes entrained into the interface, which must be due to the attractive nature of the opposing bubble as the

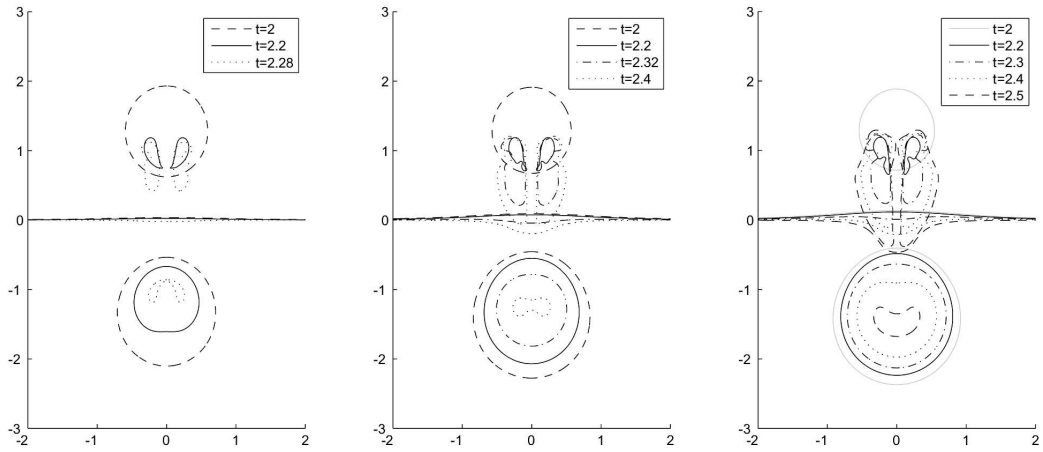

Figure 7.6: Collapse and re-expansion showing three modes of secondary bubble jetting behaviour at $h = \pm 1.5$. Bjerknes jetting (left, $\rho = 1.1$), intermediate stage (centre, $\rho = 1.3$), and deflected (right, $\rho = 1.5$).

less dense fluid would act as a repellent. As the opposing bubble collapses and becomes toroidal, one observes a very rapid elongated jet motion. This jetting is enhanced by the low pressure void given by the larger bubble. Indeed as may be observed from the pressure fields in figure 7.8, this void allows for the rapid dissipation of the high pressure region formed by jet impact. This allows the fluid in the jet to flow more freely than the equal standoff case, dragging the re-expanding bubble with it. This jetting and re-inflation causes a severe deformation to the interface, resulting in the injection of fluid 1 into the opposing bubble core. In this modelling, the surfaces of each fluid exist permanently. Thus the jet is coated by a thin layer of the denser fluid, and the two bubbles are separated by a thin layer of the two liquids. In reality however, one may envisage the liquid bridge between the two bubbles disintegrating, with the two bubbles then coalescing. This may create a mechanism to both coat a fluid droplet by another liquid, and then to heat the resulting dual liquid droplet through the oscillations of this new bubble.

The collapse of the second bubble also results in the formation of a very high region

of pressure about the far pole. This initiates the formation of an upward jet despite the buckling caused by the lighter fluid jet. This jet is still moving with a high downward velocity, and so when this is met with the approaching upward jet one may anticipate the onset of severe hydrodynamic instability with great potential for mixing the two liquids in the bubble core.

The second simulation in figure 7.7 shows the motions throughout the bubble lifetimes of the near equal jet deflection case, $h_1 = h_2 = 1.5$. In this example one observes the formation of a stagnation point before jet impact occurs in layer 1, seen in figure 7.9 containing the pressure and velocity fields of the transition into the toroidal phase of the first bubble, and the subsequent bipolar jetting of the second bubble. After the first impact has occurred and the bubble toroid begins to expand, the stagnation point is lost, and the jet forces liquid into the denser layer. The rolling of the disturbance around the bubble toroid is also visible. As the second bubble collapses further, additional liquid outside the main jet is flowing toward the denser layer away from the main jet induced surface deformation. A stagnation point is also observed to form at the top of the bubble jet, visible by velocity vectors on the axis flowing in opposite directions in the second and third time frames. The high pressure region behind the second bubble forms through the attraction between the two bubbles, whilst the region between the two bubbles also experiences a significantly raised pressure due to the jet pumping mechanism. As the bubble mass continues to shrink however, the pressure region below the singly connected bubble becomes dominant over the high pressure above, despite this region already causing the second bubble to buckle away from the first. This may result in a slight upward flow after the second bubble becomes toroidal, although this simulation was stopped before this happened. It does demonstrate however that further tuning of the standoff distances will provide a case where the circulation of the second toroidal bubble would be zero.

It is prudent to examine the effect of increasing the standoff distances on both sides of

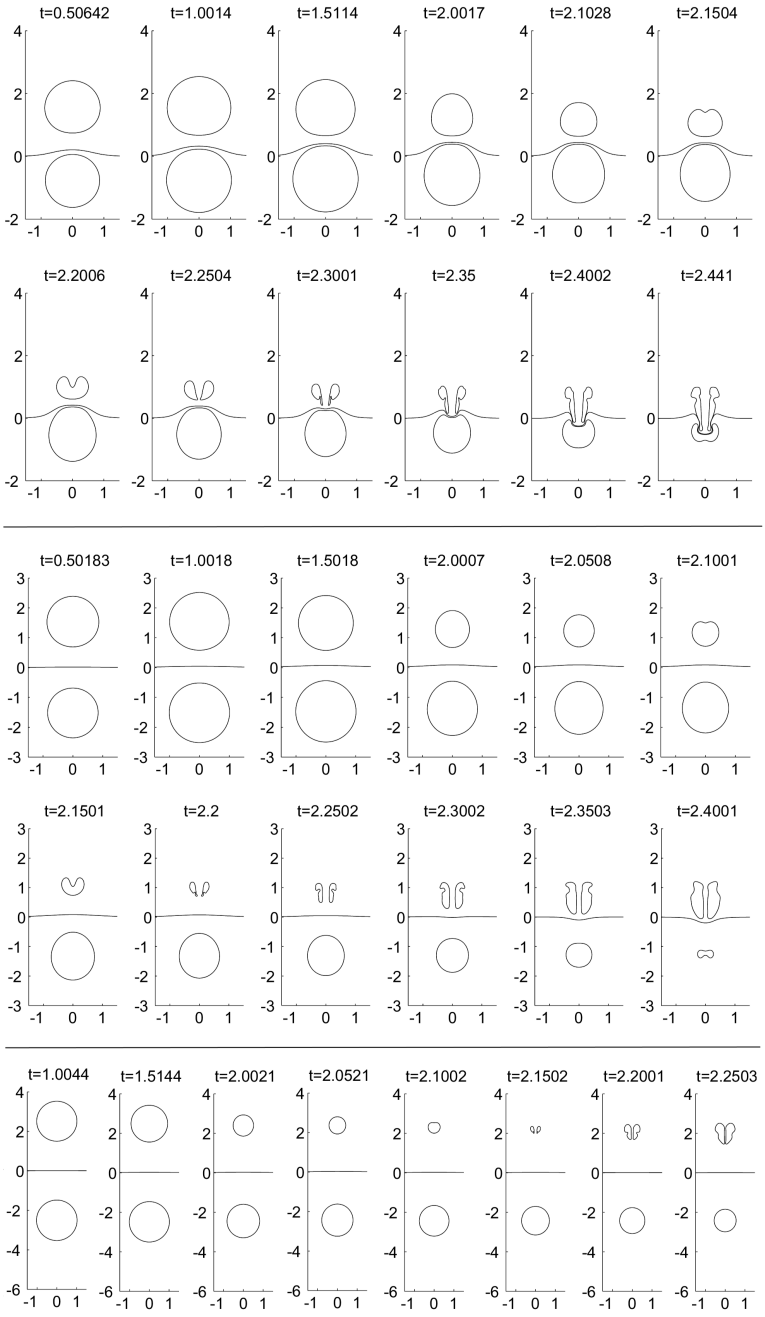

Figure 7.7: Two bubble interactions for laser type bubbles in a heterogeneous configuration about a two fluid interface with $\rho = 1.3$. Initial standoff distances are, $h_1 = 1.5,\ h_2 = 0.75$ (top), $h_1 = 1.5,\ h_2 = 1.5$ (centre) and $h_1 = 2.5,\ h_2 = 2.5$ (base).

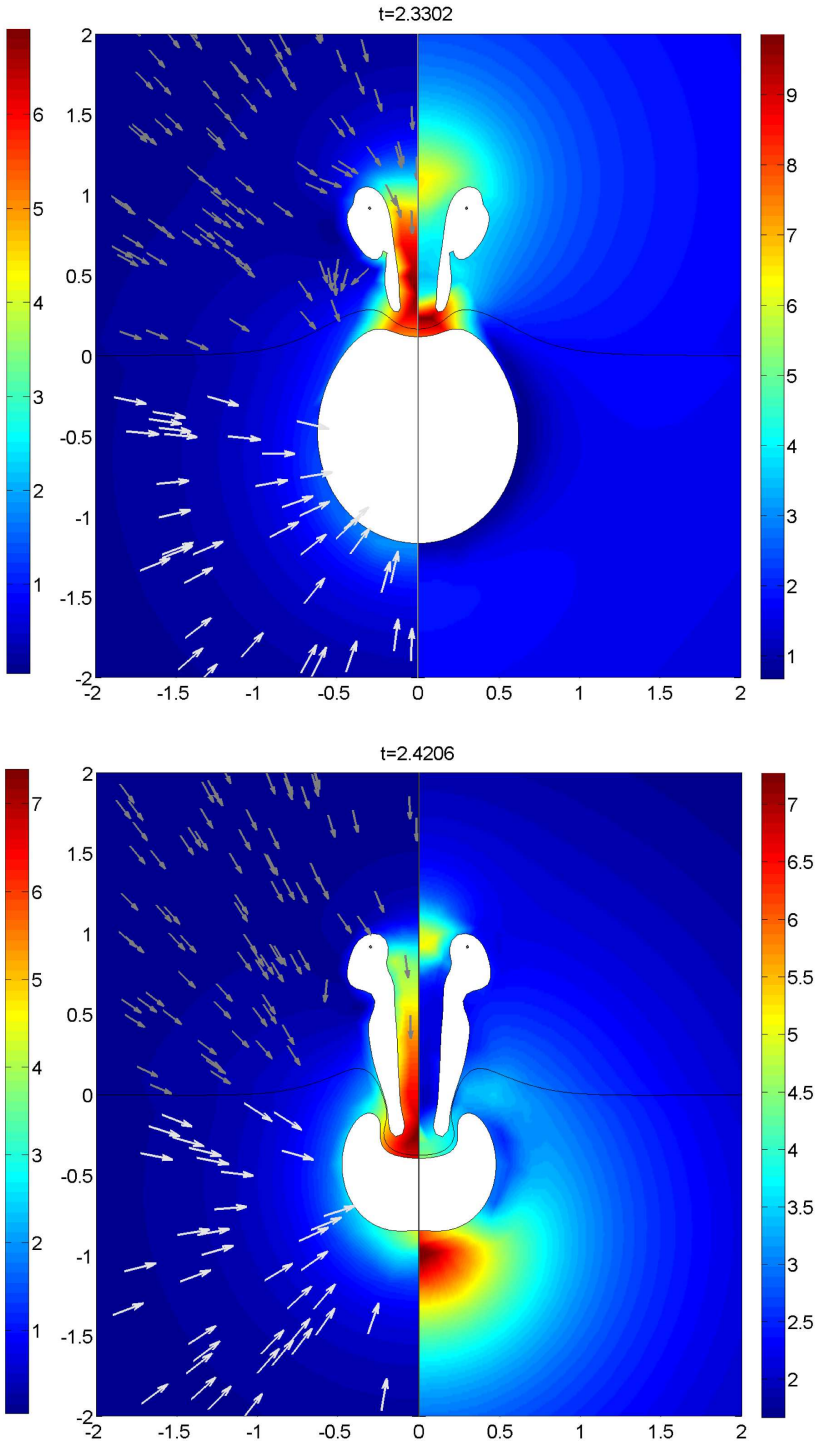

Figure 7.8: Pressure and velocity fields for the two bubble interacting near a density jump of $\rho = 1.3$. Standoff distances are $h = 1.5$ in the denser (base) layer, and $h = 0.75$ in the less dense (top) layer.

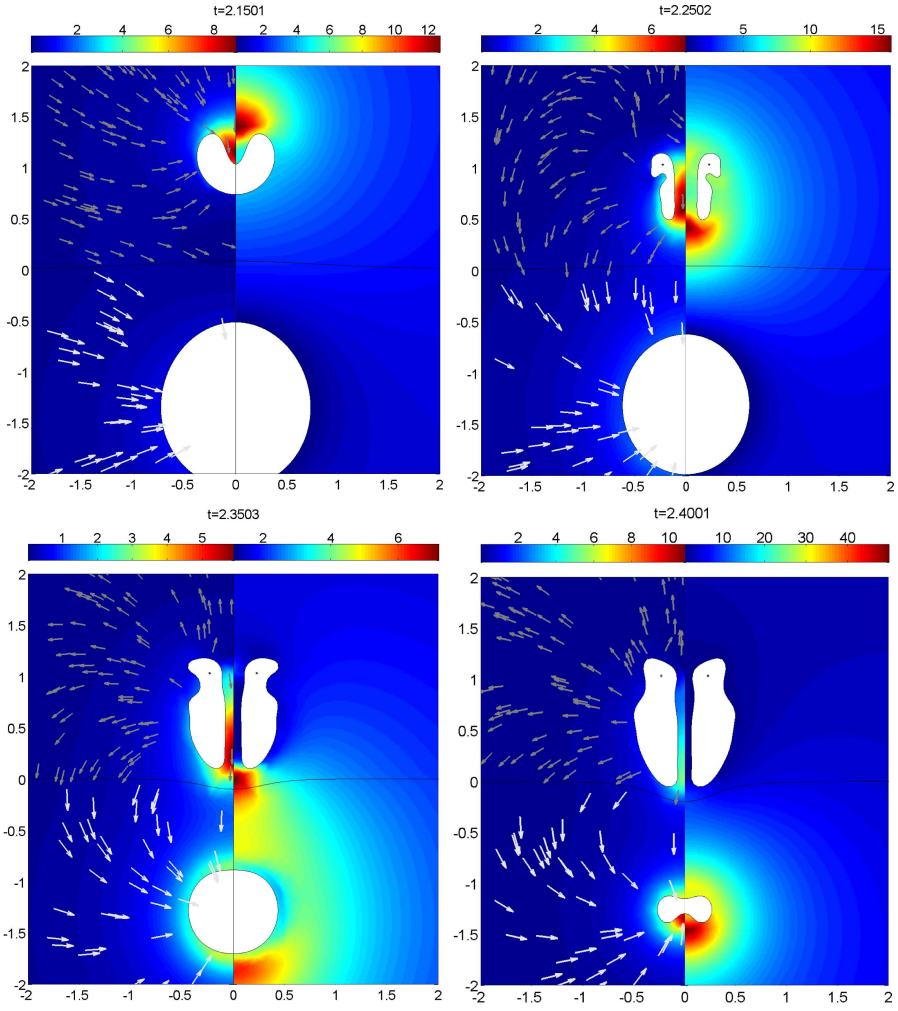

Figure 7.9: The interaction of two bubbles characterised by $\epsilon = 100$, $\gamma = 1.4$, $\sigma_b = 0$, with the initial flow field conforming to $\rho = 1.3$, $h_1 = 1.5$, $h_2 = 1.5$. These pressure and velocity fields show the transition into the toroidal phase of the first bubble, and the subsequent bipolar jetting of the second bubble.

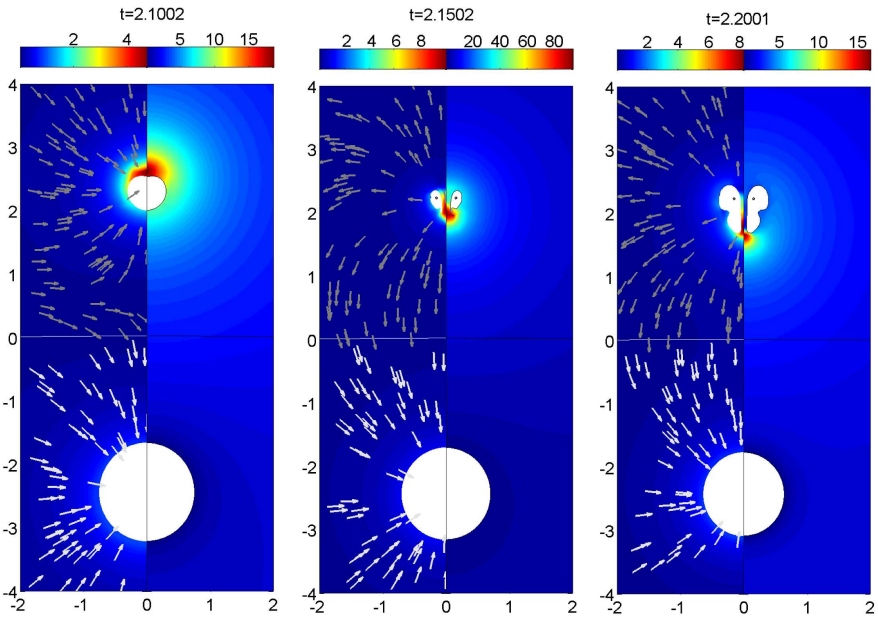

Figure 7.10: Two bubble interactions for laser type bubbles with $\rho = 1.3, h_1 = 2.5, h_2 = 2.5$.

the interface. The effect this has is shown in the lowest simulation in figure 7.7 for $h_1 = h_2 = 2.5$. Jet interaction with the interface is greatly reduced as would be expected by the increased distance. From the pressure fields associated with the jetting, as illustrated in figure 7.10, the region between the two bubbles does suffer a pressure increase, although this is not as significant as in the closer case. In this simulation no notable jet induced deformation was visible on the second bubble before pinch off of the first bubble jet, implying that the action of the bubble jet in this potential flow model is only of effect over a few maximum bubble radii.

7.3 Three bubble heterogeneous configurations

Adding additional bubbles to the column is known to cause substantial variations to the systems behaviour. Figure 7.11 contains the simulation of three bubbles in a single infinite liquid, each with separation distances of 3 maximum bubble radii. The behaviour is symmetric through a horizontal plane located at the center bubble centroid, although

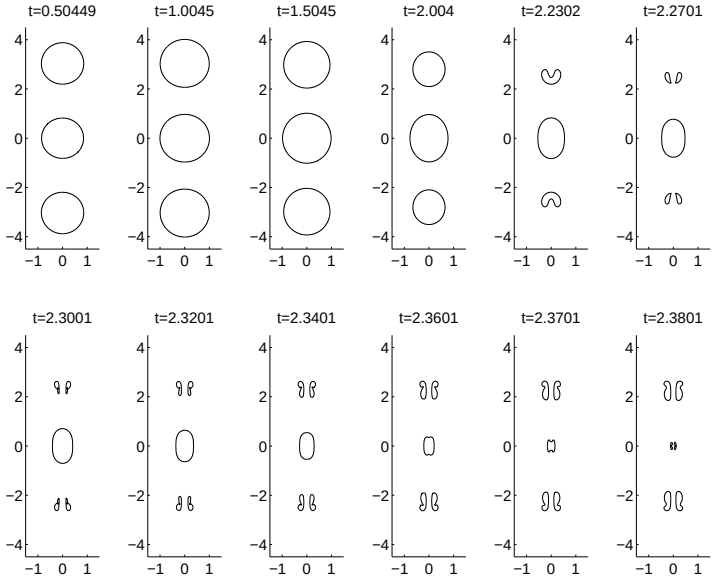

Figure 7.11: Simulation of three high pressure bubbles in an infinite fluid. The separation distance between each bubble centroid at initiation is three maximum bubble radii.

in this work this was not used to increase numerical efficiency. This bubble suffers a distinct elongation throughout the simulation, being dragged toward the two outer bubbles through the Bjerknes attraction. This same force causes the two end bubbles to jet toward the centre of the system. The inevitable result is the sudden and rapid collapse of the central bubble. This remains relatively ellipsoidal through the bulk of the pre-toroidal collapse phase. As may be seen in figure 7.12, the extent to which this central bubble is compressed is severe. Bubble jet formation occurs at both poles, with the two jets impacting each other at the bubble centroid. With an equal force being applied from both jets, the fluid flowing toward the impact site can only flow perpendicular to the axis, resulting in the formation of an oblate spheroid. This enlarges as more fluid is pumped into it until the bubble walls touch along an annulus centered along the plane of vertical symmetry. The pressure and velocity fields after the end bubbles jet are shown in figure 7.13, and illustrate how the external bubbles force the axial collapse of the central cavity.

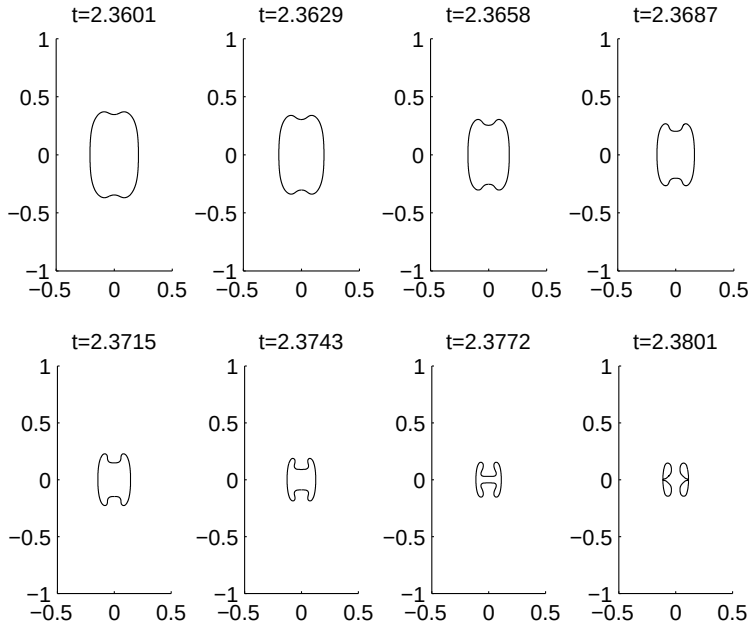

Figure 7.12: Transition to the toroidal phase of the central bubble in a column of three bubbles in an infinite fluid. The separation distance between each bubble is three maximum bubble radii.

As one expects, including a density jump between two of the bubbles results in this motion becoming asymmetric. This is shown in figure 7.14 with two bubbles in the denser layer. As before the central bubble becomes elongated, with the bubble in the less dense layer collapsing quicker and jetting toward the other bubbles and the interface. The re-expansion of this bubble is comparable to that witnessed in the two bubble cases investigated, with a surface indentation being advected around the bubble from near the jet tip. This jet then directly affects the elongated central bubble, a feature not seen in the infinite fluid case until much later. This begins to form a jet shortly after the third bubble, unlike in the infinite fluid case where jetting only occurs after the other two bubbles have jetted. The cause of this jet is a combination of the jet forcing and attraction between the two homogeneous bubbles, as the corresponding attraction to the heterogeneous bubble is lessened by the presence of the interface. This can be seen through

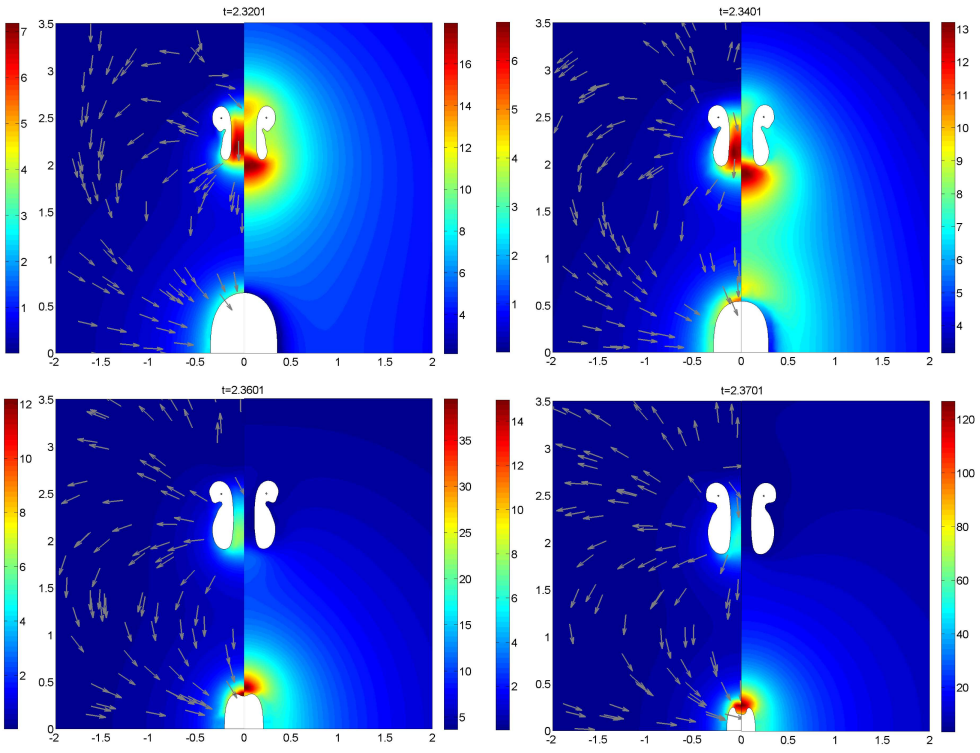

Figure 7.13: Pressure and velocity fields associated with the post-toroidal behaviour of three high pressure bubbles in an infinite fluid. This case is symmetric about $z = 0$, and so only the top half is shown.

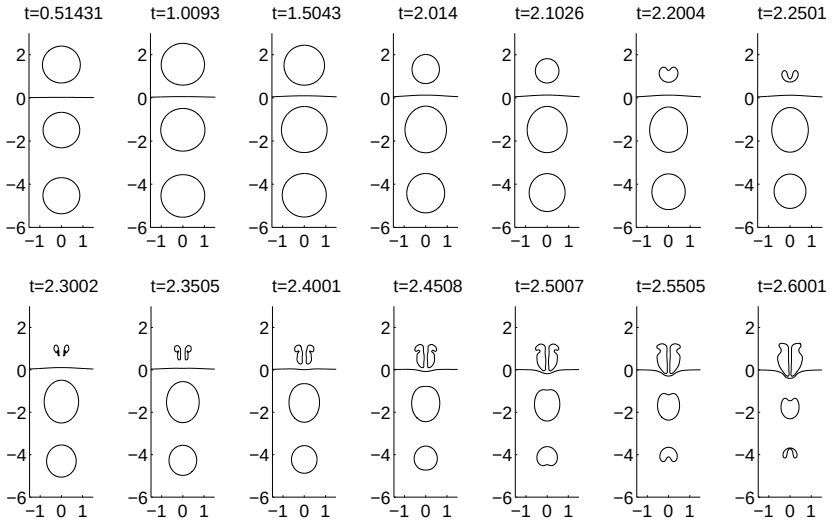

Figure 7.14: Three bubble interactions of laser type bubbles in a heterogeneous configuration about a two fluid interface with a density ratio of $\rho = 1.3$ and with two bubbles in the denser liquid layer. The standoff distances are $h_1 = 1.5$, $h_2 = -4.5$ and $h_3 = -1.5$.

the pressure fields in figure 7.15. One observes the high pressure region associated with the tip of the toroidal bubble jet extending down toward the central bubble, causing this bubble to jet when at a much greater volume than the single fluid case. The lower bubble is also about to jet toward the central bubble, as is indicated by the increasing pressure region below the opposing pole. Only the two bubbles in the same layer have a stagnation point separating them at this point, as the jetting action and re-expansion of the heterogeneous bubble has eliminated the stagnation point that would have occurred between itself and the central bubble. The central bubble may still form an upward jet due to the interaction of the liquid jet generated by the homogeneous bubble, although this simulation was stopped before such an interaction would form. Alternatively, the jet currently forming in the central bubble may impact the opposing side before this happens, resulting in extra-bubbular mixing in the fluid.

The comparable simulation with two bubbles in the lighter fluid layer generates some interesting insight into a possible improvement to fluid mixing processes. Figure 7.16

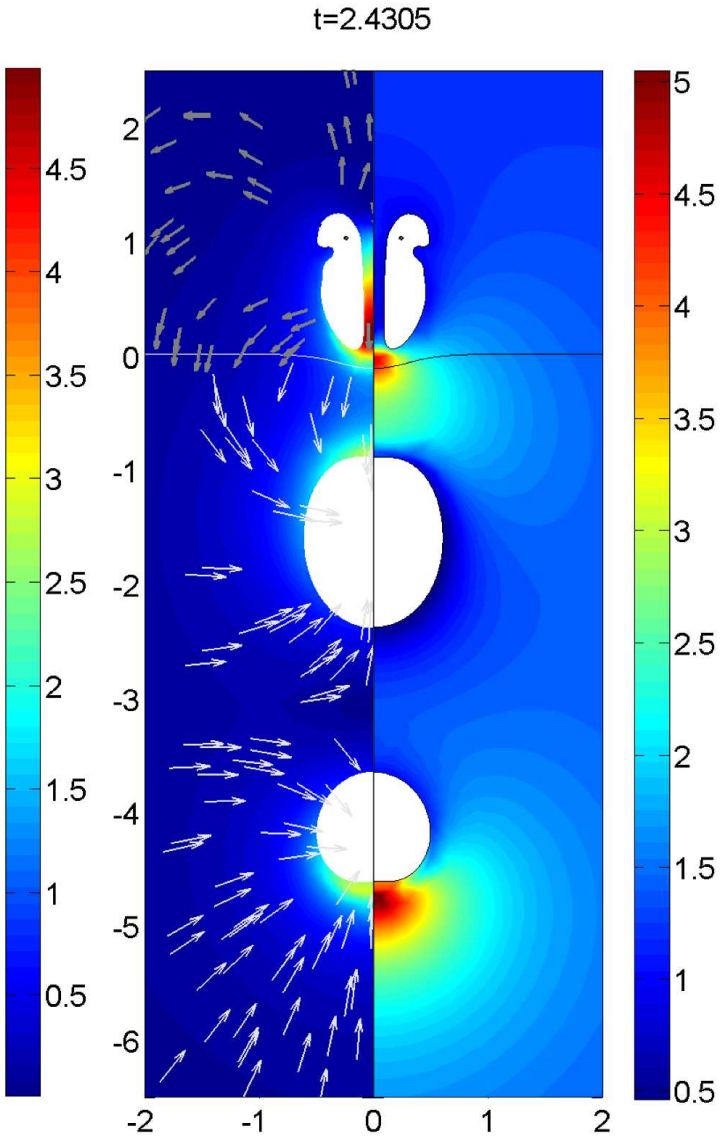

Figure 7.15: The interaction of three laser type bubbles with a fluid-fluid interface supporting $\rho = 1.3$. The bubbles have the parameters $\epsilon = 100$, $\gamma = 1.4$ and are initiated at $h_1 = 1.5$, $h_2 = -4.5$ and $h_3 = -1.5$.

shows the bubble shapes through the toroidal phases of the two homogeneously located bubbles. The toroidal behaviour of the first of these is very similar to that of the infinite fluid case. The roughly spherical bubble generates a jet toward the central bubble, and after impact the bubble forms a pronounced frontal lobe without much circumferential splashing. The collapse of the central bubble is however significantly different from the infinite fluid case. The elongation of the bubble is still present, with the denser layer bubble having more pull than the bubble in the lighter layer. The comparably earlier collapse of the homogeneous bubble nullifies the stagnation point formed between them, which in conjunction with this bubble's threading jet allows fluid to flow down about the top pole of the central bubble, seen in the first two time frames in figure 7.17. This causes this end to collapse faster, resulting in the tear drop shaped bubble in frames 4 and 5 of figure 7.16. This then causes a very fast slender jet to form through the central bubble, with velocities more than twice that of the other bubble jet. The pressures calculated by the impact of this jet are substantial as would necessarily be expected by the high flow rate. Combined with the re-expansion of the central bubble, and the accompanying translation toward the denser layer, this will subsequently cause a significant disturbance to the two liquid interface, which will be magnified by the upcoming toroidal jet of the denser layer bubble. Effectively, one has thereby generated a pumping system, forcing a great deal of fluid through the two bubble toroids toward the interface in the lighter fluid, followed by the forcing of fluid from the denser layer through the third bubbles toroidal motions. One envisages this to be more effective at mixing the two liquids than the alternate case in figure 7.14, as all bubble jets are formed in the direction of the interface.

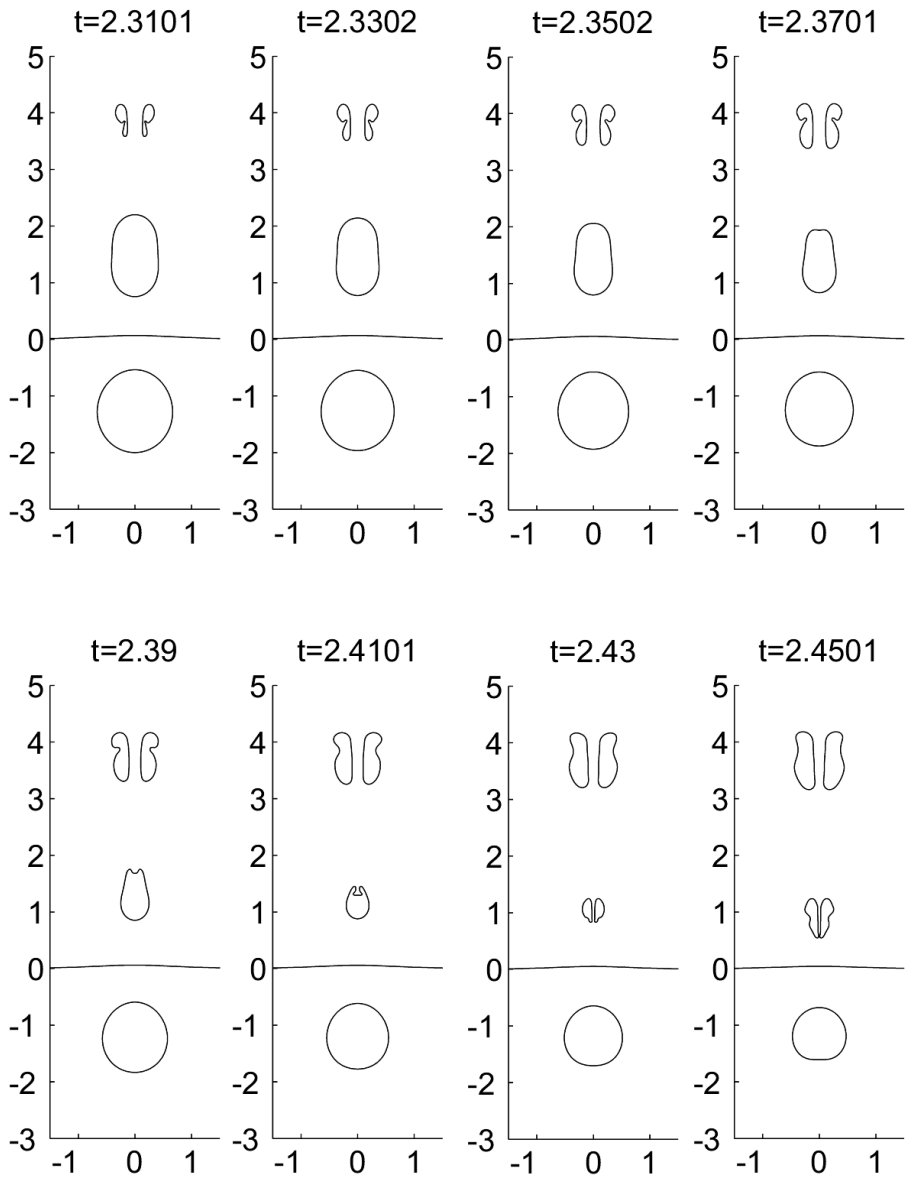

Figure 7.16: The evolution of a three bubble simulation with $\rho = 1.3$ and with two bubbles in the lighter layer. The frames show the behaviour through the toroidal phase of the two homogeneous bubbles.

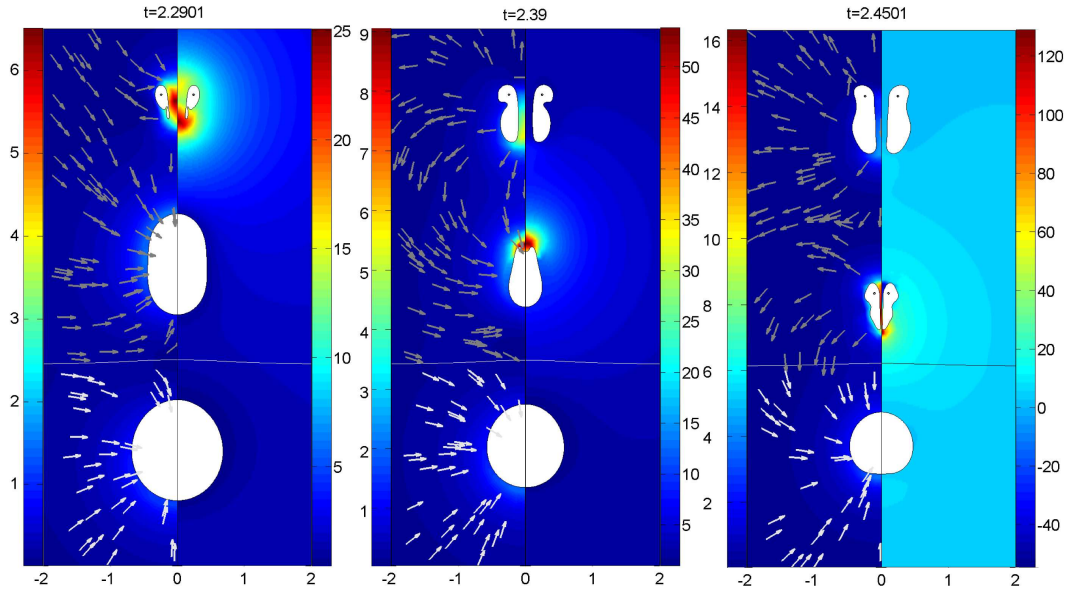

Figure 7.17: The evolution of a three bubble simulation with $\rho = 1.3$ and with two bubbles in the lighter layer. The frames show the behaviour through the toroidal phase of the two homogeneous bubbles.

7.4 Chapter Summary

This chapter has investigated the interaction of multiple high initial pressure bubbles with the fluid-fluid interface for a range of density ratios. This is of significant importance in mixing applications as it has provided some valuable insights into jet assisted mixing processes. It has shown that in purely homogeneous configurations interfacial distortion is lessened, as the jetting directions of the bubbles will be toward one another. This has been shown both when the bubbles are in a denser and a lighter fluid layer.

Straddling the interface has shown how bubble jetting can be used to increase deformations to the two fluid interface. This is not trivially expected, as in the case $\rho = 1$ for identical bubbles the effective image system will prohibit any movement of the interface in the normal direction. It has been shown that at the symmetrical standoff distance of $h_1 = h_2 = 1.5$, the jet from the faster collapsing bubble in the lighter layer may or may not have an effect on the jetting behaviour of the slower collapsing bubble in the

denser layer. It has also been shown that under certain conditions the second bubble may form jets at either pole caused by the Bjerknes attraction of the second bubble and the repulsive nature of the pre-existing jet. In other cases it has been demonstrated that the presence of the cavity in the second fluid can allow the jet from the less dense layer to deeply penetrate provided it is close enough to become entrained into the interface.

Further bubbles have been additionally simulated, and it has been shown that the presence of the interface allows jetting to occur that does not happen in a single infinite fluid. It has been demonstrated that in a three bubble case with equal separation distances, the most effective configuration for mixing will most likely be that of two bubbles in the less dense layer, as in all other configurations the central bubble is prone to jet away from the interface.

Chapter 8

Ultrasound activated cavities and their interaction with a tissue layer

In contrast to the previous two chapters, the initial behaviour observed in the following simulations is due to an acoustic field affecting an initially stable cavity. This is the type of behaviour most relevant in the use of ultrasound contrast agents, UCAs, in biomedical applications, including drug delivery and the instigation of sonoporation. The ratio of densities examined will for the most part be near unity, as this is most applicable in a biological context.

8.1 Initial conditions

At initiation, the pressure inside any cavities is taken to exactly balance the local pressure and surface tension. The minimum radius is taken dimensionally as $2.5\mu m$, the size of a typical UCA [70]. The simulations are however performed using dimensionless variables, and as such are applicable to cavities of any size accordingly. The acoustic wave is

modelled through a time dependent pressure term from the far field,

$$p_\infty(z,t) = p_\infty + p_{a\infty}\sin(kz - \omega t) \tag{8.1}$$

where p_∞ is the background pressure at infinity, $p_{a\infty}$ is the maximum amplitude of the wave, and $k = 2\pi f c^{-1}$ and $\omega = 2\pi f^{-1}$ are the wave number and radial frequency given the speed of sound of the liquid c and the frequency of the wave f. In order to ascertain the maximum bubble radius, the Rayleigh-Plesset equation (2.5) is non-dimensionalised with respect to the initial bubble radius, and is then numerically solved using a fourth order Runge-Kutta-Cash-Karp routine[1].

One notes here that a travelling pressure wave will cause fluid motion in the z direction. The behaviour of any cavitation bubbles will also be affected by their location with respect to the pressure peaks and troughs. In this work however the magnitude of this motion is assumed to be negligible in comparison to the motion induced by the expanding cavity. Hence in all cases here, a standing wave is used as opposed to a travelling wave. Whilst this is certainly expected to be valid near a rigid boundary due to wave reflection, it is not necessarily realistic in free field environments. It makes little difference however as the typical wave length is a least an order of magnitude greater than the length scale on which the bubbles oscillate. For example, a wave with frequency $0.2MHz$ and peak pressure $1.4MPa$ will have a wavelength of approximately $7000\mu m$ in water, and will cause a spherical cavitation bubble initially at equilibrium to grow to approximately $75\mu m$. For other examples see table (2.2). Additionally, the focus of this work is on the inertial effects of the cavitation bubbles, which in the situations envisaged here will most likely dominate. More violent shockwave interactions are beyond the scope of this work, although various methods have been developed to incorporate them into boundary integral simulations (see

[1]Effectively this is a fourth order Runge-Kutta method using an error estimator to determine step size. This error estimator is based on the comparison of two timesteps of size dt to one timestep of size $2dt$[31].

for example [20]).

8.2 Membrane effects

In addition to density variations across the two fluid interface, the effect of a membrane is considered. In this study various non-dimensional tension parameters are investigated, as the membrane tension present in biological structures may vary greatly.

To begin with consideration is given to the case $\rho = 1$. The surface tension along the membrane through two orders of magnitude is investigated, with the standoff distance taken at the sub-maximum radius distance $h = 0.7$. The oscillatory far field pressure term is given as $p_{a\infty} = 1MPa$ with the driving frequency given as $0.2MHz$. This provides a maximum bubble radius of approximately $60\mu m$, with a collapse time of approximately $6\mu s$. Figure 8.1 shows the collapse from maximum volume with the non-dimensional interfacial tension varying through two orders of magnitude, $\sigma_I \in \{0.01, 0.1, 1\}$. These values correspond dimensionally to tensions of $6\sigma_I Nm^{-1}$. In the first case, the behaviour remains predominantly spherical throughout the collapse, implying this tension value promotes very little deviation from the tension free case. For $\sigma_I = 0.1$ one sees non-spherical perturbations in the late collapse stage, resulting in an inverted mushroom shaped bubble. Further increasing the tension to $\sigma_I = 1$ leads to the earlier onset of this disturbance, with mushroom shaping beginning shortly after maximum volume. The effect on the membrane is also clearly visible. The initial collapse of the bubble in collaboration with the membrane tension drags the centre of the membrane downward, ending roughly 0.2 maximum bubble radii away from its rest position.

One now investigates the effect of standoff distance on this membrane behaviour, fixing the tension as $\sigma_I = 1$. This is shown in figure 8.2 for the standoff distances $h \in \{0.5, 1, 1.5\}$. At the greatest of these, $h = 1.5$, the membrane effect is heavily diminished. The bubble remains almost spherical throughout, developing only slight

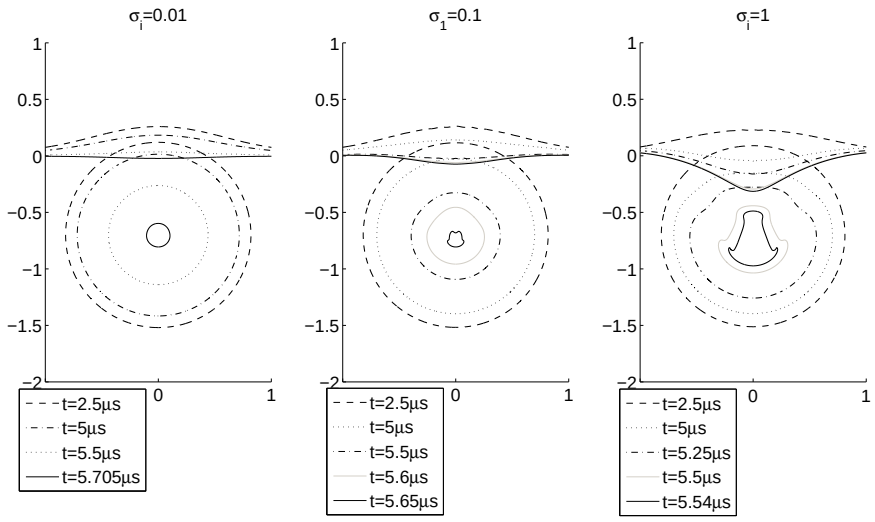

Figure 8.1: The effect of increasing the membrane tension through two non-dimensional orders of magnitude. The collapse phase for $h = 0.7$ is shown in each image at various different times.

perturbations toward the end of the collapse. The membrane itself returns to a near flat position at the end of the oscillation. Such behaviour is very different from that observed when varying the density ratio in Chapter 6, where for all the values of ρ tested at this standoff distance distinctive jetting was seen to occur. Decreasing the standoff distance by half a maximum bubble radius to $h = 1$, induces more significant perturbations. During the collapse phase there is some flattening of the near side of the cavity, which results in the development of a mushroom shaped bubble. Late in the collapse a further indentation forms on the nearer side of the bubble to the interface. The interface is more heavily perturbed, with a downward hump formed through the rebound from the earlier peak deformation. At the close standoff distance $h = 0.5$ very significant differences become apparent. The bubble expansion is retarded by the membrane, resulting in a flatter surface hump. Upon collapse, the interface remains close to the bubble. The two surfaces are however separated by a thin layer of fluid, and in this potential model do not come into

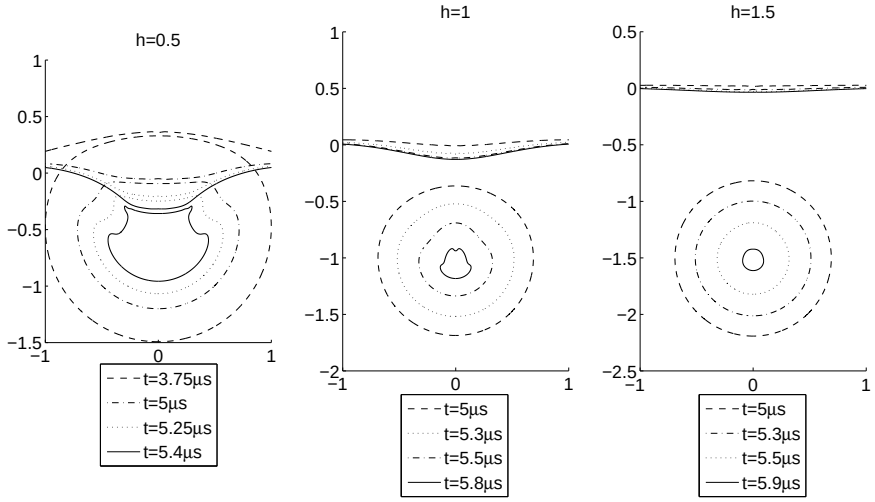

Figure 8.2: The affect of standoff distance on membrane effects with a $2.5\mu m$ bubble, driven by a standing acoustic wave with maximum amplitude $1MPa$ and frequency $0.2MHz$, with the membrane tension of $\sigma_I = 1$. From left, $h = 0.5,\ 1\ 1.5$.

contact. The bubble forms a horizontal indentation near to the interface, resulting in the severe shape perturbation at a large volume. The proximity of the rebounding interface forces the top of the bubble into a concave shape. A second indentation forms in a more horizontal direction and grows vertically along the edge of the bubble. This is unlike any of the behaviour yet seen in this work. It is however reminiscent of the experimental results in Brujan *et al* [18, 19] of laser bubble behaviour near an elastic boundary, and in qualitative agreement with the numerical and experimental result of Turangan *et al* [85], using high pressure spark generated bubbles near a thin elastic membrane with a tension of $43.6Nm^{-1}$. Some examples from the latter are shown in figure 8.3, for bubbles initiated at standoff distances of $h = 0.55$ and $h = 0.7$.

It is also important to investigate whether the membrane can affect the dynamics associated with the variation of the density ratio. In particular, it is of significant interest as to whether the direction of any bubble jetting induced by the density variation will be

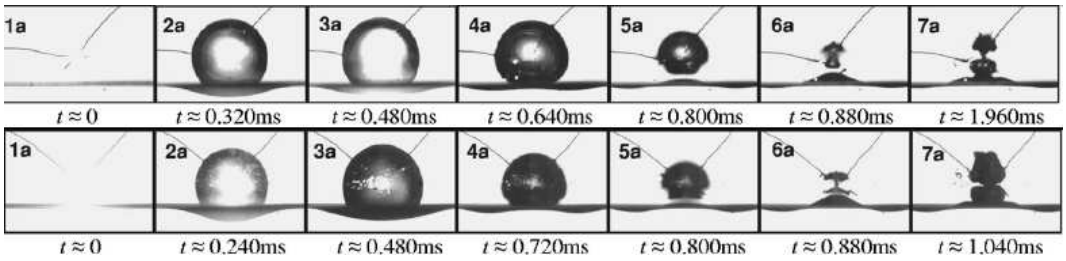

Figure 8.3: Experimental behaviour near a thin elastic membrane submerged in water with a tension of $43.6Nm^{-1}$, for standoff distances $h = 0.55$ (top) and $h = 0.7$ (base) taken from Turangan *et al* [85]. The bubbles are formed through spark discharge, with a maximum radius $R_{max} \approx 3.3mm$.

affected. Figure 8.4 contains four simulations for the density ratios $\rho \in \{0.6, 0.8, 1.2, 1.4\}$, with the fluid-fluid interface supporting unit non-dimensional tension. For the sub unity density ratios, one still observes the repulsive effect of the density discontinuity. In each case a very broad downward jet forms, which results in a non-axial impact. This is in stark contrast to the equal fluid case, where no jet formation is seen at a comparable time. The interface itself rebounds heavily in both cases, ending approximately $25\mu m$ from the initial location. This is in good agreement with the deflection observed for the unity density case.

The cases where $\rho > 1$ still show attraction toward the denser layer. The associated bubble dynamics illustrate the formation of an indentation on the near side of the bubble, giving the cavity a distinctive mushroom shape. The presence of the density jump then causes the larger far side of the bubble to collapse inwards as in the close standoff simulations in Chapter 6, which results in a fatter region near the interface. This is the opposite of the behaviour observed for $\rho = 1$ at this standoff distance. The interface behaves in a similar manner to the previous simulations, with a significant rebound toward the bubble. This may itself act as an accelerant to the subsequent jetting behaviour, which is still directed toward the interface. This is clearly seen for the case $\rho = 1.4$, the density of cornea [33]. The force of the impacting liquid jet is also sufficient to deflect the rebounded

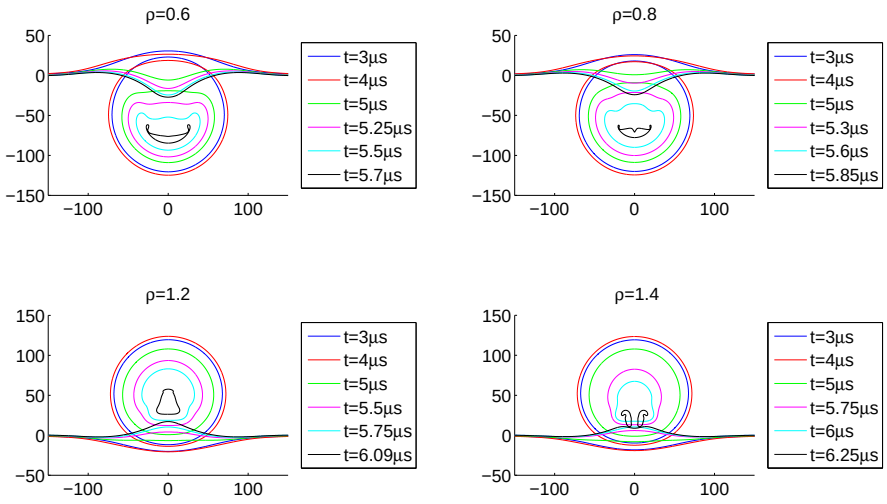

Figure 8.4: Bubble and surface shapes associated with acoustic driving with a frequency of $0.2MHz$, and a peak pressure of $p_{a\infty} = 1.4MPa$, with unit non-dimensional membrane tension.

membrane, which will lead to further elastic wave propagation along the interface. This is significant for cell permeation techniques, as it shows the rebound of the membrane is not necessarily sufficient to reverse the jet direction, and may in fact enhance the damaging mechanism further.

8.3 The influence of rigid backing

The behaviour observed can be significantly altered by the surrounding geometry. Here, one introduces a backing solid behind the second liquid layer. One may envision this as a model for sonoporation near a cell layer attached to a bone. Furthermore, this is indeed the situation in many in vitro experiments where a solid plate is used to mount a specimen, as in the investigations of Prentice *et al* [70] into UCA assisted sonoporation, for example.

The inclusion of this into the boundary integral method is performed using an image Green's function in one fluid layer, as has been done in many previous rigid boundary

simulations (see for example, [81, 65, 89]). In this work it need only be utilised for surfaces and field locations relating to the second fluid layer. The Green's function for a solid boundary located at $z = H$ is hence given by,

$$G^2(\mathbf{x}, \mathbf{x}_0) = \frac{1}{|\mathbf{x}_0 - \mathbf{x}|} + \frac{1}{|\mathbf{x}_0 - (2H\mathbf{e}_z - \mathbf{x})|}, \tag{8.2}$$

where the superscript 2 signifies this is the Green's function in liquid layer 2 only.

The normal derivative of this Green's function satisfies $\frac{\partial G^2(r,\theta,z=H)}{\partial n} = 0$. The normal velocity along the rigid boundary is also necessarily zero. Thus provided this layer remains simply connected, the corresponding surface integrals associated with equation (3.26) for the complete potential function ϕ_2 along the rigid boundary are identically zero. If any toroidal bubbles occur in this layer this will no longer be true, as the decomposed normal potential derivative will become non-zero. This has been countered in previous works by Wang [87] by incorporating an image system into the vortex ring component of the velocity in a similar way to the Green's function. In this work however one restricts the location of the cavities to layer 1 only, as this is taken to be a model for the behaviour of UCAs which by necessity will only be located in the extra cellular environment.

In vivo there may be micro cavities present inside the cell layer, which will be activated by the pressure fluctuation. However these are assumed to be inconsequential in comparison to the dynamics induced by the primary UCA. This assumption is made, as the necessary contaminant gas pockets are likely to be on the order of nanometres, whereas the UCA are on the order of micrometers and so will expand to a significantly larger size.

In layer 1 the image Green's function is not applicable in general. This can be proven using the density ratio $\rho = 0$. This layer would now suffer no influence from the wall until it came into contact. However should the image system be included, it would always be under the influence of the rigid boundary. As such the free space Green's function is still

used.

Along the two fluid interface one therefore has,

$$G^2(\mathbf{p},\mathbf{q}) = G(\mathbf{p},\mathbf{q}) + G^{im}(\mathbf{p},\mathbf{q}), \tag{8.3}$$

where the superscript im indicates the image of the free space Green's function in the rigid boundary. The boundary integral equations for the two fluid layers are coupled only through the normal velocity at the interface, and not through the choice of Green's functions. Hence the algebraic matrix equations governing the behaviour can be written as,

$$\begin{bmatrix} G_{bc} & 0 & -G_{bq} & \frac{\rho}{1+\rho}DG_{bq} \\ 0 & G^2_{de} & G^2_{dq} & \frac{-1}{1+\rho}DG^2_{dq} \\ G_{pc} & G^2_{pe} & G^{im}_{pq} & \frac{\rho-1}{\rho+1}DG_{pq} - 2\pi I_{pq} - DG^{im}_{pq}\frac{1}{1+\rho} \\ G_{pc} & -G^2_{pe} & -2G_{pq} - G^{im}_{pq} & DG_{pq} + 2\pi\frac{1-\rho}{1+\rho}I_{pq} + DG^{im}_{pq}\frac{1}{1+\rho} \end{bmatrix} \begin{bmatrix} \frac{\partial\psi_1(b)}{\partial n_1} \\ \frac{\partial\phi_2(d)}{\partial n_2} \\ \frac{\partial\phi_2(p)}{\partial n_2} \\ \psi_1(p) + \phi_2(p) \end{bmatrix}$$

$$= \begin{bmatrix} 2\pi I_{bc} + DG_{bc} & 0 & \frac{-1}{2+2\rho}DG_{bq} & G_{bq} \\ 0 & 2\pi I_{de} + DG^2_{de} & \frac{-1}{2+2\rho}DG^2_{dq} & 0 \\ DG_{pc} & DG^2_{pe} & \frac{-1}{1+\rho}DG_{pq} - \frac{1}{2(1+\rho)}DG^{im}_{pq} & G_{pq} \\ DG_{pc} & -DG_{pe} & 2\pi\frac{1}{1+\rho}I_{pq} + \frac{1}{2(1+\rho)}DG^{im}_{pq} & G_{pq} \end{bmatrix} \begin{bmatrix} \psi_1(b) \\ \phi_2(d) \\ \tilde{F}(p) \\ -vr_{1n_2}(p) \end{bmatrix}. \tag{8.4}$$

8.3.1 Membrane peeling at sub-MHz frequencies

A particularly interesting feature discovered in this research is the removal of the 'tissue', or 'cell', layer from the substrate through the toroidal action and re-expansion of the cavitation bubble or UCA. This behaviour is referred to here as membrane peeling.

To begin one examines the system governed by $\rho = 1$, under the influence of an

acoustic wave with a frequency of $0.2MHz$ and a maximum amplitude of $p_{a\infty} = 1.4MPa$. The rigid boundary is located at a dimensional distance of $H = 25\mu m$ from the two-fluid interface, roughly corresponding to a non-dimensional distance of 0.34 maximum bubble radii. The tension on the interfaces is of low order, and so it will not significantly affect the simulation. The model therefore is very close to the collapse of a bubble in an infinite fluid near to a rigid boundary, albeit in the presence of a membrane with little tension. Figure 8.5 shows the associated bubble behaviour as the standoff distance is varied through $h \in \{0.5, 0.75, 1, 1.25\}$ during the later stages of collapse, and the complete simulation of the case $h = 0.75$ is shown in figure 8.6 for clarity. For the larger standoff distance, one observes the formation and expansion of the bubble toroid, resulting in the forward lobe. This is seen to close at the tip as the bubble continues to evolve. At the closer standoff distances, the toroidal bubble interacts with the wall, resulting in the forward lobes being forced outward radially. Consequently, the bubble jet will not pinch off as rapidly as the bubble re-expands. The fluid-fluid interface in these cases is initially compressed against the wall in the region directly below the mouth of the liquid jet. The re-expansion of the forward toroidal lobes then cuts underneath the interface, lifting the fluid in the second layer away from the substrate. It is this interaction that one describes as membrane peeling.

This presents a significant new mechanism for tissue damage. Circumstantial evidence may be visible in the cornea specimen micro-graph in figure 1.1 created by Vogel [86]. Here a large area with a radius of approximately $100\mu m$ surrounding the jet impact location has been scraped away. Previous work has postulated that this is due to the shear stress caused by the high fluid velocity beneath the bubble. This membrane peeling may however provide an additional mechanism, associated with the re-expansion of the toroidal bubble.

Varying the membrane tension may provide a better approximation to a biological

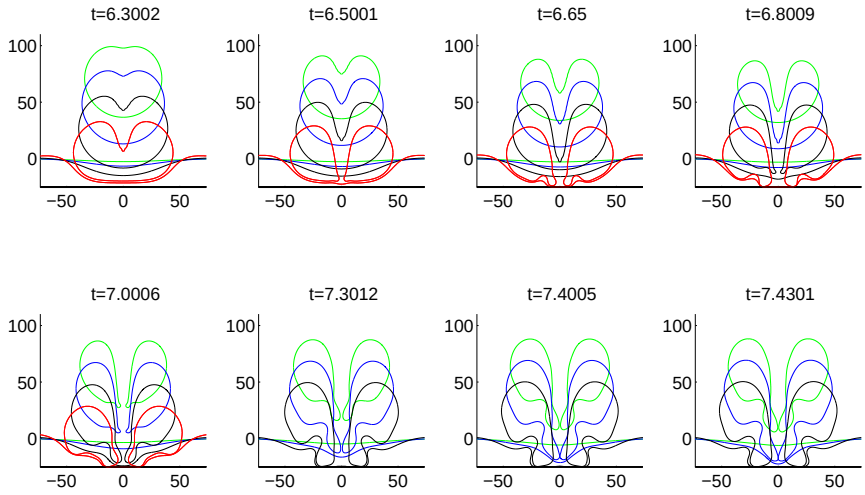

Figure 8.5: Toroidal bubble action near a cell layer of depth $H = 25\mu m$ and relative density $\rho = 1$, due to a $2.5\mu m$ micro cavity excited by an acoustic wave with a frequency of $0.2MHz$ and a maximum amplitude of $p_{a\infty} = 1.4MPa$. Bubble initiation is at $h = 0.5$ (red), $h = 0.75$ (black), $h = 1$ (blue) and $h = 1.25$ (green).

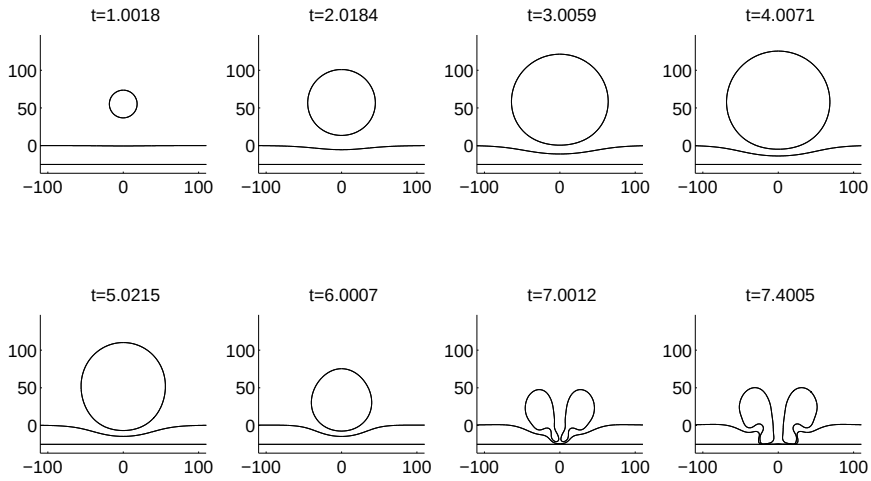

Figure 8.6: The lifetime of a bubble initiated at $h \approx 50\mu m$ to a cell layer of depth $H = 25\mu m$ and relative density $\rho = 1$. The bubble is activated by an ultrasound wave with a frequency of $0.2MHz$, and a maximum pressure of $p_{a\infty} = 1.4MPa$.

tissue. Importantly, it will show whether the bulk fluid motion is a result of the inclusion of the rigid boundary, or the influence of the membrane. Figures 8.7 and 8.8 show simulations using a $0.2MHz$ acoustic wave with maximum amplitude $p_{a\infty} = 1MPa$ at a standoff distance of $h = 1 \approx 60\mu m$. The surface tension on the bubble surfaces is $\sigma_b = 0.00165$ to model the effect of a UCA, and the membrane tensions used are $\sigma_I = 0, 1$ respectively. The backing plate is again located at $H = 25\mu m$ dimensionally. The shapes in the zero tension case naturally agrees with a single layer of fluid with $h \approx 1.35$, as did the simulation shown in figure 8.6. The bubble toroid forms as normal, with the advancing jet and lobe forcing the interface against the backing plate. The inclusion of unit membrane tension significantly inhibits this behaviour. The rebounded interface causes the near boundary side of the interface to flatten in comparison to the rounded shape observed in its absence. The bubble forms a jet directed toward the interface, in contrast to the behaviour of a bubble near a floating membrane with the same tension. As the toroid forms, the circular disturbance is initially forced outwards. The jet forms a wide pit in the tissue layer, and the advancing bubble then slides in along the sides of the pit.

The pressure and velocity fields associated with this injection into the tissue layer can be seen in figure 8.9, with the frames taken at dimensional times $5.9\mu s$, $5.95\mu s$ and $6.0\mu s$. Due to the frequency examined here, these occur roughly one microsecond after a complete acoustic cycle. The pressure applied by the sound wave is approximately $-0.95MPa$, approaching the second pressure minimum. The pressures observed near the impact zone however far outweigh this, being over $10MPa$ just after toroidal formation, although the pressure inside the second layer falls as the bubble re-expands. Before the toroidal phase, the liquid in the cell layer is flowing toward the cavitated layer to some extent, with a somewhat axial direction. After impact, this causes a point of zero velocity to form on the axis below the jet, which rapidly translates toward the wall. One then observes the translation of a stagnation point along the rigid boundary, with fluid forced

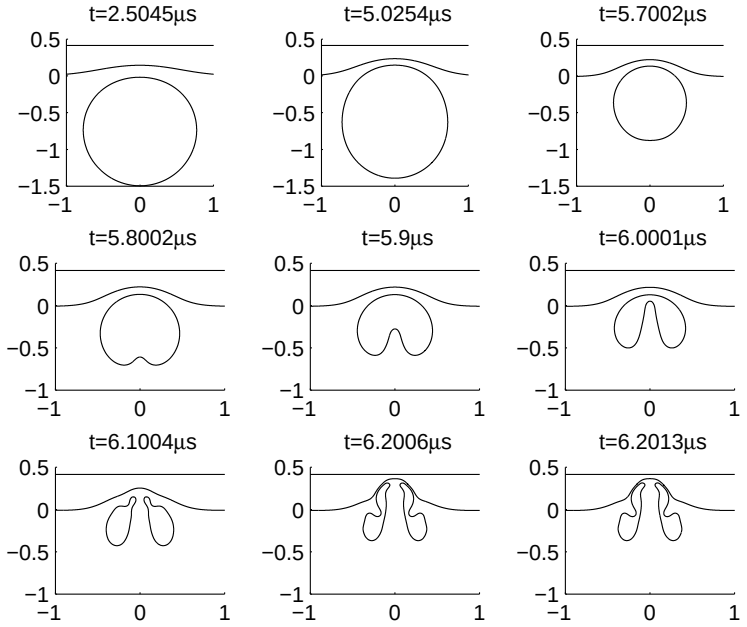

Figure 8.7: Shapes from the simulation of a bubble driven by an acoustic wave with frequency $0.2MHZ$ and peak pressure $p_{a\infty} = 1MPa$. The parameters of the flow field are $H = 25\mu m,\ \rho = 1,\ h = 1 \approx 60\mu m$. The membrane has zero interfacial tension, $\sigma_I = 0$.

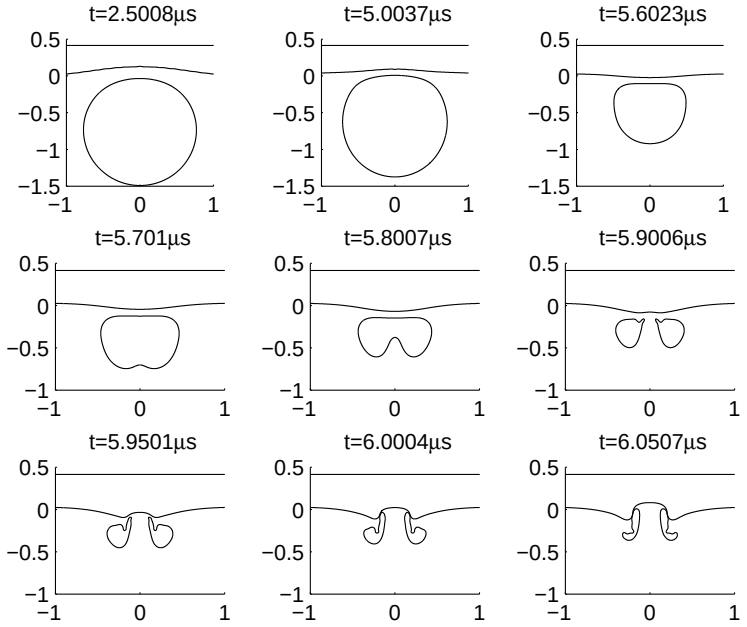

Figure 8.8: Shapes from the simulation of a bubble driven by an acoustic wave with frequency $0.2MHZ$ and peak pressure $p_{a\infty} = 1MPa$. The parameters of the flow field are $H = 25\mu m,\ \rho = 1,\ h = 1 \approx 60\mu m$. The membrane has unit interfacial tension, $\sigma_I = 1$.

radially outward by the jet being deflected toward the cavitated layer by the axially directed flow resultant of the bubble compression. The high pressure region focused at the impact site also dissipates outwards as the bubble jet continues to penetrate. These factors force the fluid near the forward bubble lobe to flow upward, exacerbating the height of the jet pit wall.

As in the floating membrane cases, one seeks to asses the effect of varying the density ratio. The following simulations were driven by a standing acoustic wave with peak pressure $p_{a\infty} = 1.4MPa$ and a frequency of $0.2MHz$. The cell layer depth is $H = 25\mu m$, with the standoff distance fixed at $h = 1$, approximately $73\mu m$. The bubble surface tension and interfacial tension are $\sigma_b = 0.01$ and $\sigma_I = 1$ respectively, before non-dimensionalisation. The bubble surface tension acts to inhibit the leading edge of the toroid from rejoining, allowing the simulation to proceed further and hence to increase the calculated peeling effects. This is more representative of a UCA than the case with zero surface tension. The extent of peeling for density ratios $\rho \in \{0.8, 0.9, 1.1, 1.2\}$ is shown in figure 8.10 for the same time frame. In all cases the under cutting of the cell layer is visible. The bubble shapes show some variation, although all form the same general 'C' shaped structure in the r, z-plane, with the density ratios furthest from unity showing slightly more peeling. However, this does not appear significant, and so one may conclude that there is little variation in peeling for density ratios close to 1.

8.3.2 Backed behaviour at 1 MHz

In the previous examples, the sub-megahertz frequency allowed the cavity to expand greatly, to a radius much larger than the typical dimensions of a cell. Indeed the peeling observed in figure 8.10 was over a region with radius approximately $40\mu m$, four time the size of a typical eukaryotic cell, and would have continued significantly further as the bubble re-expanded. At megahertz frequencies however, the bubble expansion is

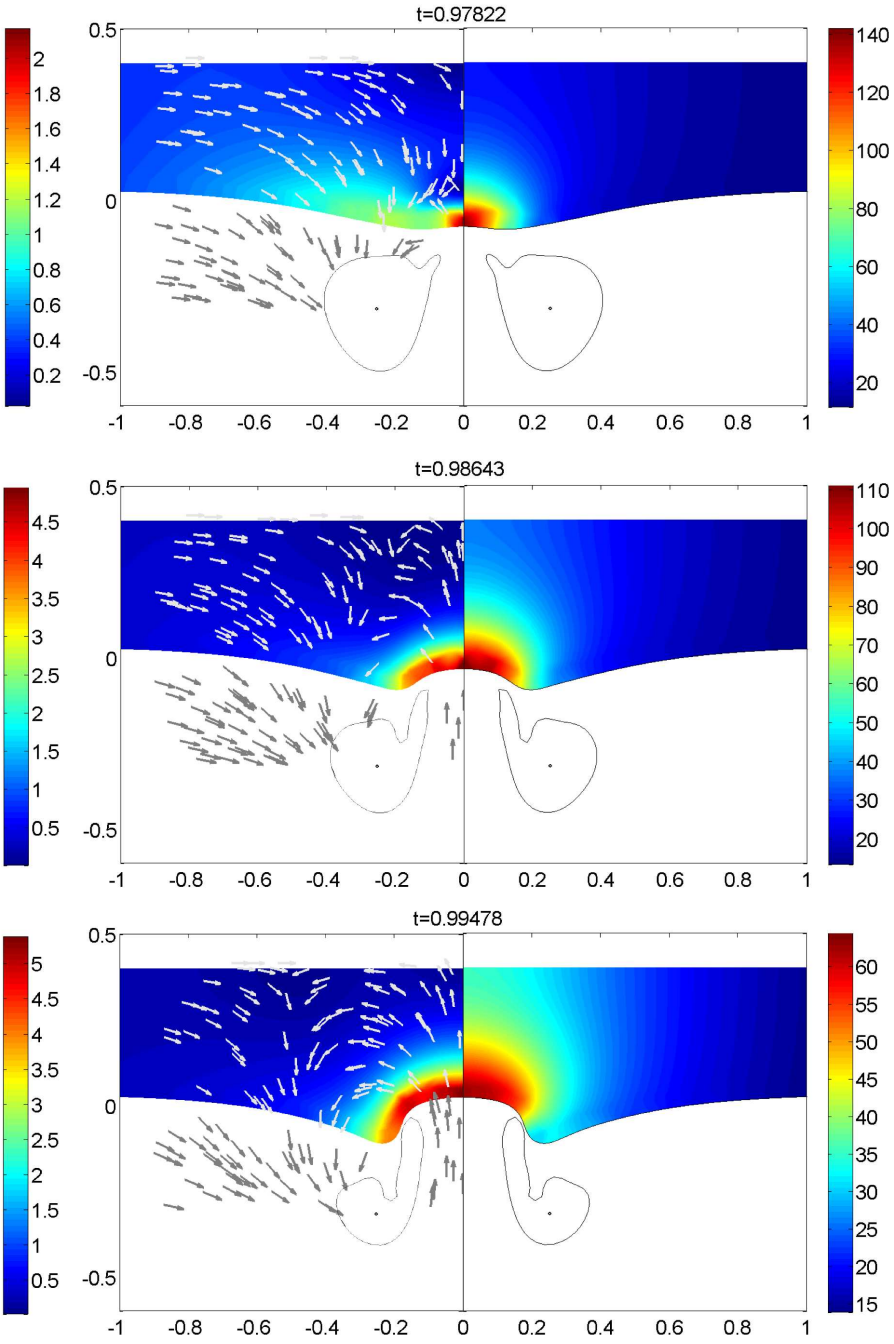

Figure 8.9: Pressure and velocity in the cell layer after bubble jet impact has occurred for $p_{a\infty} = 1MPa$, frequency$= 0.2MHz$, $H = 25\mu m$, $\rho = 1, h = 1 \approx 60\mu m$. The membrane has unit interfacial tension. Dimensional times are $5.9\mu s$ (top), $5.95\mu s$ (centre) and $6.0\mu s$ (base).

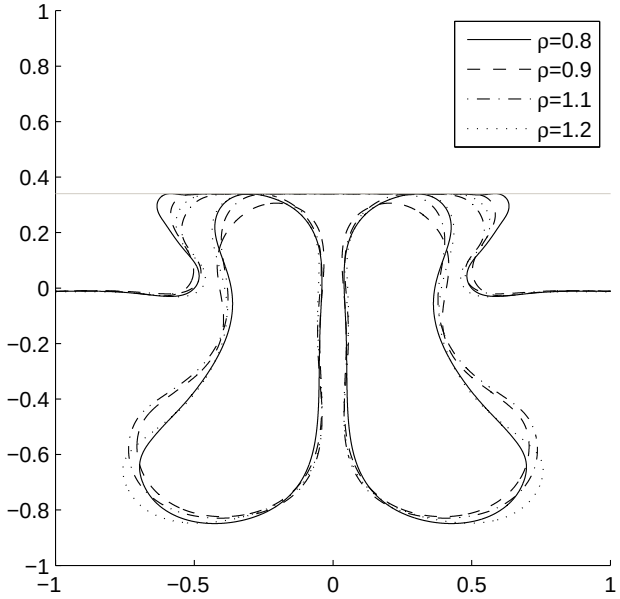

Figure 8.10: Comparison between bubble and interface shapes as ρ is varied near unity under identical acoustic forcing, surface tension and standoff distances. The depth of the second layer is dimensionally $H = 25\mu m$.

restricted, and as such it is unclear if the peeling behaviour is still observed, given that surface tension in particular will have a more significant effect. Additionally, with this restricted maximum bubble radius, it is now reasonable to investigate varying the depth of the cell layer, as the maximum radii is on the size order of a eukaryotic cell.

One simulates the dynamics of a UCA characterised by $R_{ref} = R_e = 2.5\mu m$, with dimensional surface tension $\sigma_b = 51\frac{dyne}{cm}$ representative of a Sonovue UCA [54]. The bubble is driven by an ultrasonic wave with a frequency of $1MHz$, and a peak pressure $1MPa$. This results in a maximum bubble radius of $R_{max} = 13.18\mu m$. A standoff distance of $h_{dim} = 9.881\mu m$ is chosen, corresponding to the non-dimensional standoff distance $h = 0.75$. As was seen previously, the density of the cell layer does not have a significant effect in this phenomena, and as such the density ration $\rho = 1$ is taken. The membrane is loaded with a tension of $0.5\frac{dyne}{cm}$.

The first simulation in this regime is shown in figures 8.11 and 8.12, illustrating the pre and post toroidal phases of the collapse respectively. The pressure fields in both graphs do not include the pressure wave, and as such show the pressure exerted by the collapsing bubble only. The first frame in the pre-toroidal figure is taken near the maximum radius of the bubble, at the start of the first collapse. Interestingly a stagnation point is clearly visible along the wall in the second fluid layer, as fluid is still being forced outwards by the advancing bubble front, whilst the fluid in the far field is being sucked back in toward the centre. Minimum pressures are around $1MPa$, and so the total pressure will be near equilibrium about the bubble, and between the bubble and the wall. As the collapse continues one observes the removal of the stagnation point, as the bubble contracts sucking water inward. The inevitable high pressure region begins to form behind the bubble and will drive the subsequent jet toward the cell layer. The interface itself remains similarly disturbed about the axis, whilst it has recovered toward the initial position elsewhere. As jetting begins, the bubble is rapidly moving toward the wall, and as expected liquid is being forced into the jet at high velocity. Jet tip speeds for this case were of the order of 10 non-dimensional units, corresponding to about $100ms^{-1}$ and thereby subsonic.

At impact, a peak pressure of approximately 40 atmospheres is exerted in the near vicinity. This acts to accelerate the fluid below the bubble away, and causes a distinct deformation of the interface. The bubble then begins to expand, and a stagnation point forms behind the bubble jet. The jet velocity itself is slowed to around 6 non-dimensional units at the fastest point. The high pressure decreases and becomes more focused at the axis near the wall, forcing fluid sideways. The forward lobe of the toroidal bubble expands downward, until the wall prohibits any further advancement. This acts to prohibit fluid escaping the base of the jet, which re-increases the pressure at the jet tip to approximately 40 atmospheres. The bubble lobes are forced outward along the wall, and begin to undercut the separated layer. As the process continues, the membrane becomes

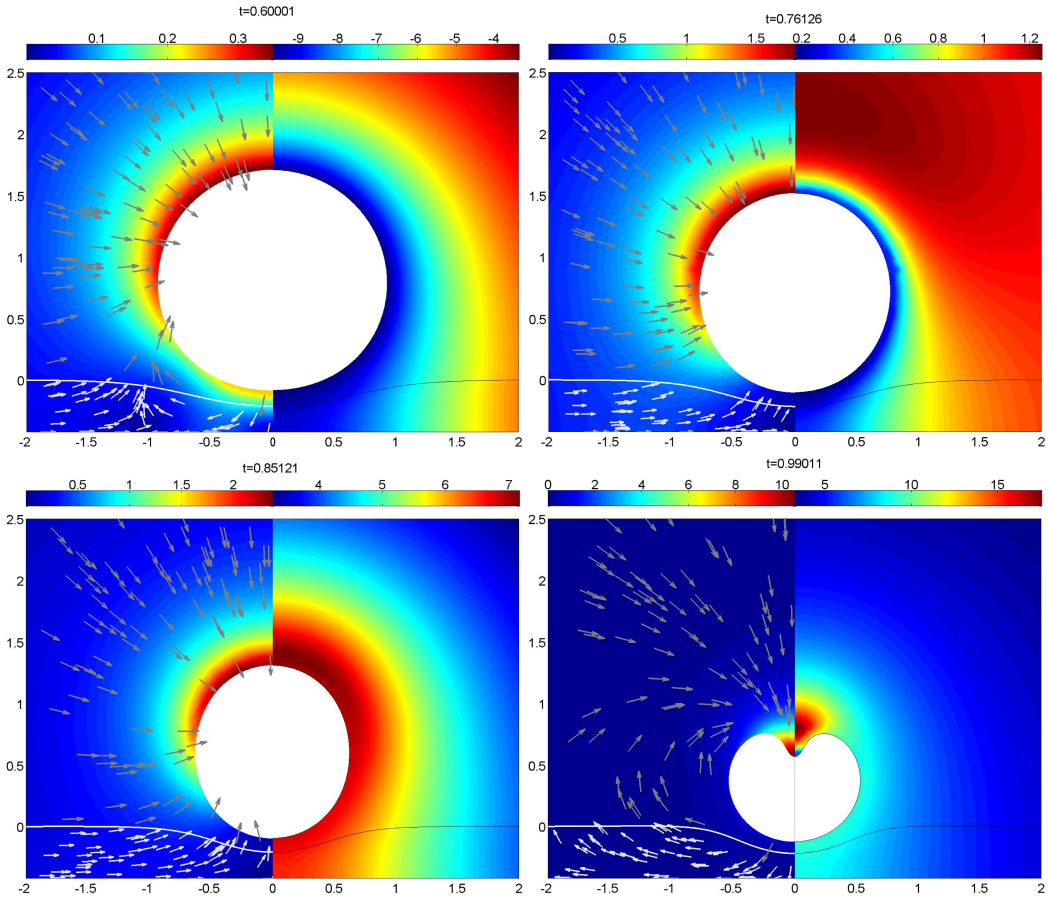

Figure 8.11: Speed and velocity (left) and pressure (right) fields during the pre-toroidal phase for a UCA undergoing a forcing of $p_{a\infty} = 1MPa$ at a frequency of 1 MHZ, at an initial standoff distance $h = 0.75$ and with a rigid wall located at $H = 0.42$. The UCA has surface tension $\sigma_b = 51\frac{dyne}{cm}$, whilst the membrane separating two equal density layers has tension $\sigma_I = 0.5\frac{dyne}{cm}$.

entrained into the fluid pocket between the two bubble lobes. The pressure drops near the wall as the jet base expands, and a region of higher pressure is observed to form on the other side of the toroidal bubble in the cell layer. Hence the peeling motion is again observed in this parameter regime, albeit at a smaller length scale than above.

Decreasing the layer depth creates some distinct differences in the peeling behaviour. Figures 8.13 and 8.14 contain bubble shapes and pressure and velocity fields for the case $H = 0.2$ respectively, with time frames beginning just after jet impact and continuing

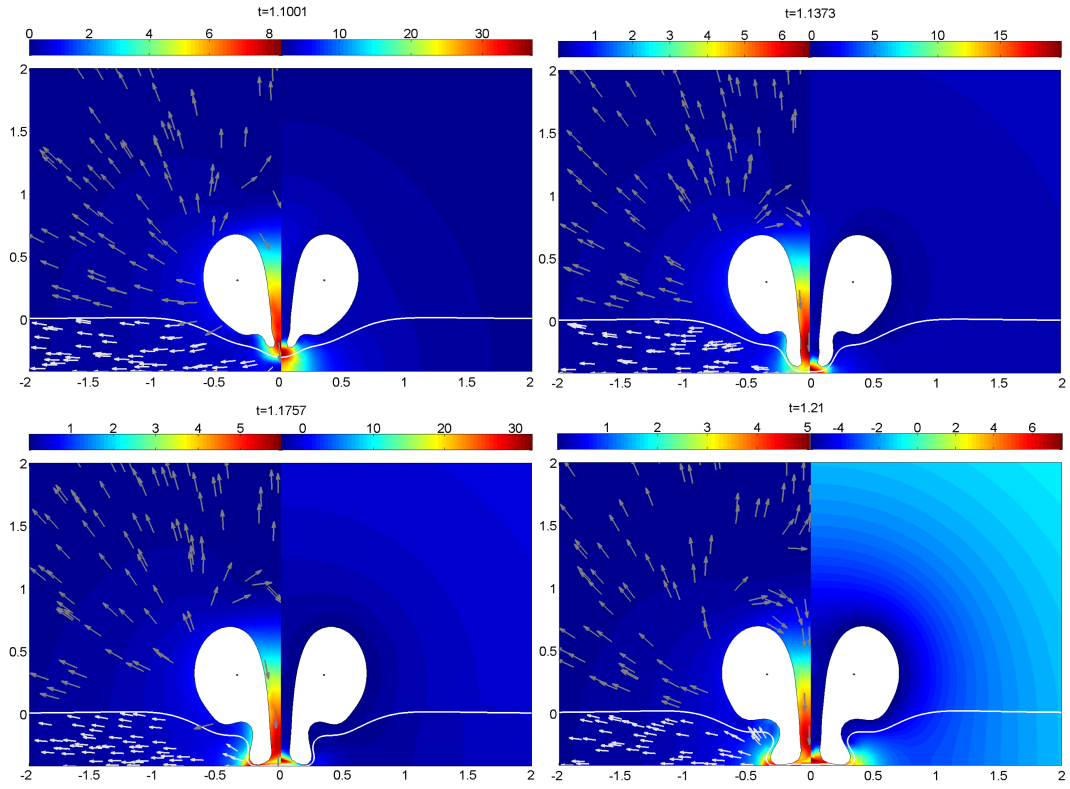

Figure 8.12: Speed and velocity (left) and pressure (right) fields during the post-toroidal phase for a UCA undergoing a forcing of $p_{a\infty} = 1MPa$ at a frequency of 1 MHZ, at an initial standoff distance $h = 0.75$ with a rigid wall located at $H = 0.42$. The UCA has surface tension $\sigma_b = 51\frac{dyne}{cm}$, whilst the membrane separating two equal density layers has tension $\sigma_I = 0.5\frac{dyne}{cm}$.

through the development of the forward bubble lobe. Impact occurs at a distance of approximately 0.1 maximum bubble radii from the wall and at half the initial depth of the second layer. Significantly high pressures are observed about the impact site, on the order of 100 atmospheres, and well above the driving pressure $p_{a\infty}$. Jet velocities are in excess of 12 non-dimensional units about this region, and are rapidly slowed to below 6 by the near stationary fluid in front of the jet. From the velocity directional arrows, it can be seen that at this point the bubble is already expanding, with fluid being forced outward along the lower layer, with the fluid in the primary layer being driven around the toroid. A stagnation point has formed at approximately 1.2 maximum bubble radii away from the initial level of the interface, although this appears to have little effect on the quantity of liquid entering the bubble jet. As time advances 0.2 non-dimensional units, the pressure about the impact point lessens significantly toward a maximum of 55 atmospheres at the end of the jet next to the rigid boundary. By this time the interface has been forced flat against the wall over a radius of 0.1 maximum bubble radii. The velocity of the jet has decreased somewhat, with the rest of the field still exhibiting the same flow properties. Advancing time by a further 0.1 non-dimensional units presents the beginning of the peeling motion. The advanced ring of the toroidal bubble has been arrested by the presence of the wall and the outer ring jet has begun to form, forcing fluid upward and toward the central jet. The pressure has again dropped, with the maximum pressure occurring inside the fluid pocket generated by the advancing bubble lobe and the wall. Maximum pressure is now approximately 40 atmospheres, still greatly in excess of the driving amplitude. A region of pressure at about 20 atmospheres has also formed directly below the secondary jet ring. At the end of the simulation, the peeling effect can clearly be seen. The forward lobe has forced the second layer to a near vertical position as the bubble has further re-expanded. The pressure now observed has massively increased toward 160 atmospheres on the outside of the bubble in the lower layer, demonstrating

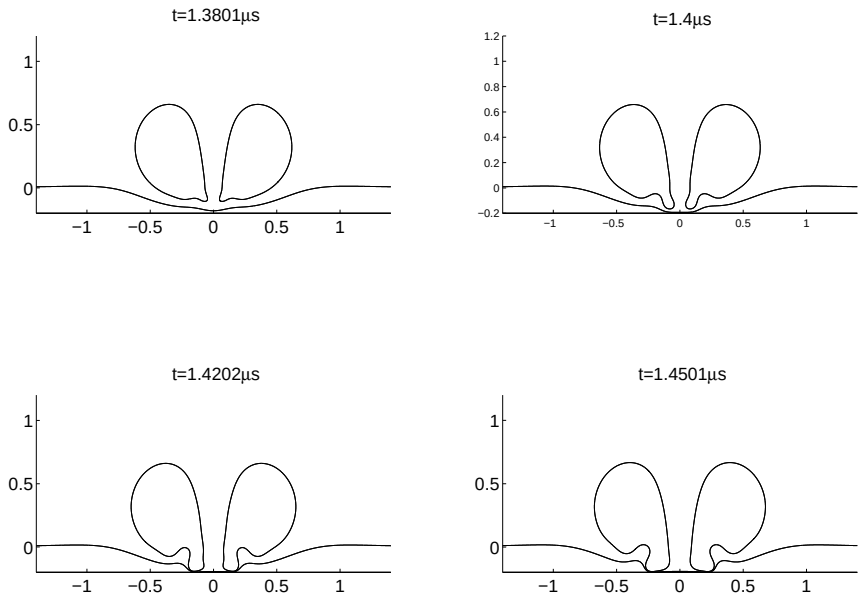

Figure 8.13: Bubble shapes during the toroidal phase of a UCA collapse near a backed liquid layer. The dimensional simulation parameters are $R_{ref} = 2.5\mu m,\ \sigma_b = 51\frac{dyne}{cm},\ \sigma_I = 0.5\frac{dyne}{cm},\ \rho = 1,\ p_{a\infty} = 1MPa$ with the acoustic wave driven at a frequency of $1MHz$. The non-dimensional standoff distance from the interface is $h = 0.75$, with the depth of the second layer $H = 0.2$.

that damage may continue to be caused well after jet impact. The velocity field also illustrates the rolling motion of the secondary ring jet about the toroid, with fluid moving upward toward the bubble centre at a significant velocity. Additionally the stagnation point has also translated downward to 1 bubble radii above the initial interface position, while the maximum jet velocity has decreased to 6 non-dimensional units. It would be reasonable to assume that significant damage would be caused to a tissue layer in this configuration through inertia alone.

Increasing the cell layer depth generates drastically different behaviour. This is first demonstrated in figures 8.15 and 8.16, containing the pre and post jet impact fluid motion and pressure fields for $H = 1.6R_{max}$. At maximum bubble radius the bubble and flow field

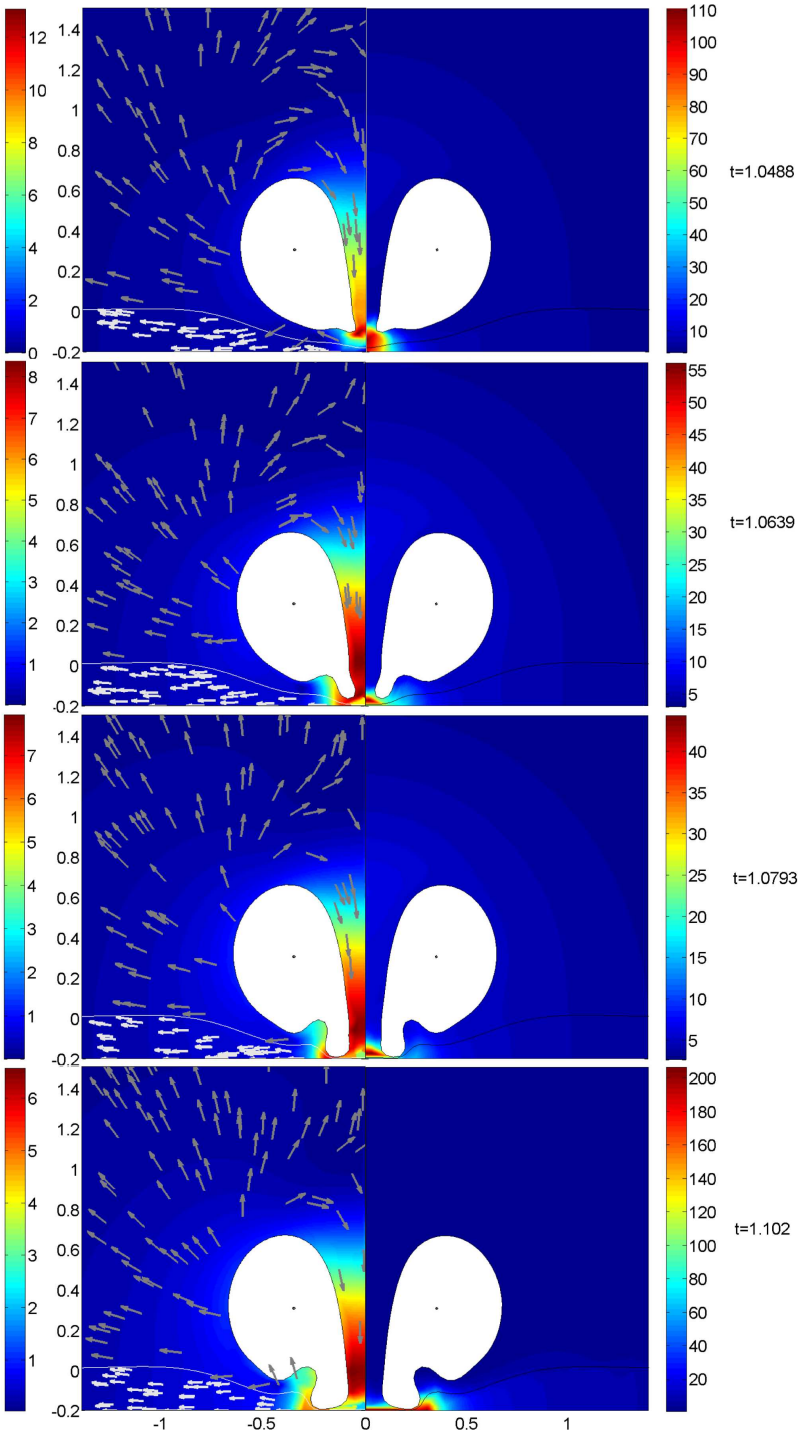

Figure 8.14: Velocity and Pressure fields for a bubble as characterised in figure 8.12, during the toroidal phase with layer thickness $H = 0.2R_{max}$

exhibit the usual characteristics. The shape is roughly spherical, with the near pressure increasing in a uniform radial manner. Toward the wall fluid is naturally advected away from the axis, although the fluid velocity is near zero. As the bubble collapses, the classical higher pressure region above the bubble may be seen, with the fluid moving slightly faster in this region. As the jet forms, one observes the liquid in the primary layer being driven about the bubble and into the jet, with the formation of a stagnation point above the bubble at approximately $2.25R_{max}$. By this point the bubble centroid has migrated approximately $0.25R_{max}$ toward the interface and the wall, whilst the interface has returned toward being flat.

The most significant differences occur during the toroidal phase. Firstly, the pressures around the jet impact site are significantly lower. This is due to the presence of a much thinner jet, caused in part by the rapid migration of the over bubble stagnation point to a position of 1, restricting fluid flow into the jet. The increased depth also allows for the pressure to dissipate more before the wall. As this phase continues, the advance of the forward lobe is not arrested by the rigid boundary, and continues to drive the interface downwards as the bubble begins to collapse. The stagnation point also disappears, allowing more liquid to flow through the toroid. The advance of the bubble is slowed by the fluid flowing upward in the lower layer due to the bubble volume compression, and which is itself deflected around the forward bubble ring. The higher pressure region about the impact site dissipates greatly, almost to equilibrium with the surrounding pressures. As the simulation continues, one observes the fluid in the lower layer flowing around the tip and back in toward the axis, causing the bubble to pinch and the interface to create an overhang. At the rear of the bubble a high pressure ring forms, creating a secondary jetting motion about a torus. Velocities about this jet are comparably high to the initial jet, being of magnitude approximately 8. It is reasonable to expect that this ring jet will cause less damage to the tissue layer than the first, as it is effectively from a smaller

bubble. The tissue layer itself has returned to its initial position over $r > 0.6R_{max}$, a significantly larger area than achieved in the closer collapses. This type of behaviour may be more beneficial for drug injection, as less damage to the cell layer appears to have occurred. Additionally, the forward bubble lobe may break off, with the interface potentially reforming above it, literally injecting a section of the bubble into the tissue. This is very different from the thin layer cases, where the section of bubble connecting the two lobes remained reasonably broad.

Increasing the layer depth further to $H = 2.0$ maximum bubble radii produces similar results. One may see this in figure 8.17 at non-dimensional times $t = 1.178$, $t = 1.216$, and $t = 1.299$. The first of these frames occurs after jet impact, with a developed forward lobe. At this time fluid in the region of the interface is flowing nearly parallel to it. The pressure spike formed by the jet impact has diminished somewhat, yet is still clearly visible. The second frame is taken shortly before the over pressure reaches its maximum. In contrast to the first frame, the fluid flow is now perpendicular to the interface, and there is a substantial movement of liquid toward the top of the threading jet. Fluid in the lower layer is still moving away from the bubble, indicating the bubble is still expanding at this point.

The final frame is taken just after the overpressure has reached a maximum, and as can be clearly seen by the velocity field the bubble is re-collapsing. Fluid near the interface is now flowing parallel to it in the direction of the bubble. A clearly visible feature is the formation of a hollow hemi-spherical pressure cap above the jet mouth, with a maximum pressure and velocity located at about $r = 0.4$. This will result in a secondary bubble jet forming from the outer edge of the ring. The bubble jet itself is still significantly faster than the fluid it is entering into, and a stagnation point will have formed between the jet and the liquid being forced upward by the decrease in bubble volume. This will inhibit the advancement of the forward bubble lobe into the second fluid layer, which may be of

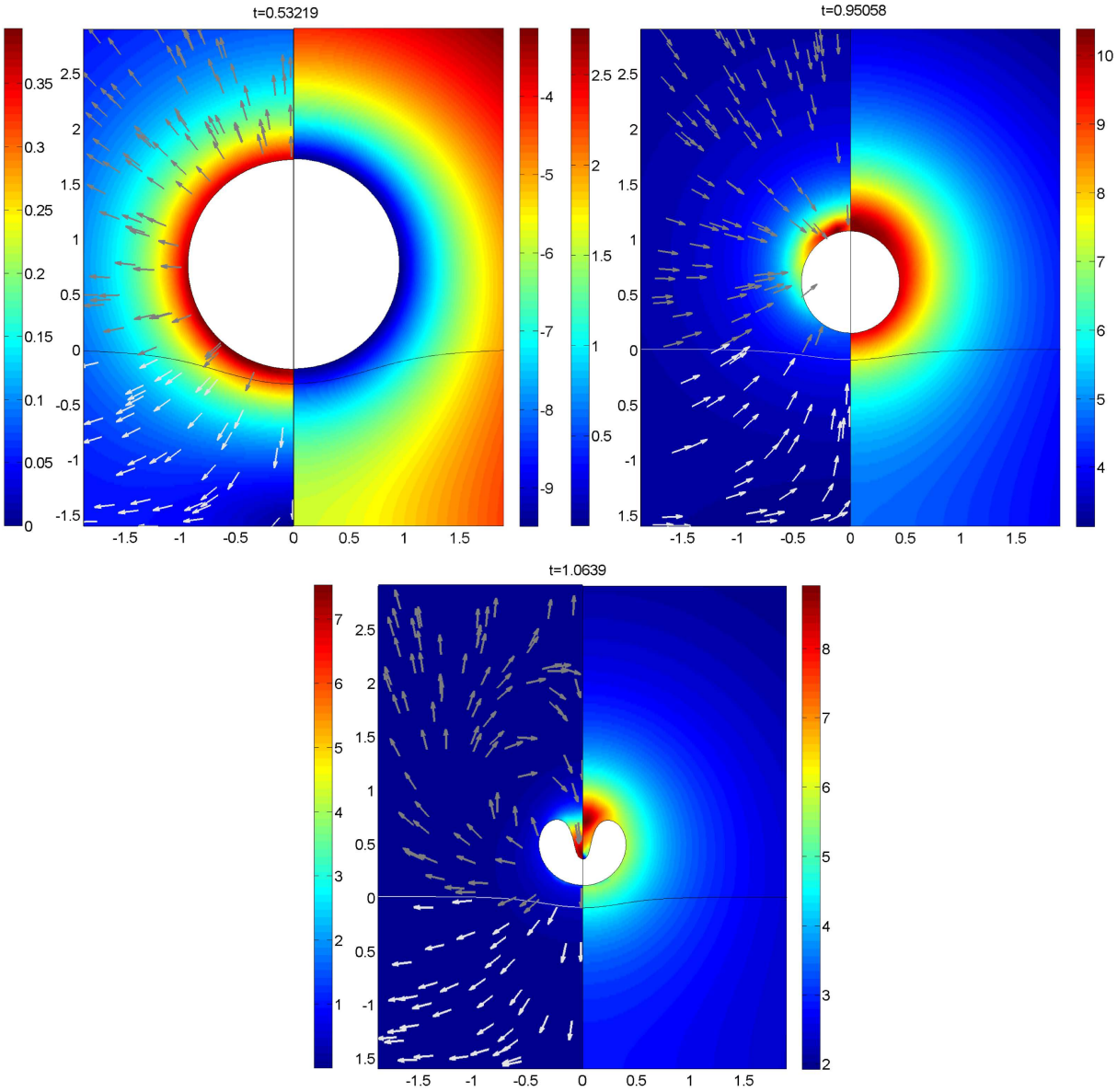

Figure 8.15: Pre-toroidal flow fields for an acoustically driven cavitation bubble with identical parameters to figure 8.12, with a rigid wall located at $H = 1.6R_{max}$ from the initially flat interface.

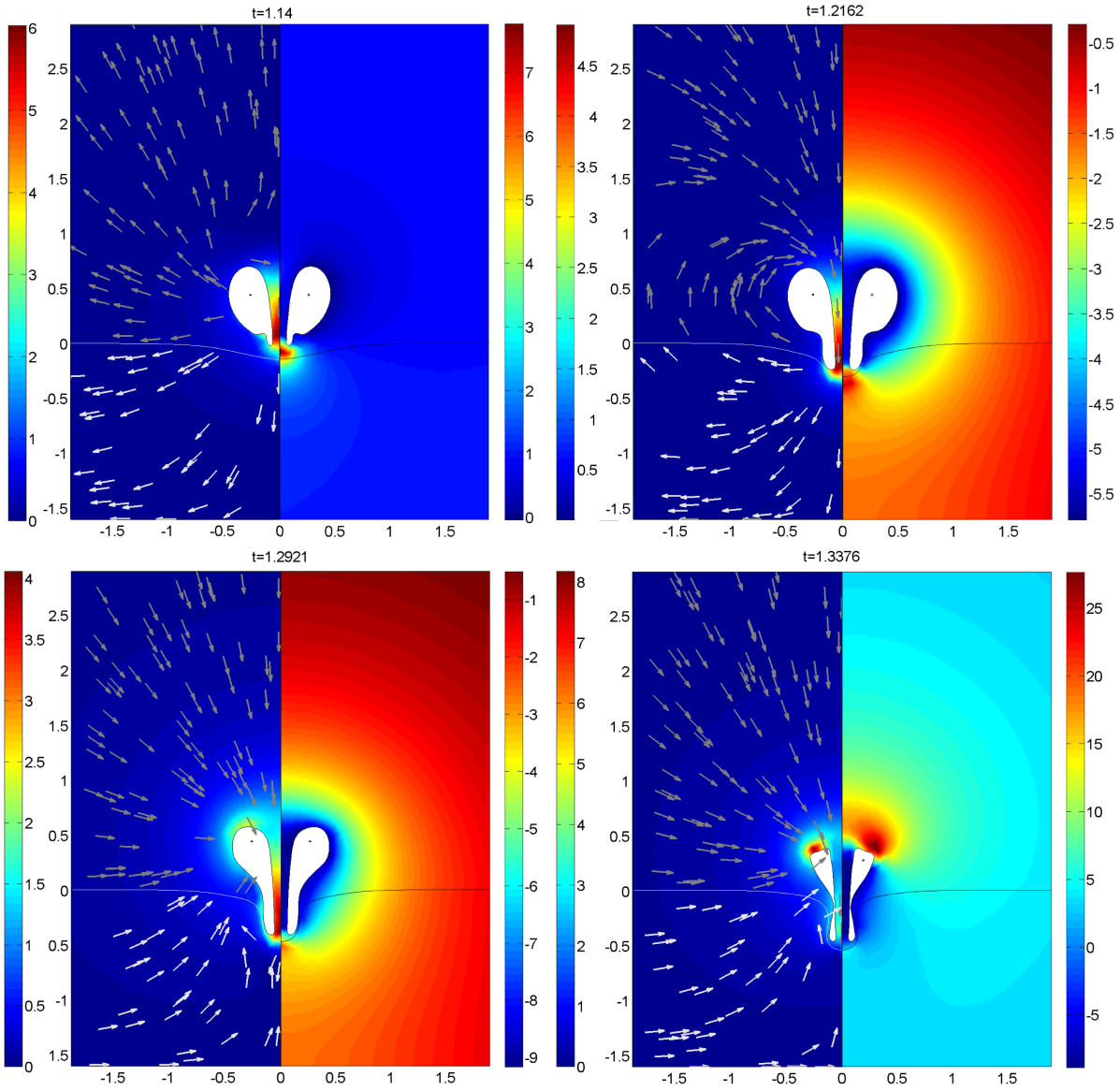

Figure 8.16: Post-impact flow fields for an acoustically driven cavitation bubble with identical parameters to figure 8.12, with a rigid wall located at $H = 1.6R_{max}$ from the initially flat interface.

significant benefit in drug delivery applications.

8.3.3 New experimental evidence of peeling

Recently, the peeling phenomena observed for very shallow layer depths has been potentially been observed experimentally by Tomita *et al* [83]. In these experiments, a backed layer of oil based ink with a near uniform depth of $3\mu m$ was submerged in water tank and insonated at $28Khz$. Photographic evidence showed that after treatment in this way, the grouping of cavitation filaments produced sufficiently large bubble clusters to remove the ink from the surface. The authors postulate this was due to both jet impact and a shear flow of water against the solid nickel surface. A photograph taken of the substrate and oil coating after the experiment is shown in figure 8.18.

The results presented here illustrate that a different physical mechanism may be appropriate. As such more detailed experiments should be performed to help identify the dominant phenomenon.

8.4 Chapter summary

This chapter has investigated various aspects of acoustically driven bubble behaviour relevant to biomedical applications. It has shown that the tension of a separating membrane can have a profound effect on the bubble dynamics, particularly when the bubble is oscillating at a close standoff distance. Furthermore, it has clearly shown that a rigid backing of the second liquid layer will cause significant differences to the fluid dynamics. This has lead to the discovery of the phenomenon of membrane peeling, a mechanism that depends on the re-expansion of a toroidal bubble to lift the second layer away from the backing plate. The simulations performed here have shown that the use of this as a sonoporation mechanism may be restricted to relatively deep cell layers, and to high frequency, high amplitude ultrasonic agitation.

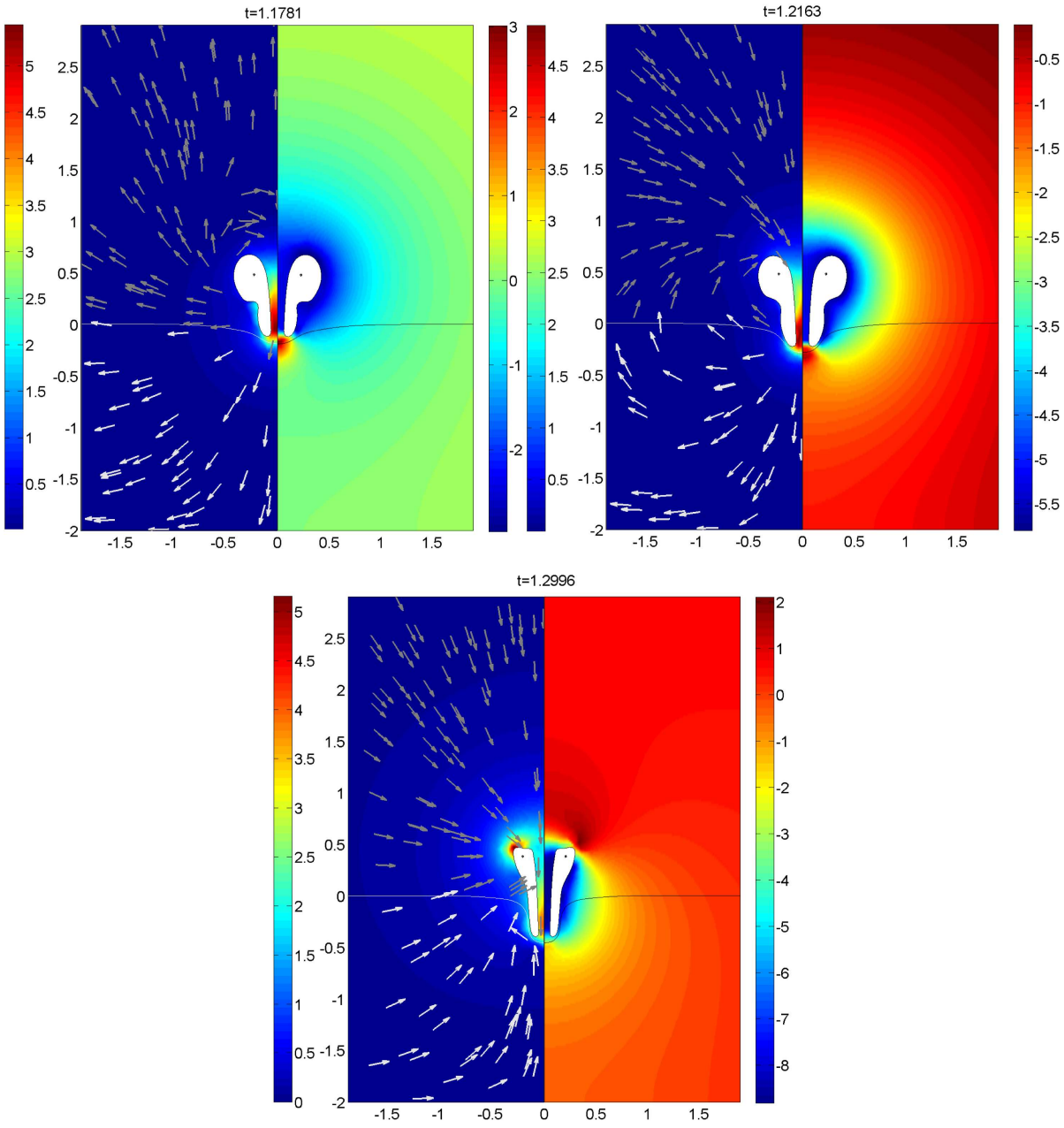

Figure 8.17: Toroidal behaviour of an acoustically driven bubble with identical parameters to figure 8.12, with the depth of the second fluid layer $H = 2.0$ maximum bubble radii.

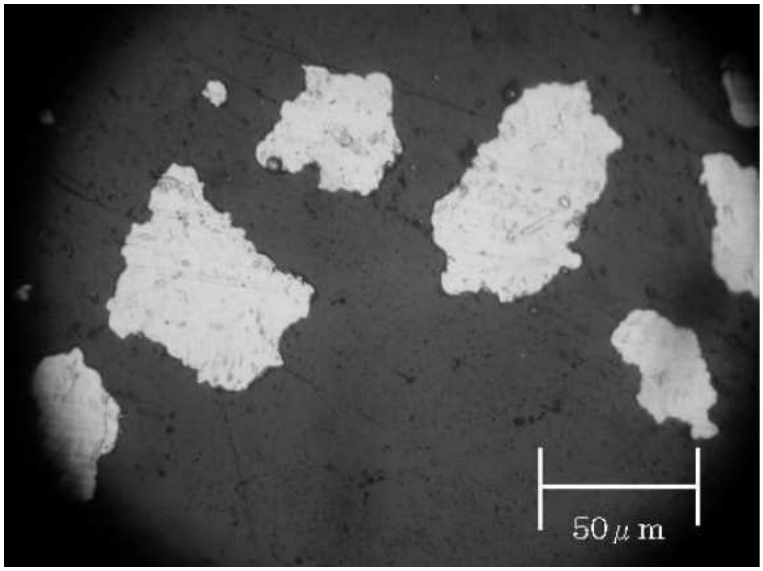

Figure 8.18: Experimental evidence of peeling of an oily ink layer by cavitation bubble interactions [83].

Chapter 9

Conclusions and avenues for future research

The violent interactions between bubbles and a two fluid interface are of critical importance in many industrial and biomedical applications. This work has sought a greater understanding of these interactions through an in depth numerical investigation over a wide range of realistic parameters, and has produced a host of new phenomena not previously predicted in this context. A highly advanced boundary integral approach has developed to simulate the essentially incompressible fluid mechanics in the exterior liquid layers during both the pre and post toroidal stages of bubble motion. Significantly this implementation, as detailed in Chapters 3 and 4, has successfully incorporated the interaction of one or more bubbles with a fluid-fluid interface, and has effectively integrated the vortex ring method for toroidal bubbles. As far as the author is aware, the combination of these mechanisms has not been implemented in a pure boundary integral scheme before [1].

A detailed overview of the simpler spherical bubble system has been provided in Chapter 2, illustrating the dependencies of the Rayleigh-Plesset equation on bubble pressures,

[1]The incorporation of the vortex ring method has been performed in the BIM/FEM coupling found in Klaseboer *et al* [44].

surface tension and visco-elastic encasement. Furthermore, an approximation to the two fluid problem has been created under a spherical bubble restriction. This has provided essential information about the far field behaviour of the system, as well as allowing for the general migratory behaviour of a single bubble to be extrapolated from the Kelvin impulse [8]. The spherical model has also be used as an excellent test case for the non-spherical boundary integral implementation in Chapter 5, both for a bubble in an infinite fluid, and for a bubble near a two fluid interface with $\rho = 1$.

Additional validation of the numerical simulator has been provided through the excellent agreement with well known free surface and rigid boundary experiments in both the pre and post toroidal phases of bubble motion. Excellent qualitative agreement has also been shown with the water/white spirit experiments of Chahine and Bovis [23] for centimetre sized bubbles in a reduced pressure environment, and the numerical simulations of Klaseboer and Khoo [45]. Further investigation of the buoyancy parameter space has demonstrated the transition through the null impulse state predicted by the spherical approximation to the Kelvin impulse, both for bubbles located in the lighter and denser of the liquid layers.

The excellent performance seen across all the test cases herein gives confident assurance that the results gained from the subsequent investigation were both realistic and representative of the behaviour one may observe in the physical system. As such the following conclusions are valid, and illustrate the benefit of using this numerical procedure to investigate the fluid dynamics as opposed to performing many expensive and potentially impossible experiments.

9.1 Conclusions

The single bubble simulations near a density discontinuity have provided some very interesting results. Notably the examination of centroid displacement over a range of density

ratios and standoff distances has demonstrated that bubble translation is heavily dependent upon non-spherical jetting effects. As a result, translation has been shown to depend greatly on the density ratio, as for near unity ratios the prolonged spherical state and late jetting phenomena result in diminished bubble motions in comparison to more extreme Atwood numbers. In addition to this, the translation of the centroid is not necessarily unidirectional, with translation in opposition to the spherical Kelvin impulse theory during the bubble expansion both initially and in the toroidal phase. Analysing the level of surface deformation through these simulations gave results in agreement with that expected from the spherical model during the first oscillation, with surface deformation decreasing with increasing ρ. The continuation into the toroidal phase has however shown that the threading jets will interact directly with the two fluid interface at sufficiently shallow standoff distances, and hence mixing between the two exterior liquids will be catalysed by bubbles in the less dense layer after the first oscillation. Such a result would not have been observed from a purely spherical approach, or even an extension to spherical perturbations.

Most significantly, the numerical investigation has allowed for the examination of the system at sub-unity standoff distances. Indeed, even in the well researched free surface case at $h = 0.5$, the modelling of the second layer by means of a zero density incompressible fluid has provided more insight into the possible fluid flow caused by the formation of the surface spike. In particular it has demonstrated that a significant vortex sheet will form between the spike and the surrounding gas, with the fluid in each flowing quickly in opposite directions. For greater density ratios, it has been shown that surface spike generation is retarded significantly as ρ is increased. This retardation is in fact total for $\rho > 0.4$, with the emergence of the new behaviour of surface mounding. The width of the bubble jets also increases with ρ, and can result in non-axial jet impact events occurring due to the greater mass of liquid above the bubble away from the axis. These may have

a detrimental effect on the ability of the bubble to form free radicals from heating the enclosed gas, as it is likely the bubble will be split into a simply connected and a toroidal component. Furthermore, the simply connected component will be advected away from the toroid by the high speed liquid jet, and hence when these bubble fragments re-expand they may not be close enough to coalesce.

As ρ approaches unity from below, non-spherical effects are delayed as expected. Bubble jet impact may in fact happen during the expansion phase of the second bubble oscillation, and due to the effects this has on the pressure flow field this may be axially located despite the earlier formation of a concave jet tip. Due to the density ratio, jetting is directed away from the boundary. Therefore there is no jet/interface interaction, and the bubble jet serves to decrease the interfacial deformation by dragging the bubble away. The fore of the toroidal bubble is hence also unrestricted by the two fluid interface, and is therefore free to form a forward lobed structure as opposed to exhibiting splash characteristics. This may subsequently allow for the thin jet to break off inside the bubble core, which may provide an effective means for creating more free radical reagents during subsequent collapses, albeit further away from the interface.

The attractive nature of the density stratification produces very interesting behaviour for density ratios greater than unity. As noted from the greater standoff simulations, this is particularly true for the toroidal phase. During the initial expansion, one has observed the bubbles becoming entrained into the interface, with further deformation caused by the high pressure regions backing the bubbles and initiating jet formation. After jet impact occurs, the rapid speed of the liquid jets promote a significant increase in the jump in tangential velocity, which will aid instability driven mixing. Moreover the inertia of the jet causes significant additional tunnelling into the denser layer. As the density ratio increases, so too does the inhibitory affect on the formation of the frontal toroidal lobes. At $\rho = 1.2$ these are able to significantly expand into the second layer. For high ratios they

form a circumventing splash about the bubble, which may result in earlier jet pinch off at the far pole. A bubble creeping behaviour has also been observed for density ratios close to $\rho = 2$, where the re-inflating bubble literally crawls down the pit formed in the second layer by the bubble jet. In several cases, the simulations progressed sufficiently far that the bubble centroid was in fact below the initial level of the interface, a feature which would again be beneficial in industrial applications, particularly when bubble creation inside the denser layer is difficult or impossible.

Investigating the effects of additional bubbles has also been paramount. This has provided valuable insights into useful bubble configurations in industrial, and potentially biomedical, applications. Firstly, it has clearly illustrated that the presence of a second bubble in a homogeneous configuration, and at equivalent standoff and bubble separation distances, will inhibit bubble jet interactions with the two fluid interface significantly. This could prove highly detrimental to industrial mixing processes if cavitation is restricted to one layer, although it would be beneficial in limiting jet induced collateral damage in intraocular photodisruption and other laser based surgical treatments. The hypothesised existence of a null impulse state for the closer bubble has been proven for the density ratio $\rho = 2$, and is anticipated to exist for all other non-unity density ratios, albeit at different standoff and separation distances. This state has been shown to be accompanied by dual polar jetting and not perpendicular pinching as was the case for the buoyancy/interface interaction shown in Chapter 5. At sufficiently large separation distances however, the two bubbles have been shown to both jet toward the denser layer, which could potentially be used to transfer fresh liquid to a reacting interface.

In heterogeneous configurations one has demonstrated the phenomenon of jet deflection through a totally aspherical mechanism. That is to say that through the interactions of a jetting toroidal bubble in the lighter fluid, one can cause the opposing bubble to jet in the same direction before the Bjerknes attraction of the lighter layer bubble causes

an interfacially directed jet. This is substantially different from the equal density case, where both bubbles behave as if near a rigid boundary, and when at equal standoff distances have a negligible influence on the two fluid interface. Additional features have been predicted, depending on the standoff distances of each bubble. When the denser layer bubble is sufficiently close to the interface for example, the opposing bubble is able to form a hyper jet, driving a large amount of liquid into the opposing bubble core. The bubble positions at the end of this simulation also indicate that the two bubbles may then coalesce, with the encapsulation of a droplet of the lighter liquid by the denser liquid. The potential applications for this are great, ranging from the production of pharmaceuticals to the catalysation of endothermic chemical processes.

Including a third bubble into the simulations has uncovered yet more interesting behaviour. Primarily it has shown that it is very likely in a heterogeneous configuration that at least one bubble will jet toward the interface. This is hugely encouraging for the aforementioned chemical processes, although it is equally problematic for surgical procedures as it will lead to unwanted tissue deterioration. For two bubbles in the lighter layer, a configuration can be constructed in which all bubbles jet toward the interface. Such a system would promote Rayleigh-Taylor and Richtmyer-Meshkov instabilities as the two fluids are accelerated into one another. In contrast if two bubbles are in the denser layer, the central bubble can be forced to jet away from the interface, which would hence limit hydrodynamic instabilities associated with the acceleration of the denser liquid into the lighter layer.

Potentially the most significant results are those from Chapter 8 involving the behaviour of acoustically driven cavities in various situations. These have shed new light on mechanisms that will occur to some extent in biomedical procedures, yet which are extremely difficult and may even be impossible to observe experimentally. Membrane interactions have clearly demonstrated that bubble behaviour may not match that of simple

rigid boundaries or free surfaces. Moreover they have shown bubble actions to be significantly non-spherical, although jetting may not occur during the first few oscillations. More significantly however is the effect of including a backing plate to the second layer, a commonly used experimental method for examining bubble-cell interactions. This has shown that the semi-infinite fluid interactions, as detailed in Chapter 6, can be almost completely dominated by the interaction with the plate. By coincidence this has also illustrated a new mechanism for tissue damage, the peeling of the attached layer through the interaction with the re-expanding toroidal bubble. The occurrence of this phenomena is truly significant, and although the resultant damage has potentially been experimental realised, as for example the cornea specimen in figure 1.1, it would be extremely difficult to identify the mechanism without this numerical approach. Previously, it was assumed that the removal of tissue about the impact site was due to the high shear rates accompanying the fluid jet [86]. While this is no doubt important, the inertial interaction of the expanding forward bubble lobes could provide an additional destructive mechanism. Moreover it may provide an efficient method for removing unwanted material layers by literally lifting it off an attached surface, such as removing cholesterol from the aortic artery.

In terms of sonoporation and gene transfection, the investigation into the cell layer depth and standoff distance of a UCA has given great insight into the significant values of these parameters. In particular the behaviour of a $2.5\mu m$ UCA with similar characteristics to Sonovue, driven by a high amplitude acoustic wave with megahertz frequency, has been investigated in detail. At shallow cell layer depths the peeling mechanism is observed, and the jetting motion will lead to a sonopore on the length scale of a cell. This of course will lead to the death of the target cell, although adjacent cells may in fact be porated through the stresses placed on them by the lifting mechanism. At cell layer depths greater than one maximum bubble radii, very different behaviour is observed. The distance from the rigid

boundary allows the frontal lobe to elongate substantially, with the separating membrane being perturbed accordingly. What is more this is followed by the secondary collapse, which may separate the frontal lobe section away from the rear, physically injecting this section into the tissue layer. Clearly such an action would be hugely beneficial in transfection, as the damaged membrane appears to close up behind this potentially DNA enclosing segment. Additionally with the destruction of the UCA shell in this manner, the gaseous contents of the bubble are likely to dissolve into the surrounding fluid, and hence the bubble itself would rapidly disappear. One may therefore anticipate very limited subsequent collateral damage associated with the continued excitation of the UCA fragments, which naturally will promote the survival of the transfected cell.

9.2 Avenues for future research

Whilst this work has provided a detailed investigation into some of the phenomena associated with the interactions of bubbles with complicated boundaries, areas for potential future research still remain and indeed have been generated by the results contained herein. Further advances are still possible in the boundary integral implementation for example. The accurate simulation of cavities with non-axially impacting threading jets is still an area of great interest. Moreover the actions of the vortex sheet generated at jet impact have not been investigated in depth, yet may be significant. Furthermore the inclusion of viscosity into the boundary conditions could introduce more unknown phenomena, and would become especially prevalent as the length scales investigated continue to decrease. Naturally the axisymmetric geometries investigated here are not perfect representations of the in vivo environment experienced in biomedical applications, and so fully three dimensional simulations should be investigated, particularly in the toroidal stages of the bubble lifetimes. The inclusion of elasticity into the surrounding boundaries is also paramount. As illustrated in Chapter 1 some methods have included linearly elas-

tic boundaries through BIM-FEM modelling, however fully non-linear elastic interactions are likely to be more representative of a realistic environment. To accurately model these types of interactions, and to include more accurate acoustic pressure fields, it is not unthinkable that more advanced field based methods will be required. Indeed the effect of compressibility has been ignored herein, although in heavily insonated liquids it will be important. This will be particularly true in the period immediately following jet impact, as the shockwaves observed experimentally may act to disperse a considerable amount of kinetic energy from the system. Therefore investigation in this area should be forwarded to gain a greater understanding of the non-inertial characteristics associated with bubble dynamics.

From an experimental perspective, the results gained in Chapter 8 clearly demonstrate that existing procedures may not be sufficient to capture in vivo sonoporation behaviour. Particularly the aforementioned dominance of a backing plate must be carefully considered when extrapolating general results from sonoporation experiments. It would also be of great interest to physically visualise the mechanism of cavitation assisted peeling in greater depth, to verify if the toroidal bubble peeling mechanism uncovered here genuinely occurs, and to what extent it may be responsible for the destruction of the surrounding tissues.

List of References

[1] M. Abramowitz and I. A. Stegun. *Handbook of Mathematical Functions with Formulas, Graphs, and Mathematical Tables*. Dover, New York, Ninth Dover printing, Tenth GPO printing edition, 1964.

[2] B. P. Barber, R. Löfstedt, K. Weninger, and S. Putterman. Sonoluminescing bubbles and mass diffusion. *Physical Review E*, 51(5):4400–4410, 1995.

[3] T. J. Beale, Y. T. Hou, and J. Lowengrub. Convergence of a boundary integral method for waterwaves. *Journal of Numerical Analysis*, 33:1797–1843, 1996.

[4] T. B. Benjamin and A. T. Ellis. The collapse of cavitation bubbles and the pressures thereby produced against solid boundaries. *Phil. Trans. R.Soc.Lond. A*, 260:221–240, 1966.

[5] J. P. Best. *The Dynamics of Underwater Explosions.* PhD thesis, The University of Wollongong, 1991.

[6] J. P. Best. The formation of toroidal bubbles upon the collapse of transient cavities. *Journal of Fluid Mechanics*, 251:70–107, 1993.

[7] J. P. Best. The rebound of toroidal bubbles. *In: Bubble dynamics and interface phenomena. Eds. J. R. Blake, J. M. Boulton-Stone and N. H. Thomas*, pages 405–412, 1994.

[8] J. R. Blake. The Kelvin impulse: Application to cavitation bubble dynamics. *Journal of Australian Mathematical Society*, 30:127–146, 1988.

[9] J. R. Blake, M. C. Hooton, P. B. Robinson, and R. P. Tong. Collapsing cavities, toroidal bubbles and jet impact. *Philosophical Transactions: Mathematical, Physical and Engineering Sciences.*, 355(1724):537–550, 1997.

[10] J. R. Blake, B. B. Taib, and G. Doherty. Transient cavities near boundaries part 1. rigid boundary. *Journal of Fluid Mechanics*, 170: 479-497:479–497, 1986.

[11] J. R. Blake, B. B. Taib, and G. Doherty. Transient cavities near boundaries part 2. free surface. *Journal of Fluid Mechanics*, 181:197–212, 1987.

[12] J.R. Blake and D. C. Gibson. Cavitation bubbles near boundaries. *Annual Review of Fluid Mechanics*, 19:99:123, 1987.

[13] M. J. K. Blomley, J. C. Cooke, E. C. Unger, M. J. Monaghan, and D. O. Cosgrove. Microbubble contrast agents, a new era in ultrasound. *British Medical Journal*, 322:1222–1225, 2001.

[14] J. M. Boulton-Stone. The effect of surfactant on bursting gas bubbles. *Journal of Fluid Mechanics*, 302:231–257, 1995.

[15] J. M. Boulton-Stone and J. R. Blake. Gas bubbles bursting at a free surface. *Journal of Fluid Mechanics*, 254:437–466, 1993.

[16] C. E. Brennen. *Cavitation and Bubble Dynamics.* Oxford University Press., 1995.

[17] E. A. Brujan, G. S. Keen, A. Vogel, and J. R. Blake. The final stage of the collapse of a cavitation bubble close to a rigid boundary. *Physics of Fluids*, 14(1):85–92, 2002.

[18] E. A. Brujan, K. Nahen, P. Schmidt, and A. Vogel. Dynamics of laser-induced cavitation bubbles near an elastic boundary. *Journal of Fluid Mechanics*, 433:251–281, 2001.

[19] E. A. Brujan, K. Nahen, P. Schmidt, and A. Vogel. Dynamics of laser-induced cavitation bubbles near elastic boundaries: Influence of the elastic modulus. *Journal of Fluid Mechanics*, 433:283–314, 2001.

[20] M. L. Calvisi, J.I. Iloreta, and A.J. Szeri. Dynamics of bubbles near a rigid surface subjected to a lithotripter shock wave. part 2. reflected shock intensifies non-spherical cavitation collapse. *Journal of Fluid Mechanics*, 616:63–97, nov 2008.

[21] M. L. Calvisi, O. Lindau, J. R. Blake, and A. J. Szeri. Shape stability and violent collapse of microbubbles in acoustic travelling waves. *Physics of Fluids*, 19, 2007.

[22] C. Carstensen, S. A. Funken, and E. P. Stephan. A posteriori error estimates for hp boundary element methods. *Applied Analysis*, 61:233–253, 1995.

[23] G. L. Chahine and A. Bovis. Oscillation and collapse of a cavitation bubble in the vicinity of a two-liquid interface. *Springer series in electrophysics 4 - Cavitation and inhomogeneities in underwater acoustics*, pages 23–29, 1980.

[24] K. Chetty, E. Stride, C. A. Sennoga, J. V. Hajnal, and R. J. Eckersley. High-speed optical observations and simulation results of sonovue microbubbles at low-pressure insonation. *IEEE Transactions on Ultrasonics, Ferroelectrics, and Frequency Control*, 55(6):1333–1342, 2008.

[25] W. Choi and R. Camassa. Fully nonlinear internal waves in a two fluid system. *Journal of Fluid Mechanics*, 396:1–36, 1999.

[26] C. C. Church. The effects of an elastic solid surface layer on the radial pulsations of gas bubbles. *Journal of the acoustic society of America*, 97:1510–1521, 1995.

[27] C.C Church. A theoretical study of cavitation generated by an extracorporeal shock wave lithotripter. *Journal of the Acoustic Society of America*, 86:215–227, 1989.

[28] R. H. Cole. *Underwater Explosions.* Princeton University Press., 1948.

[29] D.O. Cosgrove. Ultrasound contrast agents: An overview. *European Journal of Radiology*, 60:324–330, 2006.

[30] S. Dahnke, K. Swamy, and F. J. Keil. Modeling of three dimensional pressure fields in sonochemical reactors with an inhomogeneous density distribution of cavitation bubbles. comparison of theoretical snd experimental results. *Ultrasonics Sonochemistry*, 6:31–41, 1999.

[31] R. Day. *Boundary Integral Simulations of Inviscid flow for inkjet printing.* PhD thesis, The University of Cambridge, 1998.

[32] D. J. Flannigan and K. S. Suslick. Plasma formation and temperature measurement during single-bubble cavitation. *Nature*, 434:52–55, 2005.

[33] S. W. Fong, E. Klaseboer, C. K. Turangan, B. C. Khoo, and K. C. Hung. Numerical analysis of a gas bubble near biomaterials in an ultrasound field. *Ultrasound in Medicine and Biology*, 32(6):925–942, 2006.

[34] D. Fructus and J. Grue. Fully nonlinear solitary waves in a layeredstratified fluid. *Journal of Fluid Mechanics*, 505:323347, 2004.

[35] S. Georgescu, J. Achard, and E. Canot. Jet drops ejecting in bursting gas bubble processes. *European Journal of Mechanics B/Fluids*, 21:265–280, 2002.

[36] D. C. Gibson and J. R. Blake. Growth and collapse of a vapour cavity near a free surface. *Journal of Fluid Mechanics*, 111:123–140, 1981.

[37] D. C. Gibson and J. R. Blake. The growth and collapse of bubbles near deformable surfaces. *Applied Scientific Research*, 38:215–224, 1982.

[38] J. Grue, H. A. Friis, E. Palm, and P. O. Rusas. A method for studying fully non-liner interfacial waves. *Journal of Fluid Mechanics*, 351:223–252, 1997.

[39] Y. Hao and A. Prosperetti. The effect of viscosity on the spherical stability of oscillating gas bubbles. *Physics of Fluids*, 11(6):1309–1317, 1999.

[40] K.R. Helfrich and W. K. Melville. Long nonlinear internal waves. *Annual Review of Fluid Mechanics*, 38:395–425, 2006.

[41] L. Hoff. *Acoustic Characterization of contrast agents for medical ultrasound imaging.* Kluweer Academic Publishers, 2001.

[42] T. Y. Hou, J. S. Lowengrub, and M. Shelly. Boundary integral methods for multicomponent fluids and multiphase materials. *Journal of Computational Physics*, 169:302–362, 2001.

[43] Lighthill J. *An Informal Introduction to Theoretical Fluid Mechanics.* Oxford University Press, 1986.

[44] E. Klaseboer, K. C. Hung, C. Wang, B. C. Wang, C. W. andKhoo, P. Boyce, S. Debono, and H. Charlier. Experimental and numerical investigation of thedynamics of an underwater explosion bubblenear a resilient/rigid structure. *Journal of Fluid Mechanics*, 537:387–413, 2005.

[45] E. Klaseboer and B. C. Khoo. Boundary integral equations as applied to an oscillating bubble near a fluid-fluid interface. *Computational Mechanics*, 33:129–138, 2004.

[46] E. Klaseboer and B. C. Khoo. An oscillating bubble near an elastic material. *Journal of Applied Physics*, 96(10):5808–5818, 2004.

[47] H. Koike, N. Tomita, H. Azuma, Y. Taniyama, K. Yamasaki, Y. Kunugiza, K. Tachibana, T. Ogihara, and R. Morishita. An efficient gene transfer method mediated by ultrasound and microbubbles into the kidney. *Journal of Gene Medicine*, 7:106–116, 2005.

[48] H. Lamb. *Hydrodynamics.* Cambidge University Press, 1932.

[49] W. Lauterborn and H. Bolle. Experimental investigations of cavitation-bubble collapse in the neighbourhood of a solid boundary. *Journal of Fluid Mechanics*, 72:391–399, 1975.

[50] M. Lenoir. Calcul numérique de l'implosion d'une bulle de cavitation au voisinage d'une paroi ou dunesurface libre. *Journal Mécanique*, 15:725751, 1976.

[51] D. Leppinen and J. R. Lister. Capillary pinch-off in inviscid fluids. *Physics of Fluids*, 15(2):568–578, 2003.

[52] M. S. Longuet-Higgins and E. D. Cokelet. The deformation of steep surface waves on water. 1. A numerical methodof computation. *Proceedings of the Royal Society of London Series A*, 350:l–26, 1976.

[53] T. S. Lundgren and N. N. Mansour. Vortex ring bubbles. *Journal of Fluid Mechanics*, 224:177–196, 1991.

[54] P. Marmottant, S. van der Meer, M. Emmer, M. Versluis, N. de Jong, S. Hilgenfeldt, and D. Lohse. A model for large amplitude oscillations of coated bubbles accounting for buckling and rupture. *Journal of the Acoustical Society of America*, 118:3499–3505, 2005.

[55] T. J. Matula, Roy R. A., P. D. Mourad, W. B. McNamara III, and K. S. Suslick. Comparison of multibubble and single-bubble sonoluminescence spectra. *Phys. Rev. Lett.*, 75(13):2602–2605, Sep 1995.

[56] H. Miao and S. M. Gracewski. Coupled FEM and BEM code for simulating acoustically excited bubbles near deformable structures. *Computation Mechanics*, 42:95–106, 2008.

[57] D. Miller and J. Quddus. Diagnostic ultrasound activation of contrast agent gas bodies induces capillary rupture in mice. *Proceedings of the National Academy of Sciences of the United States of America*, 97:10179 – 10184, 2000.

[58] D. L. Miller, S. Bao, and B. D. Thrall. Transfection of a reporter plasmid into cultured cells in vitro. *Ultrasound in Medicine and Biology*, 23(6):953–959, 1997.

[59] D. L. Miller, S. V. Pislaru, and J. F. Greenleaf. Sonoporation: Mechanical DNA delivery by ultrasonic cavitation. *Somatic Cell and Molecular Genetics*, 27(1):115–134, November 2002.

[60] L. M. Milne-Thomson. *Theoretical Hydrodynamics*. Dover Publications, 5 edition, 1968.

[61] S. Nagrath, K. E. Jansen, and R. T. Lahey. Computation of incompressible bubble dynamcis with a stabilized finite element level set method. *Computational Methods in Applied Mechanical Engineering*, 194:4565–4587, 2005.

[62] Q. Nie and G. Baker. Application of adaptive quadrature to axi-symmetric vortex sheet motion. *Journal of Computational Physics*, 143:49–69, 1998.

[63] M. Nitsche and P.H. Stenn. Numerical simulation of inviscid capillary pinchoff. *Journal of Computational Physics*, 200:299–324, 2004.

[64] A. Pearson. *Hydrodynamics of Jet Impact in a Collapsing Bubble.* PhD thesis, The University of Birmingham, 2003.

[65] A. Pearson, J. R. Blake, and S. R. Otto. Jets in bubbles. *Journal of Engineering Mathematics*, 48:391–412, 2004.

[66] A. Phillip and W. Lauterborn. Cavitation erosion by single laser-produced bubbles. *Journal of Fluid Mechanics*, 361:75–116, 1998.

[67] M. S. Plesset and T. P Mitchell. On the stability of the spherical shape of a vapour cavity in a liquid. *Quaterly Journal of Applied Mathematics*, 13:419–430, 1956.

[68] S. Popinet and S. Zaleski. Bubble collapse near a solid boundary: a numerical study of the influence of viscosity. *Journal of Fluid Mechanics*, pages 137–163, 2002.

[69] C. Pozrikidis. Theoretical and computational aspects of the self induced motion of three dimensional vortex sheets. *Journal of Fluid Mechanics*, 425:335–336, 2000.

[70] P. Prentice, A. Cuschieri, K. Dholakia, M. Prausnitz, and P. Campbell. Membrane disruption by optically controlled microbubble cavitation. *Nature Physics*, 1:107–110, 2005.

[71] A. Prosperetti. Thermal effects and damping mechanics in the forced radial oscillations of gas bubbles in liquids. *Journal of the Acoustic Society of America*, 61(1):17–27, 1977.

[72] N. Rapoport, W. G. Pitt, Sun H., and J. L. Nelson. Drug delivery in polymeric micelles: from in vitro to in vivo. *Journal of Controlled Release*, 91:85–95, 2003.

[73] Lord. Rayleigh. On the pressure developed in a liquid during the collapse of a spherical void. *Phil.Mag.*, 34:94–98, 1917.

[74] P. B. Robinson, J. R. Blake, T. Kodama, A. Shima, and Y. Tomita. Interaction of cavitation bubbles with a free surface. *Journal of Applied Physics*, 89(12):8225–8237, 2001.

[75] S. Seemann, P. Hauff, M. Shultz-Mosgau, C. Lehmann, and R. Reska. Pharmaceutical evaluation of gas-filled microparticles as gene delivery system. *Pharmaceutical Research*, 19(3):250–257, march 2002.

[76] S. Shin. Internal wave computations using the ghost fluid methodon unstructured grids. *International Journal for Numerical Methods in Fluids*, 47:233–251, 2005.

[77] A. Skolarikos, G. Alivizatos, and J. Rosette. Extracorporeal shock wave lithotripsy 25 years later:complications and their prevention. *European Urology*, 50:981 – 990, 2006.

[78] B. D. Storey and A. J. Szeri. Water vapour, sonoluminescence and sonochemistry. *Proceedings of the Royal Society of London Series A*, 456:1685–1709, 2000.

[79] K. S. Suslick. Sonochemistry. *Science*, 247:1439–1445, 1990.

[80] M. Sussman and P. Smereka. Axisymmetric free boundary problems. *Journal of Fluid Mechanics*, 341:269–294, 1997.

[81] B. B. Taib. *Boundary Integral Method Applied to Cavitation Bubble Dynamics.* PhD thesis, The University of Wollongong, 1985.

[82] N. Takada, M. Misawa, A. Tomiyama, and S. Hosokawa. Simulation of bubble motion under gravity by lattice Boltzmann method. *Journal of Nuclear science and Technology*, 38:330–341, 2001.

[83] Y. Tomita, T. Inaba, R. Uchikoshi, and T. Kodama. Peeling off effect and damage pit formation by ultrasonic cavitation. *Scientific Bulletin of the Politehnica University of Timisoara*, 2008.

[84] Y. Tomita and A. Shima. Mechanisms of impulsive pressure generation and damage pit formation by bubble collapse. *Journal of Fluid Mechanics*, 169:535–564, 1986.

[85] C. K. Turangan, G. P. Ong, E. Klaseboer, and B. C. Khoo. Experimental and numerical study of transient bubble-elastic membrane interaction. *Journal of Applied Physics*, 100:054910–1:054910–7, 2006.

[86] A. Vogel, P. Schweigner, A. Frieser, M. N. Asiyo, and R. Birngruber. Intraocular Nd:YAG laser surgery: Light tissue interaction, damage range, and reduction of collateral effects. *Journal of Quantum Electronics*, 26:2240–2260, 1990.

[87] Q. X. Wang. Numerical simulation of violent bubble motion. *Physics of Fluids*, 16(5):1610–1619, 2004.

[88] Q. X. Wang, K. S. Yeo, B. C. Khoo, and K. Y. Lam. Vortex ring modelling of toroidal bubbles. *Theoretical and Computational Fluid Dynamics*, pages 1–15, 2005.

[89] Q. X. Wang, K.S. Yeo, B. C. Khoo, and K. Y. Lam. Nonlinear interaction between gas bubble and free surface. *Computers and Fluids*, 25(7):607–628, 1996.

[90] S. Zhang and J. H. Duncan. On the non-spherical collapse and rebound of a cavitation bubble. *Physics of Fluids*, 6(7):2352–2362, 1994.

[91] S. Zhang, Duncan J. H., and G. L. Chahine. The final stage of the collapse of a cavitation bubble near a rigid wall. *Journal of Fluid Mechanics*, 257, 1993.

[92] Y. L. Zhang, K. S. Yeo, B. C. Khoo, and C. Wang. 3D jet impact and toroidal bubbles. *Journal of Computational Physics*, 166:336–360, 2001.